University of Southampton

Faculty of Physical Sciences and Engineering

School of Electronics and Computer Science

Plasmonically-enhanced microbolometric sensing and metasurface phased arrays based on the phase transition of vanadium dioxide

by

James Donaldson Frame IV

Thesis for the degree of Doctor of Philosophy.

22nd November 2021

Abstract

Solid-solid phase transition materials are a fascinating and diverse topic in the field of condensed matter physics. These extraordinary materials have exotic electronic properties that allow them to switch between distinct phases, each of which may have very different material properties. The implications of this may present, for example, in terms of their optical transmission, thermal characteristics and electrical behaviour. The allure of these materials has spawned an enormous amount of research which aims to understand, classify, and exploit the transition mechanisms in useful ways. The aim of this thesis is to explore novel applications for vanadium dioxide (VO_2), a material with a close-to-room temperature phase transition that can behave either as an insulator or as a metal.

The first application is improving the performance of microbolometric infrared detectors by means of integrating plasmonic nanoparticles with VO_2. Surface plasmons are coherent oscillation modes of plasma density which can be excited at the interface between a material with negative real permittivity and a material with positive real permittivity, most commonly a metal and dielectric, respectively. In plasmonic nanoparticles, localised surface plasmons can be directly excited by incident electromagnetic radiation. Localised surface plasmon resonance modes arise at specific frequencies depending on the permittivity and geometry of the nanoparticle and its surroundings and, for anisotropic geometries, are also polarisation-sensitive. Resonance amplitude, bandwidth and frequency are therefore highly tuneable by a variety of means. The resonance condition is characterised by concentration of the electric near field and enhanced absorption and scattering cross-section. Plasmonic nanoparticles can thus be used in a variety of ways, for example to control light at the nanoscale, efficiently convert light into heat and modulate forward or backward scattering. The flexibility and utility presented by localised surface plasmons has led to a wealth of research into reconfigurable metamaterials and tuneable plasmonic devices, and applications have been found in such diverse fields as medicine, photodetection, sensing and catalysis.

The interplay between plasmonic nanostructures and phase change materials is an emerging field, largely because 1.) phase change materials display strong contrast in optical and electronic properties and their behaviour can be strongly modulated by temperature, electromagnetic fields, mechanical forces etc.; 2.) plasmons can be used to modulate the phase transition behaviour and thus effective properties of the material; 3.) controlling the optoelectronic properties of phase change materials allows modulation of plasmon resonance characteristics; 4.) nanoparticles can be designed as localised heaters, frequency filters and polarimeters. Applying these principles to microbolometric photodetection could improve performance and functionality of devices, thus broadening the low-cost photodetector market and greatly benefitting users.

The first investigation involved measurement of the optical transmission spectrum (400 – 900 nm) and electric resistivity of a sample consisting of a silver nanorod array / VO_2 / sapphire. Localised surface plasmon resonance was identified by a strong dip in transmission (~30 %) and it was found to correlate with a dip in resistivity (~0.3 Ωcm). The resistance change was attributed to the thermoplasmonic effect, whereby high concentration and dissipation of electromagnetic energy by nanoparticles leads to localised heating in the film. The amplitude, position and shape of plasmon resonance peaks, as identified by transmission spectra, was observed to be strongly polarisation dependent.

The second work further investigated the thermoplasmonic effect in embedded gold nanorods between 2 – 16 μm by quantifying the suppression of VO_2 effective phase transition temperature. Effective phase transition temperature suppression of up to 4 °C was observed and greatest suppression corresponded to highest nanorod density. Transmission spectra showed that localised surface plasmon resonance can affect the effective material properties of VO_2 film far from the resonance wavelength. The findings demonstrate a reversible, in-situ method for tuning the effective phase transition temperature, significant for lowering energy requirements and device optimisation.

The observation of hysteresis in transmission spectra during the second work, as previously reported in literature, provided the motivation for the third investigation. Hysteresis is an important consideration in device design; it is sought after for memory because it allows multiple states to be stored; however, in sensing it is avoided, because typically sensor readout should not depend on the history of the system. To further investigate hysteresis in VO_2 films it was necessary to numerically model its behaviour. A modified version of the Maxwell Garnett effective medium approximation was developed and numerically tested using the Fresnel equations. The modified equation was justified by a novel approach to the VO_2 phase transition. Although intended as a phenomenological approach to interpreting hysteresis and intermediate states, experimental validation is required. Potentially the work can be used as a simple-to-implement model for hysteresis modelling in phase change materials.

The final project in this thesis used numerical analysis to investigate the potential for VO_2 as an active element in a metasurface phased reflectarray designed to control the deflection angle of an incident infrared beam. Ultimately a successful design using justifiable VO_2 parameters was not found, but some success was found by adjusting the 'polarisation factor' used in the material permittivity model. This suggests that perhaps with a different combination of materials, such a design could be possible and the design process used in future work. Following the electromagnetic numerical analysis, a thermal analysis was conducted to investigate if thermal isolation could help maintain specific temperatures for each element, a feature necessary for this type of beam steering platform. These simulation results suggest that etching trenches 1 μm deep could improve both intra-element temperature variation and overall power efficiency of such a device.

Publications arising from this thesis

1. Takeya H, **Frame JD**, Tanaka T, Urade Y, Fang X, Kubo W. *Bolometric photodetection using plasmon-assisted resistivity change in vanadium dioxide*. Scientific Reports, 8, 12764, **2018**.

2. **Frame JD**, Green NG, Fang X. *Modified Maxwell Garnett model for hysteresis in phase change materials*. Optical Materials Express, 8, 1988, **2018**.

3. Kubo W, Ogata Y, **Frame JD**, Tanaka T, Fang X. *Polarization-dependent phase transition temperature in plasmonic thin films*. Japanese Journal of Applied Physics, 59, 052001, **2020**.

4. Yin S, He F, Kubo W, Wang Q, **Frame JD**, Green NG, Fang X. *Coherently tunable metalens tweezers for optofluidic particle routing.* Optics Express, 28, 26, 38949038959, **2020**.

Conference proceedings

Oral presentations

1. **Frame JD**, Green N, Kubo W, Fang X. *Controlling the phase transition of vanadium oxide using plasmonic metamaterials*. The 7th Advanced Lasers and Photon Sources (ALPS 2018), 1p ALPS9-G1-4, **2018**. OPTICS & PHOTONICS International Congress 2018 (OPIC 2018). PACIFICO Yokohama, 1-1-1, Minato Mirai, Nishi-ku, Yokohama 220-0012, JAPAN. 23rd – 27th April 2018.

2. **Frame JD**, Green N, Kubo W, Fang X. *Plasmonic vanadium dioxide microbolometers with wavelength and polarisation sensitivity.* Plasmonics: Design, Materials Fabrication, Characterization, and Applications XVI. Proceedings vol. 10722, SPIE, **2018**. SPIE Optics + Photonics, Nanoscience + Engineering 2018. San Diego Convention Center, 111 W Harbor Dr, San Diego, CA 92101, USA. 19th – 23rd August 2018.

Poster presentation

3. **Frame JD**, Kubo W, Fang X. *Plasmonic Tuning of Effective Phase Transition Temperature and Electrical Conductivity*. Conference on Lasers and Electro-Optics (CLEO 2018) 2 p.2931256, **2018**. San Jose McEnery Convention Center, 150 W San Carlos St, San Jose, CA 95113, USA. 13th – 18th May 2018.

Declaration of Authorship

I, James D. Frame, declare that this thesis and the work presented in it are my own and has been generated by me as the result of my own original research.

I confirm that:

- This work was done wholly or mainly while in candidature for a research degree at this University;

- Where any part of this thesis has previously been submitted for a degree or any other qualification at this University or any other institution, this has been clearly stated;

- Where I have consulted the published work of others, this is always clearly attributed;

- Where I have quoted from the work of others, the source is always given. With the exception of such quotations, this thesis is entirely my own work;

- I have acknowledged all main sources of help;

- Where the thesis is based on work done by myself jointly with others, I have made clear exactly what was done by others and what I have contributed myself;

- Parts of this work have been published as the journal papers and conference contributions in the list of publications.

Signed:

Date: 22nd November 2021

Acknowledgements

Firstly, I would like to thank my supervisor Dr. Xu Fang for all his time and effort in keeping me grounded and guiding me through. I am sincerely grateful to him for all the opportunities he has provided, from lab demonstrating to international collaboration and conferences. Many thanks are also owed to my second supervisor Dr. Nicolas Green, whose knowledge, enthusiasm, and puppy led to many fruitful and amusing discussions, as well as first-rate guidance on academic writing and scientific principles.

I would also like to thank Prof. Wakana Kubo and her group at Tokyo University of Agriculture and Technology in Japan for their collaboration and for their warm and gracious hospitality.

Thanks also to my esteemed colleagues, Fei He, Shengqi Yin, Hailong Pi and Xiangming Xu, for their friendship, inspiration, collaboration, technical help and fantastic meals.

I am also grateful to the laboratory technicians and University support staff. In particular, I would like to thank the Iridis High Performance Computing Facility team for facilitating my simulations, and Neil Sessions, Dr. Lukas Vojkuvka and Xiangjun Wang for their excellent cleanroom training. Special thanks also to Laila Ridley for her help with travel arrangements, admin, and for brightening the office environment.

Words can little express my gratitude to my parents; Prof. Jim Frame, for being a fantastic father, role model and provider, and Jackie Frame, for her selflessness in providing such a nurturing upbringing. Thank you both so much for providing me with such opportunity and support.

Finally, a very special mention goes to Nadja Litau, my partner and rock, who has weathered it all with geniality and grace. Thank you for the giving me the confidence to succeed and for everything else you bring to my life.

Table of Contents

Nomenclature

Symbol	Value	SI unit	Description
F	-	N	Force
e	1.6E-19	C	Electronic charge
E	-	V/m	Electric field
a	-	ms^{-2}	Acceleration
m^*	-	kg	(Effective) electron mass
v	-	m/s	Velocity
τ	-	s	Relaxation time
n_e	N/V	-	Electron number density
V	-	V	Potential difference, voltage
I	-	A	Current
R	-	Ω	Resistance
L	-	m	Length
A	-	m^2	Area
V	-	m^3	Volume
ρ	-	Ωm	Resistivity
σ	-	S/m	AC conductivity
σ_0	-	S/m	DC conductivity
J	$-en_e v$	Am^{-2}	Current density
B	-	T	Magnetic flux density
i	$i^2 = 1$	-	Imaginary unit
v	-	Hz	Frequency
ω	$2\pi v$	rad/s	Angular frequency
t	-	s	Time
$\vec{p}$	-	kg m/s	Momentum
$e^{-i\omega t}$	-	-	Complex time exponential
x	-	m	Displacement
$\underline{x}$	-	m	Complex amplitude
γ	$1/\tau$	Hz	Damping frequency
D	-	Cm^{-2}	Electric flux density
P	-	Cm^{-3}	Electric dipole moment density / polarization
ω_p	-	rad/s	Plasma frequency
ε_0	8.854E-12	F/m	Electric permittivity of vacuum
ε_{mat}	-	F/m	Electric permittivity of material
ε	-	-	Relative permittivity
ε'	-	-	Real part, complex relative permittivity
ε''	-	-	Imaginary part, complex relative permittivity
$\underline{n}$	-	-	Complex refractive index
n	-	-	Refractive index; alt. $\mathrm{Re}(\underline{n})$

k	-	-	Extinction coefficient; alt. $\mathrm{Im}(\underline{n})$
j	*	-	Oscillator integer
S_j	*	-	Oscillator strength
ω_j	*	Hz	Oscillator resonant frequency
γ_j	*	Hz	Oscillator damping constant
$\nabla \times$	-	-	Curl operator
H	-	A/m	Magnetic field
K	-	$\mathrm{rad.m^{-1}}$	Wave vector
c_0	3E8	m/s	Speed of light in vacuum
μ_0	1.257E-6	H/m	Vacuum magnetic permeability
μ_r	-	H/m	Relative permeability
v_j	-	Hz	Frequency (oscillator)
ε_s	-	F/m	Complex relative permittivity, surrounding media
ε_∞	*	F/m	Relative permittivity, infinity
h	6.626E-34	Js	Planck's constant
λ	-	nm	Wavelength
f	0 - 1.0	-	Volume / filling fraction
σ'	-	-	Real part complex conductivity
σ''	-	-	Imaginary part complex conductivity
z	-	m	Propagation distance, z-axis
α	-	$\mathrm{C{\cdot}m^2{\cdot}V^{-1}}$ $\mathrm{A^2{\cdot}s^4{\cdot}kg^{-1}}$	Polarisability (SI units)
α'	$\alpha/4\pi\varepsilon_0$	$\mathrm{cm^3}$	Polarisability volume (CGS units)
α_1	-	-	Fresnel absorption / attenuation coefficient
γ_1	-	-	Fresnel propagation constant
I	-	$\mathrm{W/m^2}$	Intensity
Q	-	J	Energy
C_p	-	J/kg·K	Specific heat
m	-	kg	Mass
T	-	K	Temperature
τ_b	-	s	Bolometer response time
C	-	J/K	Heat capacity
Λ	-	W/(m·K)	Thermal conductance
ρ_r	-	Ω·m	Resistivity
σ_{abs}	-	$\mathrm{m^2}$	Absorption cross-section

* values specified in material descriptions / parameter lists

Notation

Underscore denotes a complex quantity.
Bold denotes a vector, unless specified otherwise.
Use of $\mathrm{Re}(\_\_), \mathrm{Im}(\_\_)$ for complex / imaginary values may be used to avoid confusion.
Symbols omitted from the table have been specified alongside their equations in the text.

Chapter 1: Introduction

This thesis explores the thermally-driven phase transition of vanadium dioxide (VO_2) and two specific applications. The first application is an improvement to device performance and functionality of existing VO_x-based microbolometer technology for infrared sensing and imaging. The concept is based on integrating VO_x film with plasmonic nanostructures. The second application is a novel "phased reflectarray" platform for deflection and control of near-infrared radiation. Both applications rely on the ability of VO_2 to transition between two distinct optical and electrical properties, material properties which are explored in this thesis. This 'solid-solid phase transition' is most commonly referred to as an 'insulator-metal transition' (IMT) because the behaviour and characteristics of VO_2, for example, electrical resistivity and band structure, most resemble insulating and metallic materials at either extremes of its transition region.

In vanadium dioxide, the reversible insulator-to-metal transition has been linked to reorganisation of electronic energy bands and / or reconfiguration of the crystal structure, though the exact nature of transition mechanisms is somewhat controversial. Crystallographically, the transition takes place at the femtosecond time scale **[1, 2]**, but the rate of switching between the two 'pure' VO_2 states in a given system also depends on the method of stimulation. The transition can be stimulated thermally, mechanically, electrically, magnetically and optically, making VO_2 highly flexible in terms of device design. For thermally stimulated transition, the most drastic change in optical and electric properties occurs across a temperature range known as the 'transition region'. Here the optical and electrical properties are highly temperature-dependent and display hysteresis i.e. depend on whether the sample is being heated or cooled. The thermal transition is of particular interest because it occurs around 68°C; the transition range is thus easily accessible with modest thermal control, allowing fine-tuning of VO_2 optical and electrical response. In addition, the metal-to-insulator VO_2 transition also does not require a specific rate of cooling. These factors mean that VO_2-based devices potentially have lower power requirements than most other comparable phase change materials (PCMs). As an example, GeSbTe (GST) transitions between an amorphous and crystalline state which requires melting and crystallisation temperatures of around 600°C and 100°C respectively, and an additional 'melt-quenching' step with a cooling rate of at least 1 °C/ns **[3, 4]**. Finally, the transition behaviour of VO_2, such as critical temperature and transition range, can be optimised using a broad range of techniques including induced strain, tungsten doping, spatial confinement and electrolyte gating **[5-7]**. These features make VO_2 a promising material for a wide range of nano- optoelectronic and thermal applications.

The detection of electromagnetic waves between 0.75-1000 μm, aka infrared radiation, has many uses in sensing, imaging, and analysis including radiation thermometry, flame detection, moisture and gas

analysis, spectrophotometry and thermal mapping. Microbolometers are a class of photodetector that use a photoabsorptive material to convert incident infrared radiation to thermal energy. The subsequent temperature rise alters the electrical resistance of the material which is measured and related to the incident radiation. Vanadium oxides are the most common photoabsorptive materials used in microbolometers due to their high infrared absorption and large resistivity change as a function of temperature. A detailed explanation of microbolometer design and performance metrics are discussed in Chapter 2.2. Although the performance of uncooled microbolometer-based focal plane arrays (FPAs) are inferior to cooled 'quantum-type' photonic detectors, they are less expensive, weigh less and have smaller form factor. This makes them ideal for high portability applications such as fire and rescue and automated vehicles. As expounded in Chapter 2.2, current commercial VO_x bolometer performance is limited by several factors such as signal-to-noise ratio, time and spatial resolution, and target non-specificity. Improvement in VO_x bolometer performance and the introduction of new functionality in the form of wavelength and polarisation sensitivity would broaden the low-cost photodetector market and greatly benefit users. One way to achieve this might be through the integration of plasmonic nanoparticles, structures on the scale of 10^{-9} m which are known to display unique optical behaviours, including strong wavelength and polarisation-sensitive scattering and absorption.

An understanding of the physics of light-matter interactions and plasmonics is necessary to inform the design of such nanostructures and is explored in Chapters 2 and 3, with additional derivations in the Appendix. Briefly, surface plasmons are coherent oscillation modes of plasma density which can be excited at the interface between a material with negative real permittivity and a material with positive real permittivity, most commonly a metal and dielectric, respectively. In plasmonic nanoparticles, localised surface plasmons can be directly excited by incident electromagnetic radiation. Localised surface plasmon resonance modes arise at specific frequencies depending on the permittivity and geometry of the nanoparticle and its surroundings and, for anisotropic geometries, are also polarisation-sensitive. Resonance amplitude, bandwidth and frequency are therefore highly tuneable by a variety of means. The resonance condition is characterised by concentration of the electric near field and enhanced absorption and scattering cross-section. Plasmonic nanoparticles can thus be used in a variety of ways, for example to control light at the nanoscale, modulate forward or backward scattering, and efficiently convert light into heat i.e. the thermoplasmonic effect. The flexibility and utility presented by localised surface plasmons has led to a wealth of research into reconfigurable metamaterials and tuneable plasmonic devices, and applications have been found in such diverse fields as medicine, photodetection, sensing and catalysis. Relevant background and literature is explored in Chapter 2.

The interplay between plasmonic nanostructures and phase change materials is an emerging field, largely because 1.) phase change materials display strong contrast in optical and electronic properties and their behaviour can be strongly modulated by temperature, electromagnetic fields, mechanical

forces etc.; 2.) plasmons can be used to modulate the phase transition behaviour and thus effective properties of the material; 3.) controlling the optoelectronic properties of phase change materials allows modulation of plasmon resonance characteristics; 4.) nanoparticles can be designed as localised heaters, frequency filters and polarimeters. By integrating such nanostructures into VO_x thin-film microbolometers, it should be possible to improve signal-to-noise ratio by increasing sensitivity to specified wavelength and polarisation. This is because plasmon resonance results in localised heating via the thermoplasmonic effect and VO_2 resistivity is highly sensitive to temperature around its transition region. Another benefit would be added functionality by providing wavelength and polarimetric information. To test this hypothesis, two investigations were undertaken.

The first investigation, detailed in Chapter 4, involves measurement of the optical transmission spectrum (400 – 900 nm) and electrical resistivity of a sample consisting of a silver nanorod array on VO_2 film supported by sapphire substrate. The purpose of the project is to test the wavelength and polarisation-sensitive relationship between localised surface plasmon resonance and VO_2 resistivity.

The focus of the second work, expounded in Chapter 5, is quantification of the thermoplasmonic contribution and its effect on the effective phase transition temperature in VO_x film. Transmission spectra between 2 – 16 μm and effective transition temperatures are measured for VO_x film with embedded gold nanorods. These measurements are repeated for samples with varied nanorod density to further explore the relationship. In contrast to the previous investigation, the optical behaviour of VO_x is considered across a broad spectral range to discover how the material properties far from plasmon resonance are affected.

The observation of hysteresis in transmission spectra during the second work provided the motivation for the third work in Chapter 6. Hysteresis is an important consideration in device design; it is sought after for memory because it allows multiple states to be stored. However, in sensing it is avoided because typically sensor readout should not depend on the history of the system. Numerical modelling of hysteresis in VO_2 films is attempted to further investigate the behaviour. A modified version of the Maxwell Garnett effective medium approximation is developed and numerically tested using the Fresnel equations; these equations are derived and explained in Chapters 3.1.1.7 and 3.2, respectively. The formula is used because it is easy to implement and only requires the complex permittivity of both pure phases and the volume fraction of metallic inclusions. The modified equation is justified by a novel approach to the VO_2 phase transition. Although intended as a phenomenological approach to interpreting hysteresis and intermediate states, experimental validation is required. Potentially the work can be used as a simple-to-implement model for hysteresis modelling in phase change materials.

The final project in this thesis concerns a completely different application that makes use of the same unique properties of VO_2, dynamic beam deflection. Beam engineering has huge implications for cutting-edge technologies in a wide range of diverse fields such as dynamic optical sensing, signal processing, imaging, data storage and mapping. One example application is Light Detection and Ranging (LIDAR) for autonomous vehicles, which has the potential for extreme disruptive innovation. Traditional methods for dynamic control of beam angle involve macroscale optics such as mirrors, lenses and mechanical systems. Advances in nanofabrication have led to the field of "optical metasurfaces" which demonstrate the ability to shape and direct light. Metasurfaces are fabricated thin films that include arrays of subwavelength patterns or elements. Passive metasurfaces are typically designed for a singular purpose and have a fixed configuration; the behaviour of the surface cannot be dynamically altered. In contrast, active metasurfaces can be tuned in-situ, for example through nanoelectromechanical systems or phase change materials, in this case VO_2.

In contrast to the plasmonics-based investigations, this project uses heat generated by passing electrical current through metal wires to control the complex refractive index of VO_2, where the refractive index describes how light propagates through matter relative to vacuum. Phase is the property of electromagnetic waves that defines the waveform's position at a point in time and is directly influenced by the refractive index of interacting matter. Thus the phase of light reflected from a VO_2 film can be retarded or accelerated (relative to incident phase) by controlling its temperature. Combining this with the idea of a metasurface of discrete elements, one can envisage a unit cell comprising a number of discrete, individually heated VO_2 elements. The resultant phase from each VO_2 element can be coordinated such that the reflected wavefronts present as a progressive "phase gradient". A progressive phase gradient across an array of such unit cells would have the effect of deflecting an incident wavefront. This approach, of customising the phase gradient across an array of elements to achieve desired beam angles, is known as a "phased array" and has been used for many years in the ultra-high frequency and microwave bands of the radio spectrum, as well as in acoustic systems. Increasing demand for smaller devices operating in the IR-optical regime have led to a wealth of research into such active metasurfaces, with the ultimate goal of high efficiency dynamic beam steering. Chapter 7 details the purely simulation-based investigation into the feasibility and performance of a VO_2-based phased reflectarray. Since thermal control is instrumental to physical viability of the optical system, this is followed by thermal simulation and analysis.

Chapter 2: Projects Background

2.1 Vanadium dioxide

Vanadium is a transition metal with five valence electrons and a broad range of oxidation states, from -3 to +5. Due to this rich chemistry, native vanadium is rare in nature and has only been found as sublimate inside the fumaroles of Colima Volcano in Mexico **[5]**. However, the element is relatively common, being ranked 20th in estimated crustal abundance according to the CRC Handbook **[6]**.There are around 155 vanadium-bearing minerals, many of which possess vivid colouration and striking crystalline forms, hence the namesake Vanadís, Norse goddess of beauty and fertility **[7]**.

Figure 1. Vanadium metal cube alongside three oxidised forms **[8]** and three vanadium-bearing minerals (red vanadinite **[9]**, green mottramite **[10]** and blue cavansite **[11]**).

Vanadium is mostly extracted as byproduct from various ores such as titanomagnetite, bauxite and carnotite but can also be processed from fossil fuel and black shale deposits. The metal is blueish-silver, is ductile and malleable, and is one of the hardest metals on the Moh's scale at 7.0 **[12]**. Around 85% of extracted vanadium is used in the production of specialist steels such as High-Speed Steel (HSS) where it increases hardness, especially at high temperatures; HSS is used to make fast-cutting and abrasion-resistant edged tools. Vanadium can also be used to increase strength and temperature stability of titanium and aluminium alloys e.g. Titanium-6AL-4V, for use in jet engines, airframes and dental implants. Several alloys such as V_3Si and V_3Ga exhibit superconducting behaviour and are used in superconducting electromagnetic coils **[13]**. Most of the remaining vanadium is converted to various

oxides for use in catalysis (vanadium pentoxide V_2O_5 is used to produce sulphuric acid by the contact process), redox batteries, microbolometric infrared detectors, and optical coatings.

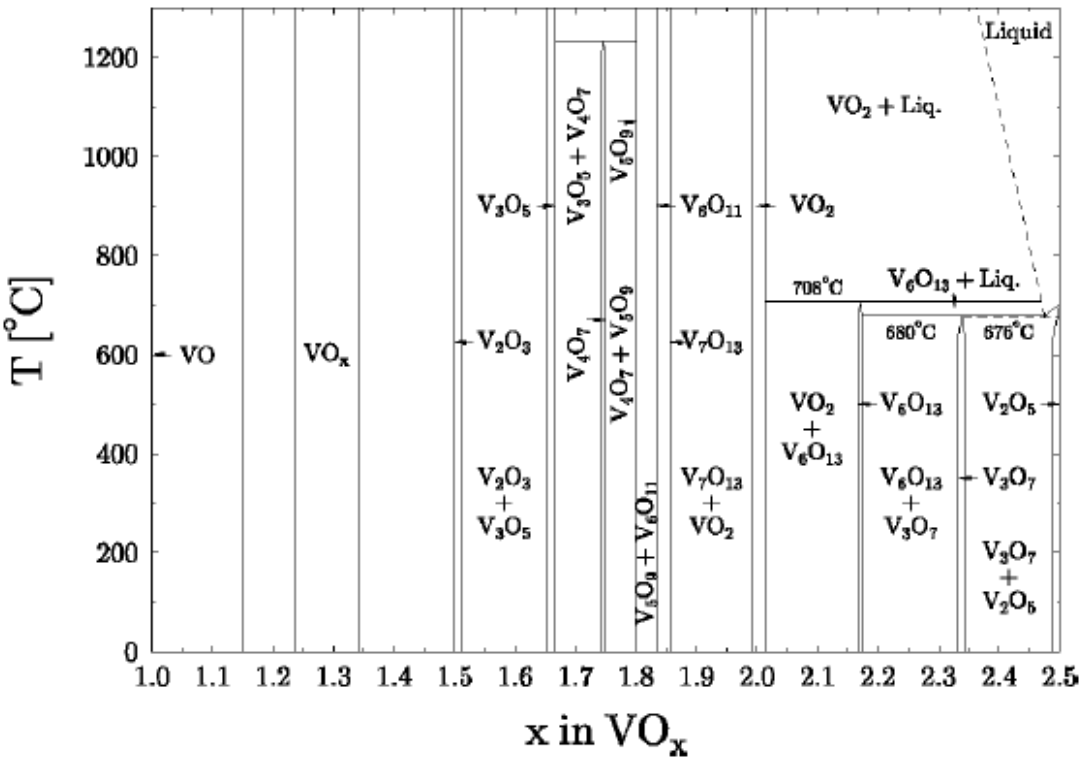

Figure 2. Experimental phase-temperature diagram for oxides of vanadium **[14]**.

As shown in the phase diagram Fig 2., at least 11 oxides of vanadium are known to exist, including the phase change materials vanadium trioxide (V_2O_3), vanadium pentoxide (V_2O_5) and vanadium dioxide (VO_2). VO_2 is remarkable because it has a close-to-room-temperature dielectric-to-metallic phase transition with highly contrasting material and optoelectronic properties between the phases. VO_2 also has a range of metastable polymorphs aka crystalline phases, such as VO_2(A), VO_2(B), VO_2(C) and VO_2(D) **[15]**. More information about vanadium oxides, VO_2 crystallographic transitions and polymorphs can be found in Goodenough (1971) **[16]** and Lee (2016) **[17]**, with detailed presentation of lattice parameters in Katzke (2003) **[14]** and Eyert (2002) **[18]**.

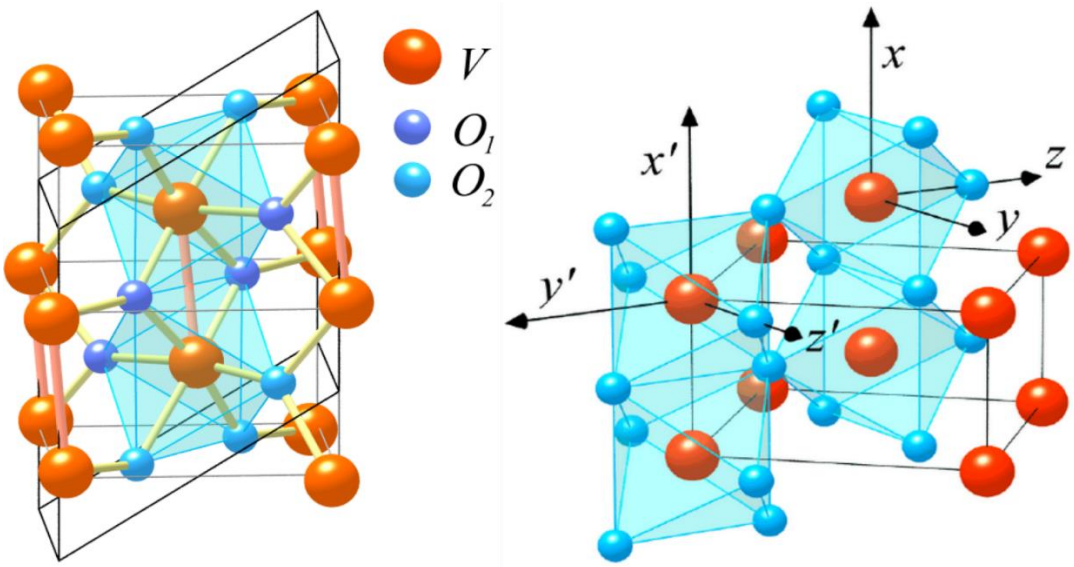

Figure 3. Left: Low temperature monoclinic M1 (insulating); Red V-V bonds (2.619 Å), yellow V-O bonds with two interatomic distances V-O1 (1.77 Å) and V-O2 (2.01 Å). Right: High temperature rutile R (metallic); tetragonal lattice of vanadium (+4) atoms surrounded by six oxygen (-2) atoms forming VO6 octohedra. No V-V bonding, but interatomic distance of 2.86 Å. From Eyert (2002) **[18]**.

The low temperature dielectric-metal transition of vanadium dioxide was highlighted following seminal work by FJ Morin in the late 1950s **[19]**. At temperatures << 68 °C, VO_2 is considered to be fully dielectric phase. The crystal structure is almost entirely monoclinic (M1), DC resistivity is high and complex permittivity is that of a typical lossy dielectric, with positive real and imaginary components. At temperatures >> 68 °C, VO_2 is considered to be fully metallic phase. The crystal structure is tetragonal rutile, DC resistivity is ~3 orders of magnitude lower and complex permittivity is that of a metal, with negative real and large imaginary component. The metallic phase arises from nonbinding 3d orbitals of neighbouring vanadium ions overlapping to form a conduction band. Within the transition region, the two phases co-exist and form complicated nanostructures, as seen in Fig. 4. These intermediate states give rise to interesting behaviour such as electromagnetic hysteresis on thermal cycling.

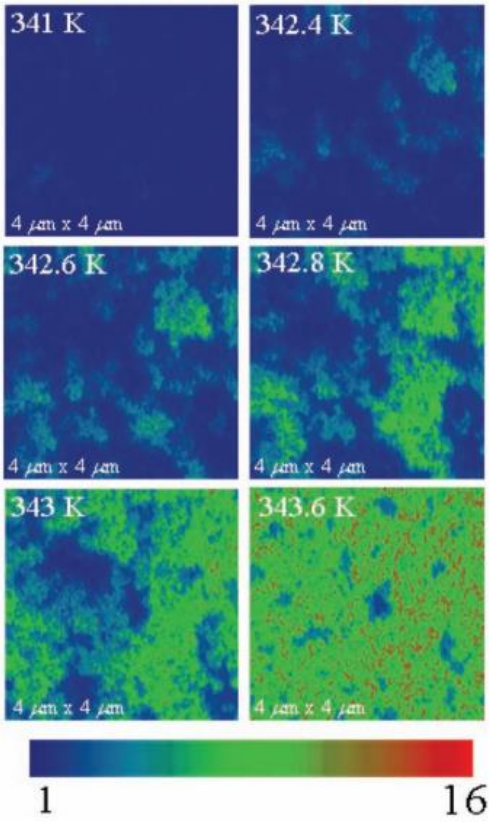

Figure 4. Near-field scattering amplitude obtained by s-SNOM at ~ 10.8 μm at representative temperatures over the phase transition regime. Metallic phase (light blue, green, red) displays higher scattering amplitude compared to dielectric phase (dark blue) **[20]**.

The mechanisms of formation and distribution of these intermediate states have long been a topic of debate. VO_2 is known as a strongly correlated electron material; that is, each d-electron is influenced by Coulomb interactions with its neighbours. In a 1949 paper **[21]**, later revisited in 1968 **[22]**, NF Mott proposed that the mechanism of phase transition in VO_2 originates from increasing Coulomb interactions and screening of positively charged vanadium ions as the charge density increases with temperature. Effectively, increasing temperature leads to higher number of electrons in the d-band and higher electron density results in stronger screening of positive ions from the electrons farthest away. Essentially these electrons become unbound, hence able to act as free electrons. An alternative to the 'Mott transition', advanced by proponents such as Adler (1968) **[23]** JB Goodenough (1971) **[16]**, is the VO_2 phase transition being driven by an energetically favourable redistribution of ions in the lattice, since lattice spacing is known to influence the band gap of dielectrics. This mechanism is known as 'Peierls transition'. The debate over which mechanism is predominant continues **[24, 25]**, but more recent work based on LDA (local density approximation) finds both Mott-Hubbard and Peierls are essential in describing the transition **[26]**. A recent comprehensive review of related work is given by Shao (2018) **[27]**.

In practice, the phase transition can be stimulated thermally, mechanically, electrically, magnetically and optically, making VO_2 highly flexible in terms of device design. In addition, the transition behaviour, such as critical temperature and transition range, can be tuned using a broad range of techniques including induced strain, tungsten doping, spatial confinement and electrolyte gating **[28]**. VO_2 is thus a promising material for potential nano- optoelectronic and thermal applications and has been extensively studied for possible applications such as non-volatile switches and memory **[29-31]**, thermal management of spacecraft **[32]**, and photodetection **[33]**. More recently, the control of intermediate states in transitions has been explored for developing dynamically tuneable antennae **[34, 35]**, beam steering metasurfaces **[36]**, grayscale photolithography **[37]** and multi-level memory **[38]**.

2.2 Microbolometric photodetection

Thin film resistive microbolometers were first proposed in the early 1980s to extend the spectral range of contemporary infrared photodetectors **[39-41]**. The operating principle is simple; incident infrared radiation is absorbed by a photoabsorptive material and converted to thermal energy. This effects a temperature rise within the material, which consequently experiences a change in electrical resistance. The resistance change is measured electrically and related to the incident radiation, thus the bolometer may be used as an infrared detector or imager. Electromagnetic radiation is emitted from all objects above absolute zero; the temperature of the source relates to the emitted wavelength and radiance by Planck's Law. The infrared regime is between ~700 nm and 1 mm, corresponding to temperatures of ~3 K in the far-infrared to ~3,864 K in the near-infrared. Infrared detectors typically target the atmospheric windows, portions of the spectrum that are not absorbed by Earth's atmosphere, between 3-5 and 8-14 μm; bolometers can be designed for broad-band detection in both regimes.

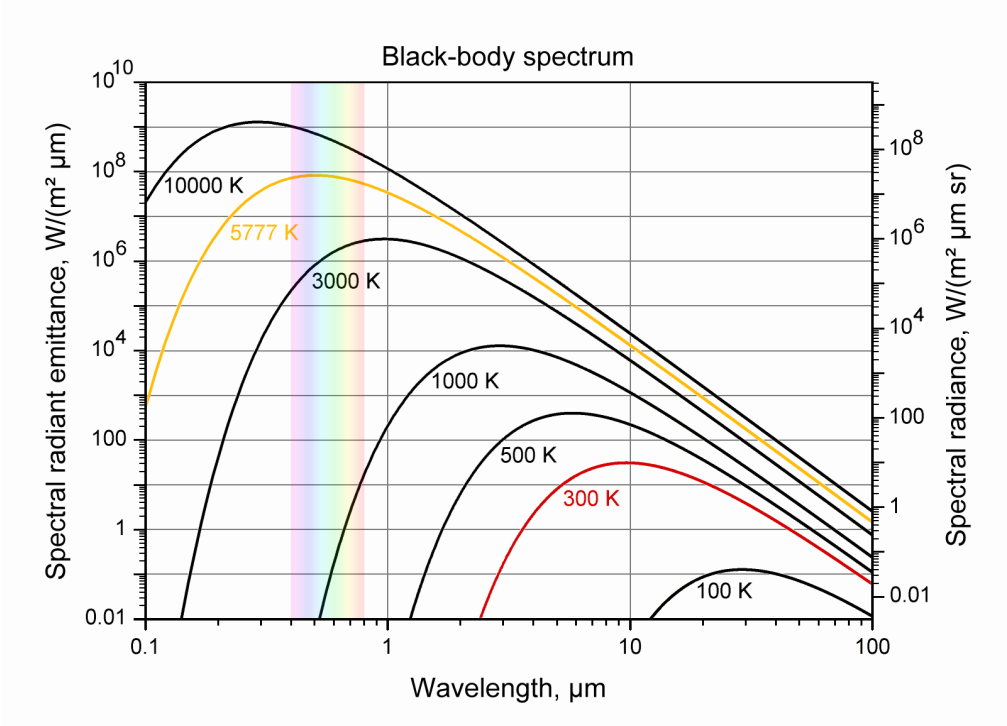

Figure 5. Black body spectrum for temperatures between 300 K and 10,000 K **[42]**.

The two main types of infrared detector are thermal, which include bolometers, thermopiles, thermocouples and Golay cells, and photonic, which generally involve electronic photo-excitation in semiconductors with band gaps tailored to a target frequency band. Photonic detectors tend to have superior performance in terms of sensitivity and response time but have narrow-band response and usually require cooling systems to limit dark current noise. Compared to photonic detectors, the main advantage of microbolometer technology is that cooling is not required; cooling systems introduce extra power consumption, design and maintenance costs, bulk and weight, mechanical vibration, and acoustic disturbance. Other advantages include broad band response, high dynamic range, good sensitivity, low cost, CMOS compatibility, high reliability, small form factor and light weight. These features have led to microbolometer technology becoming a significant market shareholder, with an estimated value of $359.9 million in 2019 **[43]**. Nevertheless, cooled photonic detectors outclass microbolometers in performance to the extent that they are found in most high-end applications. As a result, microbolometer manufacturers are now tending towards low cost applications and high-volume markets such as fire and rescue, security, and automated vehicles **[44]**.

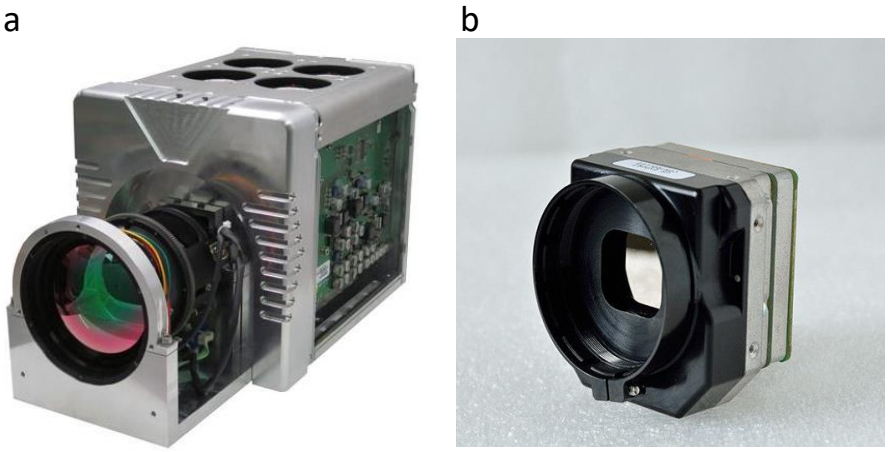

Figure 6. Infrared photoimaging systems. (a) Cooled midwave infrared mercury cadmium telluride (MCT) or indium antimonide (InSb), 15 μm pitch, 640 x 512 pixels, 3.7 - 4.8 μm, 25 mK NETD **[45]**; (b) Uncooled longwave infrared VOx focal plane array, 17 μm pitch, 640 x 512 pixels, 8 – 12 μm, 50-60 mK NETD **[46]**.

Each microbolometer constitutes a pixel of a focal plane array (FPA). Modern commercial microbolometers are structures typically <12 μm across, consisting of a suspended 'photoabsorber layer' supported by a number of 'legs'. Thermal management is paramount in microbolometer design to maximise the signal-to-noise ratio. The film is therefore thermally isolated by suspension and wafer-level vacuum packing. Vacuum of ~0.01 mbar **[47]** eliminates convective heat transfer, allowing thermal outflow to be controlled through appropriate design of the supporting legs. To minimise thermal conduction through the legs, typically to as low as 3.5×10^{-8} W/K **[48]**, legs are long, have small cross-sectional area, and are made of strong materials with poor thermal conductivity such as silicon nitride. Thin metal layers in the legs electrically connect the absorber layer to read out integrated circuitry (ROIC) in the underlying substrate. Usually the substrate surface is coated with an aluminium mirror layer, forming a Fabry-Perot optical resonant cavity around a quarter-wavelength ($\lambda/4$) in size between substrate and absorber layer **[49]**.

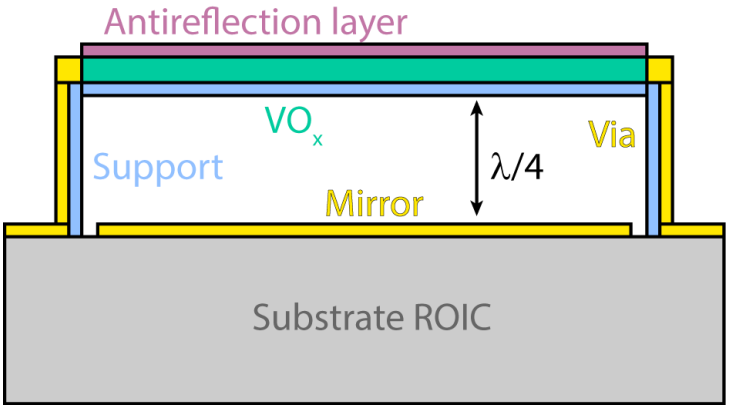

Figure 7. Basic microbolometer schematic, cross section. VO_x film is electrically connected by two metal vias, forming a variable resistor that is sensitive to absorption of infrared radiation. The VO_x film is suspended above the substrate surface by supporting legs made from electrically and thermally insulating material such silicon nitride. The metallic mirror backplane forms an optical resonant cavity that maximises IR absorption. Focal plane arrays consisting of a matrix of such microbolometers are vacuum sealed to minimise thermal crosstalk via heat transfer through air.

One design compromise is that while thicker absorber films maximise absorption of incident radiation, the heat capacity of the layer also increases, meaning more energy needs to be absorbed per unit temperature increase in the layer. This is evident from the equation $Q = \mathrm{m}C_pT$ where Q is thermal energy transferred (J), m is mass (kg), C_p is specific heat (J/kg·K) and T is temperature (K). Thermal mass also affects the bolometer response time τ_b by the equation $\tau_b = C\Lambda$ where C is heat capacity and Λ is thermal conductance **[50]**. The optical cavity design increases absorption in the film, allowing the film to be thinner and thus maximising temperature change in the film for a given energy. This is represented by the 'responsivity' of the device, defined as the output signal voltage/current per incident radiant power. The amount of incident radiation absorbed is also maximised by having a high ratio of absorbing to non-absorbing area in the array, quantified by the 'fill factor', where non-absorbing refers to legs, inter-pixel spacing, electrical vias etc. This relates to several more design compromises; for instance, high pixel density is favourable to maximise spatial resolution and lower fabrication cost, but this reduces the fill factor since a larger proportion of pixel area is inter-pixel spacing and legs. Spatial resolution is additionally limited by thermal noise between adjacent pixels.

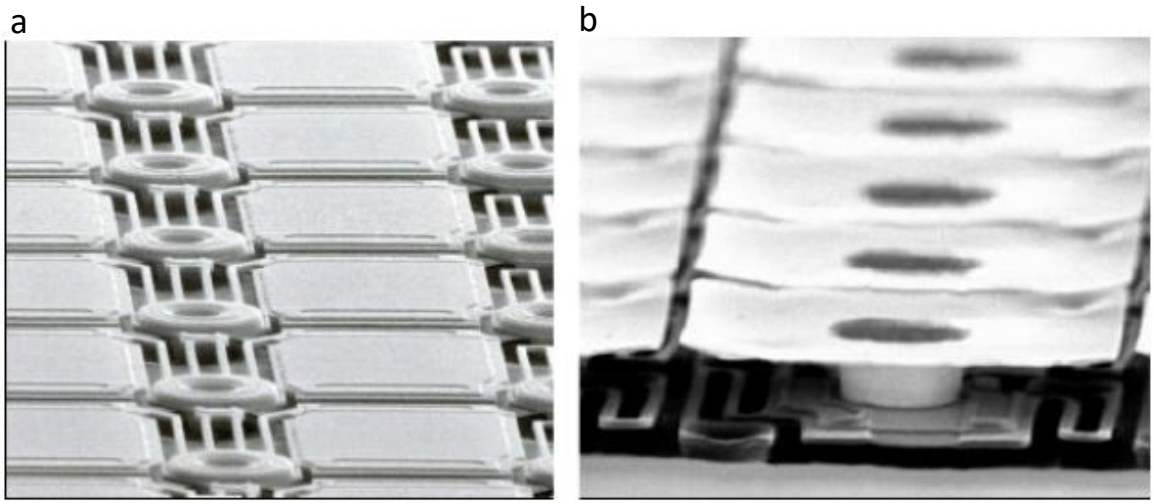

Figure 8. (a) Commercial VOx bolometer, pitch 28 μm, BAE **[48]**; (b) VOx bolometer with umbrella design, pitch 17 μm, DRS **[51]**.

The most common metric in detector literature is noise equivalent temperature difference (NETD) which is used to describe the thermal sensitivity of the device. An NETD of 50 mK means that temperature differences of 50 mK can be detected; typically, uncooled microbolometers are in the range of 30 - 200 mK **[49]**. Other common figures of merit (FOM) include noise equivalent power (NEP) and detectivity (D*). These FOM all relate to the signal-to-noise ratio of the device and noise is therefore the biggest challenge in device design.

Reducing noise and / or increasing absorption might both be possible using plasmonic nanostructures. Since the enhanced absorption of plasmonic structures is wavelength sensitive, absorber layers could be designed to have high spectral sensitivity so that targeted wavelengths are absorbed and the unwanted bands are scattered. This would reduce noise, allowing greater pixel density. Currently, such selectivity requires the use of expensive filters, which introduce additional noise and require cooling. Maier and Brückl (2009) **[52]** demonstrated wavelength-tuneable microbolometers that used square metal/insulator/metal stacks as absorber elements. They observed peak absorption of up to 80 % (contrast ~60 %) between 4.8 and 7.0 μm and were able to control the peak spectral position by tuning the absorber widths between 1.25 and 2.00 μm. Polarimetric information would also be hugely useful in applications such as remote sensing and object recognition since it gives an indication of the morphology and surface properties of the imaged object. As expounded in the next subsection, the polarisation-sensitive resonances observed in anisotropic plasmonic structures, such as nanorods, would allow differentiation between objects with indiscernible thermal signatures but different polarimetric properties **[53]**.

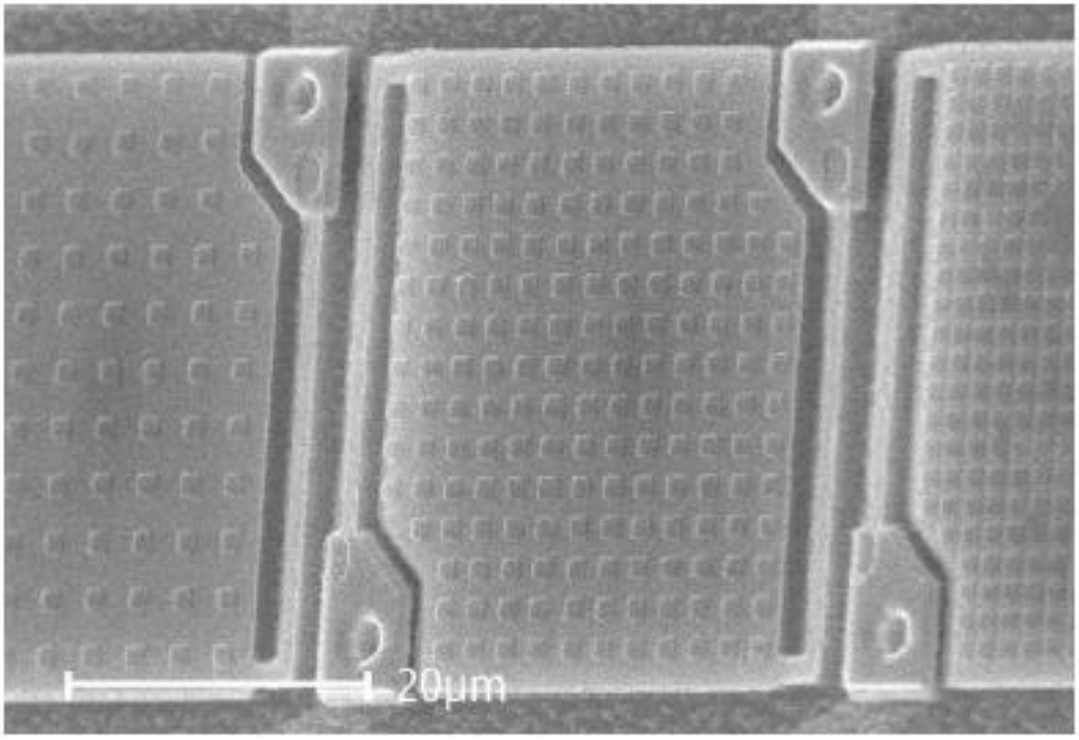

Figure 9. Scanning electron micrograph of 'microbridges' with integrated absorbers on top; oblique view **[50].**

As well as bolometer design, materials selection is key, since the wavelength and temperature-dependent optoelectronic properties of the film underpin the behaviour of the device. As previously mentioned, absorption of infrared radiation leads to heating in the film and a subsequent decrease in resistivity. Good absorber materials are therefore highly absorptive in the infrared and have a high thermal coefficient of resistance (TCR). TCR is the resistance change as a function of temperature, with units % / K and expressed as $\mathrm{TCR} = (1/R \cdot \partial R/\partial T) \times 100$ where R is resistance and T is temperature. Resistance can be expressed as $R = \rho_r L/A$ where ρ_r is resistivity, L is length of film between electrodes and A is cross-sectional area. Electrical resistance and film quality are major factors in limiting power consumption and 1/f 'flicker' noise, which presents as current or voltage fluctuations in readout **[54]**. Additionally, the material should be CMOS compatible, easy to fabricate as thin membranes and have suitable thermal properties. The most common microbolometer materials are based on amorphous silicon or vanadium oxides. Amorphous silicon is very well understood, CMOS compatible and easy to fabricate on a variety of substrates; in addition, it has high absorption and can be made into suspended thin films easily. However, it suffers from inferior electronic performance, having much higher resistivity than VO_x thus excessive 1/f noise, as well as slightly worse TCR of 2.5-5 %/K at room temperature dependent on doping **[55]**. Performance of VO_x thin films is highly dependent on film preparation and stoichiometry due to the existence of numerous VO_x polymorphs. For instance, pure V_2O_5 has high TCR of 4.4 %/K at room temperature but suffers from high resistivity, while a mixture of VO_2 and V_2O_5 may have a lower TCR of 2.8 %/K but lower resistivity ≈1.7 Ω-cm **[56]**. Although

pure VO_2 can have TCR up to 200 %/K around the transition temperature **[57]**, it is generally not considered for bolometric sensing because the transition characteristics are highly non-linear and show hysteresis. In absorber materials there is typically a compromise whereby higher TCR is associated with higher resistivity and 1/f noise **[58]**. Much work has been done to optimise vanadium oxide films for use in bolometric sensing via deposition, and annealing conditions, doping, and applied bias. $VO_{1.8}$ currently dominates the microbolometer market with TCR up to 5.5 %/K at room temperature, low 1/f noise (23.39 $nV/Hz^{1/2}$ at bias of 19.3 μA at 5 Hz) and high infrared absorption ($\eta = 0.8$) **[56, 59]**. In the simulation work presented in this thesis, stoichiometric VO_2 was modelled in lieu of $VO_{1.8}$ due to the availability of data and because the simple composition allows for easier fabrication and thus higher reproducibility **[60-62]**.

2.3 Plasmonics and VO_2

The interplay between VO_2 and surface plasmons is an emerging research topic in which there appear to be three main avenues. Most work focuses on how the phase change can modulate plasmonic resonances by controlling the sample temperature. Maaza et al. (2005) **[38]** embedded roughly spheroidal gold nanoparticles ~13 nm diameter in VO_2 and increased the temperature from 25-120 °C, observing a reversible blue-shift in localised surface plasmon resonance from 645-598 nm. This blue-shift satisfies the Fröhlich criterion for spherical particles embedded in dielectric. Dicken et al. (2009) **[63]** demonstrated frequency-tuneable metamaterial arrays consisting of 150 nm thick silver split ring resonators (SRRs) on 60 nm thick VO_2 films. Operating between 1.5 and 5 μm, they observed a red shift of magnetic resonance peak wavelength up to 110 nm upon heating the sample above the VO_2 phase transition temperature.

Attempts have been made to utilize resonance modulation in devices. Lei et al. (2015) **[64]** demonstrated 'all-optical' control of switching behaviour by exploiting phase transition hysteresis in plasmonic hybrid nanostructures consisting of gold nanodisks on VO_2 films. Samples were thermally cycled whilst ultraviolet pulses were used to excite plasmon resonance. Measurement of the extinction spectra allowed readout of the plasmon resonance shift. In the infrared, Kats et al. (2013) **[34]** demonstrated that resonances of plasmonic antennas can be tuned by varying the temperature of the sample. Samples consisted of gold Y-shaped antenna arrays on 180 nm thick VO_2 film on sapphire substrate. Reflectivity spectra of samples were measured at 10 μm and showed resonance wavelength tuneability of around 10 % (1 μm) as temperature was cycled. Hao et al. (2018) **[65]** investigated the hybridization of plasmonic structures with VO_2 thin films to achieve thermochromic 'smart coating'. A 50 nm thick VO_2 film was deposited above an array of hexagonal plasmonic TiN nanostructures. TiN blocks infrared light but displays low reflection in the visible, making it a good choice for window coatings. Due to the

change in phase composition, the degree of infrared attenuation was shown to be dependent on temperature and radiation intensity with up to 48% switching efficiency at 2000 nm. Infrared was blocked at 28 °C under strong illumination but transmitted at 20 °C under weak illumination.

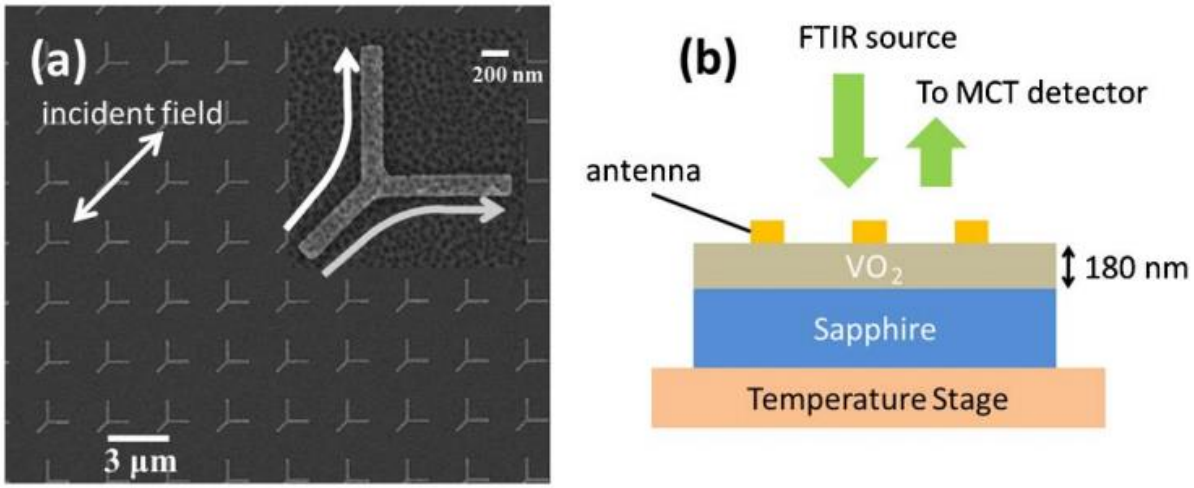

Figure 10. (a) SEM image, gold antennas on VO_2 film; inset shows flow of currents in response to incident field; (b) Sample and measurement schematic **[63]**.

Abate (2015) **[66]** took a different approach in their investigations into the effects of phase transition of local VO_2 nanodomains on infrared antennae. They employed scattering-scanning near-field optical microscopy (s-SNOM) and phase-modulation interferometry to generate near-field, topography, amplitude and phase images. The gold antenna had dimensions of 2510 x 232 x 30 nm and were designed to be resonant at 10.7 µm. They were deposited on 100 nm thick VO_2 film on silicon substrate. At room temperature, the near field images indicated that the antennae acted as electric dipoles as expected. However, as temperature was increased, metallic domains up to 15 nm in diameter randomly grew within the VO_2 film. The behaviour of the gold nanorods was affected when metallic domains grew close to them; dipole excitation was switched off or transformed into monopole depending on the precise position of the VO_2 domains in relation to the rod.

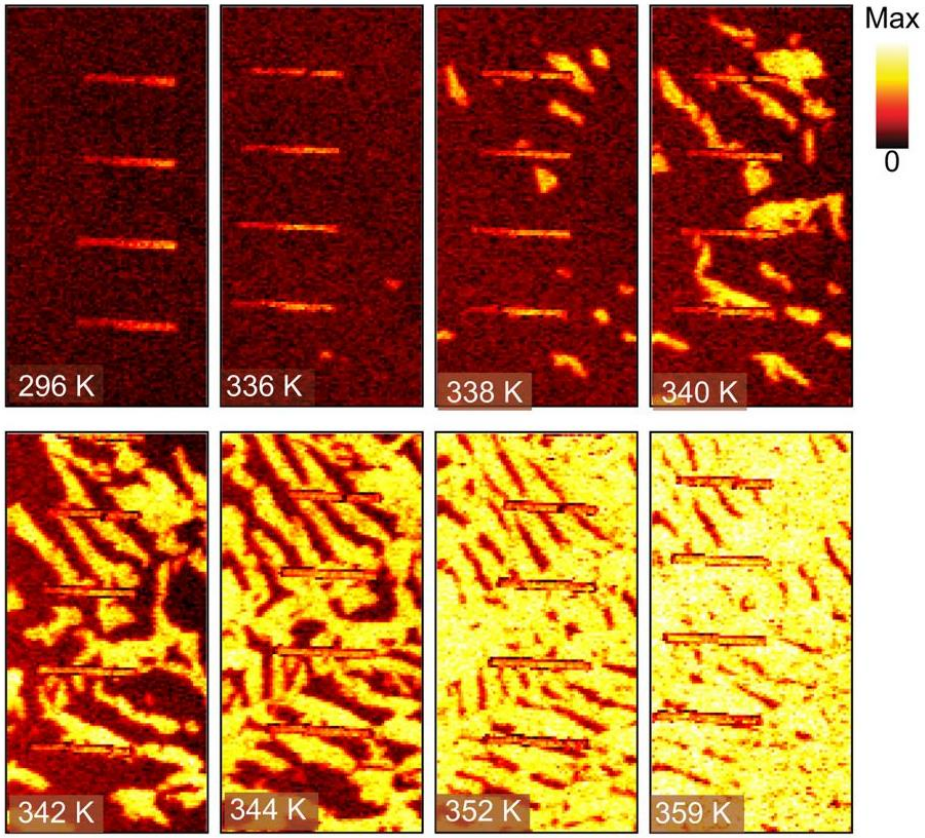

Figure 11. s-SNOM topside view of gold nanorod array showing temperature-dependent near-field amplitudes. Increased scattering amplitude indicates quasi-uniform transformation to metallic VO_2 **[66]**.

The second avenue of research investigates plasmon-induced phase change. Hong et al. (2019) **[67]** demonstrated a potential photodetector design based on plasmonically-hybridised VO_2 nanorods. Samples consisted of 250 nm thick layer of VO_2 nanorods on Si / SiO_2 substrate. The rods were 50 nm in diameter and deposited by glancing angle deposition at 80 °; they were subsequently decorated with silver nanoparticles. Photo-induced phase transition was demonstrated by comparing resistance in the dark and under illumination at wavelengths between 400 - 1000 nm and intensities up to 0.1 Wcm^{-2}. As temperature was increased, resistance was observed to decrease in the dark but increase under illumination. This was linked to dielectric behaviour in the dark and metallic behaviour under illumination, giving evidence for photo-induced transition. A much higher photoresponse (shown by up to 50x higher dark: illuminated resistance ratio) was observed for Ag nanoparticle-decorated VO_2 nanorods compared to Ag nanoparticles on VO_2 thin film, bare VO_2 film, and bare VO_2 nanorods. Using gold split-ring resonators, Liu et al. (2012) **[68]** demonstrated plasmon-induced transition and measurement of response. The sub-wavelength field enhancement was sufficient to induce VO_2 phase transition between the resonator gaps, thus the resonance behaviour of the entire array was influenced by the transition of a small volume of VO_2 in the SRR gaps. The results showed a well-defined red-shift of plasmon resonance with increasing metallic phase. The SRR structures used in this work were comparatively large, around 76 μm long with a periodicity of 100 μm, and operated in the THz regime.

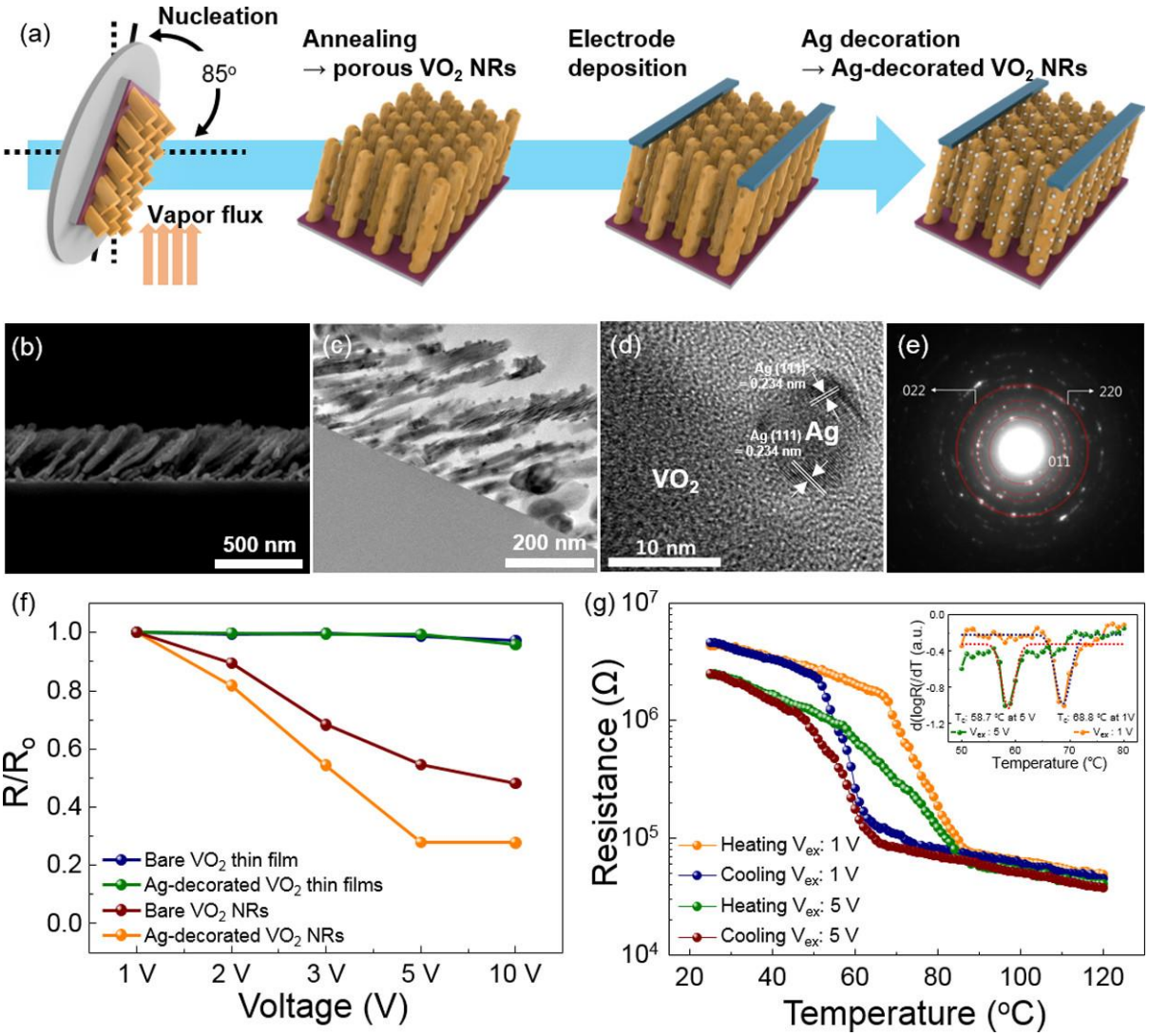

Figure 12. (a) Fabrication schematic of Ag-decorated VO_2 nanorods; (b) SEM and (c) TEM images of Ag-decorated VO_2 nanorods; (d) TEM of Ag particle on VO_2 nanorod **[67]**.

The third avenue investigates how plasmonic resonances can facilitate the phase change of VO_2, since reducing energy requirements is a key consideration. Although the phase transition temperature of VO_2 is low compared to most other phase change materials such as GST, for devices to take full advantage of the contrast in optoelectronic properties of the two phases requires temperatures elevated close to 68 °C in bulk. Lysenko et al. (2006) **[69]** demonstrated pure optically induced phase transition in VO_2 thin films using a 400 nm illumination laser which served as pump and probe. The laser was applied in 100 fs duration pulses, providing 7-14 mJ/cm^2 to the surface; variables included film thickness, pump pulse energy and delay between pulses. They observed an instantaneous response in reflectivity and transmission which occurred as fast as the pulse duration. This change in optical properties was attributed to interband transitions associated with the transition. A longer 'relaxation process' on the scale of nanoseconds was reported, indicative of phase transition hysteresis. These findings are very

promising, but practical integration for such purposes as sensors and optical components is limited, mostly due to high power operation.

Much research has thus aimed to reduce the transition threshold by suppressing the critical temperature. The most common method, aside from tuning stoichiometry, is tungsten doping. Greenberg (1983) **[70]** observed significant suppression of transition temperature in W, Mo and Nd doped films and polymorphic films (≈ 20 K suppression using W doping). Another interesting technique is electrolyte gating, whereby an ionic liquid in contact with the VO_2 surface is subjected to an applied bias. Jeong et al. (2013) **[28]** showed that the transition could be suppressed and metallic phase stabilized to temperatures as low as 5 K, even once the ionic liquid had been removed. The mechanism was explained to be electric field-induced oxygen vacancies caused by the migration of oxygen within the film oxide into the ionic liquid. This was shown to be a very promising tool for precise control over the transition temperature. However, such techniques suffer from the fact that they are not tuneable nor reversible in-situ.

In contrast, plasmonics has the potential to offer in-situ and reversible optical control over the phase composition and transition in VO_2 because localised surface plasmon resonance is strongly sensitive to incident wavelength and polarisation. Two main mechanisms are thought to contribute to this effect; hot electron injection and plasmonic heating. Although the relative contributions can be difficult to distinguish, hot electrons are thought to be the main contributor at ultrashort time scales and high irradiance, while thermoplasmonic effects dominate at longer time scales and lower irradiance **[71]**. The hot electron mechanism involves the ballistic injection of energetic electrons from the plasmon at the nanoparticle surface into the surrounding VO_2 lattice **[72-74]**. Our work has instead focused on heat generation brought about by dissipation of plasmons through electron-electron and electron-phonon scattering. As mentioned previously, plasmonic nanostructures are well known for their high efficiency in converting electromagnetic energy to thermal energy **[75]**. Although typically considered a key limiting factor for many applications in optoelectronics, heat can become a useful tool when used in conjunction with the temperature dependent resistivity of VO_2 by enabling modulation of the phase composition. For instance, Ferrara et al. (2011) **[76]** observed up to 37 % reduction in laser power needed to induce VO_2 phase transition by embedding Au 'nanoradiators' as little as 4 % by volume. The plasmonic structures increased the effective absorption coefficient by a factor of 1.5 at a wavelength of 785 nm. Being able to utilise the strong resistivity contrast within the transition region enables highly sensitive transition edge detection.

In terms of improving device functionality, polarisation dependent control over VO_2 behaviour using plasmonics can be achieved by introducing anisotropy into the design. For instance, Appavoo and Haglund (2014) **[77]** investigated 'nanomodulator' arrays consisting of Au / VO_2 nanodisk dimers and

found that presence of the Au disks greatly increases the modulation strength of the VO_2 optical response on heating. The arrays were thermally cycled to induce phase change while linear polarisation, and interparticle distance was varied. Polarisation dependence of the dimer was demonstrated by showing a small change in LSPR for transverse polarisation compared to longitudinal.

2.4 Phased arrays

Another project, detailed in Chapter 7, investigated the potential for VO_2 as an 'active element' in a metasurface phased array designed to control the angle of a deflected incident infrared beam. The remainder of this chapter include the necessary conceptual background. The following section briefly details the historical context of phased array antennas by way of the most important developmental milestones. A more comprehensive review of the history of these devices can be found in Mailloux (2006) **[78]** and a detailed discussion of early antenna evolution in Hansen (1964) **[79]**.

In 1886, Heinrich Hertz conclusively identified radio waves for the first time **[80]**, thereby supporting James Clerk Maxwell's electromagnetic theory **[81]** and ushering in the 'spark era' of radio. The experiments were conducted using spark-gap transmitter and simple dipole and loop antennas, with parabolic reflectors used to direct and focus the waves (Fig. 13 a). Directional reflectors were used because spark transmission was inefficient and the waves were found to obey the "inverse-square law" i.e. wave intensity is inversely proportional to the square distance from the source. Thus directionality was key to the success of early "wireless telegraphy" that aimed to send signals across ever larger distances, disputes between the likes of Nikola Tesla and Guglielmo Marconi notwithstanding.

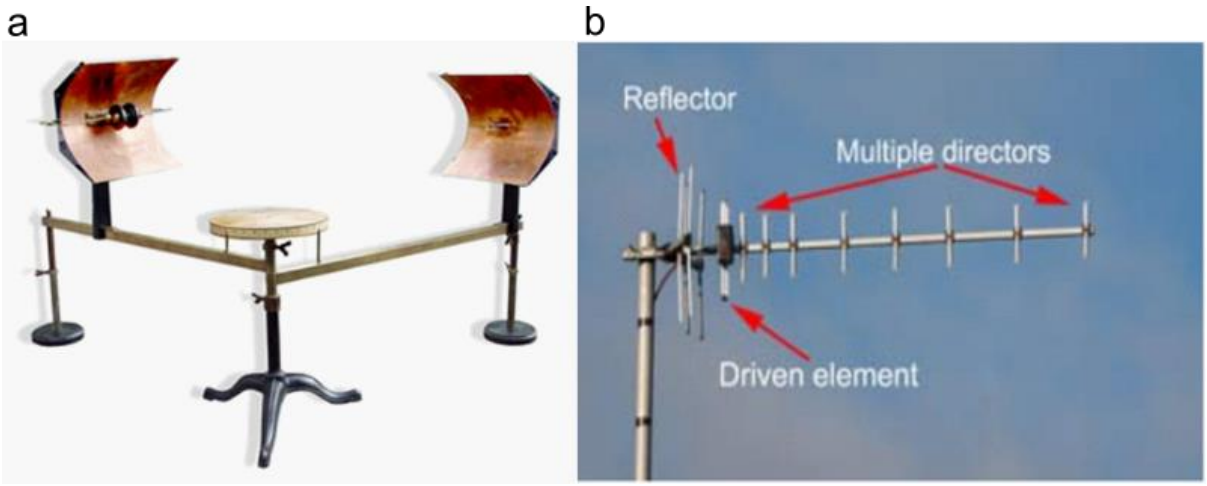

Figure 13. (a) Righi Hertzian-wave test bench c. 1895. Righi spark-gap transmitter (left) and Branly coherer receiver (right) **[82]**, (b) Yagi-Uda antenna **[83]**.

The concept of achieving directional beam control using an array of elements was put into practice and widely adopted in the 1920s with the Yagi-Uda antenna, a device that is still widely used today **[84]**.

Instead of a parabolic reflector, the antenna consists of 'director elements', a series of half-wavelength metal dipoles fixed to a 'feed dipole', a 'driven' element, to which power is applied, and a reflector. To maximise gain in the desired direction, the radiated phase from parasitic elements (directors & reflector) are designed to be different from the radiated phase of the driven element. The concept is that by wave superposition, the signal is strengthened when emitted in the desired direction but weakened in unwanted directions. The spacing between elements and the size of each element determines the resultant emitted wave, with reflector and director elements around five percent longer and shorter than the driven element, respectively. Although such antennas are highly directional, the direction can only be changed mechanically, by physically rotating the array. Also, since the element geometry is fixed post-manufacture, the phase relationship between elements cannot be dynamically altered, so the resultant wave is fixed for a given frequency.

The next significant development came with the microstrip antenna, patented in 1955 **[85]**. These antennas typically consisted of metallic patches printed on grounded dielectric substrate. The patches acted as radiating elements and were electrically fed by microstrip lines. Since each patch was individually fed, this offered the opportunity to electrically control the phase radiated from each element. In contrast to the previous antennas, this allowed dynamic tuning of the emitted wavefront. The salient point is that there was now the potential to control the direction of an emitted beam electrically, without mechanical parts such as servos and rotary joints. This represented cost savings in terms of maintenance and reliability risk since such mechanical components have shorter lifetimes than solid-state electronics **[86]**. Furthermore, such devices had relatively small form factor, could conform to a surface, and had no need of mechanical components. Unfortunately, such designs suffered from low efficiency and narrow bandwidth, which may help explain why there was little development over the subsequent couple of decades.

In the interim, the reflecting antenna was conceptualised by Berry, Malech and Kennedy (1963) **[87]**. They defined 'reflectarrays' as being *"a class of antennas that utilizes arrays of elementary antennas as reflecting surfaces".* The idea was to combine the simplicity of reflector antennas with the performance versatility of arrays. The authors demonstrated how the phase of a reflected wave could be controlled by directing a feed horn antenna at an array of varied-length waveguides and derived equations for surface impedance as a function of the desired phase front. Although promising, the structure was too bulky for lower microwave frequencies. Furthermore, phase control was still achieved by fixed geometry.

With the maturation of printed circuit board, and photolithography technology and Moore's law in full swing, circuits became cheaper and easier to fabricate for higher frequency microwave applications. There was also an urgency felt by various militaries for advances in ship and airborne radar, and

extremely-high-frequency technology for satellite communications. Rapid progress was therefore made in phase shifter technology. The main technologies can be classified in terms of how they introduce phase shift; by varying path length (coaxial digital and switched-line phase shifters), modulating impedance (PIN diode, varactor, ferroelectrics e.g. yttrium iron garnet, nonlinear dielectrics e.g. barium strontium titanate (BST)) and mechanical manipulation (micro-electromechanical system (MEMs) bridges).

Monolithic microwave integrated circuits (MMICs) revolutionised phase shifter technology with nanosecond switch time, low-loss operation. They were originally based on more expensive gallium arsenide (GaAs) because the transistors had higher switching speed for the same size when compared to Si, and the first circuits had optically patterned transistor gates around 1-micron in size **[88]**. The basic concept of an MMIC is to create two parallel 'channels' that split and reunite between an input feed and output transmitter. An extra length of line is inserted to one of the outputs and each output is gated by a transistor; thus a signal can be directed down the shorter or longer path before being emitted. The difference in path length between channels introduces a relative phase shift. Such circuits are usually operated in digital mode, with one channel off and the other on. When the states are switched, the output signal is emitted with a phase shifted relative to the original output signal. This system can be expanded to include multiple 'bits', for instance 4-bit and 6-bit are common. For more information, McQuiddy et al. (1984) **[89]** published a comprehensive historical review of the technological developments that led to MMICs, including accounts from contemporary contributors. By the late 1980s, MMICs in conjunction with Transmit/Receive (T/R) modules were being widely utilised by US defence contractors for applications in the 1 – 30 GHz and 30 – 300 GHz ranges, including lightweight satellite systems **[90]**. The development of personal communication devices led to the first commercially available 'smart antennas' by the mid-1990s.

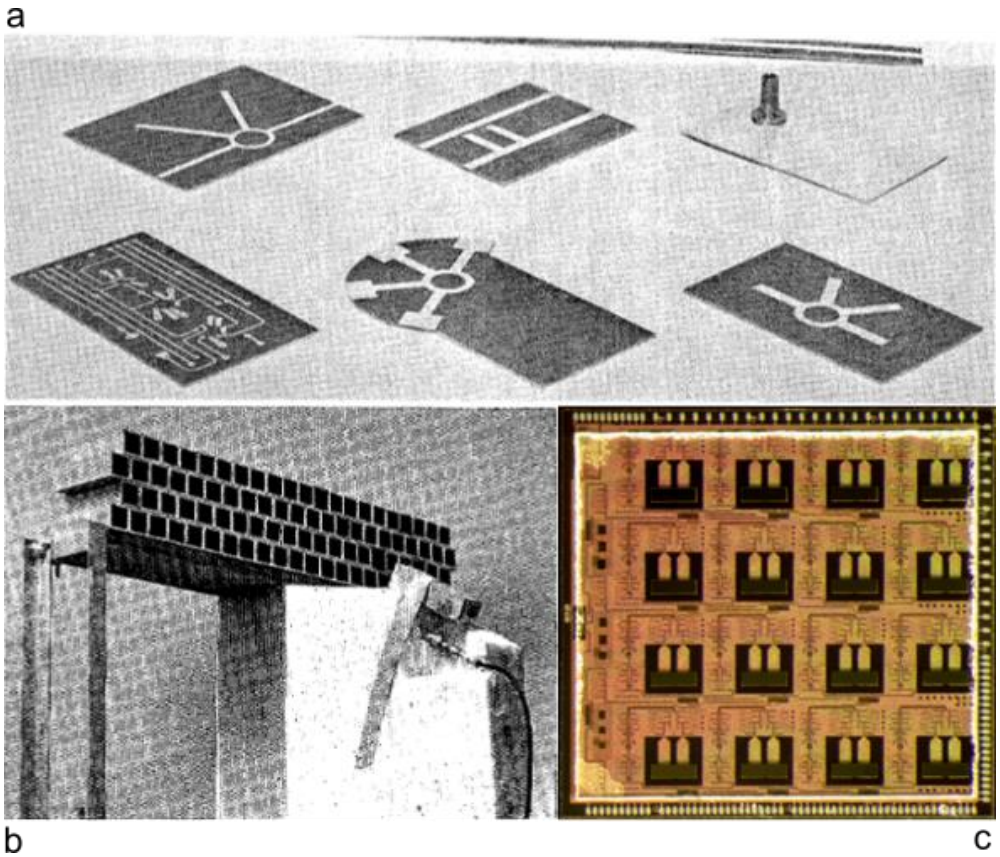

Figure 14. (a) Early microstrip antennas and printed circuits for microwave and low frequency c.1955 **[91]**. (b) Microwave waveguide reflectarray c.1963 **[87]**. A primary radiator illuminates a reflecting surface of staggered rows of waveguides. The phase and amplitude of reflected fields at any point is determined by the engineered surface impedance at that point. (c) First silicon wafer-scale phased array antenna 110 GHz c.2012 **[92]**.

2.5 RADAR to LiDAR

RADAR essentially works by simple time-of-flight (TOF) measurement. The principle is that emitted electromagnetic waves can be reflected as they interact with objects and by knowing the speed of light in a medium and measuring the time taken between emission and reception of the signal, the travel distance can be calculated. The source of the reflected signal, i.e. the objects position, can be calculated by trigonometry using multiple receivers; this is termed triangulation. Although the concept of using radio waves to detect distant objects was first demonstrated in 1904 by Christian Hülsmeyer **[93]** with the aim of preventing ship collisions in poor visibility, the first practical 'radio detection and ranging' (RADAR) system that could both detect and estimate distance to remote objects is credited to Robert Watson-Watt in 1935 **[94]**. With the Second World War looming, it was immediately recognised that smaller, lighter systems were required, particularly for airborne RADAR. This was realised with the development of the high-energy resonant cavity magnetron by John Randall and Harry Boot in 1940 **[95]**, which generated high-powered microwaves at 3 GHz (10 cm wavelength). The historical context of this development can be found in Blanchard et al. (2013) **[96]**. Although higher frequency electromagnetic waves typically experience greater attenuation due to interaction with atmospheric

particles and moisture, this allowed smaller antennas to be used, and additionally enabled the operator to ascertain more detailed, sub-metre information about the detected object.

The relationship between frequency / wavelength and "resolution", the minimum distance between two points before they become indiscernible, was explored in turn by Lagrange (1803) **[97]**, Abbe (1873) **[98]**, Helmholtz (1874) **[99]** and Rayleigh (1896) **[100]**. Ernst Abbe advanced the diffraction-limited resolution theory through experimentation with optical microscopy; the Abbe limit is generally given as $d = \lambda/2nsin(\theta)$, where d is the minimum resolvable distance, n is refractive index of imaging medium and $sin\theta$ is the aperture angle (angular half-width of light cone between the aperture and observed object). Thus the minimum resolution is approximately proportional to half the wavelength; this is the case for far-field wave phenomena, from optical microscopy to radar to acoustics. The theoretical basis for the Abbe limit and subsequent refinement as the "Rayleigh criterion" can be found in most optics textbooks **[101, 102]**.

The desire to maximise imaging resolution and minimise system bulk has driven the operational regime of detection and ranging systems to near infra-red (NIR) and optical frequencies, where the technology is referred to as light detection and ranging (LiDAR). LiDAR emerged as a distinct technology following the invention of the laser in the early 1960s. The difference is mainly in capabilities and components used; LiDAR uses photonic components such as optical lenses, diodes, lasers and photodetectors rather than electronic components as in RADAR. As well as higher 3D resolution, the potential smaller size of photonic systems promises lower power requirements and faster acquisition time. This makes LiDAR seemingly ideal for a range of disruptive technologies, including space vehicles, robotics, unmanned aerial vehicles and driverless automobiles, where it can be used for both distance finding and surface mapping. LiDAR has also found applications in consumer electronics such as the Microsoft Kinect, or more recent Orbbec, which employs skeletal tracking to integrate 3D human body movement with virtual environments and haptic feedback **[103]**. Indeed, due to the number and scale of potential applications, the LiDAR market is projected to grow from USD $1.1 billion in 2020 to $2.8 billion by 2025 **[104]**.

In many of these applications, device specifications are exacting. In particular, safety is of paramount importance, especially for driverless vehicles; devices must be reliable, robust, eye-safe, able to function in all weather conditions, operational in a wide range of temperatures, and resistant to interference from other light sources such as sunlight and other LiDAR devices. A major requirement is that the system be able to rapidly determine the scene 360° around itself at large distances so that decision times are minimised and margin for safety is maximal. Since the main driver behind driverless vehicles is to eliminate human error, devices must essentially perform much better than a human

in order to justify the cost of research and implementation. Table 1 shows the main performance characteristics required for driverless cars **[105, 106]**.

	Performance characteristic	Value required
1	Field of view	60 - 120°
2	Frame rate	High (tens of MHz)
3	Measurement range	150 m (1 μs time of flight)
4	Spatial resolution	10 cm

Table 1. Key performance characteristics of LiDAR devices and values necessary for driverless cars. 1.) 60 - 120° is the range required to provide 'full scene scanning'; 120° FOV is a requirement when LiDAR is attached to headlamps according to Shuttleworth 2019 **[107]**. While 360° detection is the aim, this can be covered by multiple-device configurations or rotating mechanical systems. 2.) High frame rate is vital for autonomous vehicles because it contributes to the overall 'decision time' when responding to danger. 3.) While a larger measurement range is obviously advantageous, the system must work at the same exacting standard for all distances within its range. 150 m is the shortest distance required due to its contribution to decision time. 4.) Finer spatial resolution allows detection of smaller objects and more precise measurements for decision making.

In addition to these, a LiDAR device also needs to either provide real-time continuous scanning across the FOV or a high-sampling point map, in both vertical and horizontal axes. Aside from LiDAR, currently used systems for driverless vehicles also include 80 GHz radar and CCD cameras and combinations of these systems. However, these implementations are generally still based on macromechanical systems to generate scene data. This introduces certain inherent limitations, such as inertia of moving parts limiting the scanning / frame rate, typically to < 50 Hz **[105]**. They are also relatively bulky and vulnerable to reliability and maintenance issues, damage, and vibration, making them less than ideal for such applications.

Many approaches are being researched to find a robust LiDAR implementation that resolves the issues associated with mechanical systems, some of which are shown in Table 2. There is much potential crossover between approaches. For instance, research into metasurface lenses aims to replace microlens diffractive optical elements (DOEs) in VCSEL flash LiDAR, thereby improving power efficiency, beam uniformity and form factor. Flash LiDAR, Si waveguides, MEMS and quantum wells are beyond the scope of this thesis and focus will be directed towards devices based on an active medium; liquid crystals, transparent conducting oxides and phase change materials. A review of current LiDAR approaches can be found in Kim et al. (2021) **[105]**.

	Approach	Description	Pros	Cons	Performance example
1	Microelectromechanical systems MEMS e.g. Si nanobeams	Electrically-actuated substrate or metasurface elements.	Flexible, widely applicable.	Vulnerable to damage and vibration, limited FOV and angular resolution. High voltage bias.	24° FOV MHz framerate 12 V bias **[108]**
2	Optical phased arrays e.g. Si, SiN, polymer	Waveguide array, elements tuned to contribute to phase gradient	Resistant to external impact and vibration. High frame rate.	Insertion loss of laser power > high power consumption and heat management issues	25° FOV **[109]**
3	Flash LiDAR	VCSEL + diffractive optical element (DOE) generate 'point cloud' over large area.	DOE eliminates need for beam scanning. Large field of view.	Conventional microlens arrays and additional lenses add bulk and weight. High power required.	120 × 120° FOV Acquisition time 100ms **[110]**
4	Multiple quantum wells (MQWs) e.g. alternating layers n-doped AlGaAs / GaAs	Quantum confined Stark effect by applying bias to MQW elements allows tuning of optical response.	High frame rate, compact, high efficiency, simple fabrication.	High reflectance contrast, limited FOV, temperature sensitive.	20° FOV Up to GHz frame rate 3 V bias **[111]**
5	Transparent conducting oxides (TCOs) e.g. Indium tin oxide ITO	Charge concentration, controlled by applied bias, modulates effective refractive index.	High speed modulation, low voltage bias, low power consumption	Expensive, complex fabrication process, easily damaged	80° FOV 10 MHz frame rate 3 V bias **[112]**
6	Liquid crystals e.g. 6CHBT	Effective refractive index dependent on crystal orientation, controllable by applied bias	Easy to fabricate, reliable.	Small steering angle, low efficiency, limited to kHz frame rate by LC orientation speed, limited resolution.	20° FOV kHz frame rate 8 V bias 15% efficiency **[113]**
7	Phase change materials e.g. chalcogenides, GST, VO_2	Modulation of refractive index by stimulating transition between electronic states / crystalline phases.	Fast switching via multiple stimuli, high refractive index contrast.	Tuning requires precise electrical and thermal control, temperature sensitive.	82° FOV 50 kHz frame rate **[114]**

Table 2. Approaches towards LiDAR implementation. Note: field of view (FOV) is taken as double the maximum deflection angle and does not necessarily imply continuous steering.

2.6 Active beam-steering metasurfaces

Liquid crystals (LCs) have been extensively studied for dynamic optical devices due to their high optical anisotropy and strong response to electrical stimuli. Nematic LCs can either impede or facilitate light depending on the orientation of crystals with respect to incident light polarisation. The orientation of crystals can be rotated by application of an electric field, thus enabling dynamic modulation of light. Algorri et al. 2020 **[115]** used this concept to demonstrate a multifunctional LC platform, based on 4-(trans-4-n-hexylcyclohexyl)isothiocyanatobenzene (6CHBT), that could be used as a lens, beam steerer and tuneable beam splitter at 632.8 nm wavelength. The structure consisted of an 87 μm thick nematic LC-filled cavity sandwiched between indium-tin oxide (ITO)-patterned glass wafers. The 26 nm thick ITO gratings were orientated perpendicular to each other; their function was to control the electric field

distribution across the LC cell area. 1kHz AC was applied through four electrodes connected to the ITO gratings, each with independently controlled phase and amplitude.

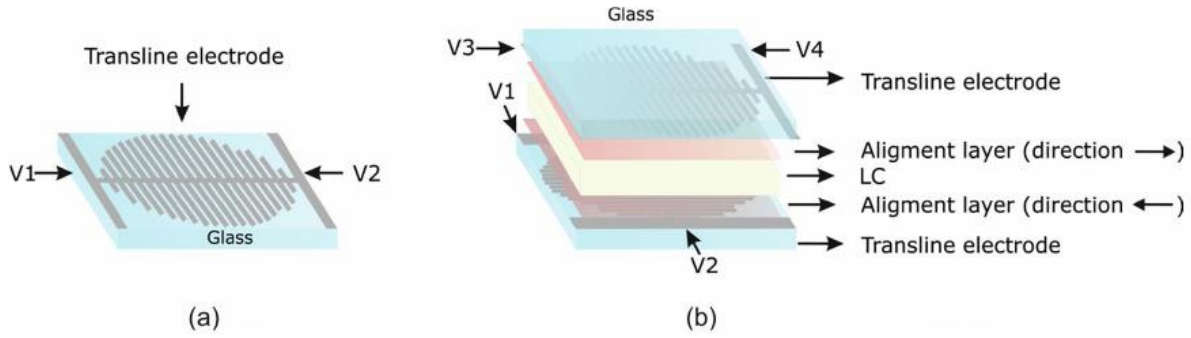

Figure 15. Liquid crystal based beam-steering platform controlled by voltages applied to ITO electrodes **[115]**. (a) Glass substrate with patterned ITO microelectrode. (b) entire stack including liquid crystal and alignment layers. Typically made of polyimide, alignment layers are used to achieve defect-free alignment of liquid crystals via interactions between LC and polyimide molecules.

By controlling the voltage at each electrode, the orientation of LCs was tuned across the unit. At no applied voltage, light polarisation that matched crystal orientation experienced a refractive index of 1.68. At 10V, LCs aligned perpendicular to the substrate and the effective refractive index decreased to 1.52. In this manner, a predetermined distribution of 'average refractive index', thus phase gradient, was established across the cell. For the beam-steering application, a LC-induced phase gradient was established for each desired beam deflection. For example, applying combination of V=[1,2,0,0] and V=[1,2,4,0] for each electrode allowed horizontal and vertical steering, while V=[1.5,0,1,2] was used for an intermediate angle. The steering angle was controlled by adjusting the steepness of the gradient profile via voltage amplitudes and due to device symmetry, angles could be reversed by inverting the voltages. The device was demonstrated to be a lightweight, power-efficient platform that could be used for a variety of applications including dynamic 2D beam steering. However, presumably because of the small difference in refractive index between orientations, the actual steering angle only spanned ±0.036° in horizontal and vertical directions and is thus not suitable for LiDAR applications. Despite this, there appears to have been some success utilising LCs for LiDAR commercially, for instance Lumotive claims their LC metasurface-based platform can achieve field-of-view of 120° horizontal and 25° degrees vertical at 905 nm wavelength **[116]**.

ITO-based platforms have been demonstrated to achieve high phase shifts that can be integrated into nanoscale metasurfaces. Smaller arrays are beneficial in that they minimise reflected side lobes (criteria $< \lambda/2$) and increase beam deflection angle. The basic concept of ITO is as follows. An applied electric field perturbs the free electron density, leading to formation of accumulation (or depletion) regions. This can switch the permittivity of the region negative or positive, respectively; effectively the region switches between optically metallic or dielectric. At a specific wavelength, the permittivity of the region

is close to zero (epsilon-near-zero, ENZ) and here optical intensity is enhanced. By controlling the applied voltage and thus tuning the permittivity of ITO to cross this ENZ point, a large modulation in reflected amplitude and phase can be achieved. The ENZ wavelength can be established by fixing the carrier concentration during fabrication.

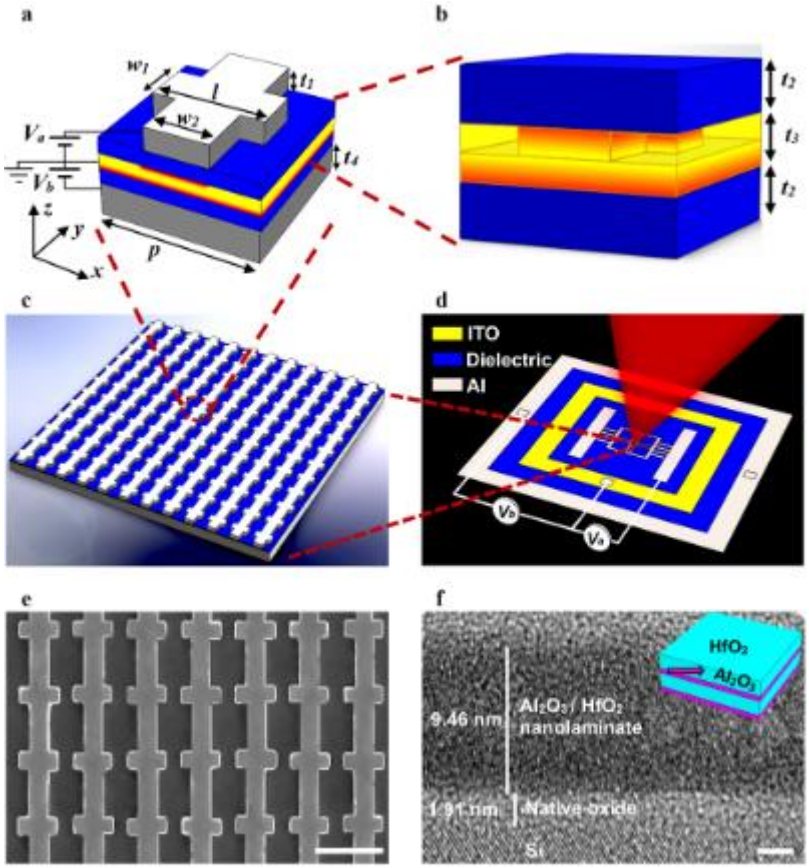

Figure 16. Dual-gated ITO reflectarray **[117]**, (a) Unit cell schematic. Thicknesses of antenna array, gate dielectrics, ITO layer and back reflector: t1 = 40 nm, t2 = 9.5 nm, t3 = 5 nm, t4 = 80 nm. Antenna dimensions: l = 280 nm and w1 = 120 nm and w2 = 170 nm. Period of metasurface p = 400 nm.

Shirmanesh et al. (2018) **[117]** demonstrated a 'dual-gated' ITO-based reflectarray metasurface that used two independently biased metal-oxide-semiconductor field effect channels. The structure, as seen in Fig 16. consisted of a dielectric-ITO-dielectric stack sandwiched between top and bottom gate electrodes that comprised of periodic arrays of Al fishbone antennas connected to external Al pads. Between the bottom dielectric and Si substrate was an Al back reflector. Two DC bias voltages were applied, one between the top antennas and ITO and the other from the bottom reflector and ITO. This led to the formation of two accumulation or depletion regions at the ITO / dielectric interfaces and consequent variation in complex refractive index of ITO. Using this dual-gated design, they were able to achieve up to 303° phase shift at bias voltages of -6.5 V / +6.5 V. However, due to absorption in ITO, 'relative reflection modulation' ranged from 28 – 89 % at 1550 nm wavelength; this means that there was a large difference in reflectance depending on the bias configuration, not ideal for applications such as LiDAR.

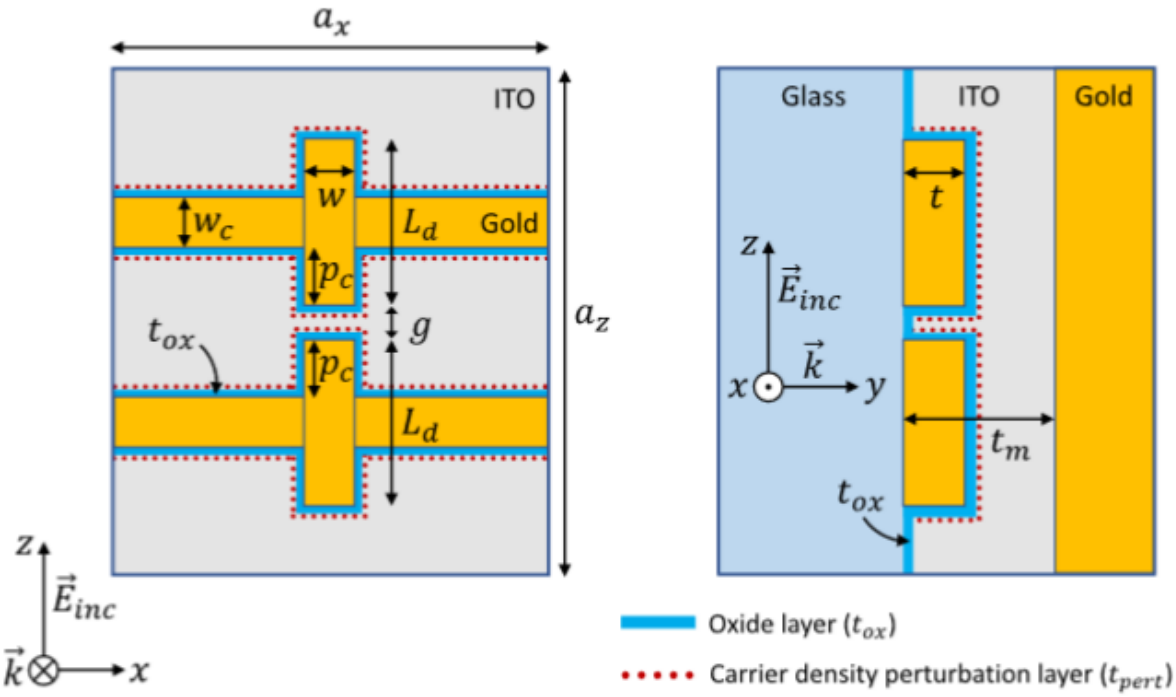

Figure 17. Plasmonic pixel metasurface for optical phased array **[118]**. Unit cell, plan (left) and cross-section (right). Dimensions: ax = 500 nm, w = 50 nm, wc = 50 nm, t = 50 nm, tox = 5 nm.

Lesina et al. (2021) **[118]** used a similar fishbone antenna structure for their simulated plasmonic optical phased array. The gold antennas were deposited on glass, then covered by an insulating thin oxide and conductive ITO layer. The ITO layer was sandwiched between the antenna / glass and reflective gold backplane. The antenna / oxide / ITO structure formed a MOS capacitor, with antennas as the electrical contact, with pairs of antennas forming individually-addressable plasmonic 'pixels'. As before, the ITO carrier density is altered by voltage applied to the antennas, leading to an accumulation or depletion region and consequent localise change in complex permittivity. The key concept here is that the bias-controlled local change in permittivity of ITO occurs around the enhanced plasmonic near field (i.e. at the dipole extremities and gap between dipoles) and so has a significant effect on the plasmon resonance condition. This effect drives the phase shift of a reflected wave. Simulations suggested that such a structure could achieve 330° phase shift with an average (accumulation and depletion) reflectance of 25% and a reflectance contrast of 30%.

In contrast to transparent conducting oxides such as ITO where the changes to complex permittivity occur as a result of free carrier accumulation and depletion, the permittivity of solid-state phase change materials (PCMs) changes concurrently with fundamental changes to their electronic band and crystallographic structure. These changes generally occur on the sub-nanosecond scale and can be prompted by a variety of stimuli including thermal, electrical, magnetic, and mechanical, making PCMs very flexible in terms of device design and application. A wide range of PCMs are increasingly being

researched for reconfigurable nanophotonic devices. Chalcogenides are the best known group, having been used extensively with lasers for non-volatile optical disk storage.

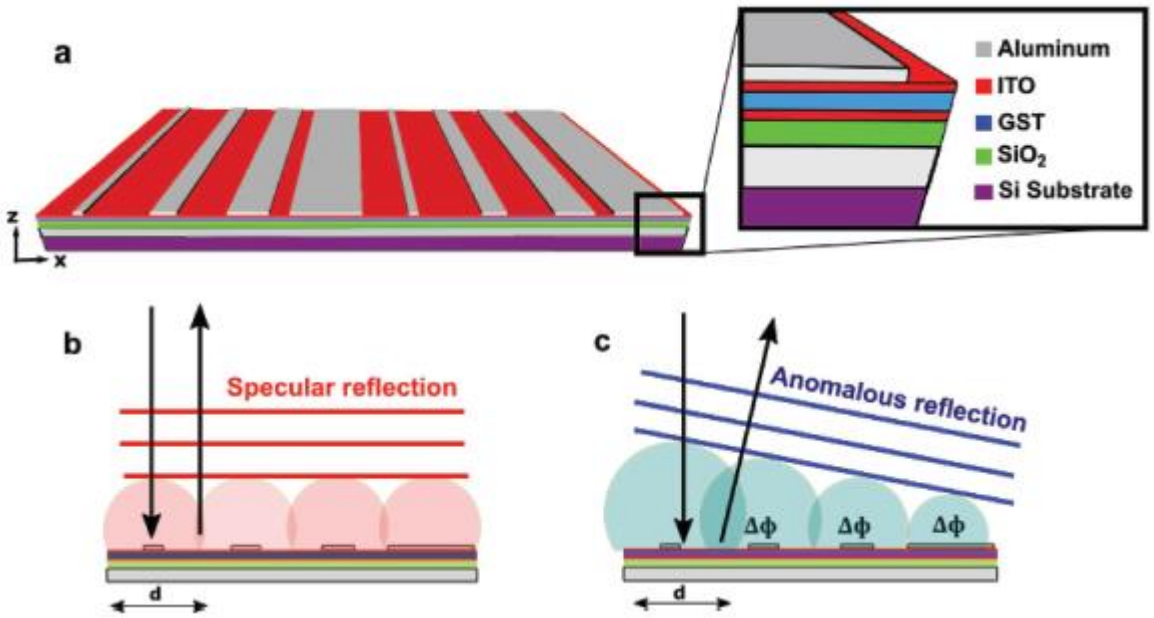

Figure 18. GST-based reconfigurable phase-change beam-steering device **[119]**. (a) Device schematic. (b) Wavefront reconstruction from Huygens wavelets for specular reflection (crystalline state) and (c) anomalous reflection (amorphous state).

Germanium-antimony-tellurium $Ge_2Sb_2Te_5$ (GST) is one chalcogenide that has been researched for use in beam steering reflectarrays. Galarreta et al. (2018) **[119]** demonstrated a device that combined GST, ITO and Al plasmonic antennas. The structure consisted of a SiO_2 / ITO / GST / ITO multilayer stack, sandwiched between a backplane Al reflector on Si and top array of periodic plasmonic Al antennas. The design relied on a shift in the plasmon resonance condition, this time magnetic resonance between Al patches and Al bottom plane, as the state of GST was changed between crystalline to amorphous states. In the amorphous phase, resonance and subsequent scattering for each Al patch depended on the specific geometry. The designed antenna widths were set as 166 nm, 214 nm, 239 nm and 650 nm, which established a reflected phase gradient with a coverage of ~300° and consequent wavefront deflection as determined by the unit cell pitch. For period 700 nm and wavelength 1550 nm, experimental anomalous reflection was found to be 34% and deflection angle 33°. At the crystallisation (SET) stage, the extinction coefficient of GST increased such that the plasmon response was damped. This led to a near invariant reflected phase response between antenna widths, thus zero wavefront deflection and reflection of 22% (reflection contrast of 12% between GST phases). Although the authors claim the bottom Al plane or ITO layer could be used as a resistive heater in real-time in-situ device switching, this was not demonstrated, and instead crystallisation and reamorphisation (SET and RESET) cycling was done by use of a 405 nm scanning-pulsed laser, with each scan taking ‘minutes’. Thus the real world switching performance cannot be inferred, but it is clear that the planar GST layer would need to be heated and cooled uniformly and rapidly, since successful recrystallisation of GST

requires melting temperatures above 150°C and rapid cooling (>20°C ns^{-1}). The relative contribution of ITO and GST components towards the demonstrated optical behaviour is also unclear.

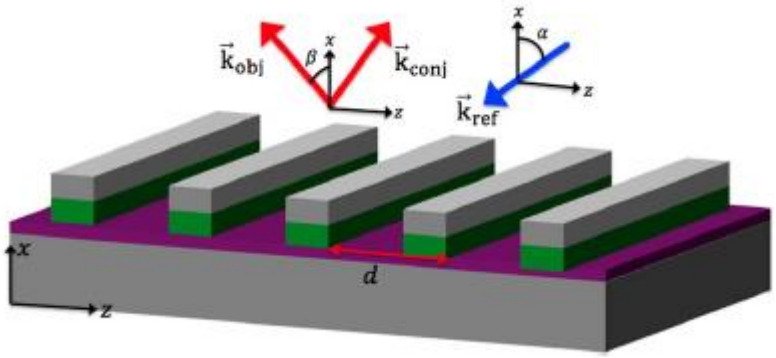

Figure 19. VO2 based 'digital optical metasurface' **[114]**. Au (grey) nanowires and backplane, SiO2 (purple) spacer, VO2 (green) active medium. Nanowires are 210 nm wide while thicknesses of gold, VO_2 and silica are 50, 100 and 10 nm respectively. Unit cell periodicity *d* is 387.5 nm, one-quarter of the operating free space wavelength (1550 nm).

Another prominent phase change material, vanadium dioxide has the advantages of comparatively lower transition temperature ~68° and no requirement for rapid cooling, though rapid cooling is beneficial for faster switching. Given that the VO_2 transition transpires optically at sub-picosecond timescales **[120]** and electrically < 3 ns **[121]**, it follows that the thermal dynamics of the system is the limiting factor when it comes to switch speed. In contrast to Galarreta **[119]**, where the entire continuous active layer must be heated uniformly, Kim M. et al. (2016) **[114]** proposed a 'digital optical metasurface' where individual VO_2 elements were heated via current flowing through gold nanowires. As well as the flexibility afforded by individually addressable elements, the thermal mass of active medium was smaller, thus temperature changes should take place faster and with less power input. Predicted time response for their device was compared to similar structures that have been reported to have a 'roll-off' frequency of 50 kHz, giving a total response of around 20 milliseconds **[122]**. Their thermal simulations suggested that the current density required in the Au nanowire to raise VO_2 temperature above transition temperature was one order of magnitude lower than the failure current density of gold nanowire **[123]**. The operational concept of their device was based on encoding a digital pattern of -1 or +1 on an array of subwavelength nanowires, where the code indicated whether a DC current was allowed to flow through each nanowire element. Current flowing through the specified nanowires caused ohmic heating until VO_2 exceeded its IMT temperature and transitioned to its metallic state. Each element was a stack of Au nanowire / VO_2 / SiO_2 spacer / Au backplane and heatsink. This structure was interpreted as a Fabry-Perot resonator, with VO_2 acting as a tuneable cavity. In the 'cold' VO_2 state (293 K), the elements could be seen as an array of on-resonance cavities; the magnetic field is strongly enhanced within the VO_2 and SiO_2 layers as in a Fabry-Perot resonator. In the 'hot' state (363 K), VO_2 becomes metallic and the cavity is reduced to the thin SiO_2 layer. In effect, the Au-VO_2 part of the resonator becomes more like a non-resonating metallic unit, changing the phase of reflected light. The reflected phase difference between 'cold' and 'hot' VO_2 states was 180°, and by arranging

the digital pattern across the array, varied phase gradients, thus deflection angles, were achieved. For light incident at 20° and two periodically alternating elements (CC/HH), the reflected angle was 41°, for three (CCC/HHH) the angle was 18° and for four (CCCC/HHHH) the angle was 9°, with all configurations achieving a similar 20% reflectance. Digital operation was used to avoid high temperature sensitivity that may be experienced by using intermediate VO_2 phases. They also point out that the Ohmic loss of the unit cell is highest between 315 – 325 K, at the start of the insulator-metal transition.

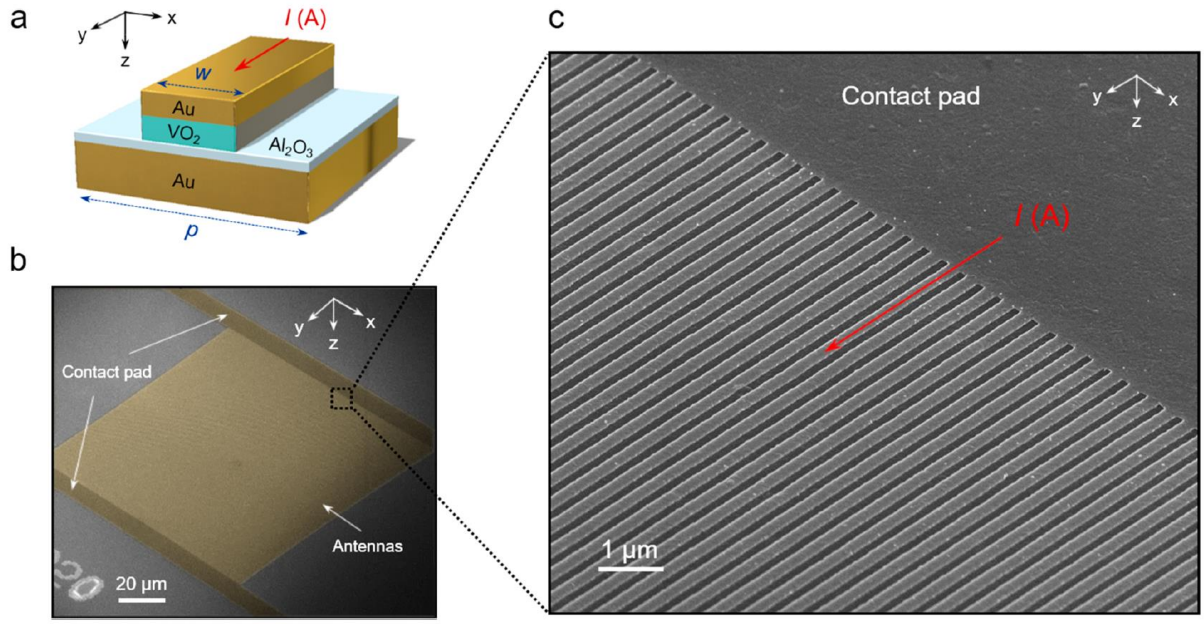

Figure 20. Gold / VO2 subwavelength antenna array **[124]**. Voltage applied to contact pads causes current flow through Au nanowires and subsequent joule heating. Temperature rise in underlying VO2 causes phase transition and consequent change in permittivity, resulting in change in reflected phase and amplitude. Thickness of Au and VO2 comprising antenna 40 nm. Antenna width and period 240 and 400 nm, respectively. Thicknesses of Al2O3 layer and Au backplane 50 and 150 nm, respectively.

Kim Y. et al. (2019) **[124]** fabricated a similar subwavelength antenna array where VO_2 elements were heated via joule heating through gold nanowires. Although this work demonstrates that phase modulation is possible via electrical heating of VO_2 metasurface elements, this is not a practical design for beam deflection because the array does not constitute a phase gradient; all elements within the array experience the same degree of heating and thus reflect a singular phase. However, their investigation into the electrical behaviour and switching dynamics is directly relevant to the work in this thesis. As seen in Fig. 20, the nanowires were electrically connected by contact pads at both ends; applying a potential difference between these pads led to current flowing through the nanowires and subsequent heating of the VO_2 elements. The mechanism of phase shift is the same as in Kim M. (2016) **[114]**, with the added observation of a 175 nm shift in resonance wavelength between insulator and metallic VO_2 phases. A potential of 11 V was found to generate enough heat to achieve full insulator-metallic transition, with the 'transition region' evident from 9 V. The on (11 V) and off (0 V) switching times

for 1 Hz pulses were measured as 500 ms and 250 ms, but using high intensity short pulses (25.7 V, 15 ms), on / off times were reduced to 15 and 100 ms. They also observed a decrease in the modulated amplitude of reflectance as the electrical signal frequency increased above 2 Hz, implying that the VO_2 had not fully transitioned above this rate. Continuous reflected phase shifts of 180° and 250° were observed at 1550 and 1520 nm, respectively, with a reflectance modulation of 23.5%. Ideally, a beam steering array would have a 2π phase modulation gradient and minimal reflectance contrast between elements of the array.

Chapter 3: Simulation and Modelling

Whereas Chapter 2 detailed the contextual background for the projects in this thesis, this section covers the electromagnetics and condensed matter physics necessary to understand the material properties and methods that were used to generate data. The mathematic problem for the work in Chapter 6 was relatively simple and well-suited to an analytic method, specifically the Fresnel equations for reflection and transmission in multi-layer films. With that exception, the projects were investigated using the Finite Element Method (FEM), a numerical analysis technique.

3.1 Physics background

3.1.1 Light-matter interactions

Light is a self-propagating wave of electromagnetic energy, characterised by oscillating electric and magnetic fields. Electromagnetic waves self-propagate through space because a time-varying electric field generates a time-varying magnetic field and vice versa. In free space, the electric and magnetic fields oscillate in planes orthogonal to each other and also to the direction of wave propagation. Light-matter interactions are governed by features of the electromagnetic wave, such as frequency, polarisation and intensity, and properties of the material, which derive from its molecular and electronic band structure. The band theory of solids arises from the Pauli Exclusion Principle, which states that no two fermions can have an identical quantum number. The electronic configuration of an atom is thus discretized into 'orbitals'. When N identical atoms are bound together as in a crystal lattice, the orbitals of corresponding electrons split into N distinct energy states. A bulk material contains a huge number of allowed electron energy levels which may overlap to form energy continua aka bands. The outermost band beneath the Fermi surface is known as the valence band and contributes to chemical bonding. Above the valence band and separated by an energy gap lies the conduction band. In dielectrics this energy gap can be very large. Electrons in the valence band are considered bound and can only move a limited distance from their positive ion in response to electromagnetic waves. In metals, the conduction and valence bands overlap and the energy gap is negligible. Very little energy is required to promote electrons from the valence to conduction band. Electrons in the conduction band are considered 'free' in that they are not locally constrained to individual ions in the atomic lattice and thus are easily displaced in response to an applied electric field. The delocalised electron cloud is thus easily polarised by an incident electromagnetic wave and the consequent charge separation of electrons and positive ions creates a restoring force. The system is therefore analogous to a classical oscillator, with light the driving force and polarisation the restoring force. The perturbation of electron distribution within a conductor is opposed by a restoring force due to the separation of charge; a conductor will therefore return to equilibrium once the driving force is removed. The time of the system to return to equilibrium

is quantified by the plasma frequency $\omega_p = \sqrt{(n_e e^2/\varepsilon_0 m^*)}$ which is related to the electron number density n_e and effective mass m^* of electrons.

In the classical regime, an electromagnetic wave propagating in air and impinging on a material with disparate refractive index can be reflected, refracted (transmitted) or absorbed. Specular reflection is coherent and associated with mirror-like smooth surfaces, whilst diffuse reflection (sometimes called scattered light) is incoherent due to surface irregularities and gives a 'matt' appearance. In the quantum regime, light-matter interactions are instead characterised by photon-electron scattering events, whereby photons can energetically excite electrons and excited electrons can lose energy by generating photons. Scattering is characterised by two main interactions; inelastic and elastic. Inelastic scattering occurs when there is net energy loss from photon to electron; the scattered wave has less energy than the incident wave. The difference in energy is termed loss, absorption or attenuation and is eventually dissipated as heat. The main loss mechanisms are intraband transitions, where an electron is raised into an excited state by absorption of a photon, and Ohmic losses, caused by electron-electron and electron-ion scattering, as well as inelastic scattering at grain boundaries and defect sites. The degree to which a material is lossy is represented as the imaginary part of its complex relative permittivity. In transition metals an important band transition occurs as unbound valence electrons in the d-band are excited to the s-band. The transition is achieved by absorption of photons with energy corresponding to the band gap. In silver, the 4d to 5s transition has a large energy gap of 4 eV, corresponding to 310 nm (UV) photons. Since absorption does not occur in the visible spectrum, silver appears to reflect white light. In gold, relativistic effects cause contraction of the s orbital, significantly lowering the 5d to 6s transition energy gap to 2.3 eV **[125]**. This corresponds to 539 nm, blue-green in the visible spectrum. Blue-green light is thus less efficiently scattered, resulting in yellow-orange. As the size of material shrinks from bulk to nanoparticle, band gaps tend to grow as they crystallize into more well-defined levels, resulting in blue-shifted absorption spectra.

Scattering can occur both in the backward and forward direction with respect to the incident wave vector. Refraction is the result of repeated forward-scattering events between photons and electrons within a continuous medium, resulting in phase angle retardation and reduced propagation velocity of the wave relative to free space. The degree to which this occurs in a material is represented as the real part of its complex relative permittivity. Elastic scattering occurs when there is no net energy transfer between photon and electron. At certain frequencies, some dielectrics have almost no loss, thus light that is not back-scattered is elastically forward-scattered; light propagates freely through the material and it appears transparent. This would also occur at the surface of an ideal conductor at low frequencies, where free electrons are easily displaced and able to match the oscillation frequency of the electromagnetic wave. Polarisation and subsequent electron oscillation generates a second

electromagnetic wave, thus the energy of the incident wave is transferred into the energy of the scattered wave. The amplitude of an electromagnetic wave exponentially decays with a characteristic distance into a conductor, termed skin depth, which will be expounded later. Due to this, electromagnetic waves are unable to propagate through a bulk conductor at low frequencies $\omega \ll \gamma$, corresponding to visible / near infrared. Since light is unable to penetrate further than a few skin depths most is back-scattered. Below visible frequencies most metals behave in this manner (albeit with some loss), giving them their characteristic lustre. At higher frequencies approaching the plasma frequency, the optical behaviour of metals becomes more complex and requires a more rigorous explanation, provided in part by the Drude model. Derivations in the next section are mostly from references **[126]** and **[127].**

3.1.1.1 Drude model

In 1900 Paul Drude proposed a classical model of electron transport in metals to account for electron transport phenomena such as electrical and thermal conductivity **[128]**. In this model, free electrons in the metal are analogous to the particles of an ideal gas, constantly in motion relative to the fixed lattice of immobile positive ions. The number of free electrons per volume of a metal is given by the electron number density $n_e = N/\mathrm{V}$. Electrons in an applied electromagnetic field travelling at velocity $\mathbf{v}$ for a duration of ∂t will travel a distance $\mathbf{v}\partial t$. Hence the number of electrons passing through a cross sectional area A over time interval ∂t is $n_e \mathbf{v} A \partial t$. Since each electron carries charge $-e$ and current = charge / time, current density $\boldsymbol{J} = -e n_e \mathbf{v}$. Electrons continue to accelerate until they collide with immobile ions; this model assumes no other interactions such as electron-electron or electron-ion Coulomb forces. Other sources of damping such as radiation from accelerating charges and scattering are also unaccounted for. Collisions are assumed to be instantaneous; electrons have maximum average velocity $\mathbf{v}_{max}$ and minimum average velocity $\mathbf{v}_0$ immediately pre- and post-collision, respectively. Emergent electrons have a random direction and kinetic energy according to local thermal equilibrium $3/2\, k_B T$, resulting in $\mathbf{v}_0$.

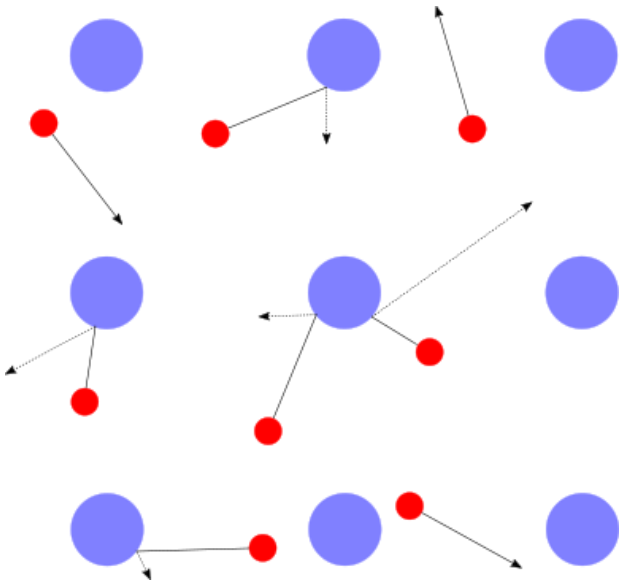

Figure 21. Free electron model; electrons free to move and collide with immobile positive ions.

By definition, the force experienced by an electron in an applied electromagnetic field is given by $\boldsymbol{F} = e\boldsymbol{E}$ where F force (Newtons), e charge of electron (coulombs C), $\boldsymbol{E}$ electric field (V/m). This force results in acceleration of the electron according to Newton's second law a $= \boldsymbol{F}/m$ where m is electron mass (kg) and a acceleration (ms^{-2}). Combining the above gives:

$$\boldsymbol{F} = m\frac{\partial \mathbf{v}}{\partial t} = e\boldsymbol{E}$$

Thus the instantaneous velocity of an electron which has accelerated for a length of time t is given by:

$$\mathbf{v} = \mathbf{v}_0 - \mathbf{v}_1 = \mathbf{v}_0 - \mathrm{at} = \mathbf{v}_0 - \frac{\boldsymbol{F}t}{m} = \mathbf{v}_0 - \frac{e\boldsymbol{E}t}{m}$$

since $\boldsymbol{F} = e\boldsymbol{E}$. It follows that the average velocity $\mathbf{v}_{av}$ of electrons in a constant electric field then depends on the average time between collisions, often termed the relaxation time τ. Current density is thus related to relaxation time by:

$$\boldsymbol{J} = -en_e\mathbf{v}_{av} = \left(\frac{n_e e^2 \tau}{m}\right)\boldsymbol{E} \qquad (1)$$

According to Ohm's law:

$$V = IR \qquad R = \frac{\rho l}{A}$$

$$V = \frac{I\rho l}{A} \qquad \rho = \frac{1}{\sigma_0}$$

$$\frac{V}{l} = \frac{I}{A}\frac{1}{\sigma_0}$$

$$\mathbf{E} = \frac{J}{\sigma_0}$$

$$\boldsymbol{J} = \sigma_0\boldsymbol{E} \qquad (2)$$

From (1) and (2) the relationship between DC conductivity σ_0 and relaxation time is therefore **[126, 127]**:

$$\sigma_0 = \frac{n_e e^2 \tau}{m} \tag{3}$$

For an oscillating electromagnetic field, the AC conductivity needs to be considered. The harmonic time dependence of $\boldsymbol{B}$ and $\boldsymbol{E}$ as components of the EM driving field can be represented as complex exponential functions of angular frequency $\omega = 2\pi v$:

$$\boldsymbol{B} = \boldsymbol{B}(\omega)\mathrm{e}^{-i\omega t}, \boldsymbol{E} = \boldsymbol{E}(\omega)\mathrm{e}^{-i\omega t} \tag{4}$$

where the imaginary unit $i^2 = -1$. Equation (2) can thus be rewritten:

$$\boldsymbol{J} = \sigma(\omega)\boldsymbol{E}(\omega)e^{-i\omega t}$$

Momentum of the electron with respect to time varies according to oscillation of the driving field as:

$$\vec{\rho}(t) = \vec{\rho}(\omega)e^{-i\omega t} \tag{5}$$

The equation of motion for an electron in an AC driving field is given by **[126, 127]**:

$$\boldsymbol{F}_e = -\vec{\rho}\gamma - \boldsymbol{F}_d$$
$$\frac{\delta\vec{\rho}}{\partial t} = -e\boldsymbol{E} - \vec{\rho}\gamma$$

where $\boldsymbol{F}_d$ is driving force, $\boldsymbol{F}_e$ is experienced force, $\vec{\rho}$ is electron momentum and $\gamma = 1/\tau$ damping frequency (aka relaxation rate). The negative factor is due to the electron charge; electron movement opposes the direction of the driving field by convention.

Substituting (4) and (5) gives:

$$-i\omega\vec{\rho}(\omega) = -e\boldsymbol{E}(\omega) - \frac{\vec{\rho}(\omega)}{\partial t}$$
$$\Rightarrow \vec{\rho}(\omega) = \frac{e\boldsymbol{E}(\omega)}{\gamma - i\omega} \tag{6}$$

Current density as a function of angular frequency can be described as:

$$\boldsymbol{J}(\omega) = -\frac{n_e e\vec{\rho}(\omega)}{m}$$

Substituting in equation (6):

$$\boldsymbol{J}(\omega) = \frac{\left(\frac{n_e e^2}{m}\right)\boldsymbol{E}(\omega)}{\frac{1}{\tau} - i\omega}$$

Thus the AC conductivity is found to be:

$$\sigma(\omega) = \frac{\sigma_0}{1 - i\omega\tau}$$

where σ_0 is DC conductivity as given in equation (3).

3.1.1.2 Complex relative permittivity

At optical frequencies, preference over conductivity is usually given to the relative permittivity ε, also known as dielectric constant or function; $\kappa = \varepsilon = \varepsilon_{mat}/\varepsilon_0$. Separation of charge in a material due to an applied electric field constitutes storage of electrical energy. The amount of energy stored is related to the degree of polarisation and related to the materials *susceptibility*, the ease in which the material polarises due to the electric field. The frequency-dependent absolute permittivity represents the capability of a material to store electric energy, i.e. the amount of charge needed to generate one unit of electric flux in a medium. Relative permittivity is the absolute permittivity of a material relative to vacuum permittivity.

The equation of motion for an electron is the sum of forces acting upon it. In an AC driving field this can be written in terms of position remembering $\boldsymbol{F} = e\boldsymbol{E}$ as:

$$m\frac{\partial^2 x}{\partial t^2} + \gamma m\frac{\partial x}{\partial t} = -e\boldsymbol{E}(t) \tag{7}$$

Essentially this describes a damped driven oscillator with no restoring force; the electron can be described in terms of momentum (as in the AC conductivity derivation above) or position (complex relative permittivity, below). The displacement of an oscillating electron as a function of time in a driving field can be expressed as **[126, 127]**:

$$x(t) = \underline{x}\mathrm{e}^{-i\omega t}$$

where:

$\underline{x}$ complex amplitude

$\mathrm{e}^{-i\omega t}$ complex continuous time exponential

This form presents the amplitude, phase lag (between driving field and electron oscillation) and frequency of electron oscillation as a coordinate on the 2D complex plane. The phase difference arises because of the necessary causal relationship between driving field and electron displacement. $\tilde{x}$ represents the amplitude and phase difference while $e^{-i\omega t}$ represents frequency and time dependence. Electron displacement as a function of time can be rewritten as:

$$x(t) = \frac{e}{m(\omega^2 + i\gamma\omega)}\boldsymbol{E}(t)$$

Displacement of electrons relative to equilibrium (position at no applied field) causes an electric dipole moment density, termed polarisation, given by:

$$\boldsymbol{P} = -n_e e x$$

Substituting x:

$$\boldsymbol{P} = -\frac{n_e e^2}{m(\omega^2+i\gamma\omega)}\boldsymbol{E} \tag{8}$$

Movement of charge back and forth through a unit volume of metal constitutes an electric flux density D, the charge per unit area displaced in electric field, related to polarisation by:

$$\boldsymbol{D} = \varepsilon_0\boldsymbol{E} + \boldsymbol{P}$$

Substituting $\boldsymbol{P}$ from (8) :

$$\boldsymbol{D} = \varepsilon_0\left(1 - \frac{\omega_p^2}{\omega^2+i\gamma\omega}\right)\boldsymbol{E} \tag{9}$$

where ω_p is the plasma frequency (derived in Appendix A1) given by:

$$\omega_p = \frac{n_e e^2}{m e_0}$$

Comparing (9) with the constitutive relation linking electric flux density to electric field $\boldsymbol{D} = \varepsilon_0\varepsilon\boldsymbol{E}$ reveals the Drude model of complex relative permittivity to be:

$$\underline{\varepsilon}(\omega) = 1 - \frac{\omega_p^2}{\omega^2+i\gamma\omega} \tag{10}$$

$\underline{\varepsilon}(\omega) = 1 + \frac{i\sigma_0(\omega)}{\varepsilon_0\omega}$ relates DC conductivity to complex relative permittivity.

3.1.1.3 Imaginary and real components of the relative permittivity

Complex relative permittivity can be decomposed into its real and imaginary components **[127]**:

$$\underline{\varepsilon}(\omega) = \varepsilon'(\omega) + i\varepsilon''(\omega) \tag{11}$$

where each component can be written in terms of $\tau = 1/\gamma$ as

$$\varepsilon'(\omega) = 1 - \frac{\omega_p^2 \tau^2}{1 + \omega^2 \tau^2}$$

$$\varepsilon''(\omega) = \frac{\omega_p^2 \cdot \gamma}{\omega(1 + \omega^2 \tau^2)}$$

Complex relative permittivity $\underline{\varepsilon}$ is related to the optical constants of a material by:

$$\underline{\varepsilon} = \underline{n}^2$$

where the complex refractive index is given by:

$$\underline{n} = n + ik$$

Thus, for a given frequency:

$$\varepsilon' = n^2 - k^2$$

$$\varepsilon'' = 2nk$$

The real part of the complex refractive index is the refractive index n, representing phase velocity. The imaginary part k is known as the extinction coefficient and represents attenuation of the electromagnetic wave as it passes through the material. The optical constants n and k of a material can be obtained experimentally from reflectivity studies in conjunction with Kramers-Kronig analysis. Permittivity models for given materials can therefore be obtained from experimental data and used to simulate the optical response of real materials.

Despite the apparent simplicity of the Drude model, it is remarkably successful at describing observed behaviour of metals over specific frequency ranges. However, as alluded to in the beginning of this section, the model fails at frequencies corresponding to interband transitions and cannot be used for dielectrics. Recognizing these shortcomings, Hendrik Antoon Lorentz extended the Drude model in 1905. The resultant Drude-Lorentz model represents a classical interpretation of light-matter interactions which can be adapted for many materials and has been used successfully ever since, although a quantum mechanical adaptation was later developed by Arnold Sommerfeld and Hans Bethe. The classical, rather than quantum, interpretation is valid for nanoparticles even smaller than the scale used in this work because of the high electron number density of the metals **[127].**

Lorentz approached the problem by imagining an electron and nucleus as two masses bound by a spring pursuant to Hooke's law **[129]**. Applying an electric field sets the electron into harmonic oscillation thereby stretching and compressing the 'spring'. The natural resonant frequency of each transition can be derived as for a driven harmonic oscillator and added to equation (7):

$$m\frac{\partial^2 x}{\partial t^2} + \gamma m\frac{\partial x}{\partial t} + m\omega_j^2 x = -e\boldsymbol{E}$$

All interband transitions relevant to the frequency range of interest can in this manner be accounted for and their contribution to the overall relative permittivity added to the free electron Drude term, typically in the form **[127]**:

$$\sum_j \frac{S_j}{\omega_j^2 - \omega^2 - i\omega\gamma_j} \tag{12}$$

where:

S_j strength of oscillator j

ω_j resonant frequency of oscillator j

γ_j damping constant of oscillator j

Now that the frequency dependent optical response of materials has been established, propagation of electromagnetic waves through the material can be considered.

3.1.1.4 Wave propagation and the dispersion relation

The dispersion relation describes how plane wave propagation through a medium depends on the frequency dependent complex relative permittivity of that medium. Derivation starts with the differential forms of Maxwell's equations relating the curl of an electric field with magnetic flux density and the curl of a magnetic field with electric flux density:

$$\nabla \times \boldsymbol{E} = -\frac{\partial \boldsymbol{B}}{\partial t}$$

$$\nabla \times \boldsymbol{H} = \boldsymbol{J}_e + \frac{\partial \boldsymbol{D}}{\partial t}$$

where:

$\nabla \times$ delX operator (curl); length and direction (vector) between origin and any point in 3D Euclidean space characterises rotation at that point.

$\boldsymbol{E}$ electric field

$\boldsymbol{B}$ magnetic flux density

$\boldsymbol{H}$ magnetic field

$\boldsymbol{D}$ electric flux density

J_e external current density

The above 'curl equations' can be combined to give the wave equation:

Time domain form:

$$\nabla \times \nabla \times \boldsymbol{E} = -\mu_0 \frac{\partial^2 \boldsymbol{D}}{\partial t^2}$$

Frequency domain form:

$$\boldsymbol{K}(\boldsymbol{K} \cdot \boldsymbol{E}) - \boldsymbol{K}^2 \boldsymbol{E} = -\varepsilon(\boldsymbol{K}, \omega) \frac{\omega^2}{c_0^2} \boldsymbol{E} \quad (13)$$

$\boldsymbol{K}$ wave vector

c_0 speed of light in vacuum $= 1/\sqrt{\mu_0 \varepsilon_0}$

$\nabla \times \nabla$ Curl of the curl i.e. the negative of the second partial derivative of **E** with respect to time

For light incident on a surface, transverse electron motion is perpendicular to driving wave propagation and so the dot product of wave vector and electric field is zero:

$$\boldsymbol{K} \cdot \boldsymbol{E} = 0$$

Inserting into equation (13):

$$\boldsymbol{K}^2 = \varepsilon(\boldsymbol{K}, \omega) \frac{\omega^2}{c_0^2}$$

This equation is known as the dispersion relation. The magnitude of $\boldsymbol{K}$ represents the increase in phase accrued by an EM wave propagating through a material relative to the incident wave. This phase lag thus depends on the incident frequency and the frequency dependent complex relative permittivity of the material.

3.1.1.5 Localised surface plasmons

As previously mentioned, metals can be thought of as a plasma of delocalised electrons and fixed lattice ions. These electrons can be excited to oscillate with respect to the fixed ions and Coulomb interactions in the plasma cause coherent oscillation modes. Just as photons are the quanta of electromagnetic wave oscillation and phonons are the quanta of mechanical vibration, plasmons are the quanta of plasma oscillation. The term plasmon was proposed in the early 1950's by Pines & Bohm in their series of papers entitled *A Collective Description of Electron Interactions* **[130-132]**. Unlike bulk plasmons, which are charge density oscillations in bulk metal, surface plasmons can be excited by light incident on the surface of a metal. Indeed, at frequencies $< \omega_p$, light is unable to penetrate bulk metal. The

penetration distance z of an electromagnetic wave into a metal is related to the Beer-Lambert law which describes the exponential decrease in wave intensity I as:

$$I(z) = I_0 e^{-\alpha z}$$

where attenuation constant $\alpha = \sqrt{2\sigma_0 \omega \mu_0}$ is the sum of absorption and reflection coefficient (Maier 2007 p.12 **[127]**). The attenuation constant is proportional to the imaginary part of refractive index by:

$$\frac{\alpha}{2} = \frac{\omega}{c} \mathrm{Im}\left(\underline{n}(\omega)\right) = \frac{2\pi}{\lambda} \mathrm{Im}\left(\underline{n}(\omega)\right)$$

The skin depth of a metal is the depth at which the magnitude of the electromagnetic field has decayed to $1/e$ of its initial value, or in terms of power $1/e^2$ (~13% of initial value). This is roughly 2 - 5 nm for silver between 0.4 – 2.0 μm incident wavelength and can be calculated by:

$$\delta = \frac{2}{\alpha} = \sqrt{\frac{2}{2\sigma_0 \omega \mu_0}} \tag{14}$$

where:

δ	skin depth (m)
ω	angular frequency (rad/s)
μ_0	free-space permeability (H/m)
σ_0	DC conductivity (S/m)

Surface plasmons occur at the interface of a material with positive real permittivity (dielectric) and a material with negative real permittivity (metal). Excitation of surface plasmons relies on certain conditions being met; namely when $\varepsilon(\vec{K}, \omega) = 0$, wave vector and frequency of the incident wave matches that of the electron oscillation and a longitudinal mode is excited. The longitudinal wave propagates across the metal / dielectric interface and decays exponentially with distance from the source. An evanescent field results from this photon-plasmon coupling, termed the surface plasmon polariton (SPP). This work is not concerned with SPPs so further detail will be avoided; suffice to say that matching frequency and wave vector to excite SPPs requires additional techniques such as highly focused beams, grating coupling and prism coupling, which are discussed in detail in **[127]**.

The geometry and size of a nanoparticle enforces boundary conditions on electron oscillation, resulting in unique, frequency-dependent *localized surface plasmon resonance* (LSPR) modes that can be directly excited by incident light. Coulomb interactions between the free electron 'cloud' and positive ions of the lattice ensure that electron displacement is bound by polarisation of the particle. Nanoparticles in an applied electromagnetic field can thus be thought of in classical terms as driven oscillators, with negatively charged electrons accelerating back and forth relative to the fixed positive

ions of the lattice. The resulting shift in charge induces an instantaneous dipole moment density, or polarisation. In addition, the incident angles on nanoparticles differs to that of continuous films; for example, the curved surface of a spherical metallic nanoparticle surrounded by a dielectric medium interacts with an incident wave at a range of angles. For linearly polarised light incident on a flat nanorod, electron displacement is confined along the axis of polarisation.

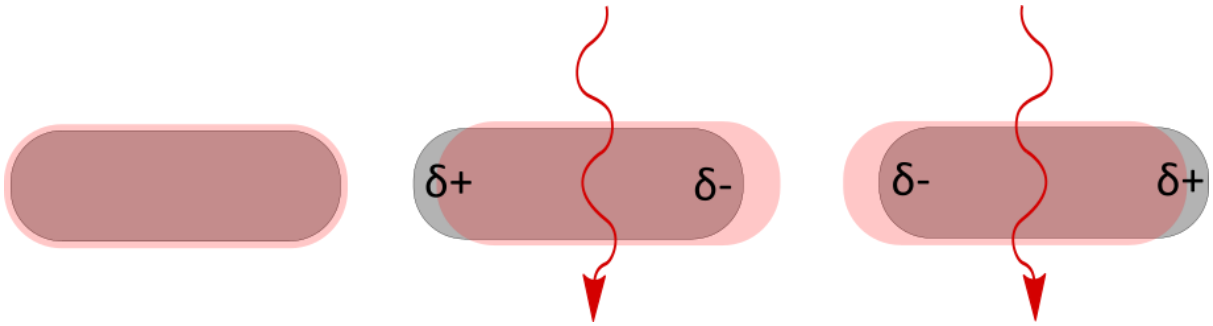

Figure 22. Dipole moment in metallic NR induced by oscillating incident wave. Silver metal, red electron 'cloud'.

Analogous to a classical driven harmonic oscillator, the resonance condition is obtained when the phase of the propagating wave approaches 90 degrees relative to the electron oscillation phase. The resonance condition for spherical nanoparticles surrounded by a homogenous dielectric medium can be estimated using the Frölich criterion $\varepsilon'(\omega) = -2\varepsilon_s$. When plotted against wavelength, the intercept of the real part of the complex relative permittivity of plasmonic material $\varepsilon'(\omega)$ and relative permittivity of the surrounding dielectric ε_s corresponds to the resonance wavelength. The condition is met when driving frequency $\omega = \omega_p/\sqrt{3}$ (Maier 2007 p.68 **[127]**). Resonant surface plasmon modes of noble metal particles on the order of a few hundred nanometres are typically within the visible regime. Importantly, the Frölich criterion implies that the resonance behaviour can be tuned by altering the complex permittivity of the surrounding dielectric.

3.1.1.6 Features of localised surface plasmon resonance

In far-field spectra, the resonance condition is indicated by distinct peaks in extinction and corresponding dips in transmission. The spectral peak amplitude, bandwidth and frequency are all highly dependent on the specific structure, geometry and materials used. The ability of plasmonic nanostructures to efficiently and selectively absorb or reflect light depending on frequency can be most readily observed in metallic nanoparticles excited by an external field, for example light reflected from or refracted through colloidal silver and gold in stained glass. In such a system, high absorption of electromagnetic energy relative to incident power implies efficient conversion of light into heat (dissipation) by electron scattering processes; indeed, metallic nanoparticles as localised heat sources have found many applications such as heat assisted magnetic recording **[133]**, photothermal cancer therapy **[134]** and catalysis **[135]**.

Light absorption and subsequent heat generation by nanoparticles is directly related to the degree of concentration of the electromagnetic field around the particles. In the near-field, resonance in nanoparticles leads to confinement of the electric field close to the particle surface and electric field magnitude enhancement. The near-field refers to distances between the nanostructure surface and the Fraunhofer distance $D_f = 2D^2/\lambda$, where D is a representative dimension of the nanostructure. The degree of field concentration and its specific distribution can be tailored by nanoscale engineering of particle geometry and spacing. In particular, designs which incorporate areas of high charge density, such as nanogaps and sharp edges, are known for field enhancement on the order of 100x **[12]**. This is the basis of the ubiquitous nanoparticle dimer **[136]**, split ring resonator **[137-139]** and bowtie antenna **[140]** designs.

The rate of heat generation is equal to $\omega \cdot \mathrm{Im}[\underline{\varepsilon}] \cdot \frac{\boldsymbol{E}^2}{2}$, where ω is angular frequency, ε is relative permittivity, and E is electric field. Plasmonic heating at a given frequency is therefore strongly dependent on the imaginary permittivity, which quantifies loss in materials, and is proportional to the square of the electric field strength. Heat generation is consequently highly localised to 'hot spots' in the electric near-field. A broad review of thermoplasmonics is offered by Baffou et al. (2013) **[75]**, including numerical and experimental methods and applications.

Since localised surface plasmon resonance is intrinsically linked to nanoparticle geometry, there is great potential for device tuneability. In general, one expects a red-shifted resonance both for increasing nanoparticle thickness and increasing aspect ratio (i.e. lengthening) **[141]**. Plasmon modes within specific nanoparticle systems are highly dependent on incident frequency and polarisation **[142]**. In this work nanorods are used because the anisotropy gives rise to at least two frequency-distinct resonance modes depending on the polarisation of incident light with respect to rod orientation. The two modes typically result in enhanced electric fields at the transverse or longitudinal edges. In principle these features enable control over device behaviour and could be used to improve device functionality by adding polarisation and wavelength dependence.

The opportunities provided by plasmonic nanoparticles have led to an enormous volume of research into tuneable plasmonic devices and reconfigurable metamaterials, some of which will be discussed later. Our work focuses on exploiting the features of plasmonic nanoparticles to introduce new functionalities to established technologies and so has immediate relevance to practical applications. One such application that could benefit from plasmonics is uncooled microbolometric photodetection, where plasmonic nanostructures have great potential for maximising device functionality and performance of low-cost photodetectors.

Features of LSPR	Implications
Confinement of light to subwavelength dimensions	Control over light at the nanoscale; able to fine-tune electric near-field distribution
Enhancement of incident electromagnetic waves	Localised areas of high electric field strength, useful in many applications e.g. particle trapping, fluorescence, photo-catalysis, heating
Large extinction cross section	Highly efficient absorption and scattering allows control of light propagation and energy conversion e.g. light to heat
Incident wavelength & polarisation sensitivity	Resonance modes are strongly affected by nanoparticle geometry, orientation and proximity to other particles
Strong local permittivity dependence	Permittivity of surrounding dielectric strongly affects resonance condition of nanoparticle. Plasmon resonance can also strongly affect the permittivity of surroundings. Key for many applications e.g. sensing, reconfigurable metamaterials.

Table 3: Summary of characteristic features of plasmonic nanostructures.

3.1.1.7 Maxwell Garnett effective medium theory for modelling VO_2 optical properties

In order to be able to represent vanadium dioxide in simulation, it is necessary to understand the theoretical basis upon which its material models are derived. At any temperature between the pure phase temperatures i.e. in the transition region, VO_2 can be understood as a mixture of the two phases, with the mixture getting progressively more metallic as the temperature increases. To simulate VO_2 behaviour, these intermediate states must be modelled. Fortunately, this kind of problem is not new and mixing formulae capable of predicting the behaviour of composite materials have been developed since at least the end of the 19th Century. Today, growth in the field of metamaterials and nanocomposites means mixing formulae are more widely used than ever. Popular formulae include Maxwell Garnett, Bruggeman, Prandtl-Ishlinkskii and General Effective Medium **[143-145]**. However, despite many iterations of formulae addressing the problem, the subject remains somewhat controversial and there appears to be no single model that can be used for all situations.

Effective medium theories (EMTs) are the most common method of approximating the macroscale properties of composite mixtures. Also known as 'average field approximations', 'mean-field theories' or 'self-consistent estimates' **[146]**, they allow a nanocomposite to be treated as a homogenous material, with physical properties related to the relative contribution of its constituents. EMTs were originally derived to approximate the relative permittivity of a gas given the polarisability of its molecules **[147, 148]** but have since been adapted for uses as diverse as magnetics **[149]** and elasticity **[150]**. The Maxwell Garnett effective medium formula, derived below, was chosen because it is simple and requires no experimental information besides the widely available permittivity of each phase.

The Maxwell Garnett effective medium formula is derived through the Clausius-Mossotti and Lorentz local field relations. JCM Garnett initially used the formula to calculate the complex permittivity of metal colloids i.e. metallic inclusions within dielectric, non-absorbing media.

i.) Lorentz local field relation

An electromagnetic field propagating through a dielectric medium causes the electric polarisation of molecules. The goal of the Lorentz local field is to express the uniform macroscopic polarisation of the medium in terms of the sum of electric fields felt by a constituent molecule. The key concepts are therefore that Maxwell's equations operate on microscopic scales and that by a suitable averaging process, a macroscopic electromagnetic representation for the material can be derived.

The derivation begins by defining the system. Molecules are represented by spherical dipoles arranged as a regular cubic lattice; an important assumption to the Lorentz field is that the molecules are non-interacting and no higher-order multipoles exist in the medium (Choy 2015 p.3 **[150]**). A spherical cavity is established to evaluate the electric field experienced by a point dipole in the medium. The size of the cavity should be on the order of tens of Å. The 'local field' affecting a point dipole at the centre of this cavity is understood to be the sum of the fields contributed by external sources and polarised molecules within the sphere, but excludes the field generated by the point dipole itself. In this way the problem is reduced to a system of bound charges, with their fields given as:

$$\boldsymbol{E}_l = \boldsymbol{E}_e + \boldsymbol{E}_d + \boldsymbol{E}_s + \boldsymbol{E}_n$$

where $\boldsymbol{E}_l$ is the local field experienced by the central point dipole; $\boldsymbol{E}_e$ is the external field; $\boldsymbol{E}_d$ is the depolarising field caused by bound charges on the outer surface of the bulk medium; $\boldsymbol{E}_s$ is the field arising from bound charges on the cavity surface; $\boldsymbol{E}_n$ is the field contributed by surrounding molecules.

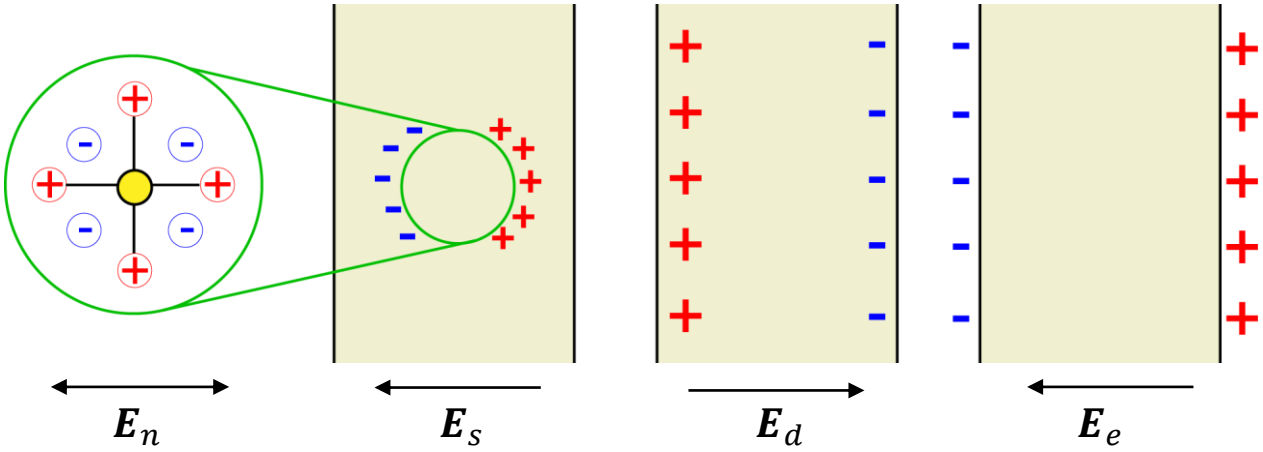

Figure 23. Lorentz 'local field' as the sum of contributing fields acting on a test charge (yellow).

The expressions for each contribution are derived and explained in detail in **[150]**. The system reduces to the Lorentz local field relation, which connects the local field $\boldsymbol{E_l}$ to the macroscopic field $\boldsymbol{E}$ via the macroscopic polarisation $\boldsymbol{P}$:

$$\boldsymbol{E}_l = \boldsymbol{E} + \frac{4\pi}{3}\boldsymbol{P} \tag{15}$$

ii.) Clausius-Mossotti relation

The Clausius-Mossotti relation relates the microscale (effective) molecular polarisability to the macroscale (effective) relative permittivity. First, the local field $\boldsymbol{E_l}$ experienced by a molecule is related to the dipole moment $\boldsymbol{p}$ of the molecule by the polarisability volume $\alpha' = \alpha/4\pi\varepsilon_0$:

$$\boldsymbol{p} = \alpha'\boldsymbol{E}_l$$

The effective polarisation $\boldsymbol{P}$ of the medium is then the sum of total molecules j with polarisability volume α' experiencing the local field $\boldsymbol{E}_l$:

$$\boldsymbol{P} = \sum_j N_j \boldsymbol{p_j} = \sum_j N_j \alpha_j' \boldsymbol{E}_{l(j)}$$

Substituting $\boldsymbol{E}_l$:

$$\boldsymbol{P} = \left(\sum_j N_j \alpha_j'\right)\left(\boldsymbol{E} + \frac{4\pi}{3}\boldsymbol{P}\right)$$

Polarisation and electric field are linked to the relative permittivity ε by the dielectric susceptibility χ_e:

$$\boldsymbol{P} = \varepsilon_0 \chi_e \boldsymbol{E} = \varepsilon_0(\varepsilon - 1)\boldsymbol{E}$$

In SI units, $\varepsilon = 1 + \chi_e$ but in CGS units $\varepsilon = 1 + 4\pi\chi_e$. Solving for $\boldsymbol{P}$:

$$\chi_e = \frac{\boldsymbol{P}}{\boldsymbol{E}} = \frac{\sum_j N_j \alpha_j'}{1 - \frac{4\pi}{3}\sum_j N_j \alpha_j'}$$

Rearranging for ε_r gives the Clausius-Mossotti relation in CGS units:

$$\frac{\varepsilon - 1}{\varepsilon + 2} = \frac{4\pi}{3}\sum_j N_j \alpha_j'$$

or in SI units:

$$\frac{\varepsilon_{eff} - 1}{\varepsilon_{eff} + 2} = \frac{\sum_j N_j \alpha_j}{3\varepsilon_0} \tag{16}$$

where ε_{eff} is the effective relative permittivity. The Lorentz-Lorenz equation is equivalent to the Clausius-Mossotti but is written in terms of refractive index.

iii.) Maxwell Garnett formula

Finally, the polarisability of an 'inclusion' molecule is introduced by modelling a sphere with relative permittivity ε_1 and radius a. The polarisability α of the sphere is given by:

$$\alpha = \left(\frac{\varepsilon_1 - 1}{\varepsilon_1 + 2}\right) \mathrm{a}^3 \tag{17}$$

Substituting eq. (17) into eq. (16) gives Maxwell's mixture formula **[151]**:

$$\left(\frac{\varepsilon_{eff} - 1}{\varepsilon_{eff} + 2}\right) = f\left(\frac{\varepsilon_1 - 1}{\varepsilon_1 + 2}\right)$$

where $f = N_j(a/a_0)^3$ is the volume fraction of inclusions in the mixture and a_0 is the radius of the spherical cavity. The mixing formula is most commonly expressed in terms of spherical inclusions of permittivity ε_1 in a host of permittivity ε_2:

$$\left(\frac{\varepsilon_{eff} - \varepsilon_2}{\varepsilon_{eff} + 2\varepsilon_2}\right) = f\left(\frac{\varepsilon_1 - 1}{\varepsilon_1 + 2}\right)$$

This is the Rayleigh mixing formula. Thus far both the inclusions and the host have been assumed lossless. For lossy materials, the permittivity values are substituted for their complex counterparts $\underline{\varepsilon} = \varepsilon' + i\varepsilon''$. When rearranged for ε_{eff}, this is known as the Maxwell Garnett effective medium equation. The form used in this work is therefore:

$$\underline{\varepsilon}_{eff} = \underline{\varepsilon}_2 \frac{\underline{\varepsilon}_1(1+2f) - \underline{\varepsilon}_2(2f-2)}{\underline{\varepsilon}_2(2+f) + \underline{\varepsilon}_1(1-f)} \tag{18}$$

In summary, the equation determines the wavelength-dependent complex permittivity of a homogenous material $\underline{\varepsilon}(\omega)$ consisting of two materials with disparate complex permittivity. Volume fraction f represents the proportion of metallic inclusions within a dielectric matrix. This gives ε_{eff} value of $\underline{\varepsilon}_1$ at $f = 1$ and $\underline{\varepsilon}_2$ at $f = 0$. Replacing $\underline{\varepsilon}_1$ with $\underline{\varepsilon}_m(\omega)$ and $\underline{\varepsilon}_2$ with $\underline{\varepsilon}_d(\omega)$ gives the effective permittivity of the mixture for any f. The calculated wavelength-dependent complex permittivity of both pure phases of VO_2 are shown in the following figure.

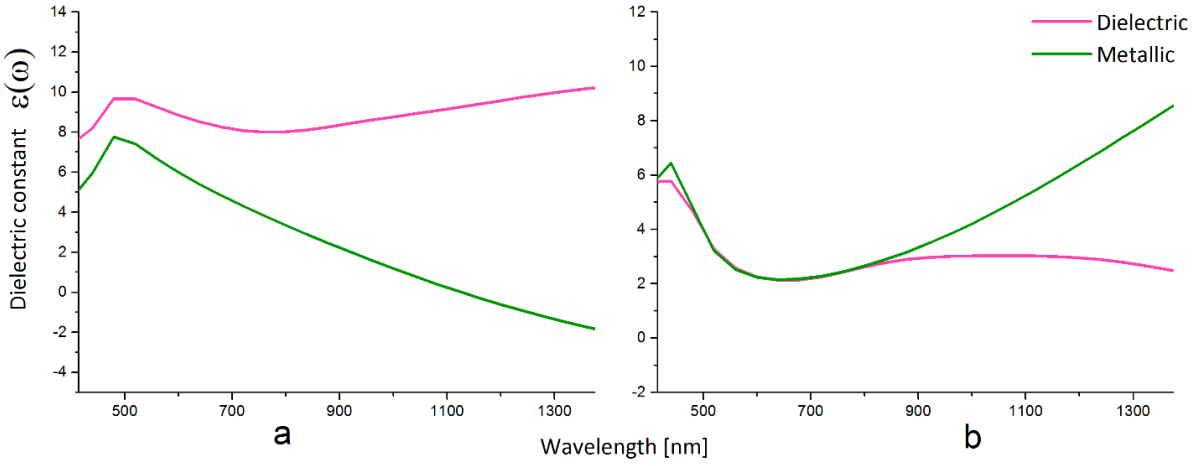

Figure 24. Dielectric (f=0) and metallic (f=1) relative permittivity of VO2 calculated using the conventional Maxwell Garnett Effective Medium Theory. (a) Real part complex relative permittivity VO2 for dielectric and metallic phases. (b) Imaginary part complex relative permittivity VO_2 for dielectric and metallic phases.

3.1.2 Heat transfer

Heat is a term used to describe the net flow of thermal energy between parts of a system, where thermal energy is the total microscopic kinetic energy. Thermal energy can be thought of as the vibration of atomic and subatomic particles, such as molecules within a fluid, electrons in a conductor, and "phonons", waves of atomic motion, within a crystal lattice. "Temperature" represents the average kinetic energy of these particles within a volume of interest. In the classical regime and in a closed system, i.e. without any external work, heat flows from areas of higher temperature to areas of lower temperature. Heat flow to or from an object is related to its temperature by the object's mass and specific heat capacity (defined as the energy required to raise the temperature of 1 kg of matter by 1 °C), and is given as $E_h = cm\Delta T$, where E_h is thermal energy (J), c_p is specific heat capacity (J/kg·°C), m is mass (kg) and ΔT is the change in temperature.

There are three main mechanisms of heat transfer; conduction, convection, and radiation. Conduction is the process of energy transfer from more energetic to less energetic particles via direct interaction, also known as diffusion. The rate of energy transferred by this mechanism at steady-state is given by Fourier's law $\boldsymbol{q} = -k\nabla T$ where $\boldsymbol{q}$ is heat flux density (W/m^2), k is the thermal conductivity of the material (W/m·K) and $-\nabla T$ is the temperature gradient (K/m). With a known flux density, this equation can be used to calculate the spatial temperature distribution. Conduction is the main transfer mechanism within solids, where particles are relatively densely packed and fixed in space.

In fluids, particles are more free to move and may do so collectively. In the presence of a temperature differential in a fluid, warmer regions with more energetic particles become less dense compared with cooler regions and experience a buoyancy force. The interactions between cooler and warmer regions

leads to "convection currents", collective motions of fluid mass, also known as advection. Heat is therefore transferred both by diffusion and by macroscale mass and energy transfer. Since convection largely relies on aggregate mass transfer, convective contribution to heat transfer becomes decreasingly significant as the scale of the system reduces. In microscale systems, heat transfer is dominated by individual particle interactions, aka diffusion or conduction. The relative contribution of diffusive and advective flux is indicated by the Péclet number $Pe = Lu/\alpha$, where L is the characteristic length (m), u is local flow velocity (ms^{-1}), and α is thermal diffusivity (m^2s^{-1}). Thermal diffusivity can be calculated by $\alpha = k/\rho c_p$ where k is thermal conductivity (W/(m·K)), ρ is density ($kg \cdot m^{-3}$) and c_p is specific heat capacity (J/kg·K). For a system in which $L = 100$ µm (a roughly 200 element array), $u = 0.1$ m/s (typical indoor air velocity) and α_{air} = 1.9 x 10^{-5} m^2s^{-1}, $Pe \approx 0.5$. Since a Péclet number much greater than 1 indicates advective heat flux is the dominant mechanism, it is evident that it is not a significant contributor in this system **[152]**, thus heat flux within the system can therefore be assumed as purely conductive.

At the interface of a solid and a fluid there lies a "boundary layer" that is defined by the velocity and temperature distribution with distance from the interface. The dynamics of the boundary layer can be quite complex, as they depend on a wide range of factors such as surface morphology, fluid properties (e.g. viscosity) and flow dynamics. Heat transfer from the solid to the fluid at the interface is given by the rate equation for convection, Newton's law of cooling: $\boldsymbol{q} = h(T_s - T_\infty)$, where T_s is temperature at surface, T_∞ is temperature of fluid and h is the heat flux coefficient ($W/m^2 \cdot K$). This coefficient is used to account for the boundary dynamics and is generally estimated based on typical values but is also a function of the characteristic length scale of a system (Incropera (2007), Chapter 6 **[153]**). The convective heat flux equation can thus be used as an external boundary condition to define heat flux out of the system into the ambient air. Thus although convection within the system is not modelled, convection is assumed to significantly contribute to heat outflow through the boundaries.

Radiation is the process whereby thermal energy is transferred between objects via the emission and absorption of electromagnetic waves. All matter above absolute zero emits thermal radiation and energy exchange involves changes to the electronic energy configuration of the matter involved. The degree of radiation emitted and absorbed by matter is determined by its emissivity, absorptivity and temperature. Radiation has the most significant contribution to heat transfer when the "transfer medium" is vacuum, since electromagnetic waves, and not particles, are the dominant transfer mechanism. Radiative heat transfer at the nanoscale has only been studied relatively recently, mainly due to the challenges in maintaining a large thermal gradient within nanoscale volumes while isolating the radiative contribution from conductive and convective mechanisms. However, there are indications of additional heat transfer mechanisms such as exponentially decaying evanescent waves **[154]** and phonon-coupling due to quantum fluctuations of the electromagnetic field aka "Casimir heat transfer" **[155]**. Whilst this is an

important consideration for future work, the simulations in this thesis assume no radiative heat transfer in order to minimise complexity and introduce less assumptions e.g. in material radiative properties.

3.1.3 Modelling heat transfer and material thermal properties

COMSOL's *Heat Transfer in Solids (ht)* module solves the following equation in three dimensions:

$$\rho C_p(\boldsymbol{u}_{trans} \cdot \nabla T) + \nabla \cdot (\boldsymbol{q} + \boldsymbol{q}_r) = -\alpha T + Q$$

The simulations were solved in two dimensions for efficiency, however COMSOL sets the 'out-of-plane' length a unit value of 1 m by default. The 2D formulation is justified as the nanowires are designed to be at least an order of magnitude longer than their width i.e. infinitely long, and thus out-of-plane flux can be assumed to be zero.

Simulations performed in this thesis addressed the steady state heat transfer problem, though further work could investigate time-dependent temperature distributions which would give information about potential switching capabilities. Steady state refers to a problem where the influx and outflux of heat energy within a problem space is equal, resulting in a constant temperature difference, in this case between heated elements and ambient external boundaries. Therefore, the time-dependent terms in the above equation disappear and the result is a spatial distribution of temperature that is time invariant. The steady state problem was chosen because the main challenges are achieving set temperatures within specific elements whilst minimising thermal crosstalk between adjacent elements, features that are independent of time.

In each simulation, the domain consisted of a hemispherical air domain, a substrate domain, and an array of nanostructured elements. After geometric convergence testing, the size of the air domain was set to 1.5 mm, with the external boundary defined as convective heat flux with heat transfer coefficient of 10 $W/m^{2}{\cdot}K$. The substrate was simulated 'full-thickness', i.e. no domain truncation was used and the substrate wafer was 0.3 mm thick. The bottom boundary was set to a fixed ambient temperature of 293.15 K to simulate a room-temperature heat sink, while the side boundaries were set as an 'external natural convection' boundary with wall height 0.3 mm.

Heat influx into the system was provided by assigning heat source powers to the Al wires to simulate joule heating, with a fixed 'heat rate' $Q_0 = P_0/V$ where heat flux Q is calculated from power per volume. In 2D, the area is multiplied by a 'out of plane' unit 1 m. P_0 (Heat source (W)) is given in Fig. 57. The power for each heat source was obtained by manual trial-and-error but could also be solved as an optimisation problem.

3.1.4 Nelder-Mead optimisation

Nelder-Mead optimisation was developed in 1965 as a 'direct search method' based on the concept of a simplex and direct comparison of function values **[156]**. A simplex is a polytope of n+1 vertices in n dimensions, i.e. a triangle for 2D functions. The "downhill simplex method" performs a sequence of steps whereby the function values at each vertex are compared and the 'highest' point of the simplex at each step (where the function is largest) is "reflected" through the opposite face of the simplex. Expansions and contractions are also used to explore the function space. In this way the objective function is minimised. The Nelder-Mead method is more resource intensive than derivative-based solvers that use the gradient of the function, but is more robust since it does not struggle with discontinuous or noisy functions.

Prior to the thermal simulations in Chapter 7, electromagnetics simulations were used to generate phase and reflection maps as a function of VO_2 metallic volume fraction *f*. In this manner, the *f* values required to establish a phase gradient were obtained. Using the relation between temperature and *f* as in **[157]**, the temperature necessary for each element was inferred. Since the aim of the thermal simulation was to obtain the temperature distribution surrounding each element, the elements that needed to be heated needed to be defined as a heat source. To find the heat source power required, an optimisation routine was used.

Optimisation problems are generally structured to have objective functions, control variables and constraints. Here the objective function was set to be the maximum temperature in elements adjacent to those chosen for heating, and the problem type was set to minimisation. In other words, the model optimises the power all of the 'chosen' heat source elements to obtain the smallest maximum temperature in elements that were not heated. The smallest maximum temperature in adjacent elements is desired because it implies the lowest degree of thermal crosstalk. The constraints were set to minimise the lowest acceptable temperature in chosen elements, with the lowest acceptable temperature being 353.15 K, corresponding to $f = 1$. The control variables then represented the individual heat source powers of the elements selected for heating, with additional parameters being an initial value, scale, lower bound and upper bound. These parameters are essentially user-specified guesses so that the optimiser starts within the bounds of the problem. This is the most labour intensive part of the process since the settings are manual and require some trial and error. The remaining user inputs were optimality tolerance and maximum number of model evaluations, which were set as 0.01 and 1000, respectively.

3.2 Analytical methods

i.) Fresnel equations: defining the system

The following aims to provide a summary outline of the derivation and understanding of the key concepts and expressions relating to the Fresnel equations for reflectance from a film on substrate. We begin by visualising a sinusoidal plane wave approaching a film at θ_0 angle of incidence through semi-infinite lossless dielectric with refractive index n_0. Both wave and film are considered infinitely wide. The film is lossless, homogenous and isotropic, has a thickness d and refractive index n_1, and is supported by a semi-infinite lossless substrate with refractive index n_2. The two interfaces that separate the film and dielectric media are considered to be mathematically sharp discontinuities in refractive index. Each time the wave traverses one of these boundaries, a portion of it is reflected or transmitted. The Fresnel coefficients represent the amplitude of the wave reflected or transmitted at the boundary relative to the incident amplitude. The system is illustrated below.

ii.) Light propagation at a single interface between lossless media

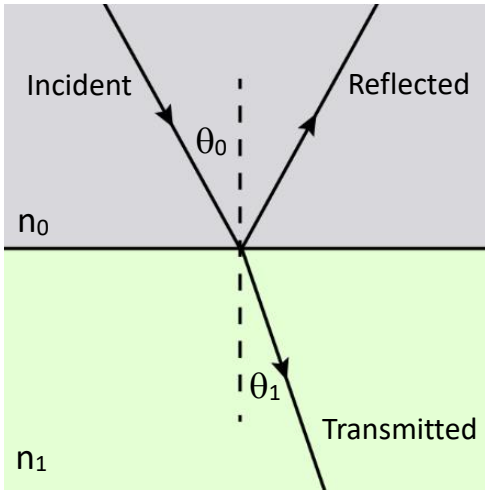

Figure 25. Light propagating through adjacent lossless media at incident angle θ_0. In a lossless system, a portion of the incident wave is reflected at the interface and the remainder is transmitted. In a lossy system, a portion is also absorbed.

First the Fresnel coefficients for a single interface are found by defining the x and y components of the electromagnetic field on reflection and transmission and applying appropriate boundary conditions at the interface. The boundary conditions to Maxwell's equations are commonly derived using the 'pillbox and loop' method **[158]**. Derivation of the boundary conditions and Fresnel reflection coefficient for the simplest case (normal incidence, lossless system, single interface) is given in Appendix A7. The boundary conditions state that the tangential components of the electric and magnetic field vectors are continuous across the boundary. The following expressions and notation are sourced from the very comprehensive book by Heavens (1955) **[159]**. Applying the boundary conditions to the electric and magnetic field vectors at the boundary gives the Fresnel coefficients:

$$\frac{\boldsymbol{E}_{0_p}^{-}}{\boldsymbol{E}_{0_p}^{+}} = \frac{n_0 cos\theta_1 - n_1 cos\theta_0}{n_0 cos\theta_1 + n_1 cos\theta_0} = r_{1_p}$$

$$\frac{\boldsymbol{E}_{1_p}^{+}}{\boldsymbol{E}_{0_p}^{+}} = \frac{2n_0 cos\theta_0}{n_0 cos\theta_1 + n_1 cos\theta_0} = t_{1_p}$$

$$\frac{\boldsymbol{E}_{0_s}^{-}}{\boldsymbol{E}_{0_s}^{+}} = \frac{n_0 cos\theta_0 - n_1 cos\theta_1}{n_0 cos\theta_0 + n_1 cos\theta_1} = r_{1_s}$$

$$\frac{\boldsymbol{E}_{1_s}^{+}}{\boldsymbol{E}_{0_s}^{+}} = \frac{2n_0 cos\theta_0}{n_0 cos\theta_0 + n_1 cos\theta_1} = t_{1_s}$$

Where θ_0 and θ_1 are the angles of incidence and refraction, respectively, and s and p refer to the polarisation of the incident wave: s-polarised light has electric field perpendicular to the plane of incidence and p-polarised light has electric field parallel to the plane of incidence. For normal incidence (0 degrees), this is irrelevant since $\cos\theta = 1$, making the s and p terms identical.

iii.) Fresnel coefficients for film bounded by two media in lossless system

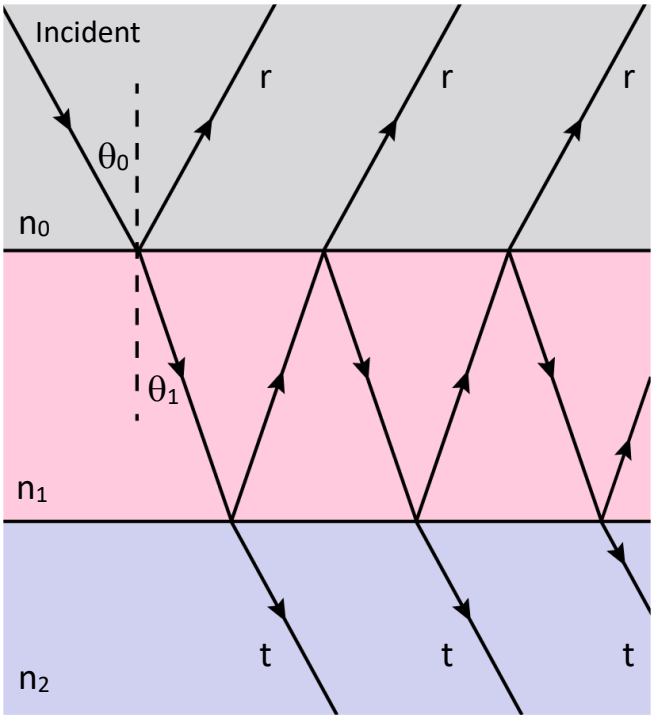

Figure 26. Light beam incident on a film-on-substrate at incident angle θ_0. In a lossless system, a portion of the incident wave is reflected or transmitted at each interface. In a lossy system, a portion is also absorbed; r = reflected, t = transmitted light.

For a film bounded by two media, there exists two interfaces and the problem becomes more complicated. Portions of the wave amplitude are successively reflected and transmitted each time the wave traverses a boundary (Fig. 26). The total reflected and transmitted amplitudes can be obtained by summing the multiply-reflected and multiply-transmitted amplitudes. The values of reflection and transmission coefficients depends on the direction the wave is propagating; thus for light propagating

$n_0 \rightarrow n_1$ the reflection and transmission coefficients are $(n_0 - n_1)/(n_0 + n_1)$ and $2n_0/(n_0 + n_1)$. In the reverse direction $n_1 \rightarrow n_0$, the coefficients become $(n_1 - n_0)/(n_1 + n_0)$ and $2n_1/(n_0 + n_1)$. In the case of normal incidence upon a film bounded by two dielectric media with no system loss, the Fresnel coefficients reduce to:

$$r_1 = \frac{n_0 - n_1}{n_0 + n_1} \quad r_2 = \frac{n_1 - n_2}{n_1 + n_2}$$

$$t_1 = \frac{2n_0}{n_0 + n_1} \quad t_2 = \frac{2n_1}{n_1 + n_2}$$

Each time the wave traverses the film, it undergoes a change in phase, given by:

$$\delta_1 = \frac{2\pi}{\lambda} n_1 d_1 cos\theta_1 \tag{19}$$

The reflected and transmitted amplitudes are then given by:

$$R = \frac{r_1 + r_2 e^{-2i\delta_1}}{1 + r_1 r_2 e^{-2i\delta_1}}$$

$$T = \frac{t_1 t_2 e^{-2i\delta_1}}{1 + r_1 r_2 e^{-2i\delta_1}}$$

The reflectance $\boldsymbol{R}$ and transmittance $\boldsymbol{T}$ are the defined as the ratios of reflected and transmitted energy to incident energy, equal to the amplitude squared. In terms of n they are thus equal to:

$$\boldsymbol{R} = \frac{(n_0^2 - n_1^2)(n_1^2 + n_2^2) - 4n_0 n_1^2 n_2 + (n_0^2 + n_1^2)(n_1^2 - n_2^2) cos2\delta_1}{(n_0^2 + n_1^2)(n_1^2 + n_2^2) - 4n_0 n_1^2 n_2 + (n_0^2 - n_1^2)(n_1^2 + n_2^2) cos2\delta_1} \tag{20}$$

$$\boldsymbol{T} = \frac{8n_0 n_1^2 n_2}{(n_0^2 + n_1^2)(n_1^2 + n_2^2) - 4n_0 n_1^2 n_2 + (n_0^2 - n_1^2)(n_1^2 - n_2^2) cos2\delta_1} \tag{21}$$

iv.) Reflectance and transmittance of light at normal incidence to a lossy film on lossy substrate

To account for losses in film and substrate, each refractive index n must be replaced by the corresponding complex refractive index $\underline{n} = n - ik$. For normal incidence the problem is reduced. For a lossy film of thickness d_1 and refractive index $\underline{n_1} = n_1 - ik_1$ on a substrate with index $\underline{n_2} = n_2 - ik_2$, the reflectance and transmittance for a single absorbing layer on absorbing substrate can be expressed thus (Heavens 1955 p. 76 **[159]**):

$$\boldsymbol{R} = \frac{\left(g_1^2+h_1^2\right)\exp(2\alpha_1)+\left(g_2^2+h_2^2\right)\exp(-2\alpha_1)+A\cos 2\gamma_1+B\sin 2\gamma_1}{\exp(2\alpha_1)+\left(g_1^2+h_1^2\right)\left(g_2^2+h_2^2\right)\exp(-2\alpha_1)+C\cos 2\gamma_1+D\sin\gamma_1} \tag{22}$$

$$\boldsymbol{T} = \frac{n_2}{n_0}\frac{\left[(1+g_1)^2+h_1^2\right]\left[(1+g_2)^2+h_2^2\right]}{\exp(2\alpha_1)+\left(g_1^2+h_1^2\right)+\left(g_2^2+h_2^2\right)\exp(-2\alpha_1)+C\cos 2\gamma_1+D\sin 2\gamma_1} \tag{23}$$

$$g_1 = \frac{n_0^2-n_1^2-k_1^2}{(n_0+n_1)^2+k_1^2} \qquad h_1 = \frac{2n_0k_1}{(n_0+n_1)^2+k_1^2}$$

$$g_2 = \frac{n_1^2-n_2^2+k_1^2-k_2^2}{(n_1+n_2)^2+(k_1+k_2)^2} \qquad h_2 = \frac{2(n_1k_2-n_2k_1)}{(n_1+n_2)^2+(k_1+k_2)^2}$$

$$A = 2(g_1g_2 + h_1h_2) \qquad C = 2(g_1g_2 - h_1h_2)$$

$$B = 2(g_1h_2 - g_2h_1) \qquad D = 2(g_1h_2 + g_2h_1)$$

$$\alpha_1 = 2\pi k_1 d/\lambda \qquad \gamma_1 = 2\pi n_1 d/\lambda$$

α_1 and γ_1 are the attenuation coefficient and propagation constant, respectively, where the complex-valued wavenumber is $2\pi\underline{n}/\lambda$. Working with single explicit expressions for all successive reflections and transmissions at each interface is cumbersome. Fortunately, the components of the electric vector in one medium are connected to those in the preceding medium by linear relations, which enable the problem of multiple films to be solved more easily. This can be achieved by deriving the resultant vector sums (p. 59 **[159]**), introducing the concept of optical impedance and admittance (p. 66 **[159]**), or matrix methods using the Fresnel coefficients (p. 69 **[159]**). Expressing the Fresnel coefficient equations in matrix form simplifies the system and makes the reflectance and transmittance simpler to compute.

3.3 Finite Element Analysis (FEA)

Simulations are used for heuristics and prediction in cases where physical experimentation and analytical solutions are impractical. Barriers to experimentation include cost, availability of technology and scale, whilst problems can quickly become too complicated to efficiently solve via analytical methods, for example by introducing complex geometry and boundary conditions, multiple materials, or material anisotropy. Analytical methods here refer to methods of solving vector field problems using their governing differential equations i.e. calculus. Differential equations express the change in a dependent variable, such as temperature, velocity, and electric potential, with respect to change in an independent variable, such as spatial coordinates and time. These problems involve infinitesimal variables because fields are continuous and any value within the bounds of the system can be solved for exactly. The concept of the Finite Element Method (FEM) is that the field problem can be simplified by both geometric and mathematic discretisation, and then solved using numerical methods. In essence, the goal of FEM is to convert an analytic problem (differential equation) into a finite set of equations

that can be solved using algebra. The process of discretisation inherently means that the algebraic solutions are not exact solutions to the differential equation, but merely an approximation. However, this technique means that intractable or even 'unsolvable' analysis problems can be solved efficiently. *COMSOL Multiphysics*® finite element analysis software was chosen for its ease of use and inter-flexibility with various physics interfaces. The *Electromagnetic, Frequency Domain (emw)* and *Heat Transfer in Solids (ht)* modules were used to build various simulations which were subsequently solved with the aid of the University of Southampton IRIDIS High Performance Computing Facility.

3.3.1 History of finite element analysis

The first application to an applied problem of finite element analysis in the form used today is generally attributed to Richard Courant (1943) **[160]** based on his earlier work dating back to 1922 **[161]**. Prior to this, numerical approximations to partial differential equations had been proved by Hilbert (1904) **[162]** and Ritz (1908) **[163]**, but whilst these approaches used minimising sequences, they lacked piecewise test functions which are a central feature of FEM. The problem to which Courant applied the method was torsional rigidity of a hollow shaft, where the shaft cross section was discretised into triangular elements. Values of the stress function were then calculated at every intersection (node) and interpolated linearly across each triangle. The method seems to have gained widespread acceptance in applied science by the mid-1960s and the first computer programs and textbooks were published by the end of that decade. Further information about the history and evolution of FEM can be found in **[164]** and **[165]**.

3.3.2 Mathematical concepts of finite element analysis

Implementation of the finite element method begins by identifying the differential equations and boundary conditions that describe the problem. This is known as the 'strong formulation' as strict differentiability and continuity requirements are imposed upon solutions at every point throughout the problem space. The problem can be simplified by relaxing the requirements by converting the partial differential equation (PDE) to its 'weak formulation'. This form consists of a finite set of integral equations that approximate the PDE throughout the problem space while satisfying their boundary and initial conditions. The concept here is that any function can be approximated by a piecewise linear sum of N arbitrary functions with unknown coefficients. Since the weak form is an approximation of the PDE, its solutions will generally not satisfy the PDE at every point within the domain; the 'residual' is used to describe how poorly the approximate solution satisfies the governing PDE, where a residual of zero means the approximate solution exactly satisfies the PDE solution. Note that this is distinct from the difference between the exact and approximate solution, which is the 'error'.

There are various methods of obtaining the weak form equations such as the 'Direct', 'Minimum Total Potential Energy' and 'Weighted Residual' formulations. Galerkin's method is of the third type and was the method used to solve simulations featured in this thesis. As the name suggests, the method involves obtaining an equation for each element by multiplying the integrated residual by a 'weight' function. In the Bubnov-Galerkin method, the weight functions take the form of 'shape' functions. There are generally multiple shape functions that span each element and they can be linear or higher-order polynomial; together, these functions can approximate any arbitrary function. Since most classical field problems are based on continuous fields, COMSOL generally uses 'Lagrange' shape functions by default; this constrains function coefficients to be continuous across element boundaries. One advantage of these FEM techniques over other numerical analysis methods is that solutions exist for all points within the problem domain, since the field function is the sum of the products of shape function and field value at each node.

The weak form solutions will be a good overall approximation if the residual can be minimised for a large number of points throughout the problem domain. Therefore, the domain is 'sampled' by setting the residual to zero at N points or 'nodes' where elements intersect. The position and density of points is controlled by the specific 'mesh' as determined by element size, shape and distribution. This means therefore that the residual and error decrease as the mesh density is increased. In FEM software, the mesh features can be fine-tuned by the user with the aid of meshing algorithms, thus the user's discretion is very influential in terms of solution quality.

Each element within the domain is at this point represented by a discretised weak form equation, consisting of weighted residual functions, stored as an element 'stiffness matrix'. Finally, the element stiffness matrices are combined piecewise into a global stiffness matrix, with the unknown coefficients termed the 'degrees of freedom'. The use of weighting functions means that many of the values in the matrix are predetermined to be zero; this is known as a sparse matrix. The trade-off in calculating solutions using a sparse matrix are that although the model is comparatively time efficient, it requires a large amount of memory to manipulate and solve. Since the number of degrees of freedom directly relates to the mesh density and shape function, there is always a compromise for the user to address between solution quality, time, and computational resources.

For more information on FEA, please see the following references: extensive theory and problem examples **[165]**, a succinct tutorial of two weighted residual techniques **[166]**, and a brief illustrated explanation of shape functions and how they are used to discretise the weak formulation **[167]**.

3.3.3 Error

The challenge in FEM simulation is to minimise error in order to get the best possible approximation of reality given the time and computational constraints. Aside from user and software error, error can be defined as the discrepancy between the approximated FEA solution and the exact solution of the governing differential equations that model reality. Modelling error can be minimised by ensuring that the physics employed to simulate the real problem is suitable. This includes the governing PDE, boundary and initial conditions, material models and geometry. Discretisation error is another source of error where the user has a big impact; it relates to shape function, element size, element shape and 'best practice' when generating the mesh, such as perfectly matched layer (PML) anisotropy and identical meshing of paired domain faces in periodic simulations. Finally, numerical error is inherent to computational methods that process numbers with finite precision; similarly, truncation error is a result of information loss due to rounding during manipulations. Generally, this error is small, but can become significant under certain circumstances and is most often an indicator of more fundamental issues with the simulation design, such as poorly defined boundary conditions or discretisation.

3.4 Simulation methods

3.4.1 Modelling electromagnetic wave propagation and material optical properties

This section details in general terms how FEA was implemented to solve the electromagnetics problem of light interacting with a nanostructure in an infinite array. COMSOL's *Electromagnetic Waves, Frequency Domain (emw)* module was chosen; this uses the frequency domain form of Maxwell's equations in three dimensions and solves for $\boldsymbol{E}$ **[168]**:

$$\nabla \times \mu_r^{-1}(\nabla \times \boldsymbol{E}) - \mathbf{K}_0^2\left(\underline{\varepsilon} - \frac{i\sigma}{\omega\varepsilon_0}\right)\boldsymbol{E} = 0$$

where:

$\mathbf{K}_0$	free space wavenumber / wavevector; ω^2/c_0^2, units rad.m^{-1}
$\omega = 2\pi v$	angular frequency (where v = frequency)
μ_r	relative permeability (≈1 for nonmagnetic media) refers to 1x vacuum permeability μ_0
$\underline{\varepsilon}$	complex relative permittivity

In each investigation the simulated volume represented a unit cell. Geometry was defined differently for each investigation. 'Physical' domains were stacked vertically and bounded at the top and bottom by perfectly matched layer (PML) domains. PMLs truncate the simulation space by absorbing all

outgoing waves and minimising their back-reflection, thereby preventing their interference with the solution. PMLs are better than other non-reflecting methods, such as scattering boundary conditions (SBC), because they efficiently absorb outgoing waves through a wide range of incidence angles, whereas SBCs only absorb waves normal to their surface. However, because PMLs require discretised domains, they make simulations more computationally expensive.

To simulate a single unit cell of an infinite array, periodic ports were used in conjunction with Floquet periodic boundary conditions assigned to the exterior side faces. Between the 'physical' domains and PML domains, port boundary conditions were assigned; port 1, on the top, was used to launch an electromagnetic plane wave normal to the substrate surface and port 2, on the bottom, was passive. The 'full field' setting was used to provide an even field distribution since planar dimensions were small compared to typical beam diameter. To investigate the effect of electromagnetic wave polarisation on the plasmonic response of anisotropic nanorods, incident light was y-axis polarised for 'Long axis' simulations and x-axis polarised for 'Short axis' simulations.

Port boundary conditions were used to extract S-parameters. S-parameters are used as a 'black box' to obtain the inputs and outputs of a system; they are complex quantities which represent the reflection and transmission coefficients. S-parameters are numbered according to their associated port and input from another port, respectively. Since port 1 was the excitation port and port 2 was the passive port, S11 represented the reflection coefficient and S21 represented the transmission coefficient. Reflection and transmission coefficients are here defined as the ratio between incident and reflected or transmitted light intensity. Thus reflection R is given by the absolute value of S11 squared and transmission T by the absolute value of S21 squared. Dips in transmission can be used to identify plasmon resonance because this implies increased extinction through conservation:

$$\mathrm{A} + \mathrm{R} + \mathrm{T} = 1$$

$$\mathrm{A} = 1 - |\mathrm{S11}|^2 - |\mathrm{S21}|^2$$

where A is absorption. Since the size and spacing of nanoparticles was comparable to the wavelengths used in our investigations, diffraction also needed to be considered. The onset of higher order diffraction can be estimated as the product of unit cell periodicity and substrate refractive index; the result is the wavelength below which higher order diffraction occurs. COMSOL provides automatic diffraction order calculation which uses Snell's law to compute the number, direction and polarisation of all diffracted orders and assigns each a numbered S-parameter. After solving, the power in each diffracted order can be extracted by addressing its corresponding S-parameter.

Finally, materials were assigned to their respective domains. Materials were represented by modelling their complex relative permittivity in which the imaginary component represents losses. This already incorporates conductive losses via $\mathrm{Im}(\underline{\sigma})$ since $\underline{\sigma}(\omega) = \sigma'(\omega) + i\sigma''(\omega) = -i\varepsilon_0\omega(\underline{\varepsilon}(\omega) - 1)$ **[169]**; thus electrical conductivity for materials was specified as 0. Since all materials used were nonmagnetic media, permeability was specified as 1. All modelling parameters are provided in the tables of appendix A3.

i.) Air

Air properties were imported from the COMSOL material database with relative permittivity of 1.

ii.) Vanadium dioxide (VO_2)

Complex relative permittivity models were used to approximate the 'pure phases' of VO_2. The models were originally proposed by Verleur et al. (1968) **[170]** based on their reflectivity and transmission spectra of VO_2 thin films. Two separate models found in Pirozhenko (2008) **[171]** pertain to the dielectric and metallic phases, respectively:

$$\underline{\varepsilon}_d(\omega) = 1 + \frac{\varepsilon_\infty - 1}{1 - \left(\frac{\omega}{\omega_\infty}\right)^2} + \sum_{j=1}^{7} \frac{s_j}{1 - \left(\frac{\omega}{\omega_j}\right)^2 - i\Gamma_j \cdot \frac{\omega}{\omega_j}} \tag{24}$$

$$\underline{\varepsilon}_m(\omega) = 1 - \frac{{\omega_p}^2}{\omega(\omega + i\gamma)} + \frac{\tilde{\varepsilon}_\infty - 1}{1 - \left(\frac{\omega}{\omega_\infty}\right)^2} + \sum_{j=1}^{4} \frac{\tilde{s}_j}{1 - \left(\frac{\omega}{\tilde{\omega}_j}\right)^2 - i\tilde{\Gamma}_j \frac{\omega}{\tilde{\omega}_j}} \tag{25}$$

$\underline{\varepsilon}_d(\omega)$ Frequency dependent complex permittivity VO_2 (dielectric phase).
$\underline{\varepsilon}_m(\omega)$ Frequency dependent complex permittivity VO_2 (metallic phase).
ε_∞ High frequency permittivity limit
ω Incident frequency
ω_∞ High frequency limit
ω_j Resonant frequency of oscillator *j*
s_j Strength oscillator *j*
i Imaginary unit
Γ Lorentz damping frequency
~ Tilde denotes metallic parameters
ω_p Plasma frequency
γ Damping frequency

The oscillator strengths and resonance frequencies can be found in Tables B and C of the Appendix A3. The first RHS term in equation (25) is the Drude model, representing the contribution of free electrons. The next term, found in both equations, represents the contribution of high frequency electronic transitions to the real part of complex permittivity. The final term is the contribution of interband

transitions, where each transition within the spectral range of interest is represented by a Lorentz oscillator; for example, VO_2 is known to have interband transitions around 2.5 and 1.4 eV **[172]**. These models are valid from 0.25 – 5 eV, equivalently 0.25 - 4.96 μm. Beyond this range it was necessary to extend the model by extrapolation, following the practice in Dicken et al. (2009) **[63]**.

3.4.2 General principles of mesh discretisation

Finite element method modelling relies on discretisation of the simulation space into subunits known as mesh elements, which are interconnected by nodes. The outer boundaries of the simulation domain were assigned 'free triangular' and the volume elements were assigned 'free tetrahedral' shape settings. PMLs were assigned 'mapped' mesh on the sides, effectively turning PML elements into vertically orientated triangular prisms; this minimises reflection and error due to mesh discretisation. Importantly, the 'copy face' command was used to make the mesh of both opposing sides identical; this enables the use of periodic boundary conditions and reduces numerical error.

The quality of a mesh is generally determined by the element density, order and 'shape quality', or how distorted individual elements are forced to become when the mesh has been generated. Meshing affects the number and error of calculations and so impacts the quality of the solution. Meshing differs for each simulation that uses a different physics, geometry or wavelength range. Simulations in each project were thus prefaced by performing a mesh convergence study, whereby element size is scaled down until variation between subsequent solutions has reduced to an acceptable degree. Practically, this means that there is always a compromise between solution integrity and resources. An example convergence study for an electromagnetic simulation is given as follows; note that this is a general example of the method and mesh parameters do not necessarily reflect those used in the simulations in this thesis. First, an initial mesh resolution for different domains was established (scale factor 1.0). These values were chosen because COMSOL documentation recommends ten linear or five second order elements per wavelength, depending on local material properties (COMSOL documentation > RF Module > 'Meshing and solving'). The material domains are: air / silver nanorod / VO_2 film / sapphire substrate.

Entity	Max element size expression (λ = 0.4 μm)	Element size [nm]
Air	λ / 5	80
Sapphire	λ / 10	40
VO_2 / air, 'proximity zone'	λ / 15	27
Silver	λ / 25	16

Table 4. Mesh parameters and resulting element size. Note that this is a general example of the method and mesh parameters do not necessarily reflect those used in the simulations of this thesis.

Simulations were also solved with mesh scaling factors of 0.5 and 1.5 and subsequently comparing the solutions for larger and smaller element sizes. Results of this study are given below, with the comparative solution plot shown in Fig. 28.

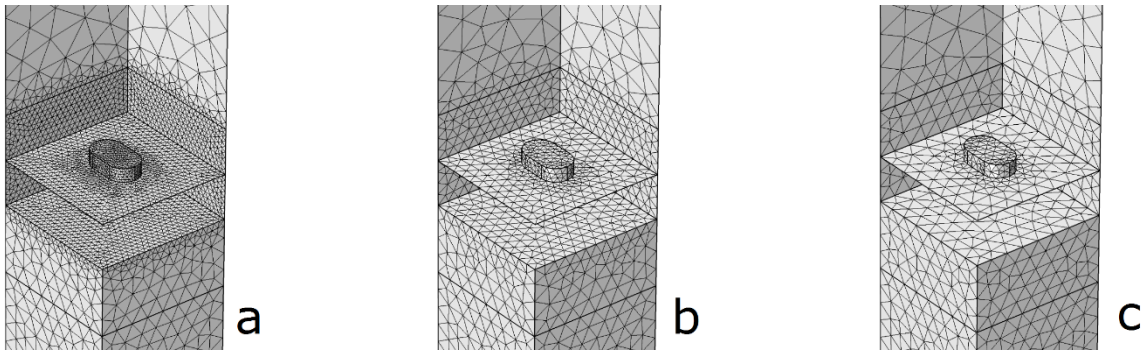

Figure 27. Effect of mesh scaling parameter on element size. (a) 0.5, (b) 1.0, (c) 1.5.

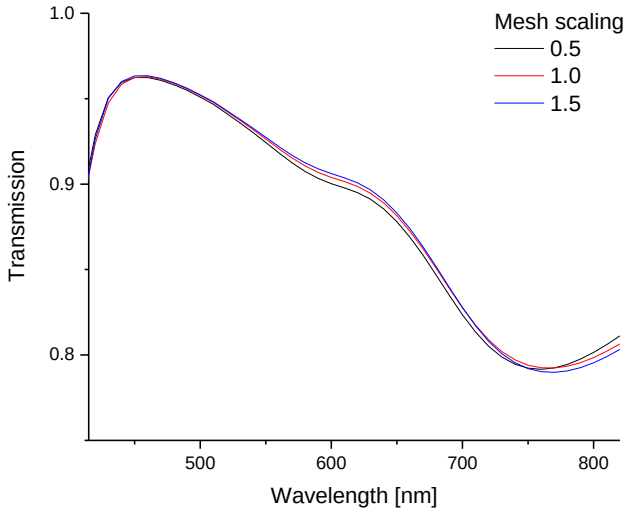

Figure 28. Effect of mesh scaling parameter on solution, dielectric phase VO_2.

Scaling factor	Element size [nm]		Covariance in solution
	Proximity zone	Silver NR	
1.0	27	16	
0.5	13	8	0.0034
1.5	40	24	

Table 5. Mesh scaling vs element size; covariance in solution between 0.5 and 1.5.

Number of elements	Degrees of freedom	Memory [Gb]		Time to solve [s]
		Physical	Virtual	
56555	371114	8.42	16.53	1645

Table 6. Typical model solving statistics.

Table 5 shows there was a modest difference in solution between most fine and most coarse mesh, with covariance of 0.0034. When generating a mesh, it is necessary to strike a balance between time, computing power and accuracy of solution which was deemed acceptable; ideally, the covariance of the solution should be less than the relative tolerance value of 0.001. Table 6 shows the solving statistics for the example mesh at 1.0 scaling. The degrees of freedom, and by extension the memory and solving time, are based on the number of unknowns in the global matrix. This is directly related to the number, shape and order of elements, as well as the specific equations used. Therefore, it is general good practice to simplify the problem wherever possible, in terms of geometry, dimensionality, and physics. For instance, in Chapters 4 and 5 the electromagnetics simulations are performed in 3D, whilst in Chapter 7 both the electromagnetic and heat transfer simulations are performed in 2D. This is because in the former, we are interested in the 3D field distribution around the nanorods as the incident polarisation is oriented in parallel or perpendicular to the nanorods. By contrast, the electromagnetic simulations in Chapter 7 only use one polarisation and are assumed to be infinitely long in the out-of-plane axis, thus it is appropriate to model the problem in two dimensions.

Chapter 4: Bolometric photodetection using plasmon-assisted resistivity change in VO_2

4.1 Abstract

The aim of the work was to demonstrate photodetection featuring wavelength and polarisation sensitivity by combining silver nanorods with vanadium dioxide, opening a path to plasmon-enhanced uncooled microbolometers. The sample consisted of a planar silver nanorod array between two silver electrodes positioned on top of pure VO_2 film with underlying sapphire substrate. Silver (Ag) was chosen as the nanorod material because (1) Ag has extremely low resistivity (1.6×10^{-6} Ω·cm at 20 ºC) compared to VO_2 (measured as 2.3 Ω·cm at 20 ºC), making a small change in VO_2 resistivity relatively easy to detect and (2) the onset of interband transitions in silver is 320 nm and Ag supports strong localised surface plasmon resonance within the entire wavelength range of interest (400 - 900 nm). Localised surface plasmon resonance was identified by measuring broadband transmission spectrum and resistivity across the sample was subsequently sampled at five specific wavelengths.

This work was published as "Takeya H, Frame JD, Tanaka T, Urade Y, Fang X, Kubo W. *Bolometric photodetection using plasmon-assisted resistivity change in vanadium dioxide*. Scientific Reports, 8, 12764, 2018". The author's contribution was limited to simulation and analysis, however, fabrication and physical experimentation have been included for completeness, and these were performed by the group of Professor Wakana Kubo at Tokyo University of Agriculture and Technology in Japan.

4.2 Simulation methods

Simulations were used to provide transmission spectra and plots of the electric near-field. The size of the entire 'physical domain' was 0.3 × 0.3 × 1.8 μm, with 0.3 μm thick perfectly matched layers (PML) added to the top and bottom as described in Chapter 3.4.1. Air was assigned to the top half of the stack. A silver nanorod was positioned at the centre, with planar dimensions 95 × 180 × 40 nm. The rod was a hemi-spherocylinder, shaped to most closely imitate the physical nanorods. Below the nanorod was 0.25 μm thick VO_2 film and the remaining bottom half of the stack was sapphire substrate. The incident electric field was linearly polarised in either the x (transverse / short-axis) or y axis (longitudinal / long axis). Since the simulations did not involve any nonlinear optical components or heat transfer physics, the incident power was inconsequential; thus its default value of 1 W was left unchanged. Preliminary simulations were conducted using a coarse, wide-ranging parametric sweep (320 – 2000 nm) to identify resonance peaks using absorbance, reflectance and transmittance spectra. In subsequent simulations the wavelength was swept from 0.4 – 1.1 μm at a 10 nm interval. The parametric sweep study specified the range in terms of wavelength and provided a conversion to frequency (Hz) by $\nu = c_0/\lambda$. Parameter

frequencies were used as inputs by defining frequency (ω) as an argument of the complex relative permittivity model $\underline{\varepsilon}(\omega)$ and linking this to the parametric values using the inbuilt *freq* global variable.

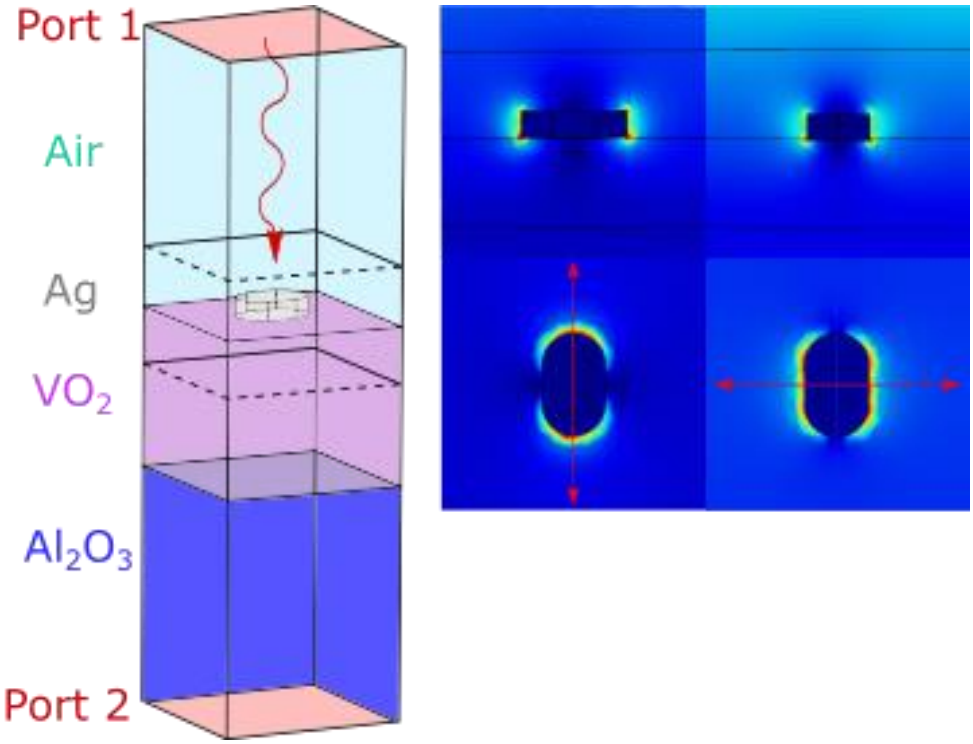

Figure 29. Left to right: finalised simulation stack (PML not shown); long axis, short axis polarised.

S-parameter transmission was extracted and normalised against a reference, comprising an air-VO_2-Al_2O_3 stack without silver nanorod. Normalization allows the effect of plasmonic nanorods on transmission to be more clearly analysed and differences compared. Mesh sizes were as follows:

Entity	**Max element size expression [λ = 0.4 μm]**	**Max element growth rate**	**Max element size [nm]**	**Average element size [nm]**
Air	λ / 8	1.2	50	50.2
Ag	λ / 40	-	10	10.7
VO_2	λ / 12	1.3	33	33.8
Al_2O_3	λ / 8	1.2	50	52.6
PML	-	-	-	77.5

Table 7. Element sizes used in simulation.

The following material models were used to calculate wavelength dependent relative permittivity and all relevant parameters can be found in Tables B and C of Appendix A3.

i.) Vanadium dioxide (VO_2)

VO_2 complex permittivity was calculated using equation 18. Simulations were first solved for VO_2 volume fractions between 0 – 1 (0.2 interval). Results agreed fairly well with the experimental data when the VO_2 permittivity was calculated using a metallic volume fraction of 0.8 and this was used for subsequent simulations.

ii.) Silver (Ag)

Due to the high density of free carriers in silver (10^{22}-10^{23} cm^{-3} **[173])**, a classical model is mostly sufficient to describe the optical behaviour down to very small scales and the Drude free electron model is valid. However, the model needs to be extended for frequencies approaching ω_p because of residual polarisation resulting from the filled d band (Maier 2007 p.13 **[127]**). The extended Drude model is shown below, where 1 is substituted for ε_∞.

$$\varepsilon^*(\omega) = \varepsilon_\infty - \frac{\omega_p^2}{\omega^2 + i\omega\gamma} \tag{26}$$

$$\omega_p = 8.9 \text{ eV}$$
$$\varepsilon_\infty = 5 \text{ eV}$$
$$\gamma = 1/\tau$$
$$\tau = 17 \text{ fs}$$

1 Hz = 4.1357E-15 eV
1 fs = 1E-15 s
γ = 4.1357/17 = 0.243 eV damping frequency (aka relaxation rate)
ω_p volume plasma frequency is related to effective mass of electron m* and electron number density n through $\omega_p = \sqrt{(n_e e^2/\varepsilon_0 m^*)}$. The plasma frequency is derived in Appendix A1.

The model is valid from $0.1 \sim 3$ eV, or $12{,}398 \sim 413$ nm. At wavelengths shorter than 413 nm, imaginary permittivity rises due to interband transitions (Maier 2007 p.14 **[127]**) and this is not accounted for in the model. Relaxation rate takes into account many physical factors which affect electron scattering such as electron-phonon interactions, surface roughness, impurities, defects and grain boundaries. The real and imaginary parts of the complex relative permittivity of silver obtained from this model are presented in Appendix A3 Fig. 54.

iii.) Sapphire (Al_2O_3)

Sapphire (Al_2O_3) is a commonly used substrate for VO_2 films. The relative permittivity model for sapphire was found in **[171]**:

$$\varepsilon(\omega) = 1 + \frac{S_1}{1-\left(\frac{\omega}{\nu_1}\right)^2} + \frac{S_2}{1-\left(\frac{\omega}{\nu_2}\right)^2} + \frac{S_3}{1-\left(\frac{\omega}{\nu_3}\right)^2} \tag{27}$$

The model consists of three Lorentz oscillators (eq.10) with no Drude component. Oscillator strengths and resonance frequencies can be found in Table A of Appendix A3.

4.3 Fabrication

The sample consisted of a thin layer of VO_2 (250 nm thick) on a bulk sapphire (Al_2O_3, ~1 mm thick) substrate. Sapphire was chosen as the substrate in this work, firstly because the material has high optical transmission within the wavelength range of interest, and secondly because deposition of high quality VO_2 film on such substrates has been widely documented in literature **[174]**. At this point it must be stressed that the as-fabricated film was not designed for microbolometric sensing. The relatively high thermal conductivity of sapphire substrate, which might be expected to be detrimental to microbolometer sensitivity in a real device, was therefore not a concern for the purposes of this experiment. As for the potential consequences of high thermal conductivity substrate on the experiment, firstly the temperature of the substrate and bulk film was maintained as explained in the next chapter. Secondly, VO_2 has a low thermal conductivity and the temperature rise due to thermoplasmonic heating was expected to be small and constrained locally to nanorods i.e. near the surface. Thus the impact of substrate thermal conductivity on degree of thermoplasmonic heating was expected to be minimal in this case. The VO_2 layer was fabricated via reactive magnetron sputtering of vanadium under continuous flow of argon and oxygen gases. Following Urade et al. (2016) **[174]**, the sputtering conditions were a substrate temperature of 400 °C, radio frequency power 200 W, argon flow rate 0.11 $Pa{\cdot}m^3/s$, oxygen flow rate $1.4{\times}10^{-3}$ $Pa{\cdot}m^3/s$, and total Ar and O_2 pressure 0.5 Pa. The high quality of the VO_2 film was verified by measuring the resistivity between the electrodes in a thermal cycle (Fig. 30). The resistivity changed by over three orders of magnitude between 20 ºC and 100 ºC, and showed a phase transition temperature, defined as the centre of the resistivity hysteresis loop, of ~68 ºC.

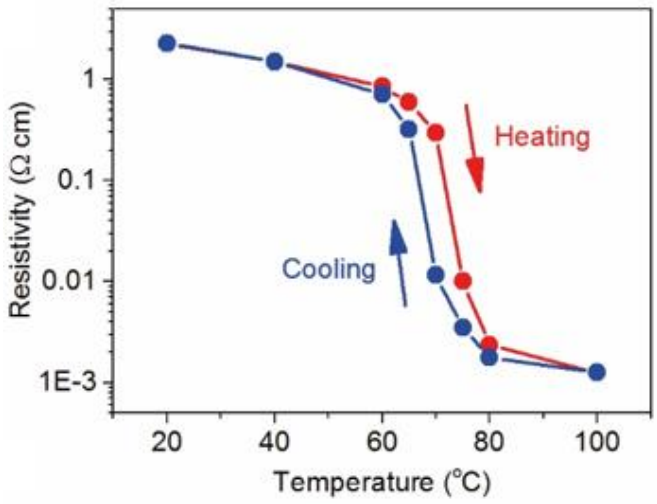

Figure 30. Experimental resistivity plot showing hysteretic phase transition of VO2 on temperature cycling. The phase transition temperature centres at ~68 °C, indicating high quality VO_2.

Two rectangular silver electrodes, of thickness 100 nm, length 7.5 mm and separation 2.0 mm, were subsequently grown on the sample surface using thermal evaporation. A periodic array of Ag nanorods was subsequently patterned between the two electrodes following a standard electron beam lithography and lift-off process. The array was 1.8 mm × 1.8 mm in size and was located at the middle of the two electrodes. The nanorods had a thickness of 40 nm, averaged planar dimensions of 180 nm × 95 nm and a periodicity of 300 nm × 300 nm.

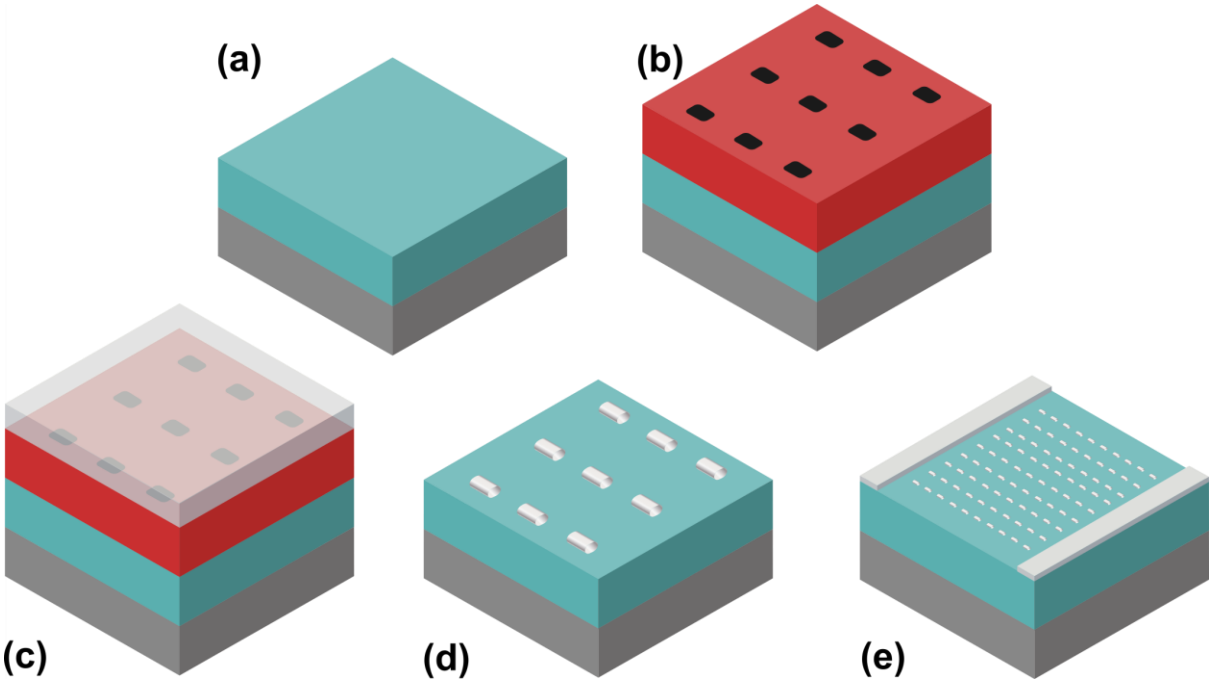

Figure 31. Fabrication process schematic (not to scale). (a) Vanadium dioxide (cyan) deposition on sapphire substrate (grey); (b) resist (red) deposition and e-beam lithography; (c) silver deposition; (d) lift-off; (e) final sample (demagnified).

4.4 Experimental methods

The VO_2-nanorod sample obtained after nanofabrication was characterised using two distinct systems. System A consisted of an optical microscope (Olympus BX51) and a fibre-coupled spectrometer (Ocean Optics HR4000) for measuring the transmission over a broad spectrum, allowing identification of plasmon resonance peaks. Incident light intensity was kept at a very low level to minimise any thermal effect. System B consisted of a Xenon lamp (Hamamatsu Photonics E7536), a monochromator (Shimadzu SPG-120S), and an automatic polarisation system (Hokuto Denko HSV-110) for measuring the resistivity. The sample was illuminated by light narrow in spectral width (~ 46 nm in full-width at half-maximum) and high in intensity (~10 $mW \cdot cm^{-2}$). The central wavelength of the incident light was tuned from 450 nm to 850 nm in 100 nm increments, with the resistivity between the two electrodes measured at each wavelength. As VO_2 has very small thermal conductivity (6 $W \cdot m^{-1} \cdot K^{-1}$) **[96]**, the sample could drift in temperature with time under light illumination. To minimise this influence on the resistivity measurement, the whole wavelength range was swept four times; Fig. 34(a) shows the average and standard error of these four measurements.

In both systems, the nanorods were illuminated at normal incidence, with the light linearly polarised along either their long or short axis. The light was focused to the centre of the array and the focal spot was slightly smaller than the array. The temperature of the sample was maintained at 66 ºC, a value slightly below the phase transition temperature, for transition-edge detection. This temperature control was achieved by using a Peltier module, attached to the bottom of the Al_2O_3 substrate, and a temperature sensor, placed at the surface of the VO_2 film close to the nanorod array.

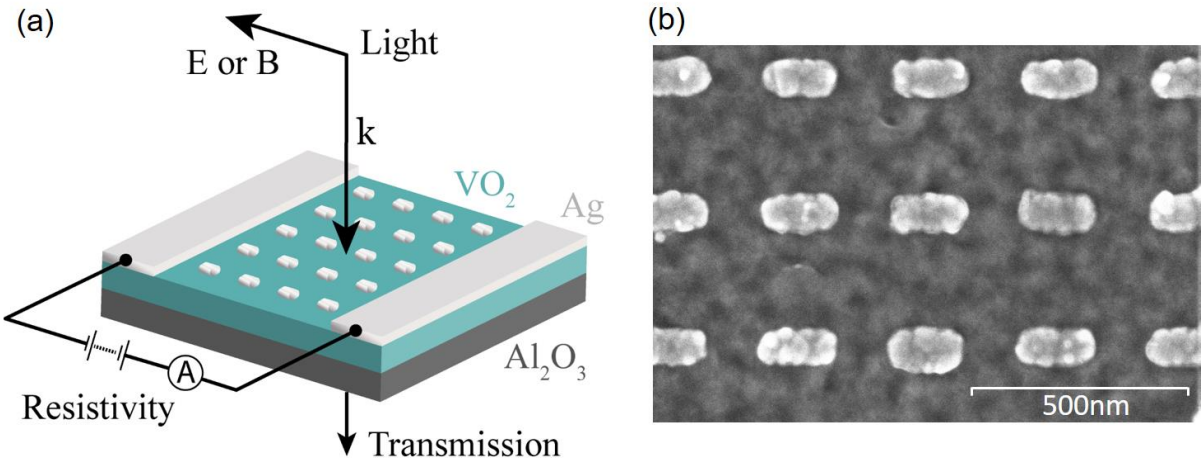

Figure 32. (a) Sample schematic and experimental setup; (b) SEM image of Ag nanorod array.

4.5 Results and Analysis

Figure 33 shows the results from a series of numerical simulations where the volume fraction f of VO_2 was swept from 0 (pure dielectric) to 1 (pure metallic) in 0.2 intervals. The simulations consisted of air / Ag nanorod / VO_2 / Al_2O_3 for short and long axis excitation. Comparison with experimental data (Fig. 34) indicated that volume fraction $f = 0.8$ had the best fit to experiment and was used for all subsequent simulations. Intuitively, a metallic volume fraction of 0.8 may seem high for the representation of film at 66 ºC i.e. not exceeding the transition temperature. A number of factors could explain this discrepancy. Firstly, the Maxwell Garnett model that was used to relate permittivity to volume fraction has no temperature input, thus fraction and temperature are not linked. In addition, it is not clear that the fraction should scale with temperature linearly. Furthermore, the material permittivities and Maxwell Garnett model itself are approximations. Indeed, as previously discussed, the model assumes only dipolar effects and does not account for other factors such as percolation threshold, inhomogeneities or other non-local effects. The approximation of $f = 0.8$ was therefore merely used to best model the behaviour of the material.

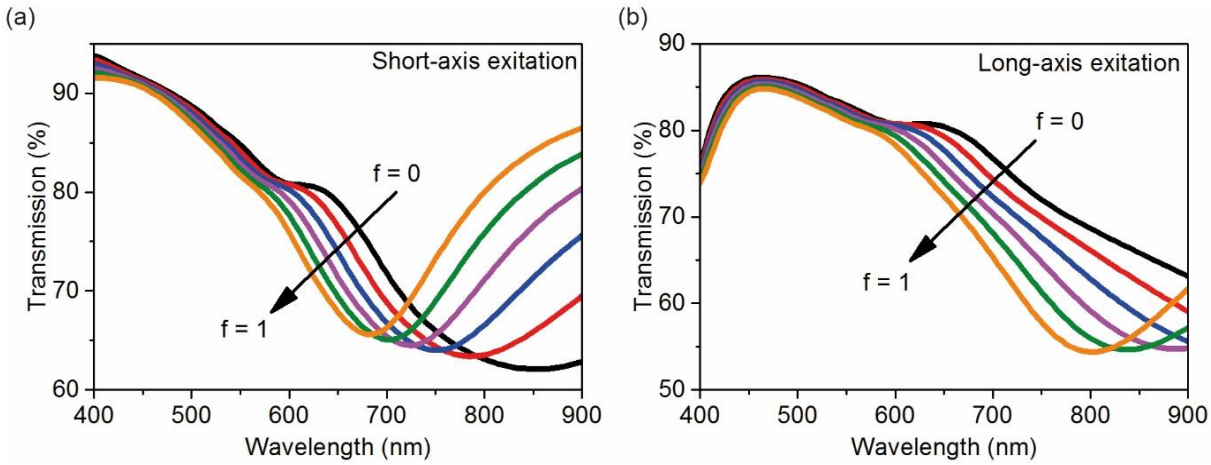

Figure 33. Influence of metallic volume fraction f, the relative volume of metallic phase inside a dielectric matrix, on the zero-order transmission. Each spectrum is normalised against a plain VO2 film with the corresponding f. Incident light is polarised along the (a) short-axis and (b) long-axis of the nanorods.

Figure 34(a) shows transmission of the sample measured using System A over a broad spectrum at low intensity. The incident light was polarised along the short axis of the nanorods. A plain area of the same VO_2 film was used as reference. The spectrum shows a strong and broad feature at 650 nm corresponding to a 30-34 % drop in transmission compared to transmission at 900 and 400 nm. Figure 34(a) also shows the resistivity measured using System B, where the sample was illuminated by light narrow in spectral width and high in intensity. The wavelength dependence of resistivity roughly correlates with the transmission spectrum. Both values are smallest at 650 nm and largest at ~450 nm.

Figure 34(b) shows the numerically simulated transmission spectrum which reproduces the experimental result reasonably well. High-order diffraction in the forward direction is observed for wavelengths below 530 nm. The zero-order spectrum corresponds to the measured spectrum due to the large distance between the sample and detector in the experiment. Compared to experiment, the simulated spectrum shows a redshift of ~50 nm, which is attributed to the difference in nanorod dimensions and material permittivity between the experiment and simulation. Figures 34 (c) and 34(d) show the electromagnetic near-field distribution at 700 nm, the wavelength with the smallest transmission in simulation, and 450 nm, the shortest wavelength for resistivity measurement. At 700 nm, the nanorod shows strong and highly confined enhancement of electromagnetic field. The electric field increases by a factor of ~ 6.5 compared to the incident light; this level of enhancement is only observed at the two sharp edges of the nanorod. These characteristics indicate that the broad and strong transmission feature is induced by localised surface plasmon resonance in the nanorods. The LSPR is significantly less pronounced at 450 nm as both the enhancement and confinement are much weaker (Fig. 34(d)). Figures 34(b) and 34(d) show that transmission amplitude directly reflects resonance strength, with low transmission corresponding to strong LSPR.

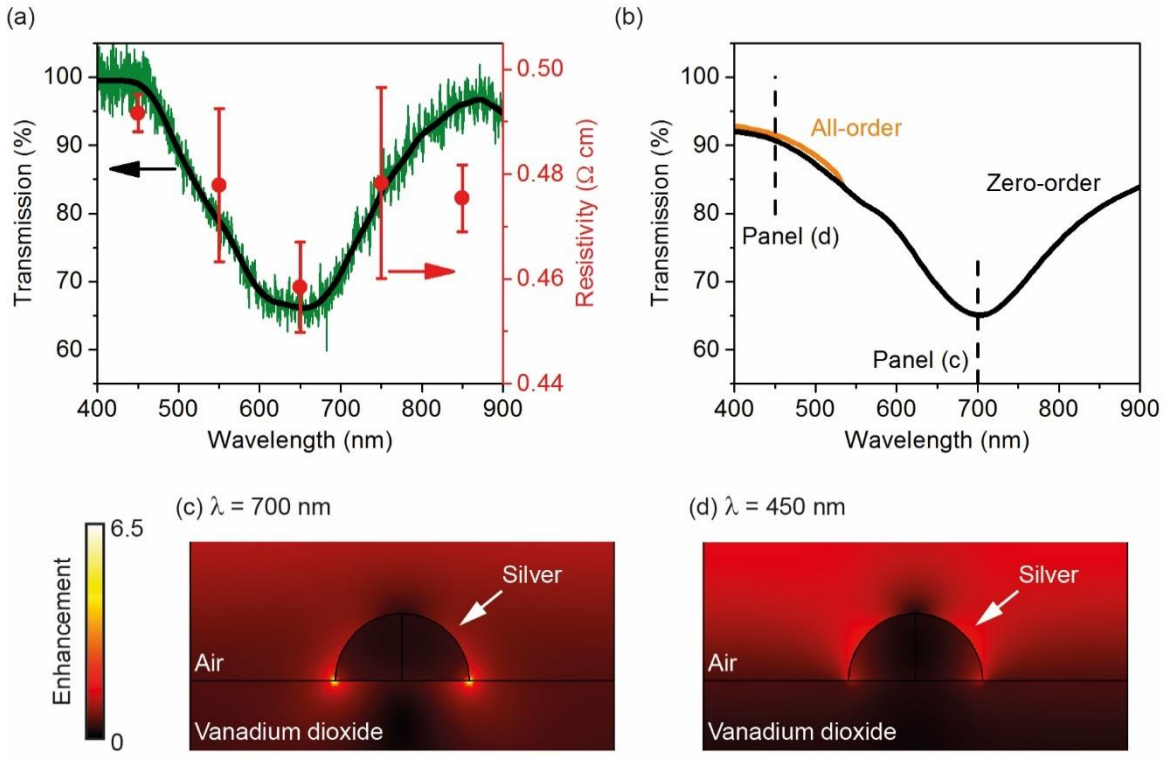

Figure 34. Sample under short-axis light excitation; (a) experimentally measured optical transmission and wavelength dependent resistivity of the sample. The incident light is polarised along the short axis of the nanorods. The green and the black line are the measured and smoothed spectra, respectively; (b) numerically simulated transmission of the sample. High-order forward diffraction is observed at wavelengths below 530 nm; (c-d) electric field distribution at a 2D plane bisecting a nanorod along the short axis at a wavelength of (c) 700 nm and (d) 450 nm. The enhancement factor is with respect to the incident field.

The correlation between transmission and resistivity in Fig. 34(a) is consequently attributed to the thermo-plasmonic effect. Conversion of light to heat is most efficient at the resonance wavelength (650 nm in experiment and 700 nm in simulation) and heating is predominantly localised around the nanorods. The nanorod array is thus at a slightly higher temperature than the temperature sensor nearby **[175]** and the VO_2 beneath the array is slightly suppressed in resistivity. For wavelengths far away from the resonance wavelength, the heating effect induced by the array is smaller, and the suppression in the resistivity is also smaller.

In addition to the wavelength dependence shown in Fig. 34, the polarisation dependence of the sample was also explored. Figure 35 shows corresponding results at the orthogonal light polarisation, i.e. the incident light is polarised along the long axis of the nanorods. The optical transmission shows two pronounced features at ~550 nm and ~850 nm, while the resistivity only traces the feature at ~850 nm (Fig. 35(a)). This difference originates from the different nature of the two spectral features; only the one at ~850 nm is induced by LSPR. This is supported by the near-field distribution in Figs. 35(c) and 35(d), where strong LSPR is only visible at 850 nm. The feature at ~550 nm, although not faithfully reproduced in simulation in Fig. 35(b), becomes more pronounced at smaller metallic volume fractions (Fig. 33). It is consequently attributed to the interplay between high-order diffraction and multiple interference inside the VO_2 layer, as both phenomena depend on the permittivity of VO_2, which in turn depends on the volume fraction. As this feature is not related to any near-field enhancement, no obvious suppression of resistivity is observed at this wavelength.

Using the geometric parameters in Chapter 4.3, the resistivity change of 0.05 Ω·cm from Fig. 35(a) and equation $\mathrm{TCR} = (1/R \cdot \partial R/\partial T) \times 100$, it can be calculated that a TCR of 2.5 %/K would result from a temperature rise of 4 K in this film. While this value is on the order of TCR for the commonly used bolometer materials detailed in Chapter 2.2, more data and improved collection methods would be required to obtain a reliable value for resistivity and temperature rise, and thus allow for direct comparison with commercial films. Unfortunately, a reliable estimate for temperature rise within the nanorod would also be difficult to obtain by simulation in this case. This is because the structure used in Figs. 34 & 35 is a poor candidate for thermal simulation since it represents a single nanorod in an infinite array. Due to this, the unit cell would experience no horizontal heat flux and all heat sources would be assumed to be equal, which is physically not the case. Indeed, because the nanorod heat sources sit on the surface of VO_2, a poor thermal conductor, it may be assumed that the physical system would involve significant horizontal thermal flux out towards the electrodes. Such a problem would be more suited to macroscale multiphysics simulations which could be part of future work.

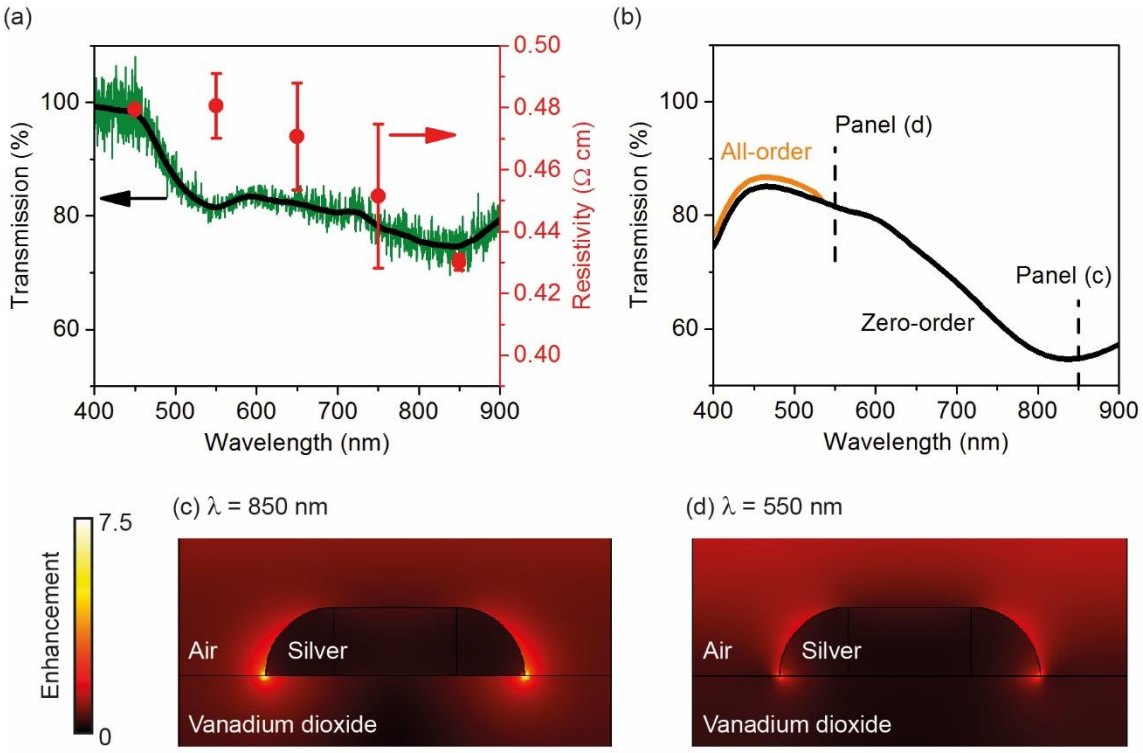

Figure 35. Sample under long-axis light excitation; (a) experimental optical transmission and electrical resistivity. The green and the black line are the measured and smoothed spectra, respectively. Incident light is polarised along the long axis of the nanorods; (b) numerically simulated transmission of the sample; (c-d) electric field distribution of a 2D plane bisecting a nanorod along the long axis at a wavelength of (c) 850 nm and (d) 550 nm.

Chapter 5: Controlling effective phase transition temperature via plasmonic resonance

5.1 Abstract

This investigation more generally sought to quantify the thermoplasmonic contribution to phase change and acted as proof of principle that the effective phase transition temperature of VO_x film can be suppressed by plasmonic heating. As mentioned previously, other methods of tuning the phase transition temperature include tungsten doping and controlling film stoichiometry, but these techniques are irreversible and cannot be altered post-fabrication. In contrast, the integration of plasmonic nanostructures provides a reversible method for tuning effective phase transition temperature. Suppression of the transition temperature is important for lowering energy requirements and optimising film behaviour for its application, for example positioning the film's highest temperature coefficient of resistance within the photodetector's operating range.

Five samples were fabricated; four consisted of gold nanorod arrays embedded in VO_x films supported on silicon wafer while the remaining sample was VO_x on silicon without nanorods. Gold was used because its onset of interband transitions is ~540 nm, far from the wavelength range of interest; additionally, gold is more stable than other common plasmonic materials like silver or copper. Nanorod density was varied between samples by changing the unit cell size (rod spacing). Transmission over a broad spectrum from 2-16 μm was measured. Localised surface plasmon resonance centred at 3.8 μm was evident only for long-axis polarised light. Transmission as a function of temperature was measured at 10 μm, far from the resonance wavelength. The effective phase transition temperature of the VO_2 film was determined using the shape of the resulting hysteresis plot measured on heating and cooling. Polarisation-dependent plasmon resonance was thus shown to suppress the effective phase transition temperature of VO_2 by up to 4 ºC and the degree of suppression was linked to nanorod density. Following theoretical analysis, it was shown that the experimentally measured ΔT_{eff} was around five times higher than predicted by theory.

This work was published as "Kubo W, Ogata Y, Frame JD, Tanaka T, Fang X. *Polarization-dependent phase transition temperature in plasmonic thin films*. Japanese Journal of Applied Physics, 59, 052001, 2020". The author's contribution was limited to simulation and analysis, however, fabrication and physical experimentation have been included for completeness, and these were performed by the group of Professor Wakana Kubo at Tokyo University of Agriculture and Technology in Japan.

5.2 Simulation methods

Simulation results were used to obtain absorption cross section, transmission spectra and electric near-field plots. The simulation space had dimensions 0.3 x 1.0 x 3.0 μm and two 1 μm PMLs at top and bottom. Air was assigned to the top half of the stack. A 70 nm thick VO_2 film was positioned on 1.5 μm thick silicon substrate. Embedded in the VO_2 layer at the silicon interface was a gold nanorod of planar dimensions 75 x 485 x 40 nm. The corners of the nanorod had in-plane radius of 25 nm. Between the gold and silicon was a 5 nm chromium adhesion layer.

Input power was set to 1 W and the electric field was linearly polarised in the x (transverse / short-axis) or y axis (longitudinal / long axis). Preliminary simulations were conducted using a coarse interval parametric sweep (2.0 – 16 μm) to identify resonance peaks using absorbance, reflectance and transmittance spectra. In subsequent simulations the wavelength was swept at a 10 nm interval. The parametric sweep study specified the range in terms of wavelength and provided a conversion to frequency (Hz) by $v = c_0/\lambda$. Sweep frequencies were used as inputs by defining angular frequency (ω, rads^{-1}) as an argument of the complex relative permittivity model $\underline{\varepsilon}(\omega)$ and linking this to the parametric values using the inbuilt *freq* global variable. S-parameter transmission was extracted and normalised against a reference, comprising an air-VO_2-Si stack without gold nanorod. Normalization allows the effect of plasmonic nanorods on transmission to be more clearly analysed and differences compared. Absorption cross section σ_{abs} was extracted by integrating power dissipation over the nanorod volume and dividing by incident power:

$$\sigma_{abs} = \iiint Q_h \, \partial \mathrm{V}/P_i$$

where

Q_h power dissipation (W)

V rod volume

P_i incident power

Mesh sizes and material models were as follows:

Entity	Max element size expression [λ = 2 μm]	Max element growth rate	Max element size [nm]	Min element size [nm]	Average element size [nm]
Air	λ / 5	1.2	400	54	202.4
VO_2	λ / 25	1.5	80	54	73.4
Au	λ / 35	1.2	57.1	35	23.4
Cr	-	1.4	275	20	18.0
Si	λ / 5	1.3	400	54	293.4
PML	λ / 10	-	200	-	200.0

Table 8. Element sizes used in simulation.

Silicon (Si)

Silicon was assigned a fixed permittivity of 11.7 for the wavelength range of interest **[176]**.

Gold (Au)

The behaviour of gold was approximated using the Drude model and experimentally fit parameters from Olmon et al. (2012), valid up to 1.8 eV (~650 nm) **[177]**.

$$\varepsilon^*(\omega) = 1 - \frac{\omega_p^2}{\omega^2 + i\omega\gamma} \tag{28}$$

$$\omega_p = 8.9 \text{ eV}$$

$$\gamma = 1/\tau$$

$$\tau = 14 \text{ fs}$$

γ = 0.048 damping frequency (aka relaxation rate)

ω_p plasma frequency

Chromium (Cr)

The behaviour of chromium was approximated by the following Drude-Lorentz model, with experimentally derived parameters from Rakić et al. (1998) **[178]** (see Table D, Appendix A3). The model is valid from 0.07 – 6 eV, equivalently 17.7 – 0.25 μm.

$$\underline{\varepsilon}(\omega) = 1 - \frac{\left(\sqrt{s_0}\omega_p\right)^2}{\omega(\omega - i\Gamma_0)} + \sum_{j=1}^{4} \frac{s_j\omega_p}{({\omega_j}^2 - \omega^2) + i\Gamma_j} \tag{29}$$

5.3 Fabrication

Five samples were fabricated on silicon substrate; four VO_x thin films with embedded gold nanorods and one plain VO_x film. Figure 36 shows the key fabrication steps and the morphology of one sample. A resist layer was spin coated on the surface of a silicon wafer (Fig. 36a) and subsequently patterned by electron beam lithography (Fig. 36b). Chromium and gold thin films, with a respective thickness of 5 nm and 40 nm, were deposited on the sample by electron beam evaporation (Fig. 36c). Nanorods were obtained after the lift-off process (Fig. 36d). They had an averaged planar dimension of 485 nm × 75 nm and an overall array size of 1 mm × 1 mm (Fig. 36g); nanorod periodicity was varied for each of the four samples (see table 9). A 70 nm thick vanadium layer was subsequently deposited by reactive sputtering (Fig. 36e). The sputtering power was 40 W, the pressure was 0.6 Pa, and the gas flow rates of argon and oxygen were 15 sccm and 0.3 sccm, respectively. Finally, the film was annealed in air to oxidise the vanadium (Fig. 36f). The oxidisation temperature was 440ºC and the temperature increase rate was 1.9 ºC/min. X-ray diffraction of the film indicated a mixed composition comprising VO, V_3O_7, V_2O_5 and less than 10% VO_2.

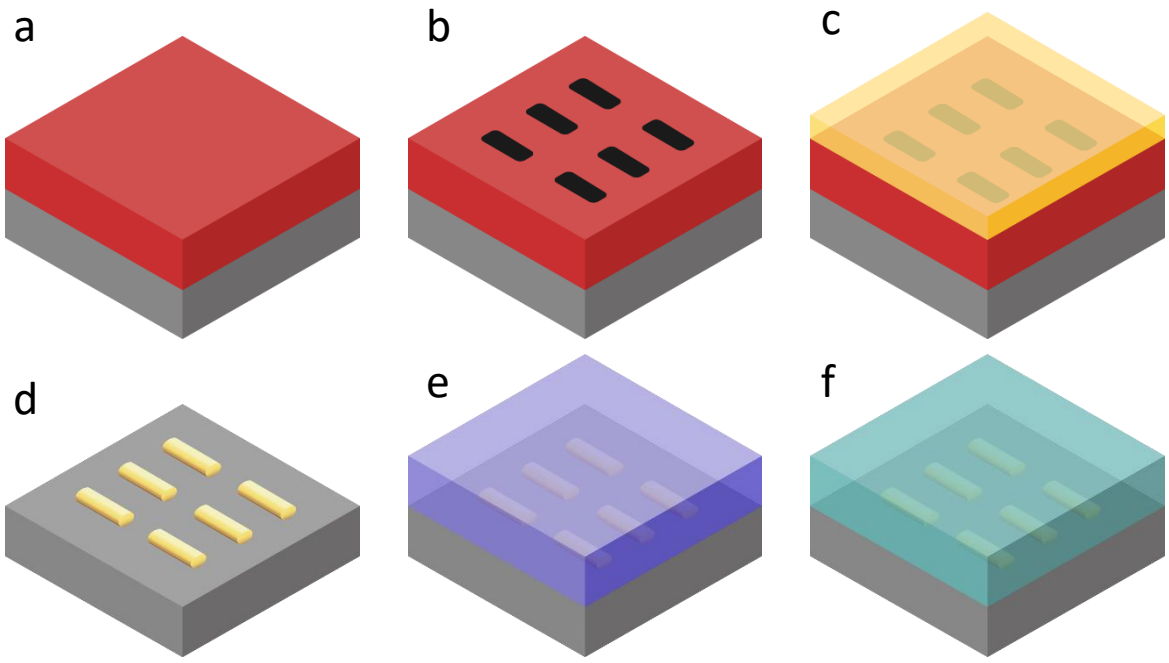

Figure 36. Fabrication process schematic (not to scale). (a) E-beam resist (red) deposited on silicon (grey); (b) e-beam lithography; (c) gold deposition; (d) lift-off; (e) vanadium deposition (blue); (f) oxygen anneal to VO2 (cyan).

5.4 Experimental methods

Infrared transmission spectra of the sample were measured using a microscopic Fourier-transform infrared spectrometer (FTIR-6300 and IRT-3000, JASCO). The light source was a high-intensity ceramic infrared source, generating a broad spectrum predominantly between 2 and 16 µm. The light

was polarised by using a polariser, which allowed for switching plasmon resonances. The incident light was loosely focused down to a diameter of 600 µm, smaller than the size of the nanorod array, and its intensity was 5.0 W at the sample surface. The transmission spectra were recorded by using a HgCdTe photodetector, and a clean silicon wafer was used as reference. Accurate temperature measurement and control were achieved by using a Peltier module and a temperature sensor attached to the bottom and topside of the sample, respectively. The spectrum at each temperature was recorded after the temperature sensor was stabilised for at least five minutes, long enough for the sample to reach thermal steady state.

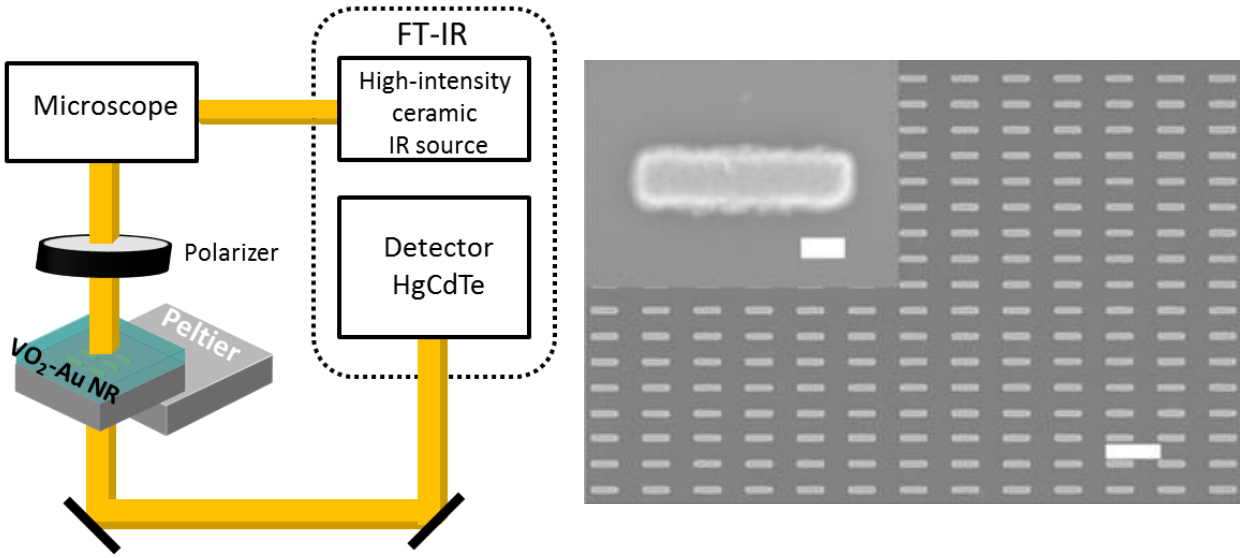

Figure 37. Left: Experimental setup; Right: SEM image of Au nanorod array. White bars represent 1 µm and 0.1 µm in the high and low magnification images, respectively.

5.5 Results and analysis

Figure 38(a) shows the long-axis polarised transmission spectra of the sample measured at each temperature interval between 25 ºC to 75 ºC. A strong resonance feature at ~3.8 µm is observed only for the long-axis polarised spectra, corresponding to a localised surface plasmon resonance mode along the longitudinal axis of the nanorods. Figure 38(a) shows a slight shift in resonance wavelength (~140 nm) with temperature, congruent with a change in VO_x permittivity. For wavelengths away from the resonance, transmission clearly decreases with increasing temperature within the studied temperature range. This is due to the transition of the film from dielectric to more reflective metallic phase. The spectral feature at ~12 µm is attributed to intrinsic loss in the VO_x **[179, 180]** and the intensity drop at ~16 µm originates from the limited spectral range of the light source and spectrometer. Fig. 38€ shows the transmission at an example wavelength of 10 µm, far from the plasmon resonance wavelength. Transmission over the complete heating and cooling process traces a hysteresis loop. The intersection at ~60 ºC, a feature that has rarely been reported in previous VO_x studies, is reproduced in numerical simulation (Figure 39).

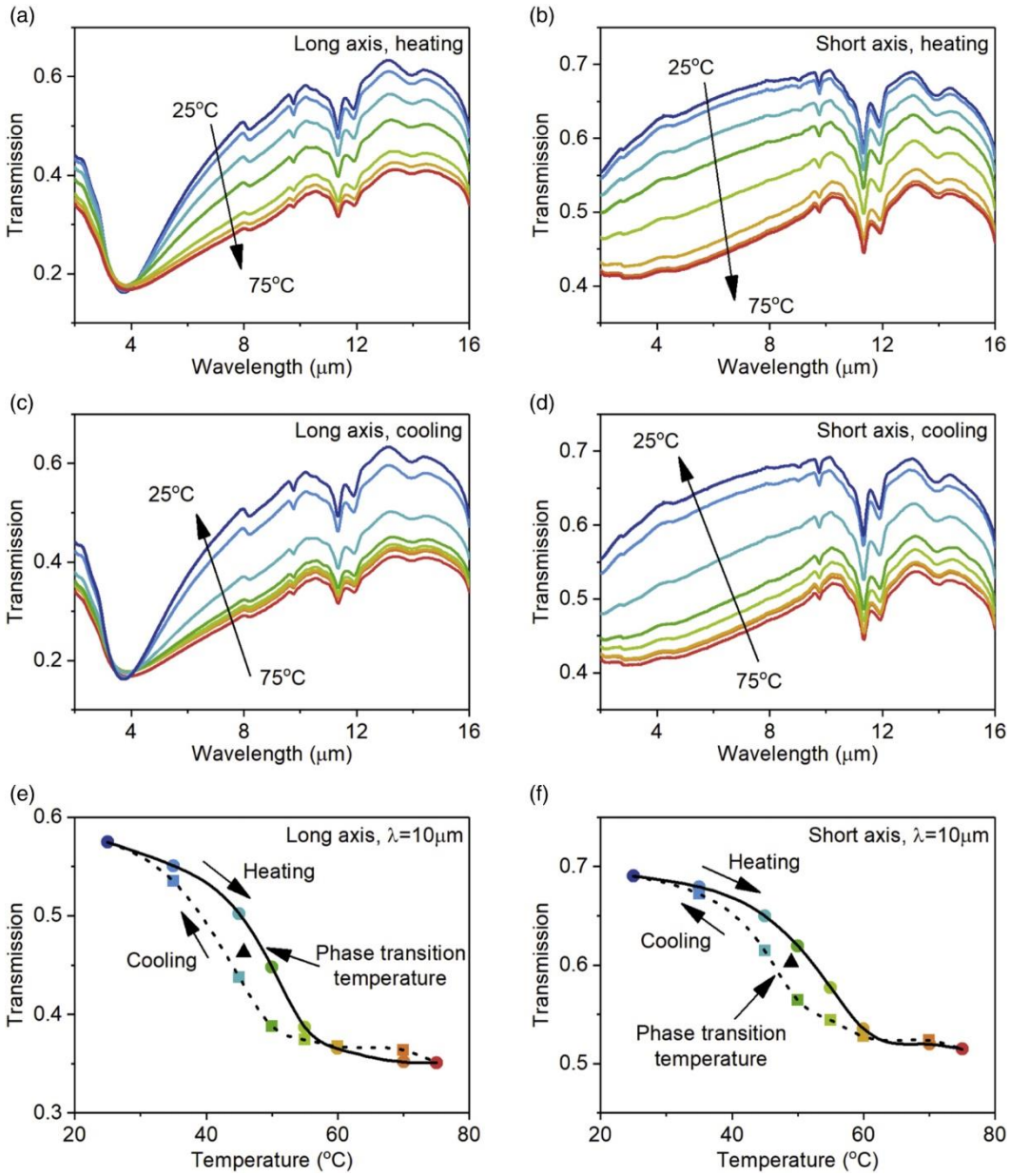

Figure 38. Optical properties of experimental sample. (a) Transmission spectra measured at different temperatures in a heating process. Incident light was polarised along the long axis of the nanorods. Spectra at eight different temperatures were measured: 25 ºC, 35 ºC, 45 ºC, 50 ºC, 55 ºC, 60 ºC, 70 ºC and 75 ºC. (b) Transmission spectra repeated for short-axis illumination. (c) and (d) Transmission spectra repeated for VO_2 in cooling process for long and short-axis polarisation, respectively. (e) Transmission hysteresis loop at 10 μm, a wavelength far away from the plasmonic resonance, obtained in a complete heating (solid line) and cooling (dashed line) process. The effective phase transition temperature T_{eff} (black triangle) is at the centre of the loop. (f) Transmission hysteresis loop repeated for short-axis polarisation.

Figures 38(b,d,f) show the corresponding spectra and hysteresis loop, for the orthogonal polarisation, i.e. along the short axis of the nanorods. The transmission spectra in Fig. 38(b,d) show similar temperature dependence as in Figure 38(a,c). Meanwhile, they lack any observable feature of plasmonic resonances, which is supported by the near-field distribution in Figure 39(g-j). Comparing the long and short axis figures of Fig. 38, there is a clear difference in transmission intensity, even far from

resonance. The reason for this is firstly because the unit cell geometry is inherently anisotropic and secondly because the longitudinal plasmon resonance mode has the effect of increasing the extinction cross-section of the nanorods i.e. a greater proportion of energy is reflected and absorbed under long-axis illumination. These two factors result in the observed higher transmission under short-axis illumination.

The numerical simulations in Figure 39 relate the near-field distribution to the optical spectra. The simulated transmission spectrum Fig. 39(a) reproduces the position of the resonance dip of Fig. 38(a) well, but shows much higher transmission, and a higher amplitude dip, than experiment. The main contributor to this discrepancy is likely the pure VO_2 permittivity and model used to represent highly mixed VO_x. The experimental films likely had additional lossy components resulting from crystalline / morphological and local effects. Regardless, the model was able to predict the resonance wavelength quite accurately. In the near-field, the resonance feature at ~3.8 µm presents as strong electric field confinement surrounding each nanorod, as shown in Fig. 39(b); this is in stark contrast to the field distribution at non-resonance wavelengths shown in Figs. 39(c-e). The lack of electric field enhancement in short axis simulations (Figs. 39(f-j)) support the absence of plasmon resonance in experiment.

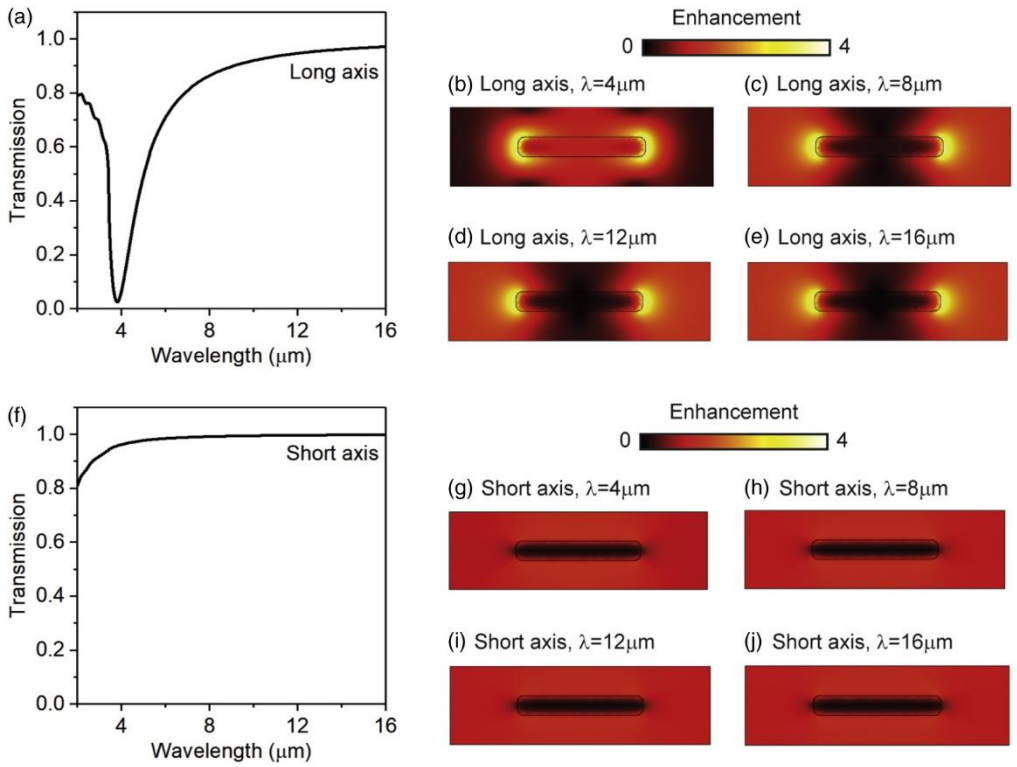

Figure 39. Numerically simulated optical properties of Sample 2, Table 9. The VO_x film is approximated by stoichiometric VO_2 in the room-temperature insulator phase. (a) Transmission spectrum of the sample under long-axis illumination. (b)-(e) Electric field distribution of a 2D plane located 10 nm above the top nanorod top surface within the VO_2 layer. The field strength is normalised against the value at the same location inside a plain VO_2 film. The whole wavelength range of interest is sampled at (b) 4 µm, (c) 8 µm, (d) 12 µm and (e) 16 µm. (f)-(j) Corresponding transmission spectrum and field distribution under short-axis illumination.

5.6 Optical hysteresis loops

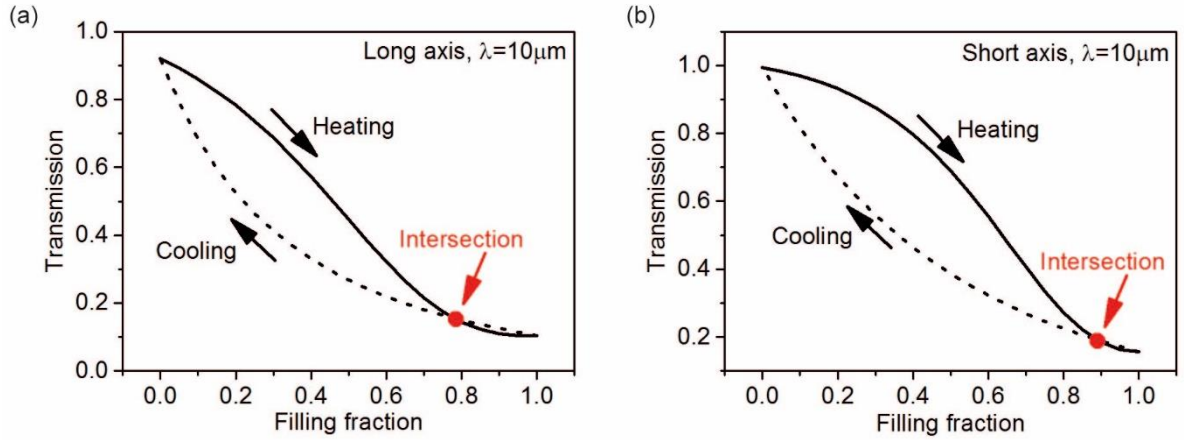

Figure 40. Numerically simulated optical hysteresis loops for Sample A under (a) the long-axis and (b) the short-axis illumination at 10 μm. These two loops, with the x axis as the filling (volume) fraction, have different shapes from the two loops in Figures 38e and 38f, where the x axis is the temperature. It is because the filling fraction does not scale with the temperature linearly. Both simulated loops reproduce the intersection points observed in experiment (Figures 38e and 38f). The effective phase transition temperature T_{eff}, defined as the centre of the loop **[74]**, was determined by the following three steps: (1) transmission at 25 ºC and 75 ºC determines the centre of the loop in the y axis; (2) the two temperatures that produce this transmission are located on the hysteresis loop; (3) the average of these two temperatures determines the centre of the loop in the x axis and consequently T_{eff}.

The two hysteresis loops in Figures 38(e) and 38(f), although similar in their shapes, have an intriguing difference in T_{eff}. The value is 45.7 ºC for the long-axis illumination and 49.0 ºC for the short-axis illumination, showing a clear difference of 3.3 ºC. Table 9 shows the results for all of the samples. Sample 1 is the control sample without any embedded gold nanorods and has $T_{eff} = 49.0$ ºC when illuminated by either orthogonal polarisation i.e. there is no polarisation dependence. Samples 2-5 are listed based on their nanorod density (defined as the planar area ratio occupied by the nanorods); figure 38 corresponds to Sample 2. In these four nanorod samples, there is a clear difference between the two polarisations. For the short-axis polarisation where there is no plasmonic excitation, T_{eff} is 49.0 ºC or 49.5 ºC, very close to the control sample. In comparison, for long-axis polarisation where there is plasmonic excitation, T_{eff} is 3.2 ºC to 4.0 ºC lower. The biggest suppression of 4.0 ºC is observed in Sample 5, which has the highest nanorod density of 24.4 %.

Sample number	Unit cell size	Nanorod density	T_{eff}, long-axis polarisation [°C]	T_{eff}, short-axis polarisation [°C]	Difference ΔT_{eff} [°C]
1	N/A (control)	0	49.0	49.0	0.0
2	1 μm × 300nm	0.121	45.7	49.0	3.3
3	750nm × 300nm	0.162	45.5	49.0	3.5
4	1 μm × 200nm	0.182	46.3	49.5	3.2
5	750nm × 200nm	0.243	45.0	49.0	4.0

Table 9. The effective phase transition temperature T_{eff} of five samples. The planar density of the nanorods ranges from 0% in Sample 1 (the control sample, a bare VOx film without nanorods) to 24.4% in Sample 5. In Sample 1, T_{eff} is measured at two orthogonal light polarisations chosen arbitrarily. In Samples 2-5, these two polarisations are along the long and short axes of the nanorods, respectively. Localised surface plasmon resonance exists only in Samples 2-5 under long-axis polarisation.

Since parameters that commonly affect phase transition temperature (e.g. stoichiometry and phase composition) do not change with light polarisation, Table 9 suggests that plasmonic resonance can suppress the effective phase transition temperature T_{eff} of VO_x. As the phase transition of VO_x involves crystal structure change that is inhomogeneous at the nanoscale **[20]**, it is possible that the presence of embedded nanostructures may physically influence the properties of VO_x even without plasmonic resonance. However, because $T_{eff} \approx 49.0$ ℃ is observed in all the control and nanorod samples, any such influence is absent or too small to detect in this experiment.

The results in Table 9 can be interpreted based on the electromagnetic and thermal properties of surface plasmons. Plasmonic resonances convert electromagnetic energy into thermal energy through mechanisms such as electron-electron and electro-phonon scatterings as mentioned in Section 1 **[181, 182]**. Due to the thermoplasmonic contribution, the transition between low-temperature dielectric phase and high-temperature metallic phase consequently appears to occur at a lower measured temperature. This phenomenon disappears under short-axis illumination since there is no plasmon resonance, hence absence of electric field concentration.

5.7 Theoretical analysis: plasmonic influence on effective phase transition temperature T_{eff}

The continuous VO_x layer and its embedded gold nanorods can be approximated as a homogenous medium according to the effective medium principle. The nano-heaters are treated as a thin sheet of heat source q at the interface between silicon and this hypothetical film. In the steady state, the system has finished evolving; the energy inflow and outflow are equal and the temperature distribution becomes fixed. The temperature distribution T at steady state obeys the heat equations of $-\tilde{k}\nabla^2 T = \boldsymbol{q}$ (Poisson's

equation) at the silicon-film interface and $-\tilde{k}\nabla^2 T = 0$ (Laplace's equation) inside the film, where $\tilde{k}$ is the thermal conductivity, ∇^2 is the Laplace operator (divergence of the gradient, how the rate of temperature change varies in space) and $\boldsymbol{q}$ is a vector field representing magnitude and direction of heat flow. The second equation indicates that at steady state, there is no heat flow and so the temperature gradient in the film remains constant.

At steady state, there is a decreasing linear temperature gradient from the heat source to the air interface. The temperature at the film centre can be viewed as its effective temperature T_{eff}. The film centre is thus ΔT_{eff} above the temperature at the air interface. Baffou et al. (2013) **[183]** established an analytical model for calculating the temperature of a metal nanoparticle array under single-wavelength light illumination. Adaptation of this model to account for broadband illumination yields:

$$\Delta T_{eff} = \frac{1}{(\kappa_f + \kappa_s)\,\pi\, D\, A}\left(1 - 2\frac{\sqrt{A}}{\sqrt{\pi}\, D}\right)\int \tilde{P}(\lambda)\sigma_{abs}(\lambda)d\lambda \tag{30}$$

where λ is the wavelength, and $\tilde{P}(\lambda)$ and $\sigma_{abs}(\lambda)$ are the wavelength-dependent radiation intensity and absorption cross section, respectively. κ_f and κ_s are the thermal conductivity of the VO_2 film (taken as $6\ Wm^{-1}K^{-1}$) and the silicon substrate ($149\ Wm^{-1}K^{-1}$), respectively **[74, 184]**. $\widetilde{D}$ is the diameter of the focal spot and A is the area of the unit cell. The integral range of λ is 2 μm - 16 μm, the main radiation range of the light source. The radiation intensity $\tilde{P}(\lambda)$ measured at the light source is shown in Figure 41(a). The theoretical spectrum was calculated by approximating blackbody radiation at 590K. After normalisation against the total incident power at $\int \tilde{P}(\lambda)\, d\lambda = 5\ W$, the theoretical values were used to calculate the absorption cross section $\sigma_{abs}(\lambda)$.

Figure 41(b) shows the $\sigma_{abs}(\lambda)$ of a single nanorod, calculated using the wavelength dependent permittivity of gold, chromium and vanadium dioxide. The narrow peak at 3.8 μm indicates localised surface plasmon resonance. Figure 41(c) shows the analytical values of ΔT_{eff} computed based on $\tilde{P}(\lambda)$, $\sigma_{abs}(\lambda)$ and the experimental parameters specified earlier. They fall on a straight line because for small unit cells A under the illumination of a significantly larger light beam $\widetilde{D}$,

$$1 - 2\frac{\sqrt{A}}{\sqrt{\pi}\widetilde{D}} \approx 1$$

As $\sigma_{abs}(\lambda)$ is independent of A (an original assumption in **[183]**), $A * \Delta T_{eff}$ is a constant under a given illumination condition. This explains the linear dependence of the theoretical ΔT_{eff} on the nanorod density in Figure 41(c). In comparison, the experimental dependence shows a similar tendency and a

relatively strong fluctuation. On average, these experimental values are about a factor of five larger than the theoretical prediction. Experimentally, discrepancies may be attributable to variation in sample quality, in particular the fine geometry of the nanorods. However, the assumptions made in theoretical analysis are likely to be more significant. Firstly, the analysis is based on stoichiometric VO_2 whereas our samples are of mixed composition; the permittivity and thermal conductivity are therefore likely to differ. Additionally, the assumption of Au/VO_2 as a homogenous medium heated from one side may be too simple. In summary, these results appear to indicate that the plasmonic hotspots are playing a more complicated role in the phase transition than what our effective medium approximation predicts.

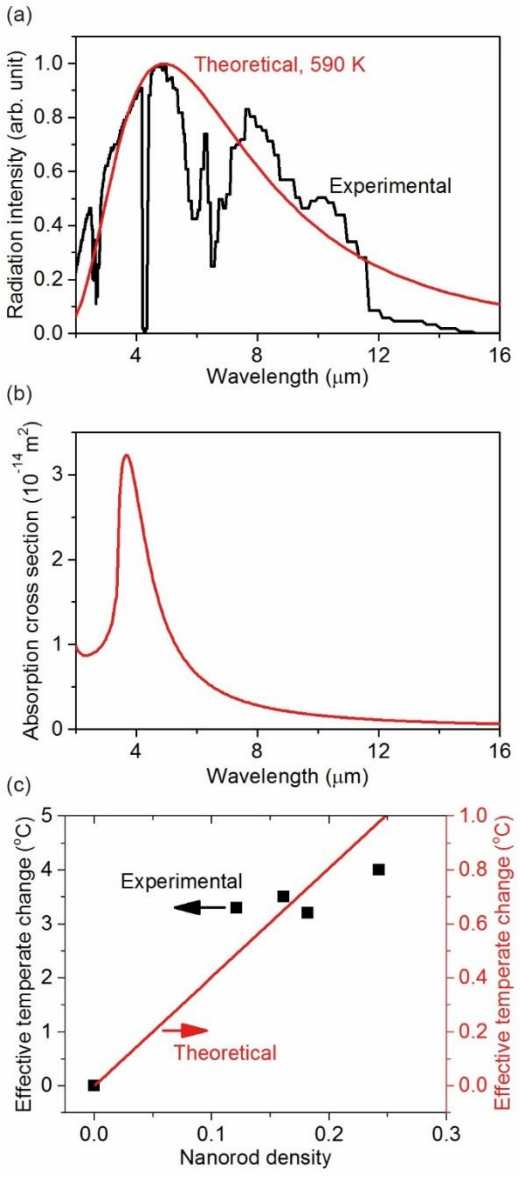

Figure 41. Plasmon-induced change in phase transition. (a) Experimental (black line) and theoretical (red line) radiation intensity of the light source. The theoretical spectrum corresponds to blackbody radiation at 590 K. (b) Theoretical values of the absorption cross section of a nanorod. (c) The effective phase transition temperature T_{eff} is suppressed by ΔT_{eff} via plasmonic resonance, and ΔT_{eff} depends on nanorod density. The experimental values (black dots) come from Table 9, and the theoretical ones (red line) are computed based on the results in (a) and (b).

Chapter 6: Modified Maxwell Garnett Model for hysteresis in phase change materials

6.1 Abstract

After observing optical hysteresis in the Au / VO_2 film in the previous study, it was decided to investigate the phenomenon further. Generally, hysteresis can be defined as a nonlinear function of a system that is dependent on the previous states of that system. Common cases include magnetisation and demagnetisation of a ferromagnet, electric polarisation in ferroelectrics, elastic/plastic deformation and phase transitions. For the thermally driven phase transition of VO_2, an electric or optical property plotted against temperature yields a hysteresis curve. Physically, this means that the measurand at a specific temperature changes depending on whether the sample is being heated or cooled. Typical features of hysteresis loops include two-fold rotational symmetry, where both curves are joined at the two extrema, and the characteristic monotonic curve shape, which is determined by hysteresis width and values at extrema. Characteristics of hysteresis plots in VO_2 thin films, such as transition width and temperature, have been shown to be related to physical parameters such as film thickness, strain, and nanocrystal size. As previously mentioned, intrinsic / induced strain and tungsten doping are common methods of suppressing the phase transition temperature in VO_2 while nanocrystal morphology, which affects hysteresis width and critical temperature, can be controlled by the deposition conditions **[185]**. Previous work has shown hysteresis width to be inversely proportional to grain size **[186]** and demonstrated widths of 2 °C in single crystals to 40 °C in thin films **[187]**.

Analytical modelling allows hysteretic behaviour to be predicted, which is crucial for device design. For example, the significant hysteresis demonstrated in pure VO_2 enables switching between distinct memory states, making it a candidate for phase change memory **[30]**. In contrast, the mixed stoichiometric VO_x films commonly used in microbolometric photodetection were developed to minimise hysteresis, since the readout of a sensor should not change depending on the history of the device. For example, in infrared sensors hysteresis is typically avoided but in memory applications, large and controllable hysteresis is integral to their operation. Many analytical models have been developed for hysteresis (e.g. the Preisach model, the Prandtl-Ishlinskii model and the Duhem model) **[188, 189]**. The choice of model, often with modification, depends on the specific material and properties under study **[190, 191]**. However, these models tend to be complex and difficult to implement. In contrast, mixing formulae are appealing due to their simplicity and ease of use for approximate predictions.

Hysteresis implies an asymmetric mechanism driving the nonlinear behaviour on heating and cooling; whether on the atomic scale (based on Mott-Hubbard / Peierls mechanism) or larger-scale (e.g. distribution of crystal reordering). Upon heating, the VO_2 phase transition is generally understood as

the nucleation and growth of nanoscale metallic "puddles" within the dielectric matrix **[20]**. The puddles expand and agglomerate until a continuous metallic film results. Upon cooling, the reverse might be expected to occur, with the metallic puddles shrinking until a continuous dielectric film results. However, in the model proposed here, the transition can instead be seen as dielectric "islands" growing within the (now) metallic host and that this asymmetry in crystal distribution on heating and cooling is a main contributor to optical hysteresis. Indeed, there is evidence that the asymmetry is due to differences in nanocrystal distribution functions upon heating and cooling**[185, 192, 193]**.

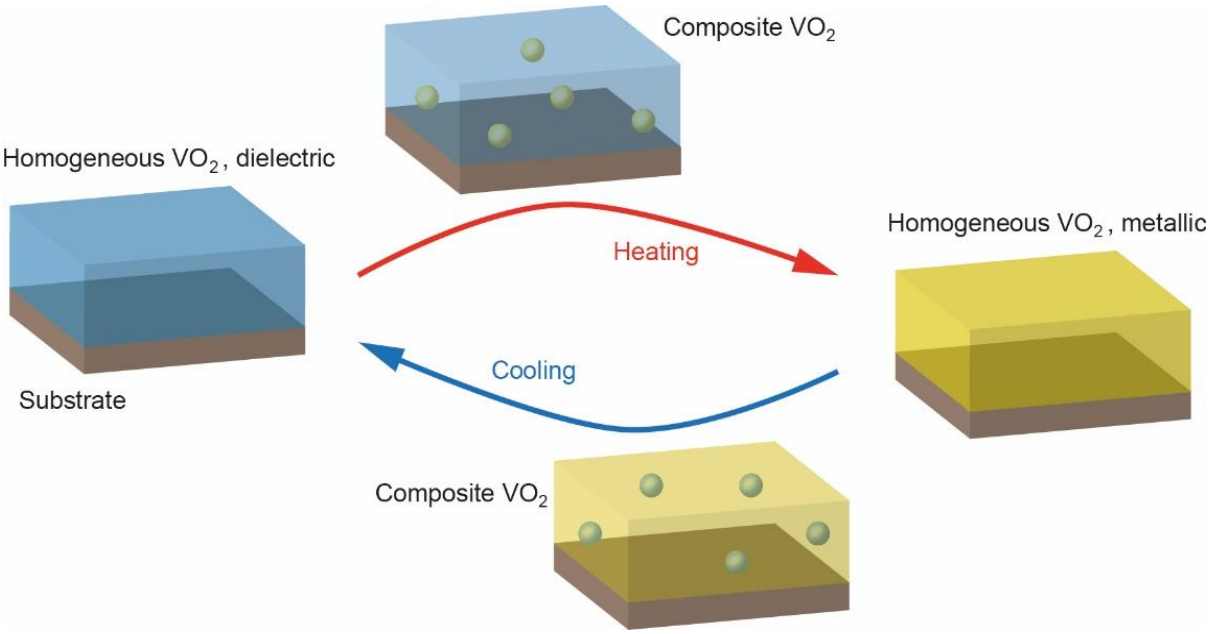

Figure 42. Hysteresis in VO2 phase transition viewed as an asymmetric structural change. The distinct structural differences upon heating and cooling give rise to asymmetry in optical behaviour.

This work was published as "Frame JD, Green NG, Fang X. *Modified Maxwell Garnett model for hysteresis in phase change materials*. Optical Materials Express, 8, 1988, 2018" and is based solely on analytical methods, specifically the Fresnel equations, as detailed in Chapter 3.2.

6.2 Methodology

A modified form of the Maxwell Garnett effective medium approximation was developed to model the effective complex permittivity of the mixture ε_{eff} on heating and cooling. The model simply requires the complex permittivity of each pure phase (ε_1, ε_2) and volume fraction f, representing the relative amounts of each phase in the mixture. The original model [equation (18)] is inherently asymmetric with respect to the two constituents, generally producing a different ε_{eff} if ε_1 and f are interchanged with ε_2 and $1-f$. This asymmetry originates from the assumption that constituent ε_1 is the inclusion while constituent ε_2 is the host. For complicated distributions of two constituents, it is often subjective

whether a constituent is the inclusion or the host. This uncertainty has been viewed as a flaw of the model because ε_{eff} should not change with a person's viewpoint **[150]**. Other models such as Bruggeman are symmetric and therefore avoid this issue, but many require experimentally determined values such as percolation threshold. In addition, the results are often similar or worse than Maxwell Garnett **[150]**. An alternative approach often presented in the literature is using the non-hysteretic original Maxwell Garnett EMT but introducing hysteresis to the volume fraction f by fitting experimental data. Leahu (2013) **[187]** took this approach, where f was assumed to be a free parameter that varied nonlinearly with temperature. The main problems with this approach are 1.) that f should not be assumed a free parameter if analytical results are used to provide quantitative support to experiment and 2.) f has not been shown to have a nonlinear dependence on temperature, as there have been very few studies to this effect **[194]**. In contrast, the modified Maxwell Garnett model does not require f to be hysteretic with temperature, with the hysteresis arising simply from different nanocrystal distribution functions in the material during the heating and cooling processes, a concept which is more straightforward and easier to adopt. In our work the original Maxwell Garnett equation was converted to a pair of equations:

$$\varepsilon_{eff,h} = \varepsilon_d \frac{\varepsilon_m(1+2f)+\varepsilon_d(2-2f)}{\varepsilon_m(1-f)+\varepsilon_d(2+f)} \tag{31}$$

$$\varepsilon_{eff,c} = \varepsilon_m \frac{\varepsilon_m*2f+\varepsilon_d(3-2f)}{\varepsilon_m(3-f)+\varepsilon_d*f} \tag{32}$$

where the effective permittivity in heating ($\varepsilon_{eff,h}$) and cooling ($\varepsilon_{eff,c}$) is generally different at the same f. $\varepsilon_{eff,c}$ was derived by substituting ε_d for ε_m, reflecting the status of metallic phase as host on cooling and substituting f for $1-f$. Unlike the conventional model where f is the volume fraction of the inclusion, this model thus uses f for a single constituent (here the metallic phase) that can be the inclusion or the host. Both equations describe the pure dielectric phase at $f = 0$ and the pure metallic phase at $f = 1$. At other values of f, normally $\varepsilon_{eff,h} \neq \varepsilon_{eff,c}$, the integral feature of hysteresis. Although this modified Maxwell Garnett concept has been mentioned before (e.g. in **[150]**), the author is not aware of another work where it is presented as a positive feature (here used to address hysteretic phase transition). To quantitatively test this approach and allow for future experimental verification, the optical spectra of three samples were analytically calculated using Fresnel equations as detailed in Chapter 3.2.

The numerically analysed system consisted of an air / VO_2 / sapphire stack where VO_2 film thickness was varied between 50, 100 and 500 nm. The wavelength was taken to be 10 μm. Using the frequency dependent complex permittivity models detailed in Chapter 3.4.1(ii), the permittivity of the two pure

phases of VO_2 was calculated as $\varepsilon_d = 9.93 + 0.15i$ and $\varepsilon_m = -15.75 + 131.16i$. The complex refractive index of Al_2O_3 was taken as $0.925 + 0.034i$ **[195]**.

6.3 Results and Analysis

i.) Hysteresis of complex permittivity

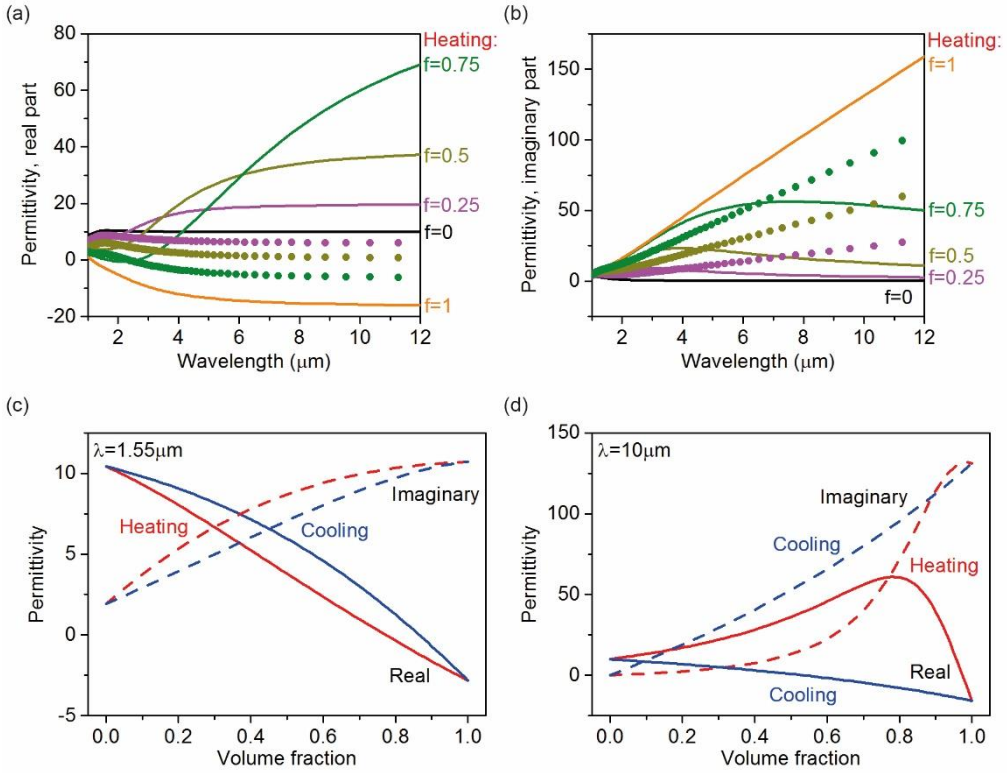

Figure 43. Complex permittivity of VO_2 calculated based on the modified Maxwell Garnett model. (a) The real part of the permittivity in heating ($\varepsilon_{eff,h}$, lines) and cooling ($\varepsilon_{eff,c}$, dots) with f equals 0 (black), 0.25 (magenta), 0.5 (dark yellow), 0.75 (olive) and 1 (orange). $\varepsilon_{eff,h}$ are labelled for further clarification. $\varepsilon_{eff,h} = \varepsilon_{eff,c}$ at $f = 0$ and $f = 1$. (b) Corresponding imaginary part of the permittivity. (c) $\varepsilon_{eff,h}$ (red) and $\varepsilon_{eff,c}$ (blue) at wavelength 1.55 μm. The real part is drawn in solid lines, and the imaginary part dashed lines. (d) Corresponding values at 10 μm.

Figure 43 shows the effective permittivity $\varepsilon_{eff,h}$ and $\varepsilon_{eff,c}$ of VO_2 calculated using the modified Maxwell Garnett model. Figures 43(a) and 43(b) show the wavelength dependence of the real and imaginary part of the permittivity, respectively, at several representative values of f. The plots confirm the difference in calculated permittivity of VO_2 upon heating and cooling, the extent of which becomes more pronounced at longer wavelengths. Interestingly, at long wavelengths, the permittivity of intermediate states is not confined by the values of the two pure phases; this is especially evident for $f = 0.75$ (heating) in Fig. 43(a).

Figures 43(c) and 43(d) compare 1.55 μm with 10 μm, two example wavelengths at each end of the calculated spectrum range. These two wavelengths are chosen also for technological relevance; 1.55 μm is a standard wavelength for optical fibre communications and 10 μm is approximately at the centre

of the infrared atmospheric window for imaging and sensing. Figures 43(c) and 43(d) show that these two wavelengths share several characteristics: (1) both the real and imaginary part of the permittivity shows hysteresis; (2) at large values of f, the real part is negative and the material effectively becomes a metal. Both characteristics agree with common understandings of the material.

The modified Maxwell Garnett model also predicts characteristics at 10 μm that to a certain extent are counter-intuitive. First, a typical hysteresis loop possesses two-fold rotational symmetry; in contrast, both loops in Fig. 43(d) are highly asymmetric and the imaginary part even shows a crossover within the loop. Secondly, a typical hysteresis loop shows the biggest contrast in its output if the input is at the centre of the loop. In contrast, for the real part in Fig. 43(d), the biggest difference between heating and cooling is at $f = 0.8$, very close to an end of the loop. Finally, in a typical hysteresis loop, the output changes monotonically with the input. This general observation is obviously invalid for the real part in heating in Fig. 43(d).

ii.) Hysteresis of optical reflection

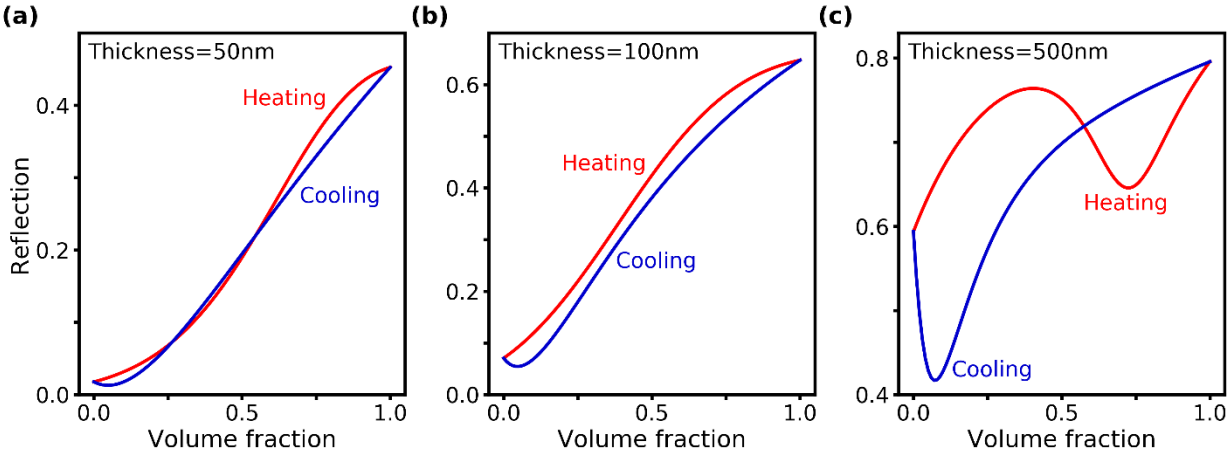

Figure 44. Reflection of a thin VO_2 film on top of a bulk sapphire substrate. The film thickness is (a) 50 nm, (b) 100 nm, and (c) 500 nm. The light wavelength is 10 μm.

Figure 44 shows the reflection spectra of three samples calculated using the Fresnel equation. For a film thickness of 100 nm [Fig. 44(b)], the hysteresis is a single loop roughly possessing two-fold rotational symmetry, a feature found in typical hysteresis loops. This result is interesting as the hysteresis of the permittivity, the only source of the reflection hysteresis, clearly lacks this feature [Fig. 44(d)].At a smaller thickness of 50 nm [Fig. 44(a)], the hysteresis develops two crossovers, which significantly diminishes the difference between heating and cooling. At a relatively large thickness of 500 nm [Fig. 44(c)], the hysteresis is two pronounced loops connected at $f \approx 0.5$. The reflection covers very different ranges in heating and cooling: its minimal value is 0.59 in the former and 0.42 in the latter. These three example thicknesses in Fig. 44 indicate that a rich variety of hysteresis loops may be observable in experiment, but that the relatively high sensitivity to film thickness may prove challenging. It is worth

noting that the crossover points in Fig. 44 do not imply that $\varepsilon_{eff,h}$ equals $\varepsilon_{eff,c}$. In fact, $\varepsilon_{eff,h} \neq \varepsilon_{eff,c}$ for the whole range of f at 10 μm as seen in Fig. 43(d).

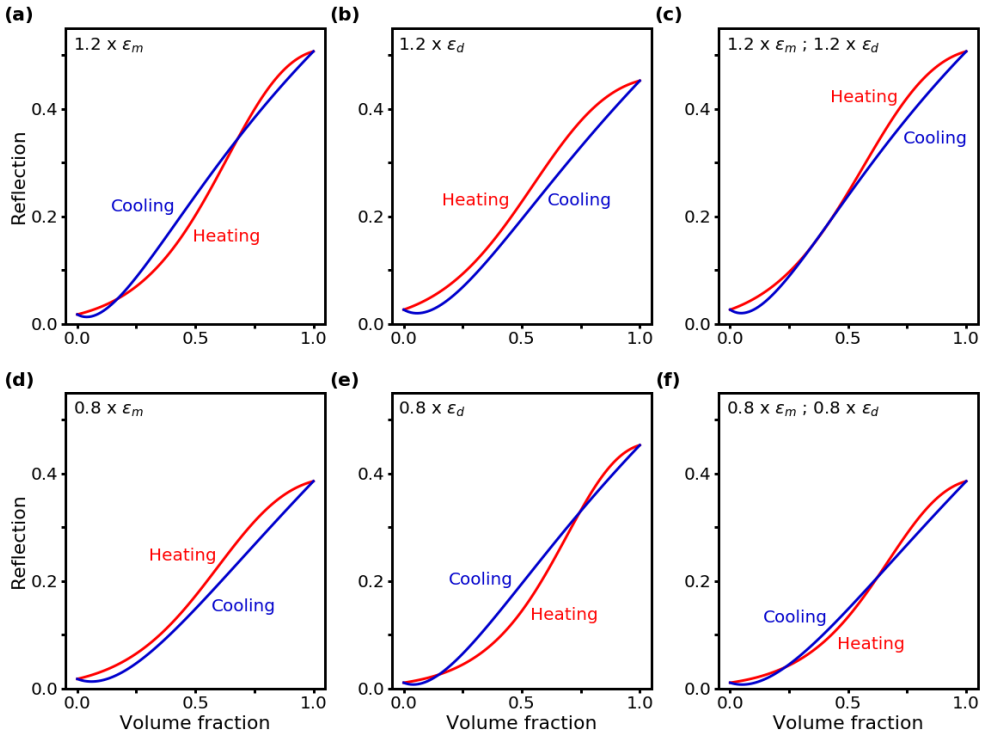

Figure 45. Dependence of light reflection from a 50 nm thick VO_2 film on Al_2O_3 on the complex permittivity of the material. The permittivity of either one or both of the pure phases is changed by 20% before applying the modified Maxwell Garnett model. From the standard values of ε_m and ε_d, the changes are (a) $1.2 \times \varepsilon_m$, (b) $1.2 \times \varepsilon_d$, (c) $1.2 \times \varepsilon_m$ and $1.2 \times \varepsilon_d$, (d) $0.8 \times \varepsilon_m$, (e) $0.8 \times \varepsilon_d$, and (f) $0.8 \times \varepsilon_m$ and $0.8 \times \varepsilon_d$.

One of the main challenges in experimental verification of the model comes from the potential discrepancy between the permittivity of real samples and the permittivity used here. Indeed, reproducible fabrication of high quality VO_2 thin films has only recently been established, triggering great interest in the study of intermediate states **[192, 196]**. Figure 45 above shows the sensitivity of reflection to changes in pure phase permittivity before they are inputted into the Maxwell Garnett model. Here one or both of the pure phase permittivity values was changed by 20% before applying the modified Maxwell Garnett model. This change was applied to the metallic phase [Figs. 45(a) and 45(d)], the dielectric phase [Figs. 45(b) and 45(e)], and both phases [Figs. 45(c) and 45(f)]. The film thickness was 50 nm, the same as in Fig. 44(a). The two crossovers in Fig. 44(a), which could serve as a unique marker in experiments, disappear in half of the cases [Figs. 45(b), 45(c) and 45(d)]. This suggests that the reflection hysteresis highly depends on the material permittivity in the pure phases.

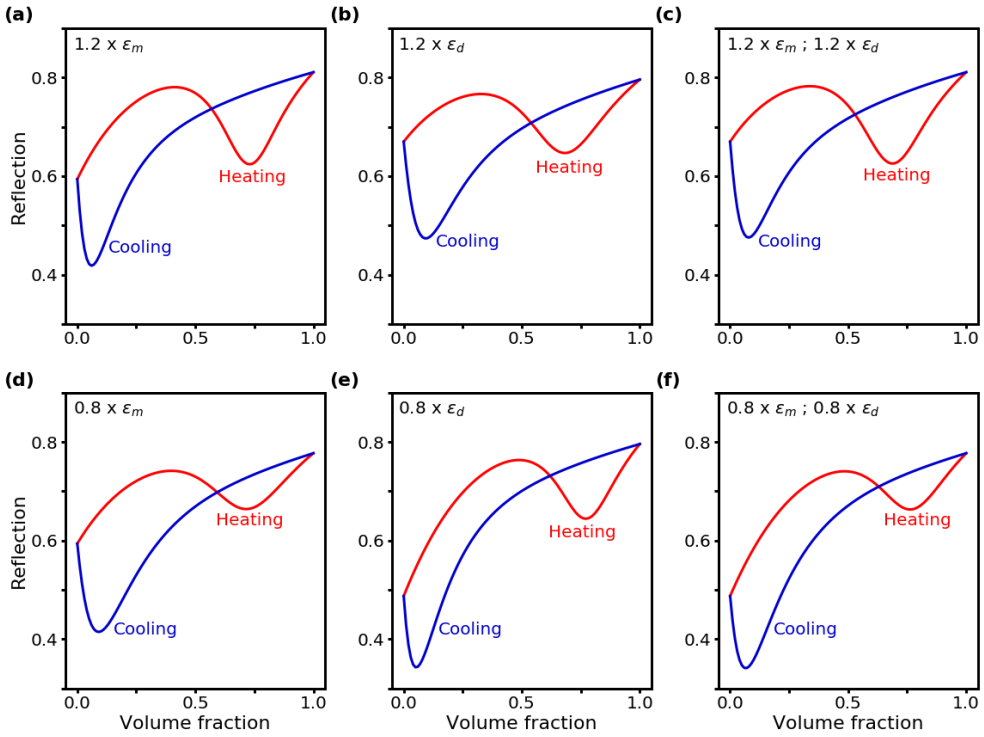

Figure 46. Dependence of light reflection from a 500 nm thick VO_2 film on Al_2O_3 on the complex permittivity of the material. The permittivity of either one or both of the pure phases is changed by 20% before applying the modified Maxwell Garnett model. From the standard values of ε_m and ε_d, the changes are (a) $1.2 \times \varepsilon_m$, (b) $1.2 \times \varepsilon_d$, (c) $1.2 \times \varepsilon_m$ and $1.2 \times \varepsilon_d$, (d) $0.8 \times \varepsilon_m$, (e) $0.8 \times \varepsilon_d$, and (f) $0.8 \times \varepsilon_m$ and $0.8 \times \varepsilon_d$.

The same analysis was conducted for 500 nm thick VO_2 on Al_2O_3. The single crossover persists in all cases. The biggest changes in reflection occur nearer $f = 0$, with a decrease in reflection of ~ 0.1 at $f = 0$ in Fig. 46(f) compared to Fig.44(c). The largest reflection contrast (max-min reflection) of around 0.44 also occurs in Fig. 46(f) between $f = 1$ and $f = 0.07$ on the cooling curve. Interestingly for thinner films, $f = 1$ appears more sensitive to permittivity variation than $f = 0$, however this is reversed for thicker films.

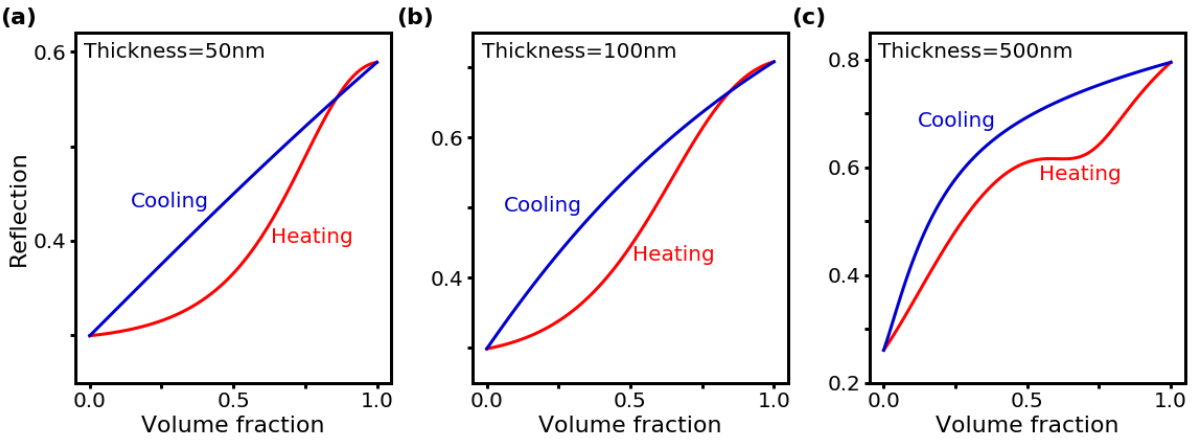

Figure 47. Reflection of a thin VO_2 film on top of a bulk silicon substrate. The film thickness is (a) 50 nm, (b) 100 nm, and (c) 500 nm. The light wavelength is 10 μm.

The analytical calculations were also repeated with silicon replacing the Al_2O_3 to investigate the influence of substrate. Silicon is another commonly used substrate material and is lossless at 10 µm, with real refractive index of 3.42. The main differences between Fig. 47 and Fig. 44 are that Fig 47(a) and (b) both show only a single crossover that disappears at 500 nm as shown in Fig. 47(c).

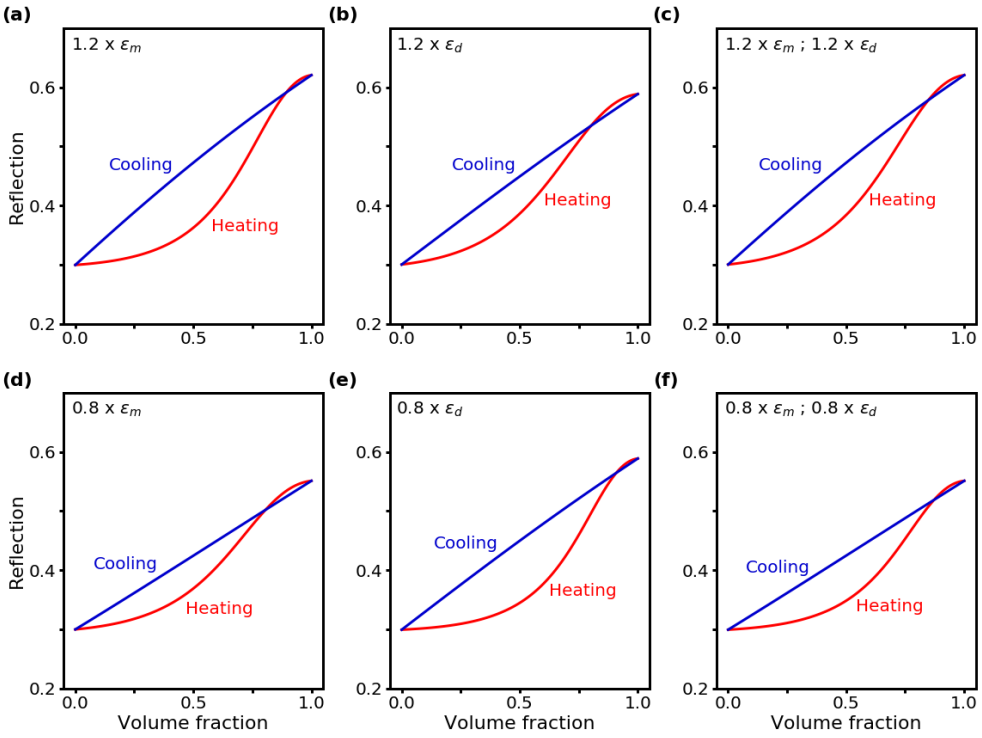

Figure 48. Dependence of light reflection from a 50 nm thick VO_2 film on Si on the complex permittivity of the material. The permittivity of either one or both of the pure phases is changed by 20% before applying the modified Maxwell Garnett model. From the standard values of ε_m and ε_d, the changes are (a) $1.2 \times \varepsilon_m$, (b) $1.2 \times \varepsilon_d$, (c) $1.2 \times \varepsilon_m$ and $1.2 \times \varepsilon_d$, (d) $0.8 \times \varepsilon_m$, (e) $0.8 \times \varepsilon_d$, and (f) $0.8 \times \varepsilon_m$ and $0.8 \times \varepsilon_d$.

Fig. 48 repeats the permittivity variation for 50 nm thick VO_2 on silicon substrate. Compared with Fig. 45, Fig. 48 shows that the crossover feature for Si substrate is much less susceptible to changes in film permittivity and the single crossover persists in all the cases. Finally, the permittivity variation was repeated for 500 nm thick VO_2 on silicon.

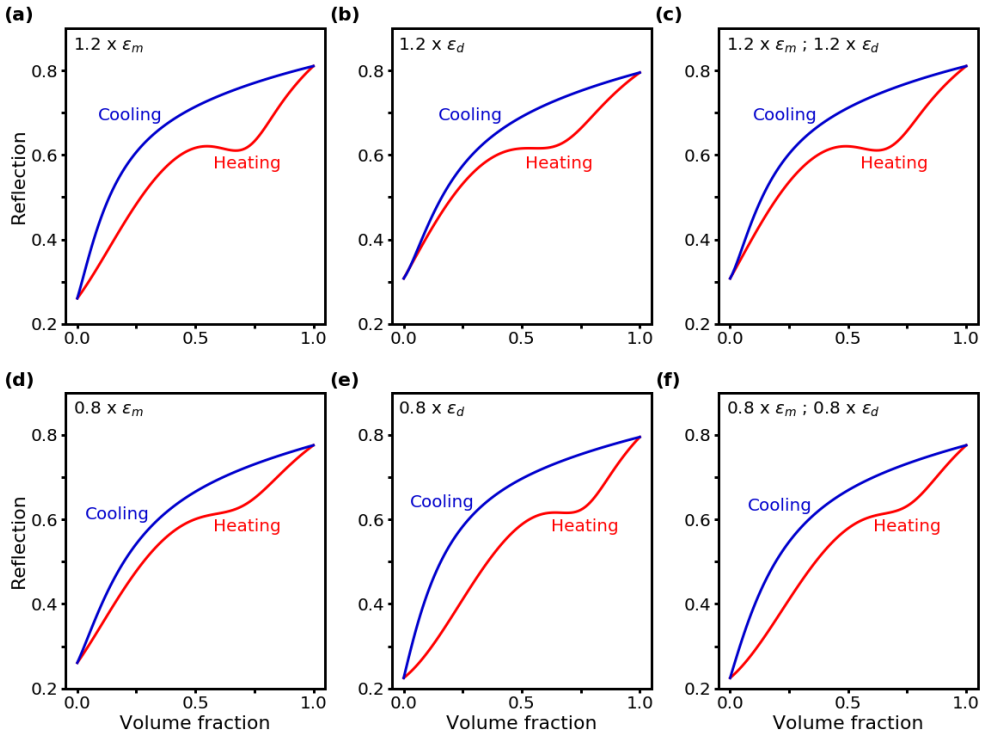

Figure 49. Dependence of light reflection from a 500 nm thick VO_2 film on Si on the complex permittivity of the material. The permittivity of either one or both of the pure phases is changed by 20% before applying the modified Maxwell Garnett model. From the standard values of ε_m and ε_d, the changes are (a) $1.2 \times \varepsilon_m$, (b) $1.2 \times \varepsilon_d$, (c) $1.2 \times \varepsilon_m$ and $1.2 \times \varepsilon_d$, (d) $0.8 \times \varepsilon_m$, (e) $0.8 \times \varepsilon_d$, and (f) $0.8 \times \varepsilon_m$ and $0.8 \times \varepsilon_d$.

The most obvious observation for 500 nm thick VO_2 on Si is that whereas the crossover feature for Fig. 46 is prominent and present in all permittivity cases, no crossover is present for any of the cases in Fig. 49. The maximum reflection contrast is greater for Fig. 49 than for Fig. 46 (0.58 and 0.45 respectively). However, the reflection contrast is lesser for Fig. 48 than for Fig. 45 (0.32 and 0.48 respectively). From this it can be predicted that reflection contrast in hysteresis of silicon substrate is more sensitive than that of Al_2O_3 to VO_2 thickness. Based on the observation that crossovers seem to occur when metallic permittivity increases relative to dielectric permittivity, another prediction is that VO_2 with greater difference between dielectric and metallic permittivity should display crossovers more readily.

Following up on the papers citing this work in 2022, it appears the modified Maxwell-Garnett model has had a mixed reception. Voloshenko et al. (2018) cites this work in the context of "simple isotropic BEMA models" that "fail to reproduce the optical and transport properties in the vicinity of the transition". The asymmetric modified Maxwell Garnett model was not used but some familiar features are observed in experiment, for instance single crossover and pre/post transition dips in Fig. 1 **[197]**.

Another paper, Currie et al. (2019), cites this work as one of a number of papers using the effective-medium approximation **[198]**. They observed an increase in hysteresis width with increasing VO_2 film thickness (8-60 nm) on Al_2O_3 substrate at 1550 nm. Also evident is increasing asymmetry of hysteresis

as the film thickness is increased. Both of these observations are predicted by the modified Maxwell-Garnett model (Fig. 44).

A third paper by Zhu et al. (2019) cites the work as being "very helpful in building the impedance matching analytical model of VO_2 in thin films" **[199]**. This work was an investigation into the terahertz reflection modulation of tungsten-doped vanadium dioxide thin films and involved building a theoretical model for impedance matching.

For some time, 'non-hysteretic branches' (NHBs) within the major hysteresis loop of VO_2 have been of considerable interest. For example, Gurvitch et al. was a proponent of transition-edge devices utilising VO_2 NHBs to replace existing VO_x infrared microbolometers **[200-202]**. It was demonstrated that small temperature excursions inside the major hysteresis loop could be used to avoid unwanted hysteresis in IR bolometers. Although the modified Maxwell Garnett equation has not been tested for such a use, the additional complexity of hysteretic and non-hysteretic regimes within the major loop mean that this model is likely under-equipped to faithfully model such behaviours. As of April 2022 no papers using other phase change or composite materials have cited this work, so the wider utility of the model is unclear.

Chapter 7: Vanadium dioxide phased array metasurface for beam deflection

7.1 Abstract

The final project in this thesis investigated the potential for VO_2 as an active element in a metasurface phased reflectarray designed to control the deflection angle of an incident infrared beam. Following Wan (2019) **[157]**, VO_2 permittivity at 1.55 μm was modelled using the Looyenga mixing rule and the metallic volume fraction was calculated as a function of temperature; these were used to perform electromagnetic and heat transfer simulations. Preliminary electromagnetic simulation results found that the VO_2 phase transition itself did not produce a large enough phase shift to span 2π (0.22π rad). To improve the phase range, the idea was to use VO_2 instead to modulate optical resonance within an underlying cavity. This method would in theory increase the phase range by combining the phase shift generated by the VO_2 transition with the phase shift on resonance. To test this theory, the design space was swept to generate phase and reflectance for metallic volume fractions between 0 and 1, with VO_2 / Al_2O_3 'active' element width as a variable between 50 – 500 nm. With the polarisation factor set to 1/3, a close representation of VO_2 thin film as per **[157]**, the phase range was still not large enough (1.09π rad) and no successful design was ultimately demonstrated. A successful design was demonstrated for polarisation factor 1 (phase range 1.35π rad), but this value was found to be unjustified in terms of the VO_2 properties used.

In parallel with the electromagnetics simulations, thermal simulations were conducted to investigate the feasibility of an array of individually-addressable nanoscale elements that would each need to be maintained at a specific temperature. Results showed that thermal isolation, by means of 1 μm deep etched trenches between nanowires, improved both the intra-element temperature variation (up to 6x less variation) and power efficiency (around 22% less power consumed) of the proposed device.

The work in this chapter has not been published but it is hoped that it can be used to inform future work in the design and simulation of phase change material metasurfaces and nanostructured arrays.

7.2 Concept

Ideally, this type of beam steering array consists of a series of identical elements which are each capable of ≥ 2π phase modulation, with minimal reflectance contrast throughout the phase gradient. 2π phase coverage is important because it means that a periodic array can be fabricated and in principle the deflection angle is then determined solely by the period of the unit cell. In contrast, for an array with sub-2π range, the number of elements is limited and the array cannot be periodic, usually resulting in poor wavefront integrity and small deflection angle. In terms of optical performance, element size and

spacing are very important; a smaller period allows a wider field of view, more elements per array improves beam integrity, and smaller thermal mass means faster dynamic switching. However, array geometry is limited by factors such as fabrication tolerances, electrical interconnection, and the electromagnetic and thermal response.

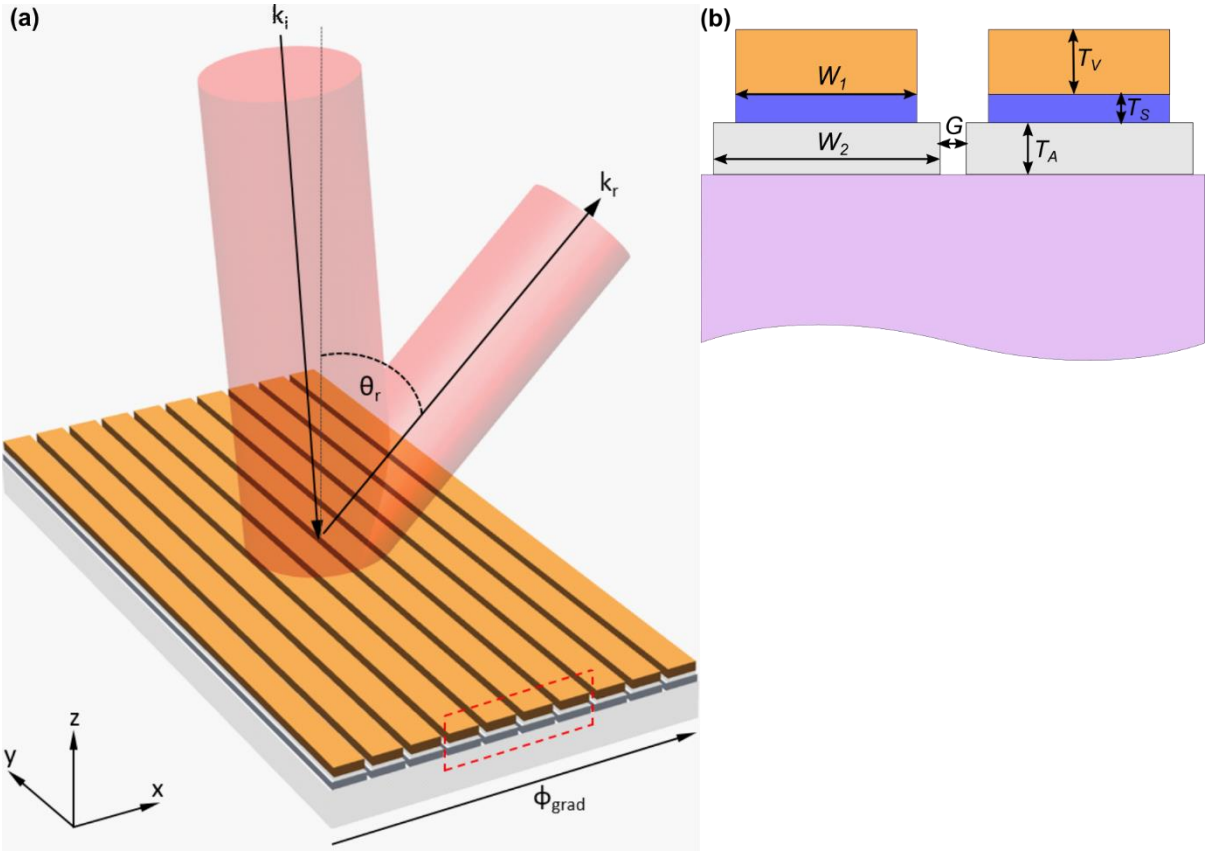

Figure 50. Schematic of the proposed VO_2 metasurface. (a) Perspective view of the metasurface, an array of identical nanowires. Each nanowire is electrically addressable via electrodes at both y-extrema (not shown), with their collective response resulting in a tuneable phase gradient φ along the *x* axis. The metasurface is illuminated at normal incidence from the top and deflects the incident light angle θ following the change in φ. (b) Two example nanowires showing simulation variables. Each nanowire is comprised of the same VO_2 (orange) / Al_2O_3 (blue) / Al (grey) tri-layer stack on a Si substrate (violet). The nanowires differ only in the complex permittivity of the 'active element', represented in simulation by the VO_2 metallic volume fraction *f*.

Figure 50 illustrates a subsection of the VO_2 metasurface. The metasurface is a periodic array of long nanowires on top of a Si substrate. All the nanowires are identical in geometry, each comprising a $VO_2/Al_2O_3/Al$ tri-layer. The whole array is illuminated by a plane wave at normal incidence from the top (i.e. along the -z direction) and light deflected by the array into free space is monitored as the output. The periodicity (550 nm along the *x* axis) is smaller than the free-space wavelength (1550 nm), and only specular reflection (i.e. light propagating along the +z direction) exists if all the nanowires are also

identical in their physical properties. In principle, the light can be deflected by a tuneable angle θ by creating a phase gradient ϕ in the planar direction across the nanowires (i.e. along the *x* axis).

The phase gradient ϕ is obtained by controlling the temperature transient IMT in the VO_2 layer of individual nanowires. More specifically, the Al nanowires are electrically connected at the two ends (not depicted in Fig. 50) so that they are individually addressable. Bias applied between electrodes at either end of each wire leads to flow of electric current and subsequent joule heating in the Al layer. Thermal energy diffuses away from the Al layer and as the VO_2 layer is heated, it becomes progressively more metallic. This affects the complex refractive index of VO_2, shifting the relative phase of light reflected from the designated nanowire. By coordinating phase shifts between adjacent elements, a desired phase gradient ϕ can be established along the *x* axis in Fig. 50. Based on the generalised Snell's law, this phase gradient can lead to a finite deflection angle θ in the *xz* plane. As compared to the Al and the VO_2 layers, which respectively provide heating and permittivity tuning, the Al_2O_3 middle layer has a number of functions: it electrically insulates the Al and the VO_2 layers to facilitate simple electrical control, acts as a thermal conduit between the layers, and contributes to optical tuning as a dielectric spacer. The air gaps separating each element act as electrical and thermal insulation so that each element is individually addressable by applying a voltage across the out-of-plane wire length. Wire length is considered infinitely long since it is orders of magnitude greater than the planar dimensions, thus a 2D approximation is used in both electromagnetic and thermal simulations. However, for the purposes of calculating heat source power density in thermal simulations, the out-of-plane wire length is set as 1 m so that power can be easily scaled to any arbitrary wire length.

7.3 Material models

As previously discussed, VO_2 during the IMT is a mixture of metallic and insulating phases that appear as puddles inside a matrix. In theoretical analysis, the materials properties of these puddles and the matrix are usually treated as identical to those of pure phases (at temperatures immediately beyond the phase transition temperature range). Based on this assumption and effective medium approximation, the permittivity of VO_2 in these intermediate states can be computed as a function of the metallic volume fraction *f*. By treating the phase transition as a first-order chemical reaction, the dependence of *f* on temperature *T* can be expressed as:

$$f(T) = \frac{1}{1+\exp\left[\frac{W}{k_B}\left(\frac{1}{T}-\frac{1}{T_{half}}\right)\right]} \tag{33}$$

where *W* determines the width of temperature range of IMT, and T_{half} is the temperature for $f = 0.5$ (i.e. at which half of the VO_2 is in the metallic state). Currently, the fabrication of high-quality VO_2 thin films is still technically challenging, with large variations in the material properties observed not only

among different fabrication methods but also among different research groups. To facilitate the numerical demonstration, here the decision was made to use the material parameters reported in a recent systematic study, which contains a VO_2 film on Al_2O_3 **[157]**. The values of W and T_{half} are set as 4.85 eV and 75.1 °C for heating, respectively. The corresponding values for cooling are slightly different at 4.15 eV and 72.2 °C, with the difference accounting for the hysteresis.

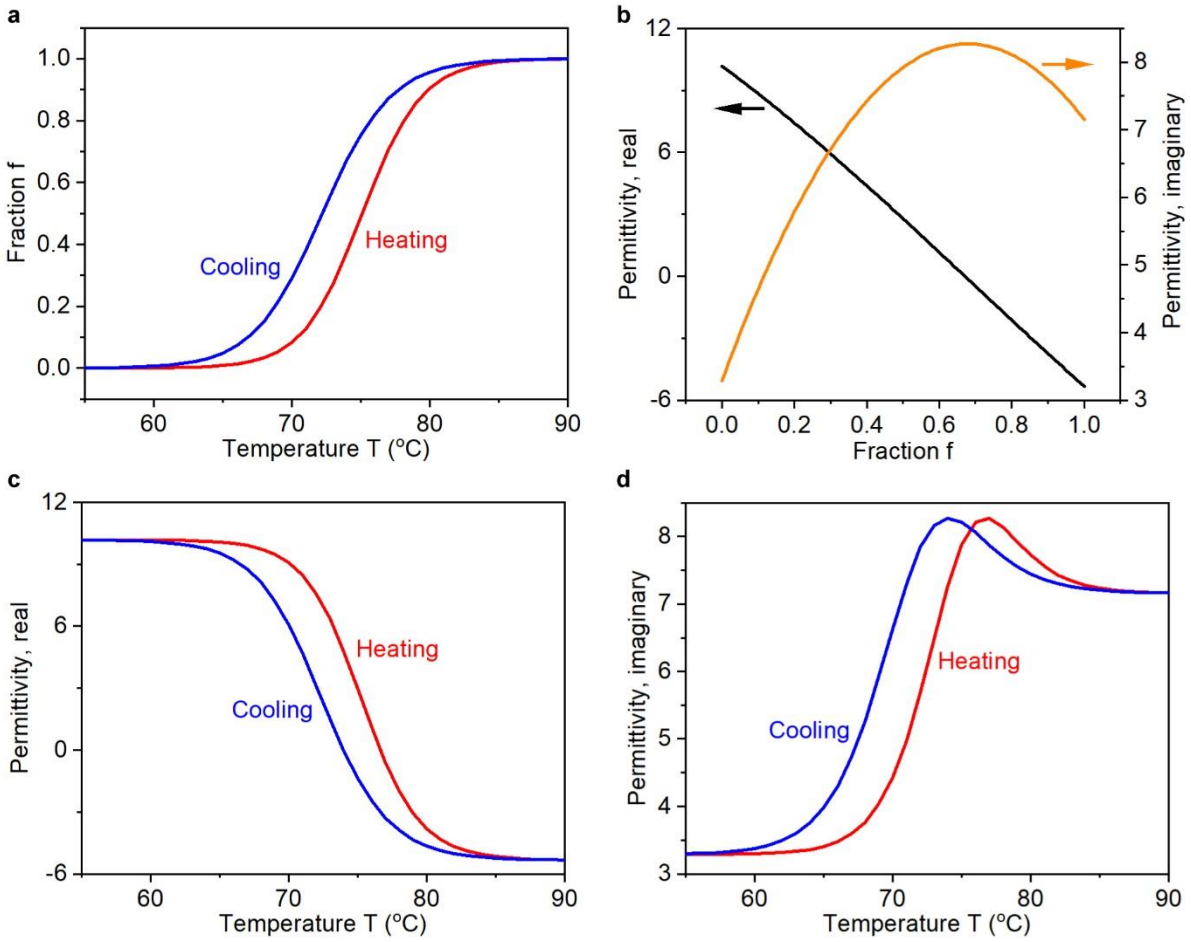

Figure 51. Optical properties of VO_2 in the IMT at the working wavelength of 1550 nm. (a) Metallic volume fraction f of VO_2 rapidly increases upon heating and decreases on cooling. (b) Both the real and imaginary parts of the effective permittivity ε_{eff} depend on f, and there is no contrast between heating and cooling. (c,d) The contrast between heating and cooling is revealed in the temperature dependence, in both (c) the real part and (d) the imaginary part of the permittivity.

Figure 51 shows the hysteretic change in the VO_2 permittivity with both f and T. Outside the phase transition temperature range, which is approximately between 60 °C and 85 °C, the volume fraction f is almost temperature independent [Fig. 51(a)]. Its value is 0 at low temperatures and 1 at high temperatures, corresponding to the pure insulating and pure metallic phases, respectively. Inside the phase transition temperature range, f increases monotonically with temperature T in both the heating and the cooling branch of a thermal cycle. In contrast to the prior projects in this thesis where the Maxwell Garnett model was used to calculate the effective permittivity of VO_2, here the Looyenga mixing formula was used for consistency with the previous $f(T)$ calculation following **[157]**:

$$[\varepsilon_{eff}(f)]^s = f\varepsilon_{met}^s + (1-f)\varepsilon_{ins}^s \quad (34)$$

where ε_{met} and ε_{ins} are the permittivities of the pure metallic phase and the pure insulating phase, respectively. The superscript s is the 'polarisation factor' which takes into account the shape of metallic inclusions during the IMT and takes the value of 1/3 for thin films. Figure 51(b) shows the variation of $\varepsilon_{eff}(f)$ in the whole range of *f*. Here $\varepsilon_{met} = x + iy$ and $\varepsilon_{ins} = x + iy$. The real part of $\varepsilon_{eff}(f)$ shows a monotonic change, decreasing from x to y as *f* changes from 0 to 1. Interestingly, the imaginary part of $\varepsilon_{eff}(f)$ shows a non-monotonic dependence on *f*, and reaches its maximal value of z at $f = 0.7$.

It is worth highlighting that the two curves in Fig. 51(b) show no hysteretic features; they are identical for heating and cooling. This is because hysteresis is embedded in equation (33), where parameters (*W* and T_{half}) take different values for heating and cooling. Figures 51(c) and 51(d) combine equation (1) and equation (34) to plot $\varepsilon_{eff}(T)$, the temperature dependence of the effective permittivity. The hysteretic features appear in both the real part and the imaginary part of $\varepsilon_{eff}(T)$ [Figs. 51(c) and 51(d), respectively], where the heating and cooling branches and distinct. As seen in Fig. 51(a), these two branches are similar in shape in both figures, with the heating branch horizontally shifted to higher temperatures with respect to the other branch. Both branches vary with *T* monotonically in Fig. 51(c) and non-monotonically in Fig. 51(d), following the behaviour shown in Fig. 51(b).

7.4 Array design and electromagnetics simulations

The first step was to establish layer thicknesses for the nanowire stack. Aluminium thickness of 100 nm was chosen because it is much greater than the skin depth (~6 nm) at λ = 1.55 μm, allowing the wire to act as a backplane for efficient reflection, and also to act as a resilient heating element. VO_2 thickness was investigated by simulating continuous VO_2 film on Al_2O_3.

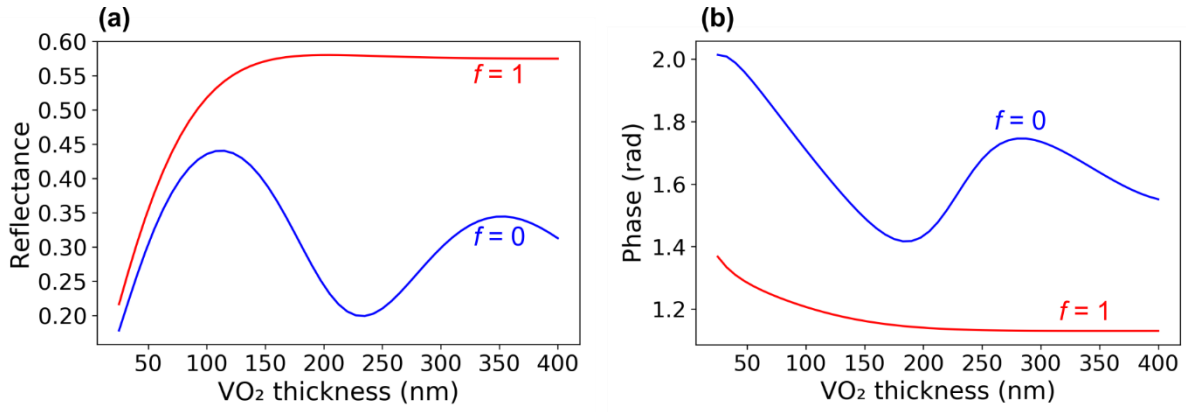

Figure 52. (a) Reflectance and (b) phase plots for varied thickness VO_2 on Al_2O_3 substrate. The oscillations of *f* = 0 in are characteristic of interference in dielectric thin films. (b) shows a reflected phase difference of between 0.27 and 0.68 rad for VO_2 at *f*=0 and *f*=1.

Figure 52(a) reveals the difference in reflectance behaviour between VO_2 in insulating and metallic phases. The oscillations in amplitude for *f* = 0 are characteristic of interference in dielectric thin films.

Interference arises as a consequence of wave interactions between incident light, light reflected from the top interface, light reflected from the film / substrate interface and multiple back-reflections within the film. For $f = 0$, the refractive index of VO_2 (n_{VO2}) is greater than the refractive index of air and Al_2O_3 ($1 < 3.23 > 1.75$). In such a thin-film system, the condition for constructive interference t_c is $(\lambda_{air}/n_{VO2})/4$ and the condition for destructive interference t_d is $(\lambda_{air}/n_{VO2})/2$. For wavelength 1550 nm, this gives $t_c \approx 120$ nm and $t_d \approx 240$ nm. These values match the corresponding increase and decrease in reflection amplitude in Fig. 52(a). Fig. 52(b) shows that the interference conditions correspond to a phase value of ~ 1.58, around which the phase oscillates. The phase shift is complicated by attenuation within the VO_2 film, which affects the amplitude of interfering waves and thus the resultant reflected phase. As the thickness increases towards the destructive condition (from 120-240 nm), the phase retards and then progresses. As the thickness proceeds to the subsequent constructive condition (> 240 nm), the phase progresses then retards. Subsequent oscillations become smaller due to increasing attenuation as film thickness increases.

In contrast to the $f = 0$ case, at $f = 1$ the VO_2 film acts as a metal and the electric field does not propagate within the film. There are therefore no multiple reflections that could cause interference. Instead the film becomes increasingly opaque up to around 150 nm where reflectance plateaus to around 57%, with the remaining electromagnetic energy absorbed.

As shown in Fig. 52(b), these preliminary results showed a maximum phase shift of around 0.22π rad, much less than the ideal 2π. Nevertheless, it was theorised that VO_2 could affect the phase of the wave to a greater extent by allowing or impeding transmission into the underlying Al_2O_3 and modulating wave interference therein, since the VO_2 / Al_2O_3 / Al structure forms a MIM optical cavity, and resonance within the cavity should produce π rad phase shift.

The downside to this concept is that by basing the phase shift around a resonance condition, the phase gradient necessarily included sections of near-zero reflection; this precludes continuous dynamic beam steering. Due to this, the design was adapted to consist of elements with discrete phase values that straddled those with near-zero reflection. For example, a three-element array can span 2π phase coverage if the phase value of each element is separated by 0.5π rad. In such a design, the available phase range of elements thus only needs to be around 1.34π rad.

Advantages of this design are twofold: (1) avoid areas with very low reflection which would negatively affect the integrity of the wavefront and (2) phase range up to 2π as long as elements cover ~ 1.34π rad. The disadvantage of this method is that since not every phase value within the gradient can be represented, either because the corresponding reflectance is too low or the value does not exist within the available range, beam deflection is not continuous and instead limited to discrete values.

With the goal now being a phase span of 1.34π rad, VO_2 and Al_2O_3 thicknesses were refined through iterative simulations in an attempt to find an optimal configuration where phase shift was maximised and reflection contrast minimised. While not exhaustive, the studies were sufficiently thorough such that no further gain in performance was expected.

The final geometric parameters were the nanowire widths W_1 and W_2. The Al wire width W_2 was set at 500 nm, far below the operating wavelength to avoid unwanted diffraction effects, whilst the 'active element' VO_2 / Al_2O_3 width W_1 was subject to sweeps of the design space to find optimal geometry. The sweeps were performed on a periodic single element stack, with 50 nm gap between elements.

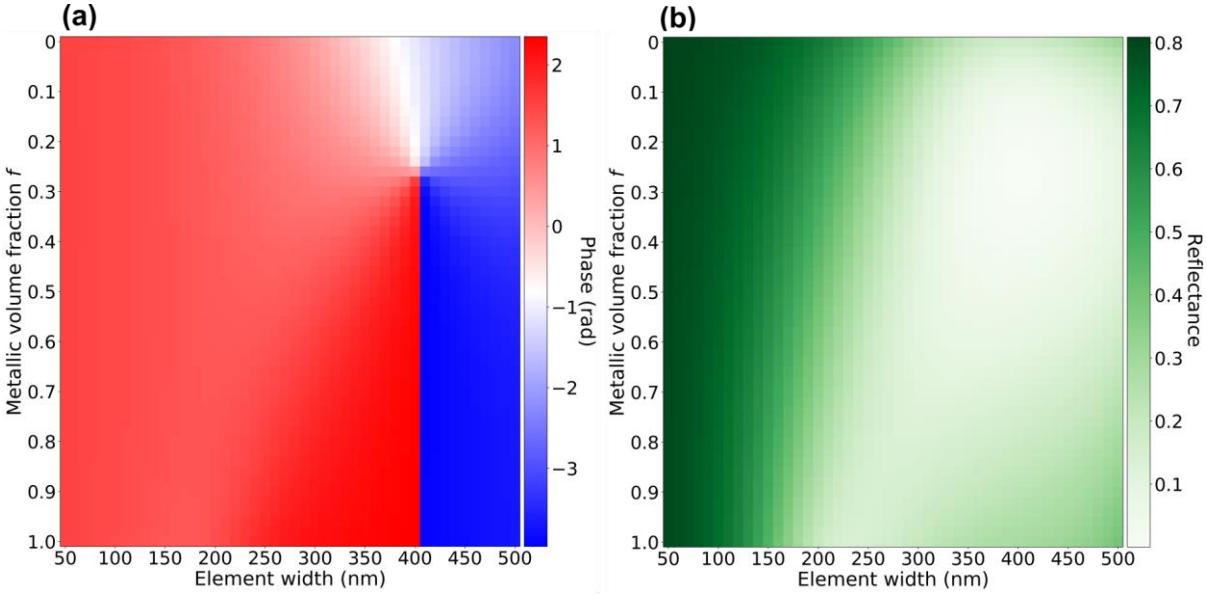

Figure 53. Colour maps used to identify element geometry that satisfied design constraints. 'Active element' (VO_2 and Al_2O_3) width was varied between 50 – 500 nm at 10 nm interval, while keeping Al wire width fixed at 500 nm. (a) Reflected phase as a function of *f* for varied active element width. (b) Reflectance as a function of *f* for varied active element width.

Figure 53 shows colour maps of simulation data that was used to inform the design process. A parametric sweep of active element widths for a single periodic element was performed between 50 – 500 nm at 10 nm interval and reflected phase and reflectance as a function of metallic volume fraction was evaluated for each iteration. The phase and reflectance were evaluated from S11 parameter at a port boundary 835 nm above the top VO_2 interface. Fig. 53 (a) shows that the maximum phase shift over a single element was ~ 1.09π rad, at an active element width W_1 = 400 nm and this width was chosen for subsequent simulations. As mentioned previously, ideal design constraints were a phase span of 2π for dynamic beam steering or a minimum of 1.34π rad for discrete deflection, and individual element phase values spaced evenly with less than 50% reflectance contrast between two adjacent elements. Figure 53 shows that neither the phase span nor reflectance constraints were met and attempts to improve these features through iterative simulations met with little success. A successful design was however

identified for a polarisation factor $s = 1$ with a phase span ~ 1.35π rad, the results of which are shown in Appendix A10, but this value was found to be unjustified in terms of the VO_2 model used.

With a maximum phase span of 1.09π rad, a periodic array was no longer possible, however a discrete array of elements could still be capable of some degree of beam deflection. To investigate this, an electromagnetic simulation of an 8-element array was performed, with parameters informed by previous results.

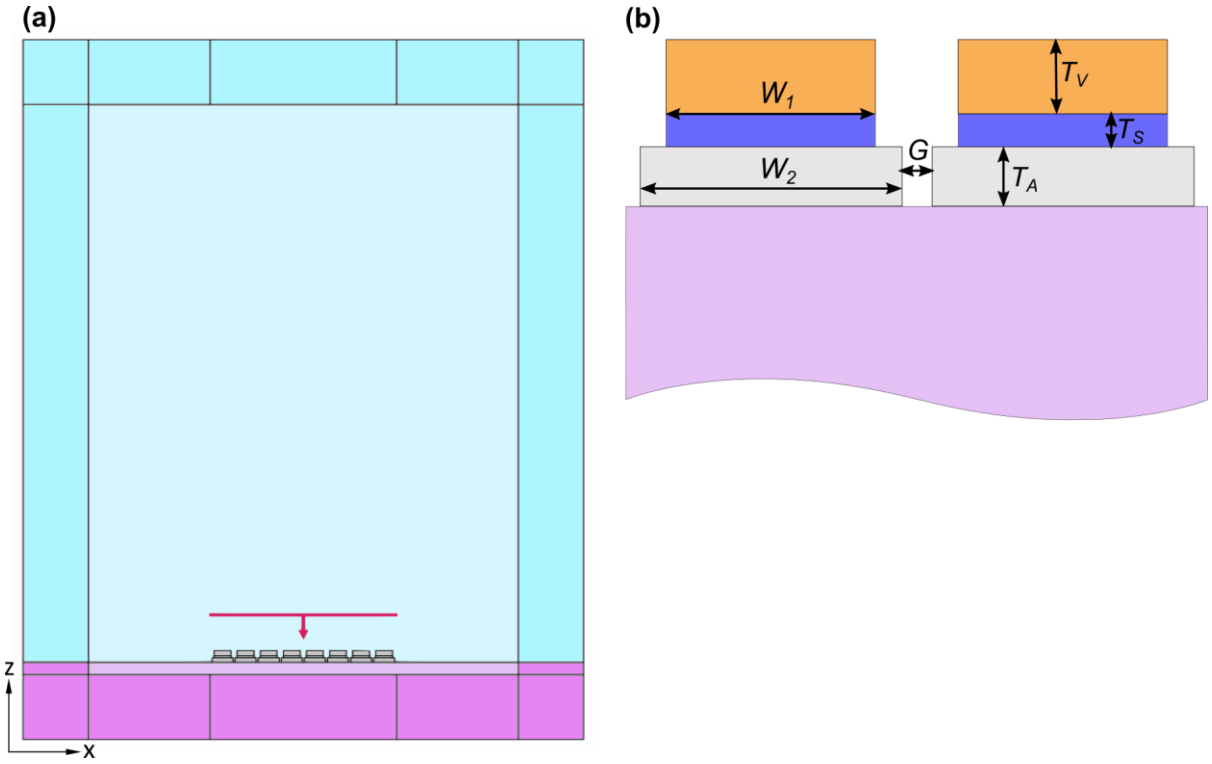

Figure 54. Setup for electromagnetic simulation of an 8-element array. (a) The array is bounded by air above and silicon substrate below. Lighter shades denote 'real' domains, whilst darker shades are perfectly matched layer (PML) domains, to which scattering boundaries are applied at the external faces. The input wave is x-polarised and the horizontal red line and vertical arrow denote the incident port and wave vector, respectively. (b) Element schematic with indicated dimensions as follows: W_1 = 400 nm, W_2 = 500 nm, T_v = 125 nm, T_s = 55 nm, T_A = 100 nm and G = 50 nm.

The aperiodic array was simulated according to the schematic in Fig. 54 in order to display the reflected wavefront. In contrast to periodic arrays where the domain is bounded by periodic conditions on side boundaries, the domain of interest here is wrapped in PML and scattering boundaries to absorb scattered waves. The electromagnetic and thermal properties of the materials used in simulation are given in Appendix A8.

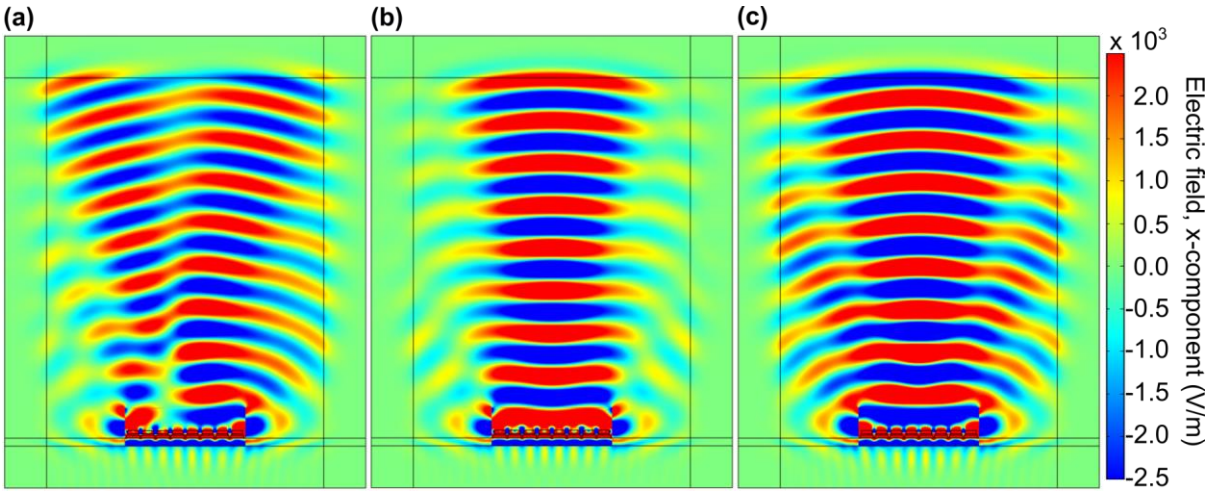

Figure 55. Electric field, x-component for (a) *f = 0-1* evenly spaced gradient (b) *f = 0* and (c) *f* = 1. The region immediately below the port and surrounding the array (Fig 54) has had incident field subtracted so that only the scattered field is shown. This was done to clearly show the reflected wave but its implementation does lead to some discrepancy in the appearance of the Ex plot around this area.

Figure 55 (a) for elements evenly spaced in *f* shows that although the array is capable of deflecting the array from the normal, the wavefront splits in opposite directions and is more representative of a diverging cone. In principle, matching the refractive index of array end elements with the adjacent substrate could help wavefront integrity but the poor performance seen here is most likely due to the contrast in reflectance between elements constituting the phase gradient. As previously discussed, the reflectance contrast is a consequence of using the resonance condition to maximise phase shift. Figure 55 (b) shows close-to-normal reflection when all elements are at $f = 0$ and (c) shows a more diverging cone with multiple side lobes, possible as a result of index mismatch at the end elements. Unfortunately, none of these configurations are particularly useful for a potential device.

Regardless of the failure of this particular design, the success of polarisation factor 1 shows that similar principles may be utilised, perhaps using a different combination of materials or geometries, to create a successful beam steering platform. Therefore, thermal simulations were conducted to investigate the feasibility of an array of individually-addressable nanoscale elements that would each need to be maintained at a specific temperature in order to create the necessary phase gradients.

7.5 Heat transfer simulations

The feasibility of such an array can be judged in terms of its ability to maintain a distinct temperature for each element within the array, since the temperature is what defines the metallic volume fraction, thus phase response, of each element. For this, the key considerations are thermal crosstalk and intra-element temperature variation across the VO_2 layer. Heat transfer simulations were performed for an 8-element array with no trenches and repeated for an array with 1 μm deep trenches between the elements.

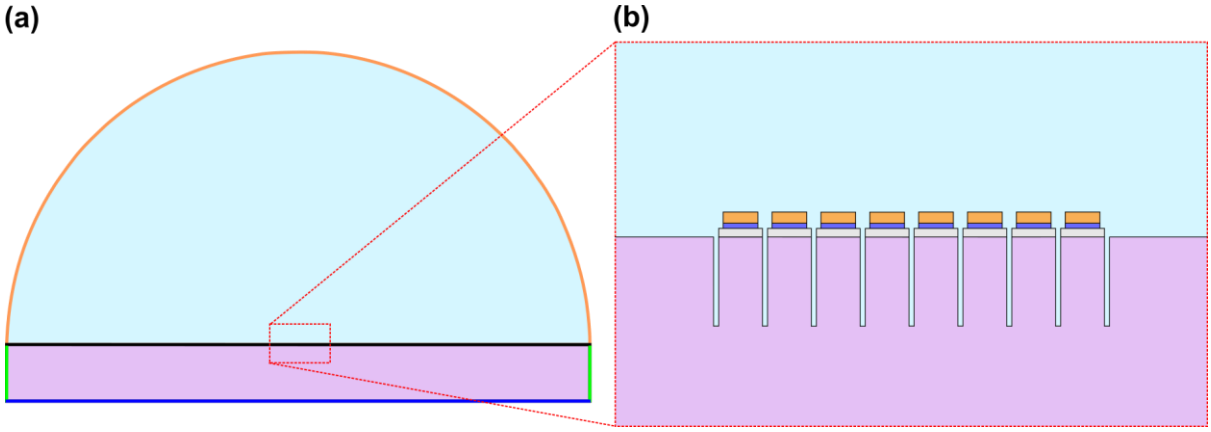

Figure 56. Setup for thermal simulation of an 8-element array. (a) Extent of the simulation domain following geometric convergence testing; radius of air domain 1.5 mm, substrate depth 0.3 mm (corresponding to commercially available thin Si wafer). The external boundary conditions are as follows: air (orange): convective heat flux, green (Si sides): convective heat flux, blue (Si bottom): fixed temperature boundary 293.15 K.

Figure 56 shows a schematic of the simulation domain and array, including 1 μm trenches between each element. Note that the extents of the domain (aside from substrate depth) merely approximate an infinite external domain and do not necessarily reflect the size of the physical device per se. Justifying the simulated domain size in terms of the adequacy of approximation is established by geometric convergence testing. The concept is that for thermal systems, the distance between heat source and external boundary has a significant effect, but beyond some defined region one should expect little change in the solution. The thermal gradient is strongly related to the separation between heat source and external boundaries, thus affecting the solution within the area of interest, and this effect reduces with increasing separation. The aim of geometric convergence testing is to identify the separation distance at which the solution no longer changes. This point is considered to be when the 'relative error' of the solution exceeds the 'relative tolerance' of the FEM solver. The relative tolerance was kept at a default value of 0.001 and relative error in maximum temperature T_{max} within the domain was evaluated by taking the absolute value of $(T_{max} - T_{min}) / T_{min}$ for each geometry iteration. Appendix A9 shows that the solution converges by 1.5 mm which was chosen as the domain size. The blue (Si bottom) boundary in Fig. 56(a) was assigned a fixed temperature of 293.15 K, representing a room temperature heat sink, whilst the air (orange) and green (Si side) boundary conditions were set as convective heat flux. The heat transfer coefficient *h* at the air boundary was set as 10 $W/m^2 \cdot K$, a standard value for air boundaries, whilst for the Si side boundaries, *h* was automatically calculated for a 0.3 mm vertical wall.

Element number	Metallic volume fraction *f*	Goal temperature (°C)	Mean temp, no trench [hs1] (°C)	Mean temp, trench [hs2] (°C)	Mean temp, no trench [hs2] (°C)
1	0	< 60	65.2	60.3	62.6
2	0.14	71.2	67.5	70.9	66.6
3	0.29	73.1	71.1	72.9	68.7
4	0.43	74.5	74.4	73.8	69.9
5	0.57	75.7	77.6	74.9	71.0
6	0.71	77.0	80.5	76.9	72.0
7	0.86	79.0	83.6	79.0	72.8
8	1	86.9	89.7	87.4	73.3

Element number	Heat Source setting 1 [hs1] (W)	Heat Source setting 2 [hs2] (W)
1	0	0
2	0	410
3	200	395
4	300	365
5	400	372
6	475	440
7	500	532
8	2150	1045

Figure 57. Simulation inputs (heat source settings) and outputs (mean temperature) for each element. Heat source settings were manually adjusted to achieve the required 'goal temperature' corresponding to a specific metallic volume fraction for each element.

Heat sources were defined on the Al wire domains, which provided heat flow into the system. The heat source powers were set assuming the default out-of-plane wire length of 1 m. These values were manually selected by iteration to try to achieve the required temperatures in the VO_2 layer as per the previously calculated fraction vs 'goal temperature' data. The three rightmost columns in Fig. 57 above show the simulated mean temperature of each element for each of the cases shown in Fig. 58. By comparing the 'goal temperature' to each of these columns it is clear that the trench case is the closest to satisfying the temperature, and thus volume fraction, constraints. In both cases of no trench, the main difficulty lies in reconciling the relatively low $f = 0$ temperature of 60°C with the higher temperatures of adjacent elements. As evidenced in the subsequent figures, this is due to high thermal crosstalk, which is reduced in the case of trenches.

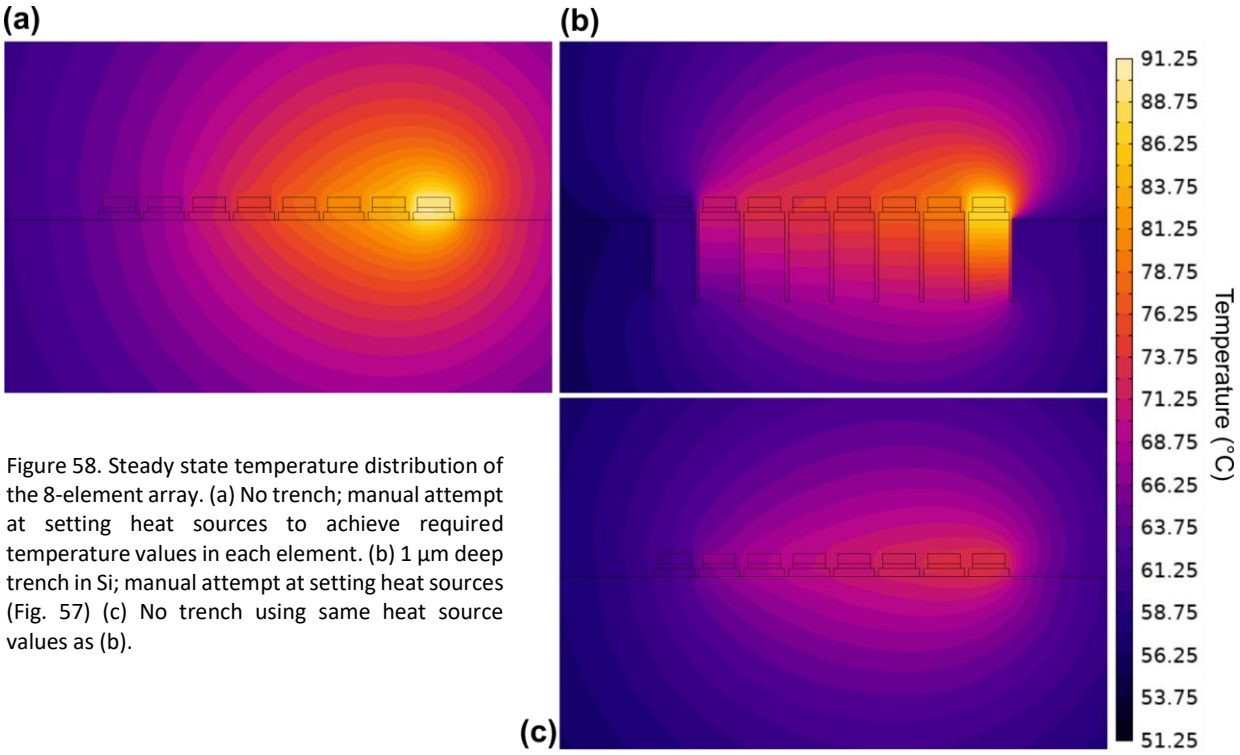

Figure 58. Steady state temperature distribution of the 8-element array. (a) No trench; manual attempt at setting heat sources to achieve required temperature values in each element. (b) 1 μm deep trench in Si; manual attempt at setting heat sources (Fig. 57) (c) No trench using same heat source values as (b).

Figure 58 shows the simulated steady state temperature distributions. Immediately noticeable is the difference between (a), with no trenches, and (b), with 1 μm trenches, vis-à-vis the degree of anisotropy in the temperature gradient, with mostly radial distribution for the no trench case and more vertical distribution for the trench case. Indeed, in the column of substrate beneath each element, the temperature gradient is completely vertical. The temperature difference ΔT between the element extrema is more pronounced in the trench case and VO_2 elements in (b) are more clearly isothermal i.e. there is less variation. When (b) is directly compared to (c) i.e. the same heat source powers are used, it is obvious that less power is required to maintain the gradient in the trench case.

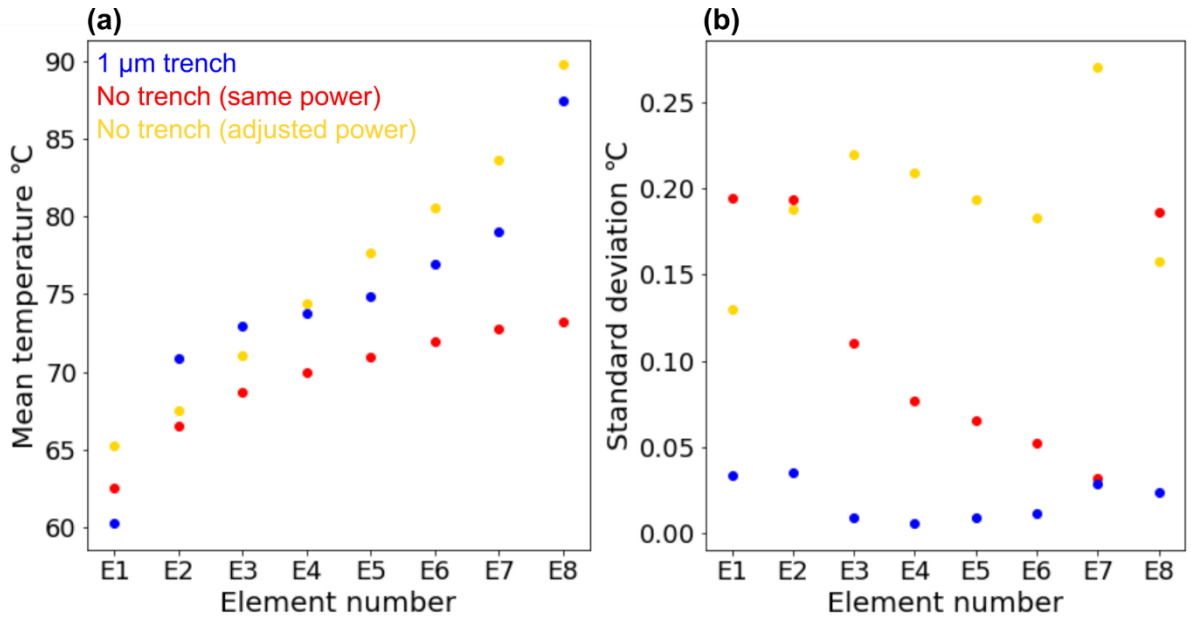

Figure 59. (a) Mean temperature and (b) standard deviation in temperature for each element in the array. Temperature is evaluated in horizontal slices through the midpoint of the VO_2 layer. Coloured dots represent no trench with manually adjusted values (as per Fig. 58 (a)), 1 m trench (as per Fig. 58 (b)), and no trench with the same heat source values as the trench case (as per Fig. 58 (c)).

Figure 59 (a) shows the mean temperature values for slices cut horizontally across the mid-plane of the VO_2 layer in each element. Although the heat source powers were selected manually, it is clear between the yellow and blue points that it is easier to maintain elements at their required temperature and keep a greater separation in temperatures between element extrema. Whereas ΔT between element extrema is around 28.5°C for Fig. 58 (a), in Fig. 58 (b) it is 24.5°C and for Fig. 58 (c) ΔT is only 8.75°C. From Fig. 59 (b), it is evident that the variation of temperature within each VO_2 element is minimised when trenches are present. Intra-element variation is important because f changes so abruptly with temperature during the transition and it is possible that this would entail a difference in expected phase output and thus negatively affect wavefront integrity. The main effect of trenches as shown in these figures is therefore the reduction in thermal crosstalk, or direct heat flux between adjacent elements. This observed effect is attributed to the large difference in thermal conductivity between air and Si (0.024 vs 149 W/[m˙K]). The introduction of air in the trenches forces a more vertical temperature gradient as the heat preferentially flows through the remaining Si, and after the trench bottom, the distribution becomes more radial again. The trenches also appear to keep more energy contained within each element, making the trench design more power efficient. The total sum of the heat source powers in the table of Fig. 57 indicates that the trench design consumes 22% less power than the non-trench design, with a total of 3559 W and 4025 W, respectively. Note that this is not indicative of physical array power consumption as the simulation is scaled to a wire unit length of 1 m as previously mentioned.

7.5 Analysis

As discussed in Chapter 3, heat flux within the domain was modelled solely as conduction. Convection within the domain was assumed negligible due to low Péclet number ~1 but was used on external boundaries. However, radiation was not also not modelled and recent literature suggests it could have a significant effect on heat transfer at the nanoscale i.e. between individual elements. Although this decision was taken in order to reduce complexity and avoid unwarranted assumptions, radiation should be considered in further work to provide a more complete approximation, especially in designs incorporating nanometer gap-sizes. In addition, only temperature-independent material properties were used and although the temperature-dependent properties do not change a great deal over the range studied, a fully integrated electromagnetic / heat transfer simulation should also take this into account. Other factors have not been included that could have potential significance are the latent heat of VO_2 transition and interface thermal resistance aka Kapitza resistance.

In the thermal simulations, it may be noted that the domain size is several orders of magnitude larger than the array, or region of interest. A more efficient method would be to truncate the domain; in COMSOL this might be achieved by using the 'Infinite Element Domain' (IED). However, issues arose during implementation and since the simulation was 2D heat transfer, the full-size simulation was considered sufficiently low on resources and justified for this purpose.

The thermal distributions in Fig. 58 were calculated using manually chosen values for heat source power, a tedious and unreliable process which grows exponentially more difficult as the number of elements increases. Nelder-Mead optimisation as described in Chapter 3 was used successfully to select power values in lieu of manual selection for the design in Appendix A10 which had a limited number of heated elements within the array to be solved for. The design in Fig. 58 however required all eight elements to be optimised for, which proved too difficult for the optimisation method. Further work should employ a reliable optimisation algorithm for such problems. The vast majority of the simulation work in this thesis was done by iteration and manual selection, but more exhaustive sweeps of the parameter spaces could likely be achieved by using optimisation and machine learning algorithms.

Finally, some other factors which could further minimise thermal crosstalk and could be investigated in further work include the use of vacuum, reducing the distance between heat source and sink, increasing the inter-element gap size, and using higher thermal conductivity substrate. Time-dependent simulations could also be investigated to optimise such a design for switching speed.

Chapter 8

8.1 Summary of conclusions

To conclude, the main findings of each project will be summarised. Chapter 4 demonstrated photodetection between 400 and 900 nm using plasmon-assisted resistivity change in VO_2. Localised surface plasmon resonance in silver nanorods was identified at 650 nm by a dip in transmission of around 30 %. The experimental transmission spectra were approximated by finite element method simulations using permittivity models for the materials. The permittivity of VO_2 was calculated using the Maxwell Garnett effective medium approximation, where the greatest correlation between experiment and simulation was found when the volume fraction of metallic inclusions was 80 %. By sampling resistivity at a number of wavelengths, a rough correlation was found between the resonance wavelength and a ~0.03 Ωcm resistivity dip across the VO_2 film. The proposed explanation is that Ag plasmonic nanostructures grown on top of VO_2 film increase heat generation via the excitation of localised surface plasmon resonance and consequently suppress its resistivity. The degree of heating, and so the change in resistivity, depends on the strength of the resonance, which can be tuned in-situ by controlling the wavelength and polarisation of incident light. The nanorod array introduced a certain degree of wavelength and polarisation sensitivity to bolometric photodetection. As plasmonic nanostructures can facilitate advanced control over light, this work can lead to the development of multi-functional, VO_2-based plasmonic microbolometers.

Chapter 5 demonstrated a reversible method for tuning the effective phase transition temperature of VO_x films in the range 2 – 16 μm. Gold nanorods embedded in vanadium oxide thin films support localised surface plasmon resonances, in turn generating thermal energy that is highly localised and inhomogeneous. This heating led to suppression of the phase transmission temperature by up to 4°C. Interestingly, experimental ΔT_{eff} was shown to be up to five times higher than predicted by theoretical analysis, which may suggest that in addition to the thermoplasmonic effect other mechanisms, such as hot electron injection, may have a significant role. The change in effective phase transition temperature was measured at the macroscopic scale and analysed based on the effective medium principle. The degree of suppression depends on nanorod density and polarisation of the incident light, making it both controllable and reversible. The degree of suppression may be further increased by utilising more advanced nanostructures and different materials **[203-206]**. This work shows a new way of controlling macroscopic material properties through thermal nano-engineering.

In Chapter 6, the importance of hysteresis analysis for phase change materials in novel device design was addressed. A phenomenological approach to describing electromagnetic hysteresis in such materials was proposed based on the Maxwell Garnett effective medium theory. The modified equations

potentially provide an extremely simple method for predicting the hysteretic behaviour of phase change materials using only the complex permittivity of each pure phase and the volume fraction of the metallic medium. Using the modified equations, the complex permittivity of VO_2 at several intermediate volume fractions was calculated from 1 – 12 μm. An interesting finding is that the permittivity of intermediate phases are not necessarily within the bounds of the pure phase values, an effect which becomes more pronounced at longer wavelengths. Reflection spectra, calculated using Fresnel equations, suggest that the degree of reflection is very sensitive to both VO_2 film thickness and pure phase permittivity. These are among the challenges that would need to be addressed experimentally in order to validate the theoretical model.

Finally, Chapter 7 investigated the potential for VO_2 as an active element in a metasurface phased reflectarray designed to control the deflection angle of an incident infrared beam. Ultimately, the design concept of using VO_2 to modulate an Al_2O_3 optical cavity failed to produce a design that could steer or deflect an incident beam. The ideal 2π or minimum 1.34π rad phase modulation was not achieved, with the final design achieving 1.09π rad. Furthermore, the use of cavity resonance and requirement of an array evenly-spaced in *f* meant that reflectance contrast was high. This led to poor wavefront integrity and failure of the design to deflect in a single direction. However, a successful design was demonstrated by changing the polarisation factor from 1/3 to 1 in the Looyenga model used for VO_2. This suggests that the design process and concept could work, perhaps by using a different combination of materials or geometries that have not been investigated. Subsequent thermal simulations of the same design suggest that thermal isolation, by means of trenches etched into the substrate between elements, can potentially improve the performance of such designs in terms of less power consumption and less intra-element temperature variation.

8.2 Future work

The investigations into plasmonically enhanced microbolometers could be extended to multispectral sensing. Multispectral refers to the detection of a small number of narrow spectral bands. Detection of multiple wavelength signatures has obvious applications in defence. 'Dual-band' imaging, using mid-wave (MWIR) and long-wave infrared (LWIR) was found to be superior to single-band imaging for vehicle tracking **[207]**; MWIR produces better images of hot objects such as engines whilst LWIR images better in adverse environmental conditions such as fog or smoke **[208]**. Land mine activity can be detected by imaging and contrasting areas of soil at two wavelengths where 10.4 μm corresponds to undisturbed soil and 9.3 μm to disturbed soil **[209]**. Detection of both body and plumage of ballistic missiles can be achieved using multispectral MWIR and LWIR detectors **[210]**. Multispectral imaging is widely used in space-based technologies such as Earth observation telescopes, for example Landsat 8 images 11 spectral bands, allowing distinct detection of features such as minerals, vegetation, aerosols, thermal sources and clouds **[211]**. Multispectral imagers have also been used to identify

distinct chemical substances such as inks, pigments and varnishes, as well as obscured features and undertext in historical documents and artwork **[212, 213]**. Applications where low-cost multispectral imaging might be beneficial include agriculture, security, biomedical imaging, security and industry.

Multispectral refers to the detection of a small number of narrow spectral bands, as opposed to panchromatic, which refers to detection of a wide, continuous spectral region. Panchromatic sensors detect total radiation intensity on each pixel and since the dissipated power is integrated over a wide spectral range, the signal is large. The high signal to noise ratio allows smaller detectors to be used, enabling high resolution imaging. However, pixel output is in greyscale; there is no differentiation between the wavelength signatures of different sources. In contrast, the narrow bands detected by multispectral sensors give the ability to distinguish between sources but correspond to a relatively low power dissipation. Pixels thus need to be larger to compensate, at the expense of spatial resolution. In high end platforms such as Earth observation satellites, this is overcome by panchromatic sharpening, where the higher resolution panchromatic images are combined with lower resolution multispectral images in postprocessing. However, this obviously requires separate detectors and postprocessing which adds expense and limitations e.g. real time imaging. Even without panchromatic detectors, multispectral sensing requires multiple detectors or filters to detect distinct bands.

The aim of plasmonic multispectral sensing is therefore to 1.) remove the need for filters or separate detectors; instead a focal plane array might consist of 2 - 3 regions of pixels, each region with different nanostructure geometry corresponding to its distinct target wavelength; 2.) enhance absorption at target wavelengths, giving higher signal-to-noise ratio. This would allow smaller pixels, thereby improving spatial resolution. This could be optimised further by incorporating the optical cavity design common in modern bolometers with the plasmonic structures to form a plasmonic 'perfect absorber'. Maier and Brueckl (2010) **[50]** demonstrated multispectral microbolometers with this type of design, consisting of 50 nm thick conductive silicon film sandwiched between plasmonic resonators and an aluminium mirror. They observed absorption peaks of up to 88% between 2.9 and 7.7 μm. The spectral range was tuned by varying the lateral dimensions of the absorber elements; multispectral sensing was thus demonstrated using a number of resonator widths between 0.6 and 2.1 μm. The absorption peak red-shifted by up to 5 μm with increasing absorber width. They also noted that the metallic mirror affected heat conduction, leading to faster response times. In VO_x based bolometers, plasmon-enhanced absorption may additionally enable lower thermal mass VO_x films, further improving response time. If successful, these features would enhance microbolometer performance and utility, thus broadening the low-cost photodetector market.

Various avenues for future work in terms of simulation and design optimisation were suggested at the end of Chapter 7, however another major avenue the author was not able to explore was the experimental validation of thermal simulation results. Specifically, the temperature and thermoelectric

properties of nanowire arrays could be measured, perhaps using a similar technique to Shin (2014) **[214]**. This could also be performed as part of an investigation into the radiative contribution to heat transfer at the nanoscale, since this is a topic of great importance in nanoscale device design. With regards to future work in metasurface arrays, the findings presented here indicate that different combination of materials or an improved design are required for successful dynamic beam steering. This is a promising field because it appears that the current technology suffers from significant drawbacks, and the potential for disruptive innovation, such as LiDAR for automata, is high.

References

1. Cavalleri A, Dekorsy T, Chong HHW, Kieffer JC, and Schoenlein RW. *Evidence for a structurally-driven insulator-to-metal transition in VO2: A view from the ultrafast timescale.* Physical Review B, 70(16): 161102, **2004**.
2. Lysenko S, Zhang G, Vikhnin V, Rua A, Fernandez F, and Liu H. *Nonlinear optical dynamics during phase transition in vanadium dioxide.* MRS Online Proceedings Library (OPL), 888, **2005**.
3. Abdollahramezani S, Hemmatyar O, Taghinejad H, Krasnok A, Kiarashinejad Y, Zandehshahvar M, Alù A, and Adibi A. *Tunable nanophotonics enabled by chalcogenide phase-change materials.* Nanophotonics, 9(5): 1189-1241, **2020**.
4. Morales-Sánchez E, Prokhorov EF, Mendoza-Galván A, and González-Hernández J. *Determination of the glass transition and nucleation temperatures in Ge2Sb2Te5 sputtered films.* Journal of Applied Physics, 91(2): 697-702, **2002**.
5. Ostrooumov M and Taran Y. *Vanadium, V–a new native element mineral from the Colima volcano, State of Colima, Mexico, and implications for fumarole gas composition.* Mineralogical Magazine, 80(2): 371-382, **2016**.
6. Lide DR. *Abundance of elements in the Earth's crust and in the sea.* CRC Handbook of Chemistry and Physics, Internet version: 14-17, **2005**.
7. Sjoberg SG. *Nils Gabriel Sefstrom and the discovery of vanadium.* Journal of Chemical Education, 28(6): 294, **1951**.
8. Alchemist-hp (Wiki Commons Contributor). *Vanadium crystal bar and 1cm3 cube.jpg*. Wikimedia Commons, the free media repository, **2011**. Available from: https://commons.wikimedia.org/w/index.php?title=File:Vanadium_crystal_bar_and_1cm3_cube.jpg&oldid=472664340 [Accessed 29.06.2021].
9. Schläfli D. *Vanadinite.jpg*. **2006**. Available from: https://www.mindat.org/photo-62811.html [Accessed 29.06.2021].
10. Lavinsky R. *Mottramite-174237.jpg*. Wikimedia Commons, the free media repository, **2010**. Available from: https://commons.wikimedia.org/w/index.php?title=File:Mottramite-174237.jpg&oldid=490684667 [Accessed 29.06.2021].
11. Lavinsky R. *Cavansite-indi-12a.jpg*. Wikimedia Commons, the free media repository, **2010**. Available from: https://commons.wikimedia.org/w/index.php?title=File:Cavansite-indi-12a.jpg&oldid=491815109 [Accessed 29.06.2021].
12. Samsonov G. *Mechanical properties of the elements*, in *Handbook of the Physicochemical Properties of the Elements*. Springer, 387-446, **1968**.
13. Moskalyk R and Alfantazi A. *Processing of vanadium: a review.* Minerals Engineering, 16(9): 793-805, **2003**.
14. Katzke H, Tolédano P, and Depmeier W. *Theory of morphotropic transformations in vanadium oxides.* Physical Review B, 68(2): 024109, **2003**.
15. Liu M, Su B, Tang Y, Jiang X, and Yu A. *Recent advances in nanostructured vanadium oxides and composites for energy conversion.* Advanced Energy Materials, 7(23): 1700885, **2017**.
16. Goodenough JB. *The two components of the crystallographic transition in VO2.* Journal of Solid State Chemistry, 3(4): 490-500, **1971**.
17. Lee S, Ivanov IN, Keum JK, and Lee HN. *Epitaxial stabilization and phase instability of VO 2 polymorphs.* Scientific Reports, 6(1): 1-7, **2016**.
18. Eyert V. *The metal ‐ insulator transitions of VO2: A band theoretical approach.* Annalen der Physik, 11(9): 650-704, **2002**.
19. Morin F. *Oxides which show a metal-to-insulator transition at the Neel temperature.* Physical Review Letters, 3(1): 34, **1959**.

20. Qazilbash MM, Brehm M, Chae B-G, Ho P-C, Andreev GO, Kim B-J, Yun SJ, Balatsky A, Maple M, and Keilmann F. *Mott transition in VO2 revealed by infrared spectroscopy and nano-imaging.* Science, 318(5857): 1750-1753, **2007**.
21. Mott NF. *The basis of the electron theory of metals, with special reference to the transition metals.* Proceedings of the Physical Society. Section A, 62(7): 416, **1949**.
22. Mott NF. *Metal-insulator transition.* Reviews of Modern Physics, 40(4): 677, **1968**.
23. Adler D. *Mechanisms for metal-nonmental transitions in transition-metal oxides and sulfides.* Reviews of Modern Physics, 40(4): 714, **1968**.
24. Haverkort MW, Hu Z, Tanaka A, Reichelt W, Streltsov S, Korotin M, Anisimov V, Hsieh H, Lin H-J, and Chen C. *Orbital-assisted metal-insulator transition in VO 2.* Physical Review Letters, 95(19): 196404, **2005**.
25. Wentzcovitch RM, Schulz WW, and Allen PB. *VO 2: Peierls or Mott-Hubbard? A view from band theory.* Physical Review Letters, 72(21): 3389, **1994**.
26. Huang X, Yang W, and Eckern U. *Metal-insulator transition in VO2: a Peierls-Mott-Hubbard mechanism.* arXiv preprint cond-mat/9808137, **1998**.
27. Shao Z, Cao X, Luo H, and Jin P. *Recent progress in the phase-transition mechanism and modulation of vanadium dioxide materials.* NPG Asia Materials, 10(7): 581-605, **2018**.
28. Jeong J, Aetukuri N, Graf T, Schladt TD, Samant MG, and Parkin SS. *Suppression of metal-insulator transition in VO2 by electric field–induced oxygen vacancy formation.* Science, 339(6126): 1402-1405, **2013**.
29. Gao Y, Luo H, Zhang Z, Kang L, Chen Z, Du J, Kanehira M, and Cao C. *Nanoceramic VO2 thermochromic smart glass: A review on progress in solution processing.* Nano Energy, 1(2): 221-246, **2012**.
30. Wuttig M, Bhaskaran H, and Taubner T. *Phase-change materials for non-volatile photonic applications.* Nature Photonics, 11(8): 465-476, **2017**.
31. Zhang Q, Zhang Y, Li J, Soref R, Gu T, and Hu J. *Broadband nonvolatile photonic switching based on optical phase change materials: beyond the classical figure-of-merit.* Optics Letters, 43(1): 94-97, **2018**.
32. Benkahoul M, Chaker M, Margot J, Haddad E, Kruzelecky R, Wong B, Jamroz W, and Poinas P. *Thermochromic VO2 film deposited on Al with tunable thermal emissivity for space applications.* Solar Energy Materials and Solar Cells, 95(12): 3504-3508, **2011**.
33. Hadfield RH. *Single-photon detectors for optical quantum information applications.* Nature Photonics, 3(12): 696-705, **2009**.
34. Kats MA, Blanchard R, Genevet P, Yang Z, Qazilbash MM, Basov D, Ramanathan S, and Capasso F. *Thermal tuning of mid-infrared plasmonic antenna arrays using a phase change material.* Optics Letters, 38(3): 368-370, **2013**.
35. Zhu Z, Evans PG, Haglund Jr RF, and Valentine JG. *Dynamically reconfigurable metadevice employing nanostructured phase-change materials.* Nano Letters, 17(8): 4881-4885, **2017**.
36. Hashemi MRM, Yang S-H, Wang T, Sepúlveda N, and Jarrahi M. *Electronically-controlled beam-steering through vanadium dioxide metasurfaces.* Scientific Reports, 6(1): 1-8, **2016**.
37. Wang Q, Yuan G, Kiang K, Sun K, Gholipour B, Rogers E, Huang K, Ang S, Zheludev NI, and Teng J. *Reconfigurable phase-change photomask for grayscale photolithography.* Applied Physics Letters, 110(20): 201110, **2017**.
38. Maaza M, Nemraoui O, Sella C, and Beye A. *Surface plasmon resonance tunability in Au− VO 2 thermochromic nano-composites.* Gold Bulletin, 38(3): 100-106, **2005**.
39. Hartmann R and Selders M. *High-sensitivity thin-film bolometers.* Sensor'82- Sensor technology and temperature measurement: 102-116, **1982**.
40. Liddiard K. *Thin-film resistance bolometer IR detectors.* Infrared Physics, 24(1): 57-64, **1984**.
41. Liddiard K. *Thin-film resistance bolometer IR detectors—II.* Infrared Physics, 26(1): 43-49, **1986**.
42. Sch (Wiki Commons Contributor). *BlackbodySpectrum loglog 150dpi en.png*. **2006**. Available from: https://commons.wikimedia.org/wiki/File:BlackbodySpectrum_loglog_150dpi_en.png [Accessed 29.06.2021].

43. Wood L. *Research and Markets: Global Microbolometer Market 2015-2019: Material, Format Type, Application and Geography*. Business Wire, **2015**. Available from: https://www.businesswire.com/news/home/20150505006680/en/Research-and-Markets-Global-Microbolometer-Market-2015-2019---Material-Format-Type-Application-and-Geography [Accessed 29.06.2021].
44. Robert J. *Uncooled IR sensing market: a virtuous cycle*. Extracted from: Uncooled Infrared Imagers and Detectors report, Yole Développement, 2019 edition. Yole Développement, **2019**. Available from: http://www.yole.fr/UncooledIR_MarketUpdate.aspx [Accessed 29.06.2019].
45. Xenics. *MWIR & LWIR cooled cores*. Xenics Infrared Solutions, **2019**. Available from: http://www.xenics.com/en/application/mwir-lwir-cooled-cores [Accessed 05.05.2019].
46. EO-IRsystems. *Uncooled VOx FPA Infrared Thermal Imaging Module for Ground Surveillance*. Wuhan Joho Technology Company LTD, Available from: https://www.eo-irsystems.com/sale-7867634-uncooled-vox-fpa-infrared-thermal-imaging-module-for-ground-surveillance.html [Accessed 05.05.2019].
47. Yon J-J, Mottin E, Biancardini L, Letellier L, and Tissot J. *Infrared microbolometer sensors and their application in automotive safety*, in *Advanced Microsystems for Automotive Applications 2003*. Springer, 137-157, **2003**.
48. Kohin M and Butler NR. *Performance limits of uncooled VOx microbolometer focal plane arrays*, in *Infrared Technology and Applications XXX*. International Society for Optics and Photonics **2004**.
49. Niklaus F, Vieider C, and Jakobsen H. *MEMS-based uncooled infrared bolometer arrays: a review*, in *MEMS/MOEMS technologies and applications III*. International Society for Optics and Photonics **2008**.
50. Maier T and Brueckl H. *Multispectral microbolometers for the midinfrared.* Optics Letters, 35(22): 3766-3768, **2010**.
51. Li C, Skidmore GD, Howard C, Han C, Wood L, Peysha D, Williams E, Trujillo C, Emmett J, and Robas G. *Recent development of ultra small pixel uncooled focal plane arrays at DRS*, in *Infrared Technology and Applications XXXIII*. International Society for Optics and Photonics **2007**.
52. Maier T and Brückl H. *Wavelength-tunable microbolometers with metamaterial absorbers.* Optics Letters, 34(19): 3012-3014, **2009**.
53. Schott JR. *Fundamentals of polarimetric remote sensing*. Vol. 81. SPIE press. **2009**.
54. Palenskis V and Maknys K. *Nature of low-frequency noise in homogeneous semiconductors.* Scientific Reports, 5(1): 1-7, **2015**.
55. Unold T and Cohen JD. *Electronic mobility gap structure and the nature of deep defects in amorphous silicon-germanium alloys grown by photo-CVD.* Journal of Non-crystalline Solids, 164: 23-26, **1993**.
56. Voshell A, Dhar N, and Rana MM. *Materials for microbolometers: vanadium oxide or silicon derivatives.* Image Sensing Technologies: Materials, Devices, Systems, and Applications IV, 10209: 102090M, **2017**.
57. Reintsema CD, Grossman EN, and Koch JA. *Improved VO2 microbolometers for infrared imaging: operation on the semiconducting-metallic phase transition with negative electrothermal feedback.* Infrared Technology and Applications XXV, 3698: 190-200, **1999**.
58. Saint-Pé O, Dubet D, Duthil P, Pope TD, and Jerominek H. *Uncooled focal plane array for thermal observation of the Earth*, in *Infrared Technology and Applications XXIV*. International Society for Optics and Photonics **1998**.
59. Chen C, Yi X, Zhang J, and Zhao X. *Linear uncooled microbolometer array based on VOx thin films.* Infrared Physics & Technology, 42(2): 87-90, **2001**.
60. Fan L, Chen Y, Liu Q, Chen S, Zhu L, Meng Q, Wang B, Zhang Q, Ren H, and Zou C. *Infrared response and optoelectronic memory device fabrication based on epitaxial VO2 film.* ACS Applied Materials & Interfaces, 8(48): 32971-32977, **2016**.
61. Joushaghani A, Jeong J, Paradis S, Alain D, Aitchison JS, and Poon JK. *Wavelength-size hybrid Si-VO 2 waveguide electroabsorption optical switches and photodetectors.* Optics Express, 23(3): 3657-3668, **2015**.

62. Wu JM and Chang WE. *Ultrahigh responsivity and external quantum efficiency of an ultraviolet-light photodetector based on a single VO2 microwire.* ACS Applied Materials & Interfaces, 6(16): 14286-14292, **2014**.
63. Dicken MJ, Aydin K, Pryce IM, Sweatlock LA, Boyd EM, Walavalkar S, Ma J, and Atwater HA. *Frequency tunable near-infrared metamaterials based on VO 2 phase transition.* Optics Express, 17(20): 18330-18339, **2009**.
64. Lei DY, Appavoo K, Ligmajer F, Sonnefraud Y, Haglund Jr RF, and Maier SA. *Optically-triggered nanoscale memory effect in a hybrid plasmonic-phase changing nanostructure.* ACS Photonics, 2(9): 1306-1313, **2015**.
65. Hao Q, Li W, Xu H, Wang J, Yin Y, Wang H, Ma L, Ma F, Jiang X, and Schmidt OG. *VO2/TiN plasmonic thermochromic smart coatings for room‐temperature applications.* Advanced Materials, 30(10): 1705421, **2018**.
66. Abate Y, Marvel RE, Ziegler JI, Gamage S, Javani MH, Stockman MI, and Haglund RF. *Control of plasmonic nanoantennas by reversible metal-insulator transition.* Scientific Reports, 5(1): 1-8, **2015**.
67. Hong KT, Moon CW, Suh JM, Lee TH, Kim S-I, Lee S, and Jang HW. *Daylight-Induced Metal–Insulator Transition in Ag-Decorated Vanadium Dioxide Nanorod Arrays.* ACS Applied Materials & Interfaces, 11(12): 11568-11578, **2019**.
68. Liu M, Hwang HY, Tao H, Strikwerda AC, Fan K, Keiser GR, Sternbach AJ, West KG, Kittiwatanakul S, and Lu J. *Terahertz-field-induced insulator-to-metal transition in vanadium dioxide metamaterial.* Nature, 487(7407): 345-348, **2012**.
69. Lysenko S, Rua A, Vikhnin V, Jimenez J, Fernandez F, and Liu H. *Light-induced ultrafast phase transitions in VO2 thin film.* Applied Surface Science, 252(15): 5512-5515, **2006**.
70. Greenberg CB. *Undoped and doped VO2 films grown from VO (OC3H7) 3.* Thin Solid Films, 110(1): 73-82, **1983**.
71. Balin I, Wang S, Wang P, Long Y, and Abdulhalim I. *Enhanced Transition-Temperature Reduction in a Half-Sphere Au/VO 2 Core-Shell Structure: Local Plasmonics Versus Induced Stress and Percolation Effects.* Physical Review Applied, 11(3): 034064, **2019**.
72. Hada M, Hontani Y, Marvel R, Haglund R, and Matsuo J. *Ultrafast Hot Electron Induced Phase Transitions in Vanadium Dioxide*, in *EPJ Web of Conferences*. EDP Sciences **2013**.
73. Hada M, Zhang D, Casandruc A, Miller RD, Hontani Y, Matsuo J, Marvel RE, and Haglund Jr RF. *Hot electron injection driven phase transitions.* Physical Review B, 86(13): 134101, **2012**.
74. Muskens OL, Bergamini L, Wang Y, Gaskell JM, Zabala N, De Groot C, Sheel DW, and Aizpurua J. *Antenna-assisted picosecond control of nanoscale phase transition in vanadium dioxide.* Light: Science & Applications, 5(10): e16173-e16173, **2016**.
75. Baffou G and Quidant R. *Thermo‐plasmonics: using metallic nanostructures as nano‐sources of heat.* Laser & Photonics Reviews, 7(2): 171-187, **2013**.
76. Ferrara D, MacQuarrie E, Nag J, Kaye A, and Haglund Jr R. *Plasmon-enhanced low-intensity laser switching of gold:: vanadium dioxide nanocomposites.* Applied Physics Letters, 98(24): 241112, **2011**.
77. Appavoo K and Haglund Jr RF. *Polarization selective phase-change nanomodulator.* Scientific Reports, 4(1): 1-6, **2014**.
78. Sarkar TK, Mailloux R, Oliner AA, Salazar-Palma M, and Sengupta DL. *A history of phased array antennas.* **2006**.
79. Hansen RC. *Microwave Scanning Antennas*. Academic Press New York. **1964**.
80. Hertz H. *XXXIV. On rays of electric force.* The London, Edinburgh, and Dublin Philosophical Magazine and Journal of Science, 27(167): 289-298, **1889**.
81. Maxwell JC. *VIII. A dynamical theory of the electromagnetic field.* Philosophical transactions of the Royal Society of London, (155): 459-512, **1865**.
82. John Jenkins Spark Museum. *Righi Hertzian-wave test bench c. 1895*. Available from: http://www.sparkmuseum.com/BEGINS_RADIO.HTM [Accessed 29.06.2021].

83. *Yagi Antenna / Yagi-Uda Aerial*. Available from: https://www.electronics-notes.com/articles/antennas-propagation/yagi-uda-antenna-aerial/basics-overview.php [Accessed 29.06.2021].
84. Yagi H and Uda S. *Projector of the sharpest beam of electric waves.* Proceedings of the Imperial Academy, 2(2): 49-52, **1926**.
85. Gutton H and Baissinot G. *Flat aerial for ultra high frequencies.* French patent, 703113, **1955**.
86. *Transmit / Receive Modules*. Available from: [https://www.microwaves101.com/encyclopedias/transmit-receive-modules] [Accessed 29.06.2021].
87. Berry D, Malech R, and Kennedy W. *The reflectarray antenna.* IEEE Transactions on Antennas and Propagation, 11(6): 645-651, **1963**.
88. Pengelly R and Turner J. *Monolithic broadband GaAs FET amplifiers.* Electronics Letters, 12(10): 251-252, **1976**.
89. McQuiddy DN, Wassel JW, LaGrange JB, and Wisseman WR. *Monolithic microwave integrated circuits: An historical perspective.* IEEE Transactions on Microwave Theory and Techniques, 32(9): 997-1008, **1984**.
90. Bhasin K, Anzic G, Kunath R, and Connolly D. *Optical techniques to feed and control GaAs MMIC modules for phased array antenna applications*, in *11th Communications Satellite Systems Conference*. **1986**.
91. Arditi M. *Characteristics and applications of microstrip for microwave wiring.* IRE Transactions on Microwave Theory and Techniques, 3(2): 31-56, **1955**.
92. *TowerJazz and UCSD Demonstrate First Silicon Wafer-Scale 110 GHz Phased Array Transmitter with Record Performance*. Available from: https://jacobsschool.ucsd.edu/news/release/1189?id=1189 [Accessed 29.06.2021].
93. Hülsmeyer C. *Wireless Transmitting and Receiving Mechanism for Electromagnetic Waves*. US810150A. Issuing Organization. Jan. 16, **1906**.
94. Watson-Watt RA. *Improvements in wireless systems*. TS 28/385. Issuing Organization. **1935**.
95. Boot H and Randall J. *The cavity magnetron.* Journal of the Institution of Electrical Engineers-Part IIIA: Radiolocation, 93(5): 928-938, **1946**.
96. Blanchard Y, Galati G, and Van Genderen P. *The cavity magnetron: not just a british invention [Historical Corner]*. IEEE Antennas and Propagation Magazine, 55(5): 244-254, **2013**.
97. Lagrange JL. *Sur une Loi generale d'Optique.* Memoires de l'Academie, Berlin, **1803**.
98. Abbe E. *Beiträge zur Theorie des Mikroskops und der mikroskopischen Wahrnehmung.* Archiv für Mikroskopische Anatomie, 9(1): 413-468, **1873**.
99. Helmholtz and Fripp H. *On the Limits of the Optical Capacity of the Microscope.* The Monthly Microscopical Journal, 16(1): 15-39, **1876**.
100. Strutt JWS (3rd Lord Rayleigh). *XV. On the theory of optical images, with special reference to the microscope.* The London, Edinburgh, and Dublin Philosophical Magazine and Journal of Science, 42(255): 167-195, **1896**.
101. Born M and Wolf E. *Principles of Optics*. 7th ed. Cambridge University Press. **2005**.
102. Hecht E. *Optics*. 4th Intl. ed. Pearson. **2014**.
103. *Orbbec is the replacement for Kinect skeletal tracking*. Available from: https://orbbec3d.com/orbbec-is-the-replacement-for-kinect-skeletal-tracking/ [Accessed 29.06.2021].
104. *LiDAR Market worth $2.8 billion by 2025*. Available from: https://www.marketsandmarkets.com/PressReleases/lidar.asp [Accessed 30.06.2021].
105. Kim I, Martins RJ, Jang J, Badloe T, Khadir S, Jung H-Y, Kim H, Kim J, Genevet P, and Rho J. *Nanophotonics for light detection and ranging technology.* Nature Nanotechnology, 16(5): 508-524, **2021**.
106. Royo S and Ballesta-Garcia M. *An overview of lidar imaging systems for autonomous vehicles.* Applied Sciences, 9(19): 4093, **2019**.
107. Shuttleworth J. *SAE Standards News: J3016 automated-driving graphic update.* SAE International, **2019**.

108. Holsteen AL, Cihan AF, and Brongersma ML. *Temporal color mixing and dynamic beam shaping with silicon metasurfaces.* Science, 365(6450): 257-260, **2019**.
109. Im C-S, Bhandari B, Lee K-P, Kim S-M, Oh M-C, and Lee S-S. *Silicon nitride optical phased array based on a grating antenna enabling wavelength-tuned beam steering.* Optics Express, 28(3): 3270-3279, **2020**.
110. Ni Y, Chen S, Wang Y, Tan Q, Xiao S, and Yang Y. *Metasurface for structured light projection over 120° field of view.* Nano Letters, 20(9): 6719-6724, **2020**.
111. Wu PC, Pala RA, Shirmanesh GK, Cheng W-H, Sokhoyan R, Grajower M, Alam MZ, Lee D, and Atwater HA. *Dynamic beam steering with all-dielectric electro-optic III–V multiple-quantum-well metasurfaces.* Nature Communications, 10(1): 1-9, **2019**.
112. Huang Y-W, Lee HWH, Sokhoyan R, Pala RA, Thyagarajan K, Han S, Tsai DP, and Atwater HA. *Gate-tunable conducting oxide metasurfaces.* Nano Letters, 16(9): 5319-5325, **2016**.
113. Li S-Q, Xu X, Veetil RM, Valuckas V, Paniagua-Domínguez R, and Kuznetsov AI. *Phase-only transmissive spatial light modulator based on tunable dielectric metasurface.* Science, 364(6445): 1087-1090, **2019**.
114. Kim M, Jeong J, Poon JK, and Eleftheriades GV. *Vanadium-dioxide-assisted digital optical metasurfaces for dynamic wavefront engineering.* JOSA B, 33(5): 980-988, **2016**.
115. Algorri J, Morawiak P, Zografopoulos D, Bennis N, Spadlo A, Rodríguez-Cobo L, Jaroszewicz LR, Sánchez-Pena J, and López-Higuera JM. *Multifunctional light beam control device by stimuli-responsive liquid crystal micro-grating structures.* Scientific Reports, 10(1): 1-10, **2020**.
116. Ross PE. *Lumotive Says It's Got a Solid-State Lidar That Really Works.* IEEE Spectrum, **2019**.
117. Kafaie Shirmanesh G, Sokhoyan R, Pala RA, and Atwater HA. *Dual-gated active metasurface at 1550 nm with wide (> 300) phase tunability.* Nano Letters, 18(5): 2957-2963, **2018**.
118. Lesina AC, Goodwill D, Bernier E, Ramunno L, and Berini P. *Tunable plasmonic metasurfaces for optical phased arrays.* IEEE Journal of Selected Topics in Quantum Electronics, 27(1): 1-16, **2020**.
119. de Galarreta CR, Alexeev AM, Au YY, Lopez‐Garcia M, Klemm M, Cryan M, Bertolotti J, and Wright CD. *Nonvolatile reconfigurable phase‐change metadevices for beam steering in the near infrared.* Advanced Functional Materials, 28(10): 1704993, **2018**.
120. Appavoo K, Wang B, Brady NF, Seo M, Nag J, Prasankumar RP, Hilton DJ, Pantelides ST, and Haglund Jr RF. *Ultrafast phase transition via catastrophic phonon collapse driven by plasmonic hot-electron injection.* Nano Letters, 14(3): 1127-1133, **2014**.
121. Markov P, Marvel RE, Conley HJ, Miller KJ, Haglund Jr RF, and Weiss SM. *Optically monitored electrical switching in VO2.* ACS Photonics, 2(8): 1175-1182, **2015**.
122. Joushaghani A, Kruger BA, Paradis S, Alain D, Stewart Aitchison J, and Poon JK. *Sub-volt broadband hybrid plasmonic-vanadium dioxide switches.* Applied Physics Letters, 102(6): 061101, **2013**.
123. Durkan C, Schneider M, and Welland M. *Analysis of failure mechanisms in electrically stressed Au nanowires.* Journal of Applied Physics, 86(3): 1280-1286, **1999**.
124. Kim Y, Wu PC, Sokhoyan R, Mauser K, Glaudell R, Kafaie Shirmanesh G, and Atwater HA. *Phase modulation with electrically tunable vanadium dioxide phase-change metasurfaces.* Nano Letters, 19(6): 3961-3968, **2019**.
125. Pyykko P and Desclaux JP. *Relativity and the periodic system of elements.* Accounts of Chemical Research, 12(8): 276-281, **1979**.
126. Tsui OKC. *Drude Model*. Boston University Dept. Physics, **2013**. Available from: http://physics.bu.edu/~okctsui/PY543/1_notes_Drude_2013.pdf [Accessed 07.09.2017].
127. Maier SA. *Plasmonics: Fundamentals and Applications*. Springer. **2007**.
128. Drude P. *Zur elektronentheorie der metalle.* Annalen der Physik, 306(3): 566-613, **1900**.
129. Almog IF, Bradley MS, and Bulović V. *The Lorentz Oscillator and its Applications*. **2011**. Available from: https://ocw.mit.edu/courses/electrical-engineering-and-computer-science/6-

007-electromagnetic-energy-from-motors-to-lasers-spring-2011/readings/MIT6_007S11_lorentz.pdf [Accessed 07.09.2017].
130. Bohm D and Pines D. *A collective description of electron interactions. I. Magnetic interactions.* Physical Review, 82(5): 625, **1951**.
131. Pines D and Bohm D. *A collective description of electron interactions: II. Collective vs individual particle aspects of the interactions.* Physical Review, 85(2): 338, **1952**.
132. Bohm D and Pines D. *A collective description of electron interactions: III. Coulomb interactions in a degenerate electron gas.* Physical Review, 92(3): 609, **1953**.
133. Challener W, Peng C, Itagi A, Karns D, Peng W, Peng Y, Yang X, Zhu X, Gokemeijer N, and Hsia Y-T. *Heat-assisted magnetic recording by a near-field transducer with efficient optical energy transfer.* Nature Photonics, 3(4): 220-224, **2009**.
134. Wang S, Riedinger A, Li H, Fu C, Liu H, Li L, Liu T, Tan L, Barthel MJ, and Pugliese G. *Plasmonic copper sulfide nanocrystals exhibiting near-infrared photothermal and photodynamic therapeutic effects.* ACS Nano, 9(2): 1788-1800, **2015**.
135. Qiu J and Wei WD. *Surface plasmon-mediated photothermal chemistry*. The Journal of Physical Chemistry C, 118(36): 20735-20749, **2014**.
136. Alrasheed S and Di Fabrizio E. *Effect of surface plasmon coupling to optical cavity modes on the field enhancement and spectral response of dimer-based sensors.* Scientific Reports, 7(10524): 1-11, **2017**.
137. Appavoo K and Haglund Jr RF. *Detecting nanoscale size dependence in VO2 phase transition using a split-ring resonator metamaterial.* Nano Letters, 11(3): 1025-1031, **2011**.
138. Chen WT, Chen CJ, Wu PC, Sun S, Zhou L, Guo G-Y, Hsiao CT, Yang K-Y, Zheludev NI, and Tsai DP. *Optical magnetic response in three-dimensional metamaterial of upright plasmonic meta-molecules.* Optics Express, 19(13): 12837-12842, **2011**.
139. Tobing LY, Tjahjana L, Zhang DH, Zhang Q, and Xiong Q. *Deep subwavelength fourfold rotationally symmetric split-ring-resonator metamaterials for highly sensitive and robust biosensing platform.* Scientific Reports, 3(1): 1-6, **2013**.
140. Malakoutian M, Byambadorj T, Davaji B, Richie J, and Lee CH. *Optimization of the bowtie gap geometry for a maximum electric field enhancement.* Plasmonics, 12(2): 287-292, **2017**.
141. Link S and El-Sayed MA. *Spectral properties and relaxation dynamics of surface plasmon electronic oscillations in gold and silver nanodots and nanorods.* The Journal of Physical Chemistry B, 103(40): 8410-8426, **1999**.
142. Payne EK, Shuford KL, Park S, Schatz GC, and Mirkin CA. *Multipole plasmon resonances in gold nanorods.* The Journal of Physical Chemistry B, 110(5): 2150-2154, **2006**.
143. Bruggeman DAG. *Berechnung verschiedener physikalischer Konstanten von heterogenen Substanzen. I. Dielektrizitätskonstanten und Leitfähigkeiten der Mischkörper aus isotropen Substanzen.* Annalen der Physik, 416(7): 636-664, **1935**.
144. Garnett JCM and Larmor J. *XII. Colours in metal glasses and in metallic films.* Philosophical Transactions of the Royal Society of London. Series A, Containing Papers of a Mathematical or Physical Character, 203(359-371): 385-420, **1904**.
145. Kuhnen K. *Modeling, Identification and Compensation of Complex Hysteretic Nonlinearities: A Modified Prandtl-Ishlinskii Approach.* European Journal of Control, 9(4): 407-418, **2003**.
146. Chettiar UK and Engheta N. *Modeling vanadium dioxide phase transition due to continuous-wave optical signals.* Optics Express, 23(1): 445-451, **2015**.
147. Bikky R, Badi N, and Bensaoula A. *Effective medium theory of nanodielectrics for embedded energy storage capacitors*, in *COMSOL Conference*. **2010**.
148. Perrin J-M and Lamy P. *On the validity of effective-medium theories in the case of light extinction by inhomogeneous dust particles.* The Astrophysical Journal, 364: 146-151, **1990**.
149. Markel VA. *Introduction to the Maxwell Garnett approximation: tutorial.* JOSA A, 33(7): 1244-1256, **2016**.
150. Choy TC. *Effective medium theory: principles and applications*. Vol. 165. Oxford University Press. **2015**.
151. Maxwell JC. *A treatise on electricity and magnetism*. Vol. 1. Clarendon press. **1873**.

152. Castellanos A, Ramos A, Gonzalez A, Green NG, and Morgan H. *Electrohydrodynamics and dielectrophoresis in microsystems: scaling laws.* Journal of Physics D: Applied Physics, 36(20): 2584, **2003**.
153. Incropera FP. *Fundamentals of Heat and Mass Transfer*. 6th ed. Wiley & Sons. **2007**.
154. Cheng C, Fan W, Cao J, Ryu S-G, Ji J, Grigoropoulos CP, and Wu J. *Heat Transfer across the Interface between Nanoscale Solids and Gas.* ACS Nano, 5(12): 10102-10107, **2011**.
155. Fong KY, Li H-K, Zhao R, Yang S, Wang Y, and Zhang X. *Phonon heat transfer across a vacuum through quantum fluctuations.* Nature, 576(7786): 243-247, **2019**.
156. Nelder JA and Mead R. *A simplex method for function minimization.* The computer journal, 7(4): 308-313, **1965**.
157. Wan C, Zhang Z, Woolf D, Hessel CM, Rensberg J, Hensley JM, Xiao Y, Shahsafi A, Salman J, Richter S, Sun Y, Qazilbash MM, Schmidt-Grund R, Ronning C, Ramanathan S, and Kats MA. *On the optical properties of thin‐film vanadium dioxide from the visible to the far infrared.* Annalen der Physik, 531(10): 1900188, **2019**.
158. Wolski A. *Part 4: Waves on Boundaries*. Course Notes, PHYS370, Advanced Electromagnetism, University of Liverpool, **2018**. Available from: http://pcwww.liv.ac.uk/~awolski/Teaching/Liverpool/PHYS370/AdvancedElectromagnetism-Part4.pdf [Accessed 30.06.2021].
159. Heavens OS. *Optical properties of thin solid films*. Courier Corporation. **1991**.
160. Courant R. *Variational methods for the solution of problems of equilibrium and vibrations.* Bulletin of the American Mathematical Society, 49: 1–23, **1943**.
161. Courant R. *Herausgegeben und ergänzt durch einen Abschnitt über geometrische Funktionentheorie*, in *Die Grundlehren der Mathematischen Wissenschaften. Band III: Funktionentheorie*. Julius Springer: Berlin, **1922**.
162. Hilbert D. *Über das Dirichletsche Prinzip.* Mathematische Annalen, 59(1): 161-186, **1904**.
163. Ritz W. *Über eine neue Methode zur Lösung gewisser Variations Probleme der Matematischen.* Journal fiir die Reine und Angewandte Mathematik 135(61), **1908**.
164. Williamson F. *Richard courant and the finite element method: A further look.* Historia Mathematica, 7(4): 369-378, **1980**.
165. Cook RD, Malkus DS, Plesha ME, and Witt RJ. *Concepts and Applications of Finite Element Analysis*. 4th ed. Wiley. **2002**.
166. Wilcox K and Wang Q. *16.90 Computational Methods in Aerospace Engineering: 2.8 Method of Weighted Residuals*. MIT Open Courseware, **2014**. Available from: https://ocw.mit.edu/courses/aeronautics-and-astronautics/16-90-computational-methods-in-aerospace-engineering-spring-2014/numerical-methods-for-partial-differential-equations/method-of-weighted-residuals/ [Accessed 30/07/2021].
167. Liu C. *Discretizing the Weak Form Equations*. COMSOL Blog, **2015**. Available from: https://www.comsol.com/blogs/discretizing-the-weak-form-equations/ [Accessed 17/07/2021].
168. *COMSOL Multiphysics 5.2a Documentation. RF Module, Meshing and solving*. [Accessed 2017].
169. Yang HU, D'Archangel J, Sundheimer ML, Tucker E, Boreman GD, and Raschke MB. *Optical dielectric function of silver.* Physical Review B, 91(23): 235137, **2015**.
170. Verleur HW, Barker Jr A, and Berglund C. *Optical properties of V O 2 between 0.25 and 5 eV.* Physical Review, 172(3): 788, **1968**.
171. Pirozhenko I and Lambrecht A. *Influence of slab thickness on the Casimir force.* Physical Review A, 77(1): 013811, **2008**.
172. Qazilbash MM, Schafgans A, Burch K, Yun S, Chae B, Kim B, Kim H-T, and Basov D. *Electrodynamics of the vanadium oxides V O 2 and V 2 O 3.* Physical Review B, 77(11): 115121, **2008**.
173. Luther JM, Jain PK, Ewers T, and Alivisatos AP. *Localized surface plasmon resonances arising from free carriers in doped quantum dots.* Nature Materials, 10(5): 361-366, **2011**.
174. Urade Y, Nakata Y, Okimura K, Nakanishi T, Miyamaru F, Takeda MW, and Kitano M. *Dynamically Babinet-invertible metasurface: a capacitive-inductive reconfigurable filter for*

terahertz waves using vanadium-dioxide metal-insulator transition. Optics Express, 24(5): 4405-4410, **2016**.
175. Bell AP, Fairfield JA, McCarthy EK, Mills S, Boland JJ, Baffou G, and McCloskey D. *Quantitative study of the photothermal properties of metallic nanowire networks.* ACS Nano, 9(5): 5551-5558, **2015**.
176. Chandler-Horowitz D and Amirtharaj PM. *High-accuracy, midinfrared (450 cm− 1⩽ω⩽ 4000 cm− 1) refractive index values of silicon.* Journal of Applied physics, 97(12): 123526, **2005**.
177. Olmon RL, Slovick B, Johnson TW, Shelton D, Oh S-H, Boreman GD, and Raschke MB. *Optical dielectric function of gold.* Physical Review B, 86(23): 235147, **2012**.
178. Rakić AD, Djurišić AB, Elazar JM, and Majewski ML. *Optical properties of metallic films for vertical-cavity optoelectronic devices.* Applied Optics, 37(22): 5271-5283, **1998**.
179. Miyata H, Fujii K, Ono T, Kubokawa Y, Ohno T, and Hatayama F. *Fourier-transform infrared investigation of structures of vanadium oxide on various supports.* Journal of the Chemical Society, Faraday Transactions 1: Physical Chemistry in Condensed Phases, 83(3): 675-685, **1987**.
180. Šurca A and Orel B. *IR spectroscopy of crystalline V2O5 films in different stages of lithiation.* Electrochimica Acta, 44(18): 3051-3057, **1999**.
181. Kang Y, Najmaei S, Liu Z, Bao Y, Wang Y, Zhu X, Halas NJ, Nordlander P, Ajayan PM, and Lou J. *Plasmonic hot electron induced structural phase transition in a MoS2 monolayer.* Advanced Materials, 26(37): 6467-6471, **2014**.
182. Zhao W, Wang S, Liu B, Verzhbitskiy I, Li S, Giustiniano F, Kozawa D, Loh KP, Matsuda K, and Okamoto K. *Exciton–plasmon coupling and electromagnetically induced transparency in monolayer semiconductors hybridized with Ag nanoparticles.* Advanced Materials, 28(14): 2709-2715, **2016**.
183. Baffou G, Berto P, Bermúdez Ureña E, Quidant R, Monneret S, Polleux J, and Rigneault H. *Photoinduced heating of nanoparticle arrays.* ACS Nano, 7(8): 6478-6488, **2013**.
184. Samsonov GV. *The oxide handbook.* Springer Science & Business Media. **2013**.
185. Klimov V, Timofeeva I, Khanin S, Shadrin E, Ilinskii A, and Silva-Andrade F. *Hysteresis loop construction for the metal-semiconductor phase transition in vanadium dioxide films.* Technical Physics, 47(9): 1134-1139, **2002**.
186. Zhang H, Wu Z, Wu X, Yang W, and Jiang Y. *Transversal grain size effect on the phase-transition hysteresis width of vanadium dioxide films comprising spheroidal nanoparticles.* Vacuum, 104: 47-50, **2014**.
187. Leahu G, Li Voti R, Sibilia C, and Bertolotti M. *Anomalous optical switching and thermal hysteresis during semiconductor-metal phase transition of VO2 films on Si substrate.* Applied Physics Letters, 103(23): 231114, **2013**.
188. Mayergoyz ID. *Mathematical models of hysteresis and their applications*. Academic Press. **2003**.
189. Visintin A. *Hysteresis and semigroups*, in *Differential models of hysteresis*. Springer, 211-256, **1994**.
190. Ito K, Nishikawa K, and Iizuka H. *Multilevel radiative thermal memory realized by the hysteretic metal-insulator transition of vanadium dioxide.* Applied Physics Letters, 108(5): 053507, **2016**.
191. Zhang J, Merced E, Sepúlveda N, and Tan X. *Modeling and inverse compensation of hysteresis in vanadium dioxide using an extended generalized Prandtl–Ishlinskii model.* Smart Materials and Structures, 23(12): 125017, **2014**.
192. Kats MA, Sharma D, Lin J, Genevet P, Blanchard R, Yang Z, Qazilbash MM, Basov D, Ramanathan S, and Capasso F. *Ultra-thin perfect absorber employing a tunable phase change material.* Applied Physics Letters, 101(22): 221101, **2012**.
193. Griffiths C and Eastwood H. *Influence of stoichiometry on the metal‐semiconductor transition in vanadium dioxide.* Journal of Applied Physics, 45(5): 2201-2206, **1974**.

194. de Almeida LAL, Deep GS, Nogueira-Lima AM, and Neff H. *Modeling of the hysteretic metal-insulator transition in a vanadium dioxide infrared detector.* Optical Engineering, 41(10): 2582-2588, **2002**.
195. Palik ED. *Handbook of optical constants of solids*. Vol. 3. Academic press. **1998**.
196. Kats MA, Blanchard R, Zhang S, Genevet P, Ko C, Ramanathan S, and Capasso F. *Vanadium dioxide as a natural disordered metamaterial: perfect thermal emission and large broadband negative differential thermal emittance.* Physical Review X, 3(4): 041004, **2013**.
197. Voloshenko I, Kuhl F, Gompf B, Polity A, Schnoering G, Berrier A, and Dressel M. *Microscopic nature of the asymmetric hysteresis in the insulator-metal transition of VO2 revealed by spectroscopic ellipsometry.* Applied Physics Letters, 113(20): 201906, **2018**.
198. Currie M, Wheeler VD, Downey B, Nepal N, Qadri SB, Wollmershauser JA, Avila J, and Nyakiti L. *Asymmetric hysteresis in vanadium dioxide thin films.* Optical Materials Express, 9(9): 3717-3728, **2019**.
199. Zhu H-f, Li J, Zhong S-c, Du L-h, Shi Q-w, Peng B, Yuan H-k, Huang W-x, and Zhu L-G. *Continuously tuning the impedance matching at the broadband terahertz frequency range in VO2 thin film.* Optical Materials Express, 9(1): 315-329, **2019**.
200. Gurvitch M, Luryi S, Polyakov A, and Shabalov A. *Nonhysteretic behavior inside the hysteresis loop of VO2 and its possible application in infrared imaging.* Journal of Applied Physics, 106(10): 104504, **2009**.
201. Gurvitch M, Luryi S, Polyakov A, and Shabalov A. *Nonhysteretic Phenomena in the Metal–Semiconductor Phase-Transition Loop of <formula formulatype="inline"><tex Notation="TeX">$\hbox{VO}_{2}$</tex> </formula> Films for Bolometric Sensor Applications.* IEEE Transactions on Nanotechnology, 9(5): 647-652, **2010**.
202. Gurvitch M, Luryi S, Polyakov A, and Shabalov A. *Treating the Case of Incurable Hysteresis in VO2*, in *Future Trends in Microelectronics: From Nanophotonics to Sensors to Energy; IEEE Press*. John Wiley & Sons, 395-409, **2010**.
203. Scuderi M, Esposito M, Todisco F, Simeone D, Tarantini I, De Marco L, De Giorgi M, Nicotra G, Carbone L, and Sanvitto D. *Nanoscale study of the tarnishing process in electron beam lithography-fabricated silver nanoparticles for plasmonic applications.* The Journal of Physical Chemistry C, 120(42): 24314-24323, **2016**.
204. Soukoulis CM and Wegener M. *Past achievements and future challenges in the development of three-dimensional photonic metamaterials.* Nature Photonics, 5(9): 523-530, **2011**.
205. Tasco V, Esposito M, Todisco F, Benedetti A, Cuscunà M, Sanvitto D, and Passaseo A. *Three-dimensional nanohelices for chiral photonics.* Applied Physics A, 122(4): 280, **2016**.
206. Todisco F, Esposito M, Panaro S, De Giorgi M, Dominici L, Ballarini D, Fernández-Domínguez AI, Tasco V, Cuscuna M, and Passaseo A. *Toward cavity quantum electrodynamics with hybrid photon gap-plasmon states.* ACS Nano, 10(12): 11360-11368, **2016**.
207. Goldberg A, Stann B, and Gupta N. *Multispectral, hyperspectral, and three-dimensional imaging research at the US Army research laboratory.* ARMY RESEARCH LAB ADELPHI MD, **2003**.
208. Opto-E. *Introduction to infrared vision: Primer on IR theory*. Opto Engineering, Available from: https://www.opto-e.com/resources/infrared-theory [Accessed 01.05.2019].
209. Makki I, Younes R, Francis C, Bianchi T, and Zucchetti M. *A survey of landmine detection using hyperspectral imaging.* ISPRS Journal of Photogrammetry and Remote Sensing, 124: 40-53, **2017**.
210. Nguyen CT, Havlicek JP, Fan G, Caulfield JT, and Pattichis MS. *Robust dual-band MWIR/LWIR infrared target tracking*, in *2014 48th Asilomar Conference on Signals, Systems and Computers*. IEEE **2014**.
211. NASA. *LandSat Science: Technical Details.* NASA, Available from: https://landsat.gsfc.nasa.gov/about/technical-information/ [Accessed 01.05.2019].
212. Baronti S, Casini A, Lotti F, and Porcinai S. *Multispectral imaging system for the mapping of pigments in works of art by use of principal-component analysis.* Applied Optics, 37(8): 1299-1309, **1998**.

213. Easton RL, Knox KT, and Christens-Barry WA. *Multispectral imaging of the Archimedes palimpsest*, in *32nd Applied Imagery Pattern Recognition Workshop, 2003. Proceedings.*: IEEE **2003**.
214. Shin HS, Lee JS, Jeon SG, Yu J, and Song JY. *Thermopower detection of single nanowire using a MEMS device.* Measurement, 51: 470-475, **2014**.
215. McPeak KM, Jayanti SV, Kress SJ, Meyer S, Iotti S, Rossinelli A, and Norris DJ. *Plasmonic films can easily be better: rules and recipes.* ACS photonics, 2(3): 326-333, **2015**.
216. Schmidt AJ, Cheaito R, and Chiesa M. *Characterization of thin metal films via frequency-domain thermoreflectance.* Journal of Applied Physics, 107(2): 024908, **2010**.
217. Lee S-M, Cahill DG, and Allen TH. *Thermal conductivity of sputtered oxide films.* Physical review B, 52(1): 253, **1995**.
218. Kizuka H, Yagi T, Jia J, Yamashita Y, Nakamura S, Taketoshi N, and Shigesato Y. *Temperature dependence of thermal conductivity of VO2thin films across metal–insulator transition.* Japanese Journal of Applied Physics, 54(5): 053201, **2015**.
219. Gomez-Heredia CL, Ramirez-Rincon JA, Bhardwaj D, Rajasekar P, Tadeo IJ, Cervantes-Lopez JL, Ordonez-Miranda J, Ares O, Umarji AM, Drevillon J, Joulain K, Ezzahri Y, and Alvarado-Gil JJ. *Measurement of the hysteretic thermal properties of W-doped and undoped nanocrystalline powders of VO2.* Scientific Reports, 9(1): 14687, **2019**.
220. Oh D-W, Ko C, Ramanathan S, and Cahill DG. *Thermal conductivity and dynamic heat capacity across the metal-insulator transition in thin film VO2.* Applied Physics Letters, 96(15): 151906, **2010**.
221. Ho CY, Powell RW, and Liley PE. *Thermal conductivity of the elements.* Journal of Physical and Chemical Reference Data, 1(2): 279-421, **1972**.
222. Swenson CA. *Recommended Values for the Thermal Expansivity of Silicon from 0 to 1000 K.* Journal of Physical and Chemical Reference Data, 12(2): 179-182, **1983**.
223. Kelley KK. *Contributions to the Data on Theoretical Metallurgy, XIII High-Temperature Heat-Content, Heat-Capacity, and Entropy Data for the Elements and Inorganic Compounds.* US Bureau of Mines, Bulletin No. 476, **1949**.

Appendix

A1 Plasma frequency derivation.

Maxwell equation linking divergence of the electric flux density $\boldsymbol{D}$ to the external charge density ρ_e **[127]:**

$$\nabla \cdot \boldsymbol{D} = \rho_e$$

and the relationship between electric flux density, electric field and polarization:

$$\boldsymbol{D} = \varepsilon_0 \boldsymbol{E} + \boldsymbol{P}$$
$$\boldsymbol{E} = \frac{\boldsymbol{D}}{\varepsilon_0} - \boldsymbol{P}$$

where $\boldsymbol{P}$ is polarisation (dipole moment per unit volume).

Polarisation is linked to the internal charge density ρ_i by:

$$\nabla \cdot \boldsymbol{P} = -\rho_i$$

thus to surface charge density ρ_t by:

$$\boldsymbol{P} = -\sigma_c = -n_e e x$$

Combining these equations gives

$$\nabla \cdot \boldsymbol{E} = \frac{\rho_e + \rho_i}{\varepsilon_0} = \frac{\rho_t}{\varepsilon_0}$$

$$\boldsymbol{E} = \frac{\sigma_c}{\varepsilon_0}$$

Using Newton's second $\boldsymbol{F} = ma$ and $\boldsymbol{F} = -e\boldsymbol{E}$ and substituting **E** gives:

$$m\frac{\partial^2 x}{\partial t^2} = -e\boldsymbol{E} = -e\left(\frac{n_e e x}{\varepsilon_0}\right)$$
$$\frac{\partial^2 x}{\partial t^2} = \frac{-n_e e^2 x}{m\varepsilon_0}$$

Thus obtaining the plasma frequency.

$$\omega_p = \frac{n_e e^2}{m\varepsilon_0} \tag{33}$$

σ_c	surface charge density (area)
ρ_e	external charge density (volume)
ρ_i	internal charge density (volume)
ρ_t	total charge density (volume)
$\nabla \cdot$	del dot = divergence

A2 Additional terms

Dipole moment is the product of the separation of the ends of a dipole and the magnitude of charges:

$$\boldsymbol{p} = q\boldsymbol{d}$$

$\boldsymbol{p}$ electric dipole moment vector

d displacement vector (separation)

q charge

Polarisability is the tendency of a charge distribution at equilibrium to have charges displaced by an external electric field:

$$\alpha = \boldsymbol{p}/\boldsymbol{E}$$

$\boldsymbol{p}$ induced dipole moment

E electric field producing the dipole moment

Susceptibility is the degree of polarisation of a dielectric material in response to applied electric field. Greater susceptibility equates to greater ability of material to polarise in response to an applied field and thereby reduce the total field inside the material (and store energy). Electric susceptibility influences the permittivity of a material by:

$$\boldsymbol{P} = \varepsilon_0\chi_e\boldsymbol{E} = \varepsilon_0(\varepsilon_r - 1)\boldsymbol{E}$$

$\boldsymbol{P}$ polarisation density

ε_0 free space permittivity

χ_e electric susceptibility $= \varepsilon_r - 1$

$\boldsymbol{E}$ electric field

Electric displacement is related to polarisation density by:

$$\boldsymbol{D} = \varepsilon_0\boldsymbol{E} + \boldsymbol{P} = \varepsilon_0(1 + \chi_e)\boldsymbol{E} = \varepsilon_r\varepsilon_0\boldsymbol{E} = \varepsilon\boldsymbol{E}$$

where:

$$\varepsilon = \varepsilon_r\varepsilon_0$$

$$\varepsilon_r = (1 + \chi_e)$$

$\boldsymbol{D}$ electric displacement field accounts for effects of free and bound charge within materials

A3 Permittivity model parameters and calculated values

Table A. Sapphire parameter values

Oscillator number j	S_j	v_j (Hz)
1	1.023	4.88 E+15
2	1.058264	2.71 E+15
3	5.280792	1.69 E+13

Pirozhenko 2008 ***[171]***

Table B. Dielectric VO_2 parameter values

Oscillator number j	s	ω (eV)	Γ (eV)
1	0.790	1.02	0.55
2	0.474	1.30	0.55
3	0.483	1.50	0.50
4	0.536	2.75	0.22
5	1.316	3.49	0.47
6	1.060	3.76	0.38
7	0.990	5.10	0.385
	ω_∞ (eV)	ε_∞	
	15	4.26	

Verleur 1968 ***[170]***

Table C. Metallic VO_2 parameter values

Oscillator number j	$\tilde{s}$	$\tilde{\omega}$ (eV)	$\tilde{\Gamma}$ (eV)
1	1.816	0.86	0.95
2	0.972	2.80	0.23
3	1.04	3.48	0.28
4	1.05	4.60	0.34
ω_p (eV)	ω_∞ (eV)	$\tilde{\varepsilon}_\infty$	γ (eV)
3.33	15	3.95	0.66

Verleur 1968 ***[170]***

Table D. Chromium parameter values

Oscillator number *j*	*s*	*ω* (eV)	*Γ* (eV)
0	0.168	10.75	0.047
1	0.151	0.121	3.175
2	0.15	0.543	1.305
3	1.149	1.970	2.676
4	0.825	8.775	1.335

Rakić 1998 ***[178]***

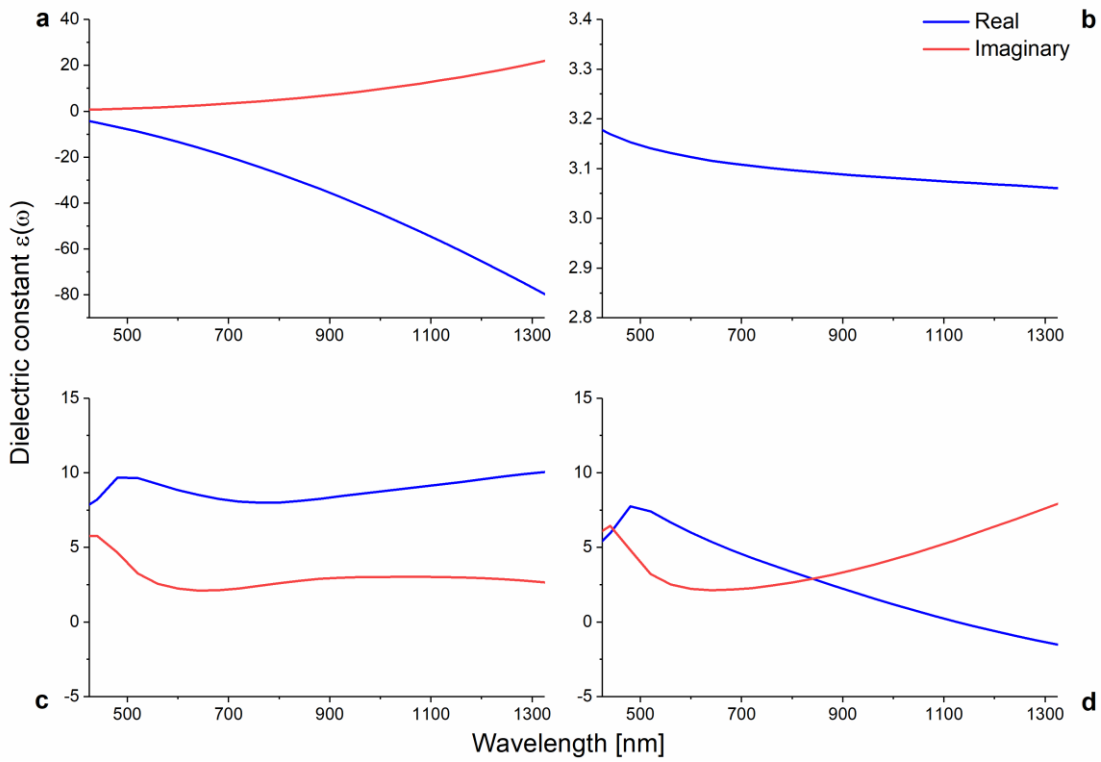

Figure 60. Complex relative permittivity / dielectric function Ag, Al2O3, VO2 (both phases); (a) real & imaginary parts of permittivity, Ag; (b) purely real permittivity, Al2O3; (c) real & imaginary parts permittivity, VO2 (dielectric); (d) real & imaginary parts permittivity VO_2 (metallic).

A4 Absence of polarisation dependence in control sample

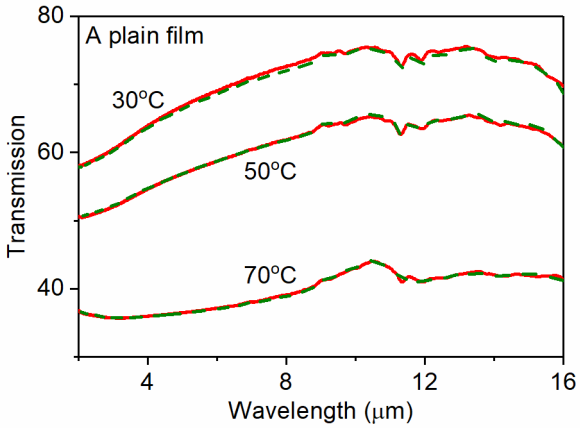

Figure 61. Transmission spectra of a control sample, a plain VOx film, under orthogonal polarisations. The sample was heated up from room temperature, when spectra was taken in sequence at 30 °C, 50 °C and 70 °C under one polarisation (red lines). The sample was then cooled down to room temperature and measured at the same temperatures in the same sequence under the orthogonal polarisation (green dashed lines). The two sets of the spectra are very similar. This result shows that the polarisation dependence observed in nanorod samples are plasmonic effects rather than experimental artefacts induced by measurement facilities.

A5 Simulated longitudinal vs transverse polarisation dependent resonance in Ag NR on VO_2

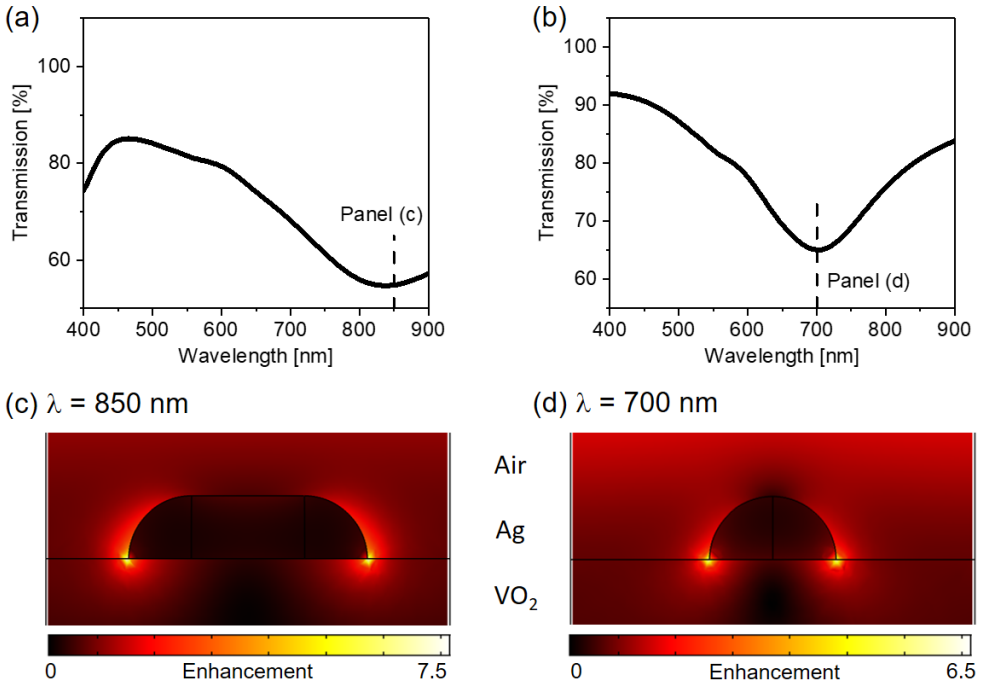

Figure 62. Simulated transmission spectra and electric near field of the sample. Transmission spectra for (a) longitudinal and (b) transverse polarised incident light. (c-d) Electric field distribution at peak resonance for (c) longitudinal (at 850 nm) and (d) transverse (at 700 nm) polarised light. Enhancement factor is with respect to the incident field.

A7 System of reflection and transmission for light incident on thin film on substrate

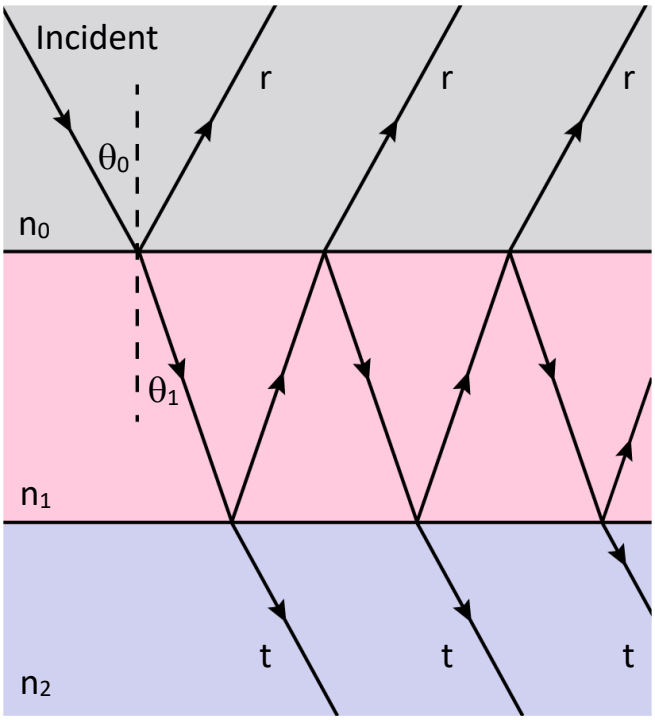

Figure 63. Light beam incident on a film-on-substrate at incident angle θ_0. In a lossless system, a portion of the incident wave is reflected or transmitted at each interface. In a lossy system, a portion is also absorbed; r = reflected, t = transmitted light.

For the problem of light incident on dielectric interface, the boundary conditions can be derived from the integral form of Maxwell's equations using the 'pillbox and loop' method **[158]**. The vertical components of the electric field can be solved using Gauss' law:

$$\oint \boldsymbol{E} \cdot \partial A = \frac{\Sigma Q}{\varepsilon_0}$$

There are no free charges in the dielectric $Q = 0$ so:

$$\varepsilon\varepsilon_0 \oint \boldsymbol{E} \cdot \partial A = \Sigma Q = 0$$

where ε is the permittivity coefficient (relative permittivity) of the dielectric, which modifies the vacuum permittivity ε_0 to permittivity of the dielectric media.

i.) Vertical (normal) components

Vertical components of the electric field pass through the top and bottom boundaries of the 'pillbox' while horizontal components pass through the sides. For an infinitesimally thin interface, the horizontal component is 0 so only vertical components contribute:

$$\varepsilon_1\varepsilon_0\boldsymbol{E}_{v1}A - \varepsilon_2\varepsilon_0\boldsymbol{E}_{v2}A = 0$$

Dividing by A and ε_0 the first boundary condition is found to be:

$$\varepsilon_1 \boldsymbol{E}_{v1} = \varepsilon_2 \boldsymbol{E}_{v2} \tag{34}$$

This states that as light passes from one dielectric to another, the relative permittivity of each dielectric determines the change in magnitude of the vertical electric field components.

Similarly, the vertical components of the magnetic field can be solved using Gauss' law for magnetism:

$$\oint \boldsymbol{B} \cdot \partial A = 0$$

$$\boldsymbol{B}_{v1} A - \boldsymbol{B}_{v2} A = 0$$

$$\boldsymbol{B}_{v1} = \boldsymbol{B}_{v2} \tag{35}$$

The second boundary condition states the vertical components of the magnetic field are continuous across the interface.

ii.) Horizontal (tangential) components

The horizontal components of the electric field can be solved using the Maxwell-Faraday equation:

$$\oint \boldsymbol{E} \cdot \partial L = \frac{-\partial \Phi_B}{\partial t}$$

Where L is the 'loop' path length. The dot product of vertical components and horizontal path lengths are zero, since they are perpendicular; likewise the horizontal components and vertical path lengths. The vertical components cancel so only the sum of horizonal components contributes:

$$\boldsymbol{E}_{h1} L - \boldsymbol{E}_{h2} L = \frac{-\partial \Phi_B}{\partial t}$$

Again, for an infinitesimally thin interface, the horizontal area is zero, so there is no horizontal flux:

$$\boldsymbol{E}_{h1} L - \boldsymbol{E}_{h2} L = 0$$

Cancelling L terms gives the third boundary condition:

$$\boldsymbol{E}_{h1} = \boldsymbol{E}_{h2} \tag{36}$$

This states that the horizontal (tangential) component of the electric field is continuous across the dielectric interface. The horizontal components of the magnetic field can be solved using Ampère's law (with Maxwell's correction):

$$\oint \boldsymbol{B} \cdot \partial L = \mu_0 I + \mu_0 \varepsilon_0 \frac{\partial \Phi_E}{\partial t}$$

Dividing by μ_0:

$$\frac{1}{\mu_0} \oint \boldsymbol{B} \cdot \partial L = I + \varepsilon_0 \frac{\partial \Phi_E}{\partial t}$$

Assuming no electrons flow in a dielectric, I is zero, giving:

$$\frac{1}{\mu_0}\oint \boldsymbol{B}\cdot\partial L = \varepsilon_0\frac{\partial \Phi_E}{\partial t}$$

Again because of the dot product and cancelling of the vertical components, only the horizontal components contribute as:

$$\frac{\boldsymbol{B}_{h1}L}{\mu_1\mu_0} - \frac{\boldsymbol{B}_{h2}L}{\mu_2\mu_0} = \varepsilon_0\frac{\partial \Phi_E}{\partial t}$$

Shrinking the rectangular path to infinitesimally small area on surface so flux term = 0 while $k_{m1}\mu_0$ and $k_{m2}\mu_0$ are the same so they cancel, also L cancels, giving the fourth boundary condition:

$$\boldsymbol{B}_{h1} - \boldsymbol{B}_{h2} = 0$$

$$\boldsymbol{B}_{h1} = \boldsymbol{B}_{h2} \tag{37}$$

The horizontal components of the magnetic field are also continuous across the interface. For s-polarised light, the electric field is always parallel to (i.e. in the plane of) the interface and the transmitted field is equal to the sum of the incident and reflected field. Thus, for light incident on an interface between two lossless dielectrics:

$$\boldsymbol{E}_i + \boldsymbol{E}_r = \boldsymbol{E}_t$$

where i, r, t denote incident, reflected, transmitted E-vector. The associated tangential magnetic field vectors are then:

$$\boldsymbol{B}_i cos\theta_1 - \boldsymbol{B}_r cos\theta_1 = \boldsymbol{B}_t cos\theta_2 \tag{38}$$

where θ_1 is the angle of both incidence and reflection by the first law of reflection and θ_2 is the angle of refraction.

From Faraday's law it can be shown that for a wave propagating through free space, the ratio of electric to magnetic fields is equal to the speed of light:

$$\frac{\boldsymbol{E}_0}{\boldsymbol{B}_0} = c$$

In dielectric media $v = c/n$ so the equation can be amended to:

$$\boldsymbol{B} = \boldsymbol{E}\frac{n}{c}$$

Substituting $\boldsymbol{B}$ in eq. 36 gives:

$$\frac{n_1}{c}\boldsymbol{E}_i cos\theta_1 - \frac{n_1}{c}\boldsymbol{E}_r cos\theta_1 = \frac{n_2}{c}\boldsymbol{E}_t cos\theta_2$$

Substituting $\boldsymbol{E}_t$ and multiplying both sides by c:

$$n_1\boldsymbol{E}_i cos\theta_1 - n_1\boldsymbol{E}_r cos\theta_1 = n_2(\boldsymbol{E}_i + \boldsymbol{E}_r)cos\theta_2$$

$$\boldsymbol{E}_i(n_1 cos\theta_1 - n_2 cos\theta_2) = \boldsymbol{E}_r(n_2 cos\theta_2 + n_1 cos\theta_1)$$

$$\therefore \frac{\boldsymbol{E}_r}{\boldsymbol{E}_i} = \frac{n_1 cos\theta_1 - n_2 cos\theta_2}{n_2 cos\theta_2 + n_1 cos\theta_1} \quad (39)$$

for electric field parallel to the interface. Since θ is 0 degrees with respect to the normal all $cos\theta$ terms are 1 so this can be rewritten as:

$$\frac{\boldsymbol{E}_r}{\boldsymbol{E}_i} = \frac{n_1 - n_2}{n_2 + n_1} \quad (40)$$

This is the ratio of the reflected and incident electric field, known as the *Fresnel reflection coefficient* r. The reflected energy per unit area (intensity) is then given by:

$$\boldsymbol{R} = |r|^2 = \left|\frac{n_1 - n_2}{n_2 + n_1}\right|^2 \quad (41)$$

$\boldsymbol{R}$ is known as reflectance (for layered / finite media) or reflectivity (for homogenous / semi-infinite) media and is always a positive real number. Reflection and transmission are dependent on the polarisation of incident light but because normal incidence is assumed, all polarisations are equal with respect to the interface.

A8 Material parameters for Chapter 7

Parameter	Value (at 293 K, 1.55 μm)	References
Si refractive index	3.48	Palik (1998) **[195]**
Al_2O_3 refractive index	1.75	Palik (1998) **[195]**
Al permittivity	-197.92 + 38.085*i	McPeak (2015) **[215]**
Complex refractive index VO_2 (insulating)	3.22982 + 0.50941*i	Wan, Kats et al. (2019) **[157]**
Complex refractive index VO_2 (metallic)	1.34 + 2.67*i	Wan, Kats et al. (2019) **[157]**

Material	Thermal conductivity [W/(m·K)]	Density [kg/m^3]	Specific heat capacity [J/(kg·K)]	References
Al, 20-100 nm film	120	2700	921.096	Schmidt (2010) **[216]**
Al_2O_3, amorphous DC sputtered	2	3510	880	Lee (1995) **[217]**
VO_2	4.4	4571	690	Kizuka (2015) **[218]**, Gomez-Heredia (2019) **[219]**, Oh (2010) **[220]**

Silicon thermal conductivity, density and specific heat capacity were modelled using COMSOL built-in material properties for "Silicon [solid, bulk]", with source references **[221]**, **[222]** and **[223]**.

A9 Geometric convergence for thermal simulations

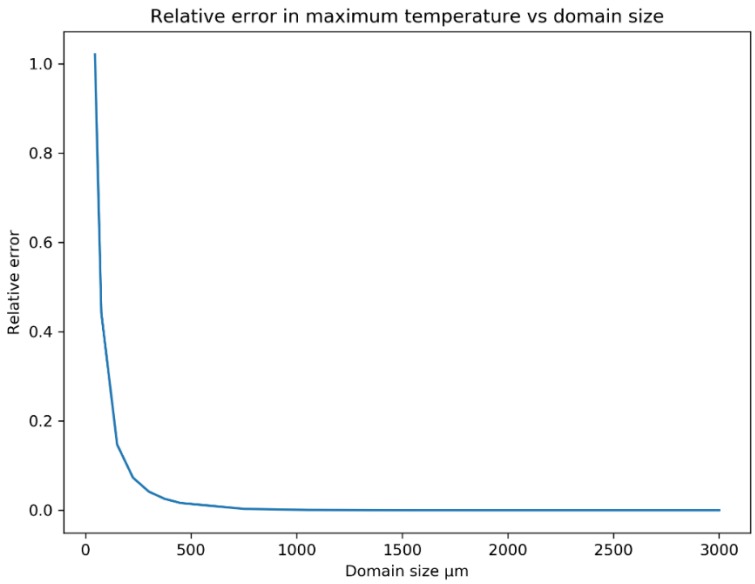

Figure 64. Geometric convergence testing for thermal simulations. Maximum temperature within the domain is evaluated as a test variable while the diameter of the surrounding hemispherical air domain (and substrate width) is increased. Relative error is calculated as abs(T_{max} – T_{min}) / T_{min}, where T_{max} is maximum temperature for a given domain size and T_{min} is the smallest max temperature of all domain sizes. This plot shows that the solution converges (relative error becomes less than the relative tolerance 0.001) by a domain size of 1.5 mm.

A10 Looyenga polarisation factor 1 results

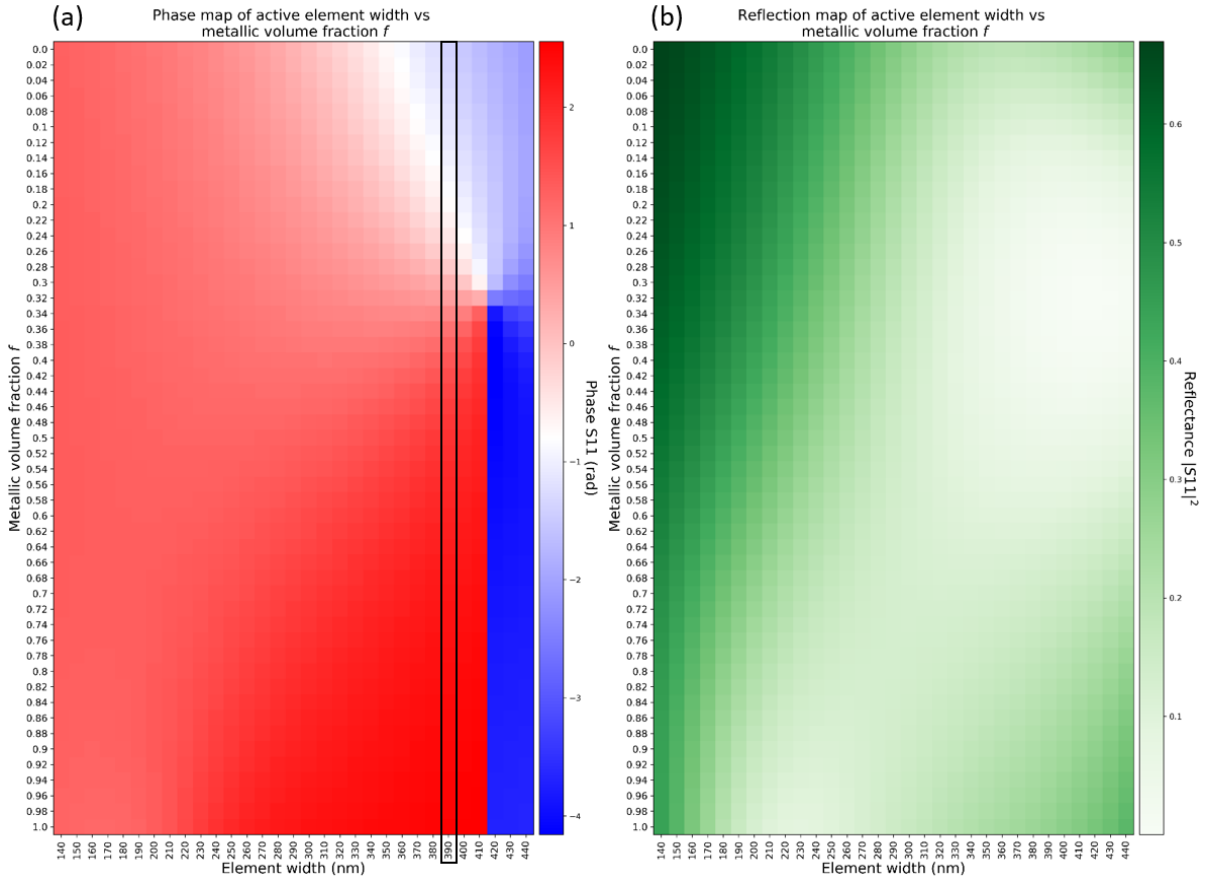

Figure 65. Colour maps used to identify element geometry that satisfied design constraints. 'Active element' (VO_2 / Al_2O_3) width was varied between 140 – 440 nm at 10 nm interval, while keeping Al wire width fixed. (a) Reflected phase as a function of *f* for varied active element width. The black box indicates the chosen active element width. (b) Reflectance as a function of *f* for varied active element width.

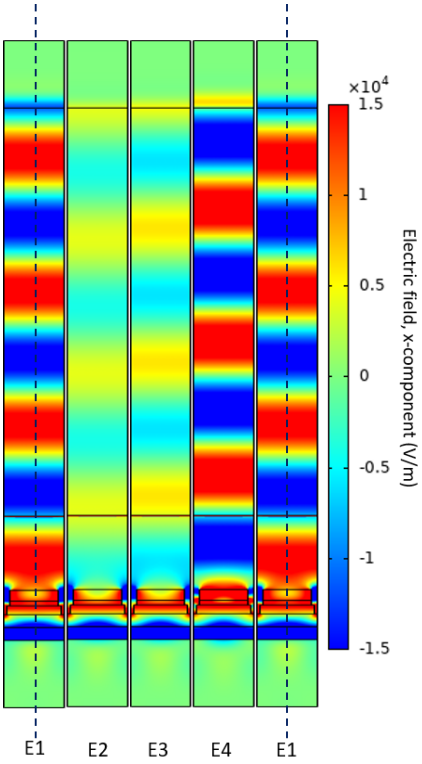

Figure 66. Electric field plots for each element of a 4-element unit cell, showing reflected intensity and phase. Each element is assigned a specific phase value in order to complete a continuous phase gradient. The phase value for each element is controlled in simulation by tuning *f*. Black dotted lines delineate a periodic unit cell. Layer thicknesses: VO_2 125 nm, Al_2O_3 55 nm, Al 100 nm; active element width 390 nm; Al wire width 440 nm, gap width 50 nm.

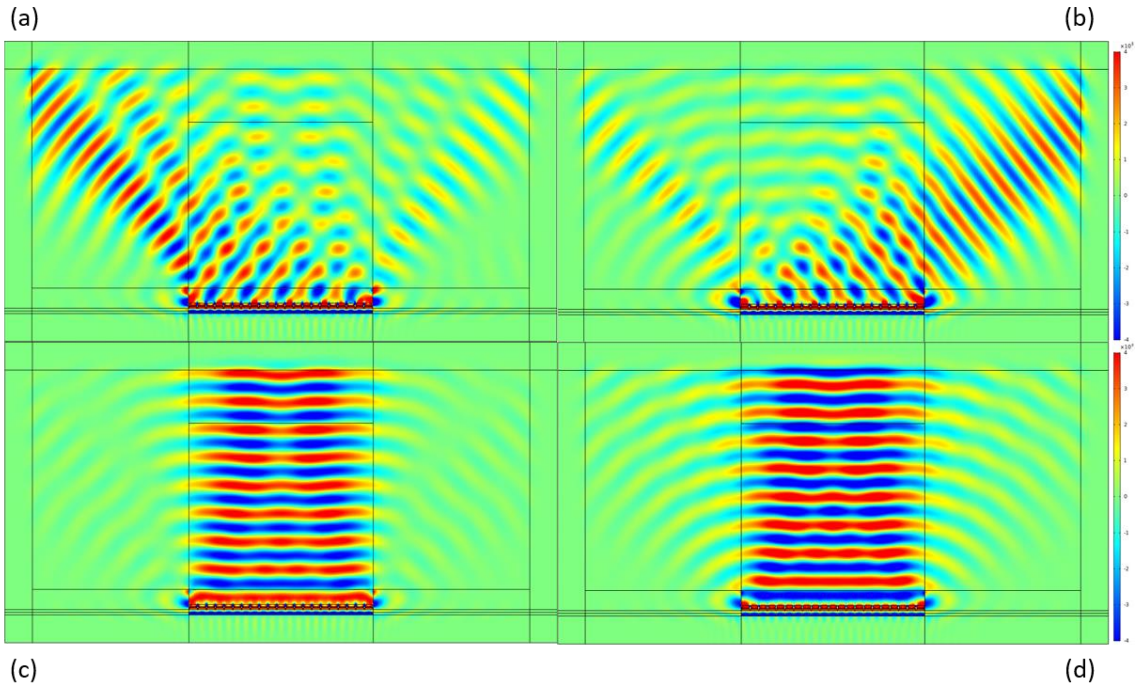

Figure 67. Electric field plots for a 21-element array comprised of 4-element unit cells. *f* values for each element are given in square brackets: (a) [0, 0.36, 0.42, 1...0], (b) [1, 0.42, 0.36, 0,…1], (c) [0, 0, 0, 0], (d) [1, 1, 1, 1]. The apparent difference in wavefront integrity between (a) and (b) demonstrates the importance of phase-matching end elements to substrate.